Transactions of the ASME

FLUIDS ENGINEERING DIVISION
Technical Editor
FRANK M. WHITE (1984)
Executive Secretary
L. T. NELSON (1984)
Calendar Editor
M. F. ACKERSON

Associate Editors
Fluid Machinery
AWATEF A. HAMED (1985)
WILLIAM E. THOMPSON (1984)
Fluid Measurements
THEODORE R. HEIDRICK (1984)
Fluid Mechanics
SHLOMO CARMI (1984)
CHARLES DALTON (1983)
KIRTI N. GHIA (1984)
THOMAS J. MUELLER (1985)
Fluid Transients
M. HANIF CHAUDHRY (1983)
Multiphase Flow
JOHN T. JUREWICZ (1985)
OKITSUGU FURUYA (1984)
Review Articles
RICHARD A. BAJURA (1985)

FOREIGN CORRESPONDENTS
Europe and Russia
JACQUES CHAUVIN
Europe and Russia
JOHN H. HORLOCK
India and Middle East
ARUN PRASAD
Japan and China
YASUTOSHI SENOO

BOARD ON COMMUNICATIONS
Chairman and Vice President
MICHAEL J. RABINS

Members-at-Large
W. BEGELL, J. CALLAHAN,
D. KOENIG, M. KUTZ, F. LANDIS,
J. W. LOCKE, J. ORTLOFF, C. PHILLIPS,
H. C. REEDER, K. REID

President, SERGE GRATCH
Executive Director
PAUL ALLMENDINGER
Treasurer,
ROBERT A. BENNETT

PUBLISHING STAFF
Mng. Dir. Publ., J. J. FREY
Dep. Mng. Dir. Publ.,
JOS. SANSONE
Managing Editor, CORNELIA MONAHAN
Editorial Production Assistant,
BETH DARCHI

The Journal of Fluids Engineering (USPS 278-480) is published quarterly for $72 per year by The American Society of Mechanical Engineers, 345 East 47th Street, New York, NY 10017. Second class postage paid at New York, NY and additional mailing offices. POSTMASTER: Send address changes to The Journal of Fluids Engineering, c/o THE AMERICAN SOCIETY OF MECHANICAL ENGINEERS, P.O. Box 3199, Grand Central Station, New York, NY 10163.
CHANGES OF ADDRESS must be received at Society headquarters seven weeks before they are to be effective. Please send old label and new address.
PRICES: To members, $36.00, annually: to nonmembers, $72.00. Single copies, $24.00 each. Add $6.00 for postage to countries outside the United States and Canada.
STATEMENT from By-Laws. The Society shall not be responsible for statements or opinions advanced in papers or . . . printed in its publications (B7.1, Par. 3).

INDEXED by the Engineering Index, Inc.

Journal of Fluids Engineering

Published Quarterly by The American Society of Mechanical Engineers

VOLUME 105 • NUMBER 2 • JUNE 1983

S. Fujii

M. Gomi

K. Eguchi

National Aerospace Laboratory,
Chofu, Tokyo, Japan

A Remote Laser-Probe System for Velocity and Temperature Measurements

This paper demonstrates the feasibility of simultaneously making velocity and temperature measurements by the combined use of a laser Doppler velocimeter and coherent anti-Stokes Raman scattering. The test area and control room were separated to avoid hostile surroundings in the combustion area. Data on probability density functions of velocity and temperature are given for reacting flows around a bluff-body flame stabilizer.

Introduction

Laser probe for use as a diagnostic tool for fluid problems has received much attention. LDV (Laser Doppler Velocimeter) has been widely utilized and continuously provides data on fluid velocities. CARS (Coherent Anti-Stokes Raman Scattering or Spectroscopy) also is a promising technique that can provide important passive scalar variables such as temperature, density, and major concentrations in a chemically reacting flowfield.

The LDV signal is generated by Mie scattering, an elastic collision process between laser light and seeded particles. In contrast, the CARS signal depends upon an energy exchange between laser light and the gas molecules to be detected. Therefore there is no necessity for seeding the particles. A benefit from selecting the CARS method, among the many Raman scattering techniques, is that a strong and coherent signal can be produced even in high interference situations. The theory and practical operation of both LDV and CARS have been discussed abundantly in the literature. For convenience, some of the plentiful references are cited herein for LDV [1-3] and CARS [4-8].

For the next step, it is possible that we conceive of a probe capable of simultaneously determining flow velocities and passive scalars in a nonintrusive manner. Such a development of light scattering measurements will lead to better understanding of the turbulence/combustion interaction and of heat/mass transfer mechanisms. Some attempts have already been reported [9-11], where the LDV and normal Raman scattering techniques, instead of CARS, were combined to furnish temperature-velocity correlation data.

The main thrust of this study is to realize a universal laser-probe system by a combined use of the LDV and CARS methods. The next aim is an extension of the work by the present authors, made on a bluff-body flame stabilizer [12, 13]. We will demonstrate the feasibility of an automated, remote LDV/CARS system and give some experimental data of pdf's (probability density functions) for the velocity and temperature in turbulent reacting recirculation flows.

Laser Aspects

Remote Transmitting and Receiving of Lasers for CARS. The CARS systems [6-8] have been applied to real-world applications, where the physical environment is often hostile to delicate instruments and high-powered lasers. For those experiments, Jet A liquid fuel, gasoline and H_2 - air diffusion mixture were employed, respectively, while the present authors used a premixed propane/air mixture to make flame. Furthermore, our test area was shared with many other combustion test facilities operated in parallel. Therefore, the noise and vibration, radicals and soot were much more intense in this experiment, and then a remote probing system was adopted for the CARS laser in determining temperatures. The

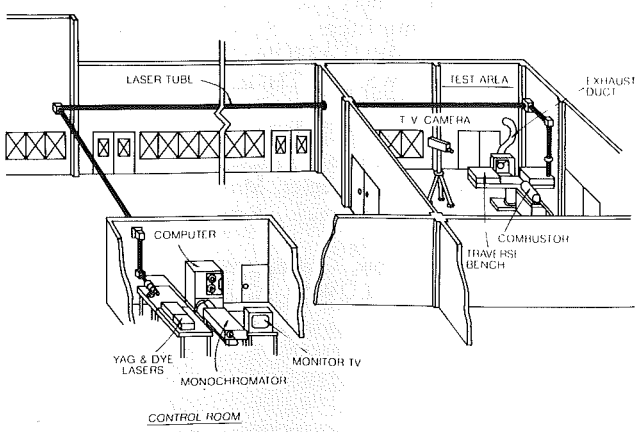

Fig. 1 Schematic of tubing for laser transmission, control room, and test area

Contributed by the Fluids Engineering Division for publication in the JOURNAL OF FLUIDS ENGINEERING. Manuscript received by the Fluids Engineering Division, February 4, 1982.

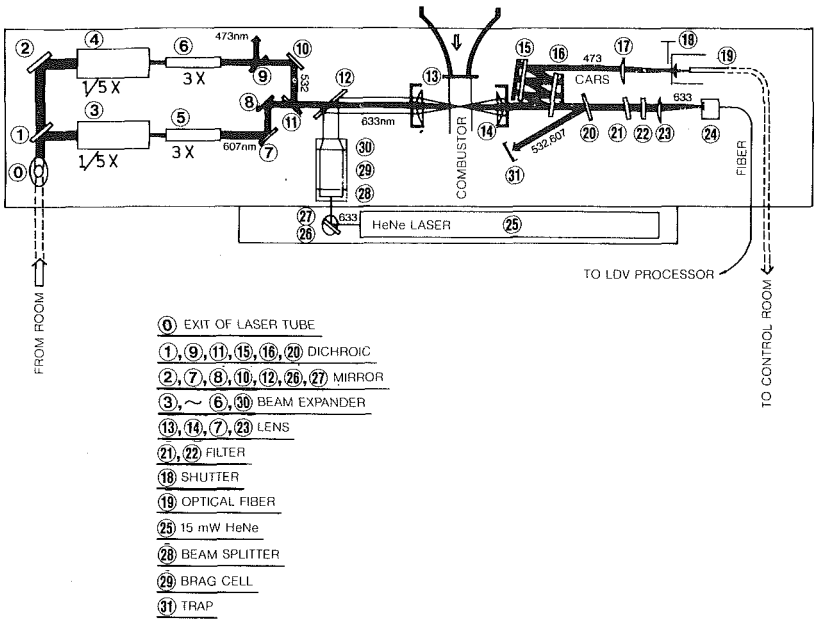

Fig. 2 Traverse bench and optical alignments

laser source and electronic equipment were placed in a room with benign surroundings and isolated from the combustion enclosure in the test area (Fig. 1). Laser beams necessary for the CARS signal were sent through a 150-mm dia steel pipe with mirrors equipped at all seven elbows. Most parts of the conduit were hung from the ceiling of the laboratory building. At the end of the 50-meter long pipe, the laser beams were delivered to a traverse bench. Due to the long distance travelled, very careful adjustments were required for every beam path. The mirrors used in the pipe were manually prealigned in three dimensions and multicoated to assure high transmission efficiency. Each mirror had a 98 percent reflection quality, coated for wavelengths of 530 to 620 nm.

The CARS signal generated on the traverse bench was transmitted back to the operator's room by an optical fiber running inside the laser conduit. A 100 μm core-diameter fiber was chosen as a tradeoff between signal/noise ratios and spectral resolution [14].

The Nd-YAG and dye laser system reported in reference [15], was upgraded to a system with a basic beam energy of 700 mJ/pulse (Molectron MY34 and DL-18). The fundamental wavelength of 1064 nm, 15 ns duration at 20 Hz, was sequentially doubled into two beams of green light (532 nm). A tunable dye was modified for use in broadband lasing and pumped by one of the green beams. The dye spectrum was centered at 606 nm of red light with about 6 nm full-width at half height (FWHH). The green and red lights thus generated were mixed in one beam for transmission. The beam diameter was enlarged at its source by a 3X telescope to reduce heat damage on the mirror surfaces.

LDV System. Our experience has shown that the LDV system is not sensitive to adverse physical surroundings characteristic of combustion areas, primarily because the Mie scattering technique does not require the use of a high-powered laser. Therefore, to avoid complexities, the LDV and its microprocessor were located as close as possible to the test stand. The LDV system employed in this experiment was the same as that reported in the references [12, 13, 16], except that a microprocessor replaced the minicomputer. The main feature is that an in-house processor was incorporated in the frequency tracker to achieve one validate signal per each particle. In order to sense reverse flows, velocity frequency offset was achieved by combining the primary and modulated beams at the detection volume where they generated moving fringes. Further details were given in references [12, 13, 17].

Optical Arrangements of CARS and LDV. On the traverse bench, (Fig. 2), all necessary optical elements were rigidly positioned by use of appropriate magnetic stands. For the CARS optical alignment, the transmitted beam made an appearance at the end of the pipe ⓪ and was again split into green and red light by dichroics ① and ②. During the passage of collinearly mixed green and red light, a rather strong CARS signal was produced from atmospheric nitrogen in the conduit. Therefore a dichroic ⑨ was set to eliminate the undesirable CARS signal in the green beam path. The signal split off in the red side was very weak and did not have an appreciable effect on the measurement. To make a final alignment, the green and red lights were again colinearly mixed at ⑪ and focused by the same lens ⑬ as that used in the LDV. The use of the same lens for both the CARS and LDV yielded a common focal point in space.

The focal length of the field lens ⑬, ⑭ was 104 mm. In front of lens ⑬, the beam diameters were evaluated as 3 mm (CARS) and 1 mm (LDV) at $1/e^2$ in assuming the Gaussian distribution of beam profiles. Sampling volumes were estimated as follows. First, the axial distance in generating the major CARS signal was determined from the experimental data on CARS signal attenuation levels when a CO_2 gas jet of different sizes was used at the focal point at room temperature. Next, other dimensions were calculated by use of such parameters as focal length, wavelength, beam diameter, and beam cross angle (for LDV). The results were 35 μm (dia.) and 10 mm (length) for the CARS and 60 μm $\times$ 0.3 mm for the LDV.

A 15-mW HeNe laser beam for the LDV was led by a two-fold reflection from the laser tube hung at the bench side and then split to achieve dual beam fringes at the sensing volume. The LDV signal generated was selectively passed through dichroic mirrors ⑯, ⑳, interference filters ㉑, ㉒, and finally received at a 100-MHz photomultiplier ㉔.

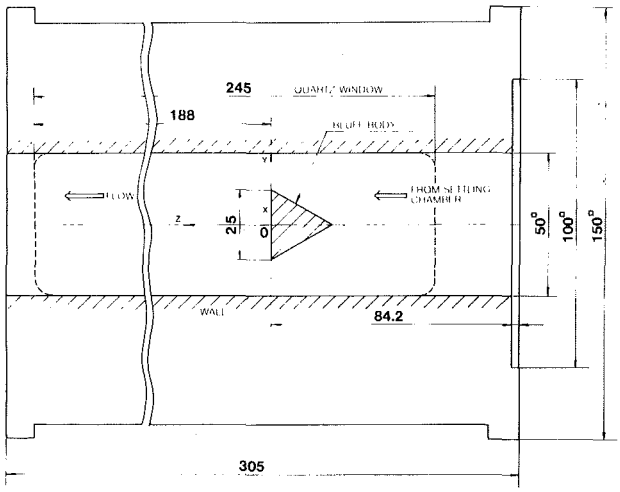

Fig. 3 Bluff-body combustor (units in mm)

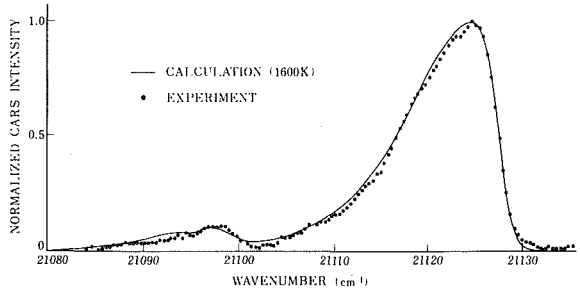

Fig. 4 Curve fitting of calculated spectrum to measured data (uncertainty of inferred temperature: ±30 degrees)

Data Acquisition System

The transmitted CARS signal was dispersed in a monochromator (Japan Spectro. Co. CT-100C, 1.0 meter, diffractive grating = 0.45 nm/mm). The slitwidth of the monochromator was set at 100 μm which coincided with the fiber diameter. As shown in Fig. 2 by two dichroics (15), (16), a novel means was used to separate the anti-Stokes signal from the pump and dye beams with multireflections on opposite sides of the dichroics. Because we used such a device together with the fiber coupling, there was no necessity for doubling the monochromator to reject stray light. The signal thus selected was sensed by an intensified vidicon and transferred onto a minicomputer disk with the help of an optical multi-channel analyzer (Princeton Appl. Research, OMA-2).

The main feature of the present system is that the computer was programmed to control the timing and number of both laser shots and data to be acquired. A set of the measured data by the CARS was stored on a magnetic tape of the minicomputer and then analyzed on a large-scale central computer to determine instantaneous temperatures.

The LDV data acquisition was made in the test area. A microprocessor with a floppy disk was used to compute a histogram of velocity probability density over 1000 events. The mean and turbulent velocity was determined with a high degree of confidence in the same manner as those of the references [12, 13, 16–18].

Experiment

Temperature Determination by CARS. Only minimal details of the CARS thermometry are given here, since the data collection/reduction are described in reference [15]. The present scheme depends entirely on a Q-branch broadband spectrum from atmospheric nitrogen which is a major inert gas in combustion flows. It is assumed that the CARS spectrum is only a function of gas temperature. Effects of pressure, of the rotational quantum number, of the Doppler broadening, and of the pump-laser bandwidth on the Raman spectral linewidth are neglected. The principle of the thermometry is to infer instantaneous temperature by giving the best fit of a calculated spectrum to an experimentally determined one. For molecules of large concentration, only a relative shape of the spectrum is needed to determine temperature because the spectrum may be almost free of nonresonant electronic contributions. In this experiment, therefore, measured intensities were normalized after subtraction of OMA background noise. The average number of photoelectrons was roughly 6000 per spectral interval at the peak of the whole Q-branch spectra and hence any error due to statistical fluctuations was not considered. To achieve a repetition rate of 20 Hz, a rather high scanning speed of 40 μs for one channel was chosen but with a reading of about 80 percent of the stored signal in a tube.

There are time-dependent variations in pulse-to-pulse energy levels of the Stokes and pump lasers. However, these variations can be removed by the normalization of each pulse because they contribute to absolute intensity rather than band profile. There may be more fluctuations in the dye signal that vary with time from one wavenumber to another. To compensate for such fluctuations, a reference cell using liquid water was employed in the basic system by the authors [15]. However, in a series of the tests made afterwards, there was only a slight difference found in the rms values of measured temperature with and without the employment of the reference cell. Furthermore, it required a rather lengthy time to make a precise adjustment of focal points and laser intensities in both the combustion gas and water cell, because we used the laser energy flux just below the breakdown limit. Therefore the water reference was not made in the present remote-probe system from a practical point of view.

Prior to all measurements, an experimental uncertainty for temperature repeatability was checked in quiescent room air. The calculated spectrum was convoluted by use of a Gaussian fit. A resolution of 2.0 cm^{-1} (FWHH) gave rise to the best fit. The test results was that a standard deviation of 100 event temperature histograms was about 30 degrees.

Burner and Test Procedure. A bluff body-flame stabilizer used in this experiment is reproduced in Fig. 3. The burner assembly was mounted on a two-demensionally translatable slide. Vertical movements were made by the traverse bench. It was positioned with a precision of 0.5 mm. Propane/air was premixed at different equivalence ratios and oncoming flow velocity was kept constant at 10 m/s in front of the bluff-body.

The main objective of the experiment was to simply make a simultaneous measurement of velocity and temperature by use of the common focal lens, when the low- and high-power lasers coexisted, together with illuminated seeded particles (TiO_2). Therefore to obtain data on velocity-temperature correlation was considered beyond the scope of this study. In the test, one hundred YAG laser pulses were fired at 20 Hz to complete a point measurement. In compliance with the CARS measurement time, care was taken to finish one thousand events of the LDV measurement in about five seconds. The set of 100 and 1000 events was chosen as a preliminary test result in which there was no appreciable change in the mean, rms, skewness, and flatness factors of histograms as the number of events increased beyond 100 for the CARS and 1000 for the LDV. It can be understood that the data obtained in this way was taken for almost the same sampling volume in space and for roughly the same time duration.

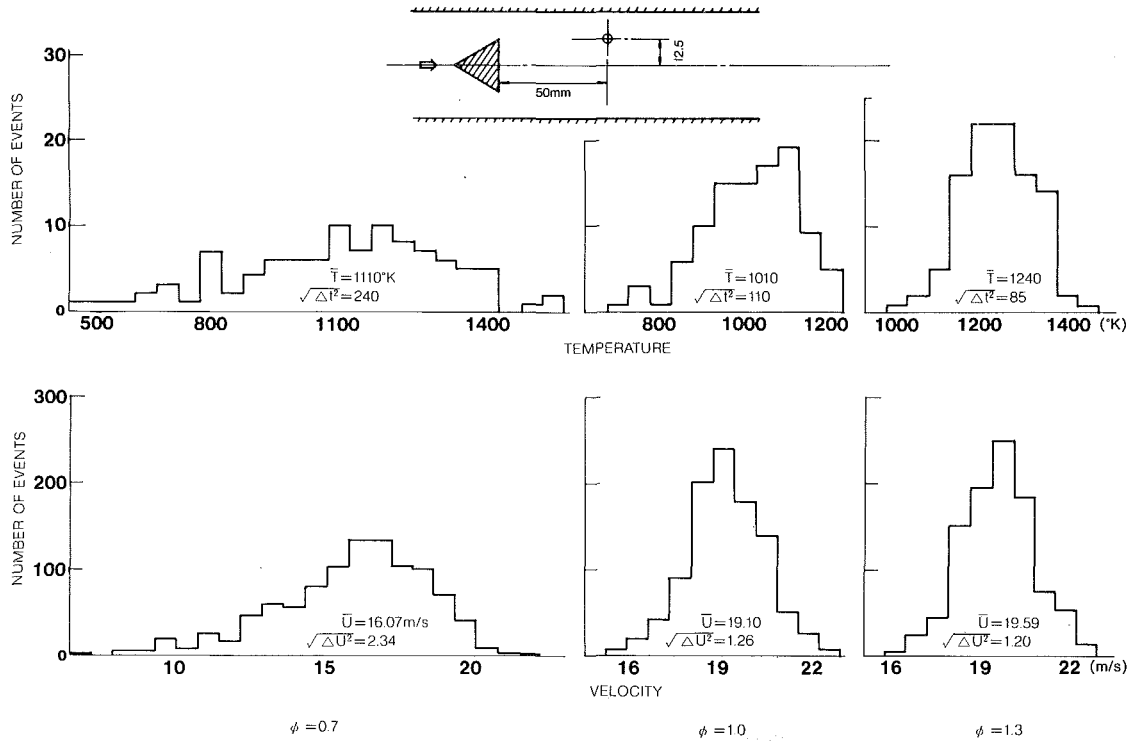

Fig. 5 Effect of equivalence ratios on temperature and velocity histograms (uncertainty of temperature: ±30 degrees; of velocity: ±0.2 m/s)

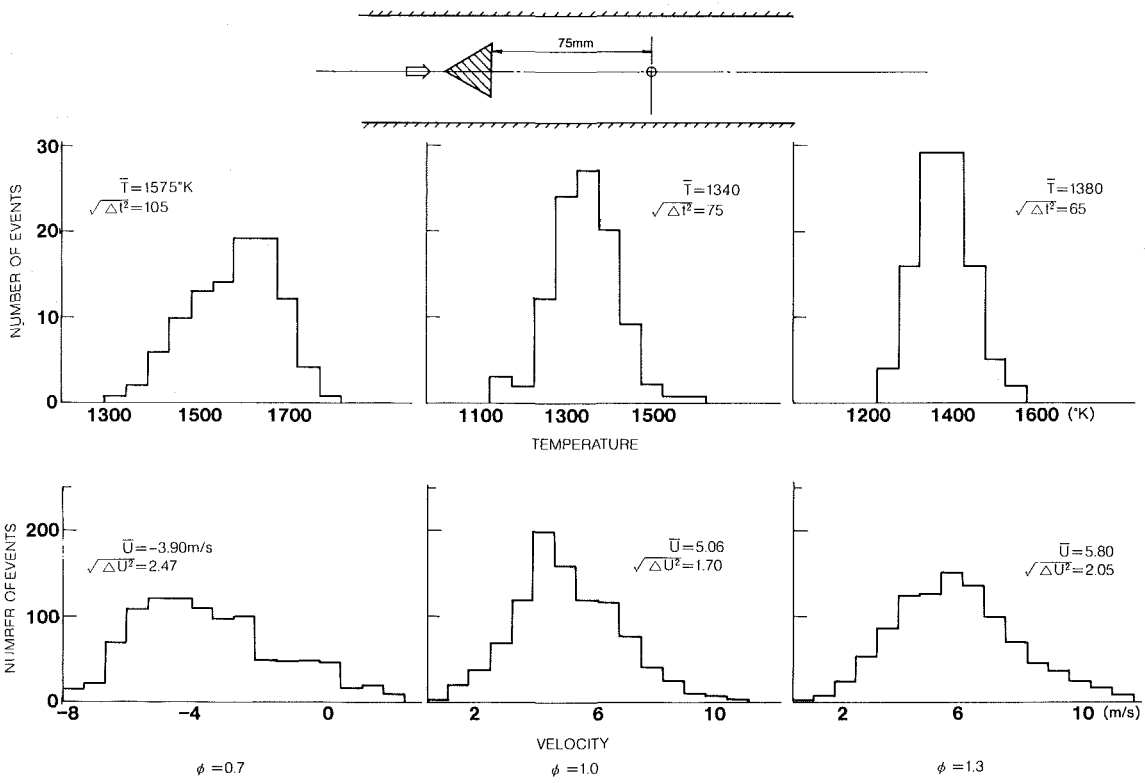

Fig. 6 Temperature and velocity fluctuations near rear the stagnation point of recirculating flow (uncertainty of temperature: ±30 degrees; of velocity: ±0.2 m/s)

Experimental Results and Discussion. Figure 4 is an example of the best-fit curve and the experimental data in the *Q*-branch spectrum, with an inferred temperature of 1600 K. The comparison method of using a whole spectrum could reduce the error due to a local scatter of the measured data.

Typical results are shown in Figs. 5 to 7, with each of the

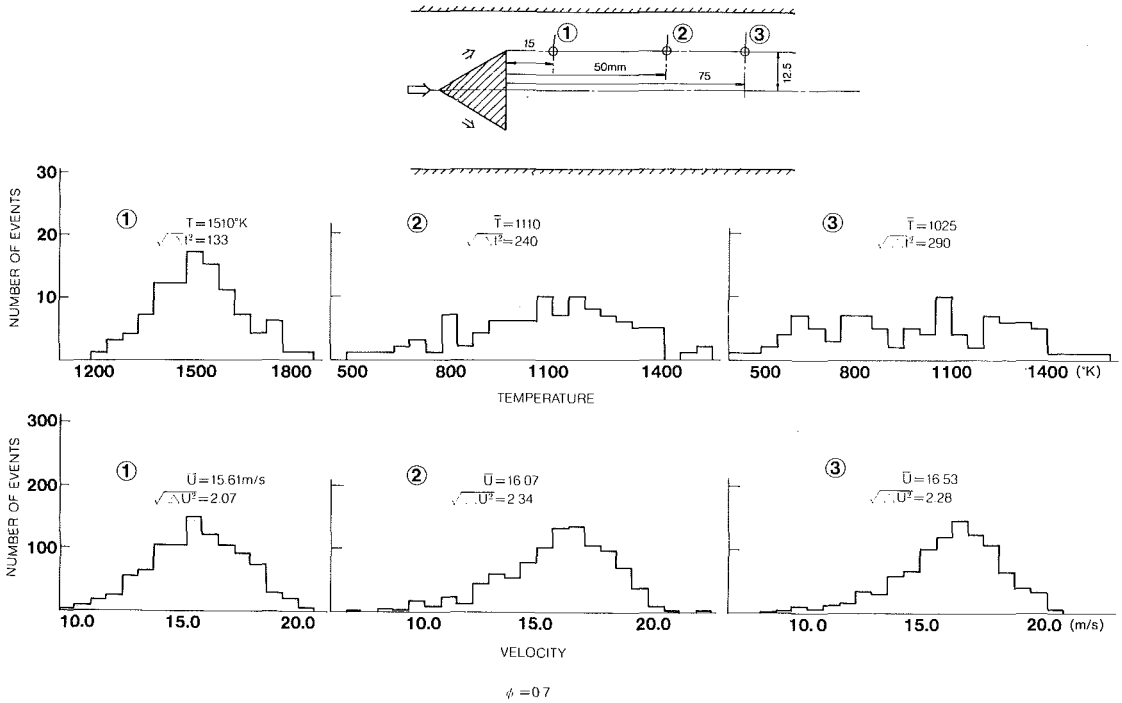

Fig. 7 Temperature and velocity data at ϕ = 0.7 with downstream traverse (uncertainty of positioning of measured point: 0.5 mm)

measuring points illustrated. The axis of the sampling volumes was parallel to the X axis of the holder rod (see Fig. 3). Mean and rms values also are indicated for each pair of temperature and velocity histograms. Velocity was measured only in the main-stream direction. During the tests, it was observed that yellow light was scattered from the illuminated seed particles, due to strong laser light incidence. However, any appreciable interference between the CARS and LDV measurements was not noticed. The actual power at the measuring point was approximately 8.5 mJ/pulse and 45 mJ/pulse for the Stokes and pump laser beams.

A visible flame was initiated at about 5 mm downstream from the flame holder face, for all fuel-air equivalence ratios (ϕ) tested. At ϕ = 0.7 the center of the visible blue flame was slightly V-shaped. As ϕ increased, the flame center became almost mainstream-wise and extended downstream considerably. Therefore the measuring points indicated in Figs. 5 and 7 were taken in the flame propagating zone, while that of Fig. 6 was for the postflame zone near the rear stagnation point of recirculating flows.

As demonstrated in Figs. 5 and 6, the temperature and velocity fluctuations concurrently were influenced by a change of equivalence ratios. It can also be said that the temperature histograms were very similar to the velocity ones, although both fields were drastically altered by varying the equivalence ratio. Almost the same pdf may be used in representing both temperature and velocity in this case. However, it should be noted that the repetition rate of data sampling was 20 Hz for temperature and roughly 200 Hz for velocity.

As ϕ = 0.7, Fig. 7, a traverse along the edge line was made in the middle of the flame zone to infer something about the turbulence/combustion interaction phenomena. At point ①, where combustion was at the initial stage with an attendant high-rate of chemical reactions, the temperature and velocity showed near Gaussian distributions. Toward downstream, but still in regions within the visible flame, as indicated by ②, ③, the main flow gradually intruded into the flame zone and therefore the mean temperature was lowered with a remarkably large rms value. It is clearly shown that cold and hot flows occasionally came into contact. This may be due to the existence of cold spikes and low temperature transients, in hot gas, as was pointed out [19]. At the far downstream point ③, where chemical reactions were probably slow but still taking place, the temperature and velocity histograms were of opposite polarities and showed considerably different pdf's. This observation may be an extreme case where significant inhomogeneities in temperatures could exist in a near Gaussian distribution of turbulent velocities. Further work is needed to obtain exact velocity-temperature correlation data.

Conclusions

We could demonstrate the feasibility of a computerized, remote laser-probe system by a combined use of LDV and CARS. The main features of the system are as follows: The high-power laser beams were transmitted for about 50 meters and then the CARS signal was sent back to the operator's room by fiber optics. The minicomputer controlled both the rates of the laser shot and data acquisition. A common focal lens was used at the measuring point for both CARS and LDV.

Data were obtained for recirculating turbulent reacting flows around the bluff-body flame stabilizer. The pdf's of the temperature and velocity were roughly similar except when temperature inhomogeneity was extremely significant. When the mainstream intruded in the flame zone, the temperature fluctuations became large due to cold spikes in the hot gas.

Acknowledgments

This study was supported in part by the Environmental Protection Agency of Japan. The authors express their thanks to Mr. Y. Jin, Nihon Kagaku Industry, for his helpful discussion.

References

1 Durst, F., Melling, A., and Whitelaw, J. M., *Principles and Practice of Laser-Doppler Anemometry*, Academic Press, 1976.

2 Buchhave, P., Delhaye, J. M., Durst, F., George, W. K., Refslund, K., and Whitelaw, J. H. (eds.), *Proceedings of the LDA-Symposium*, Copenhagen, 1975.

3 Eckert, E. R. G., (ed.), *Minnesota Symposium on Laser Anemometry*, Univ. of Minnesota, 1975.

4 Nibler, J. W., Saub, W. M., McDonald, J. R., and Harvey, A. B., "Coherent Anti-Stokes Raman Spectroscopy," *Vibrational Spectra and Structure*, ed. by During, J. R., Elsevier Sci. Publishing Co., 1977.

5 Druet, S. A. J., and Taran, J. P. E., "CARS Spectroscopy," *Progress in Quantum Electronics*, Vol. 7, No. 1, pp. 1-72, 1981, or ONERA T.P. 1982-1983.

6 Stenhouse, I. A., Williams, D. R., Cole, J. B., and Swords, M. D., "CARS Measurements in an Internal Combustion Engine," *Appl. Optics*, Vol. 19, 1979, pp. 3819-3825.

7 Eckbreth, A. C., "CARS Thermometry in Practical Combustors," *Comb. and Flame*, Vol. 39, 1980, pp. 133-147.

8 Switzer, G. L., Goss, L. P., Roquemore, W. M., Bradley, R. P., Schreiber, P. W., and Roh, W. B., "The Application of CARS to Simulated Practical Combustion Systems," *AIAA Jour. Energy*, Vol. 4, 1980, pp. 209-215.

9 Warshaw, S., Lapp, M., Penny, C. M., and Drake, M. C., "Temperature-Velocity Correlation Measurements for Turbulent Diffusion Flames from Vibrational Raman-Scattering Data," *Laser Probes for Combustion Chemistry*, ed. by Crosley, D. R., American Chemical Society, 1981.

10 Lederman, S., and Posillico, C., "Unified Spontaneous Raman and CARS System," *AIAA Journal*, Vol. 19, No. 6, 1981, p. 824.

11 Lederman, S., Celentano, A., and Glaser, J., "Temperature, Concentration, and Velocity in Jets, Flames, and Shock Tubes," *Phy. Fluids*, Vol. 22, No. 6, 1979, p. 1065.

12 Fujii, S., Gomi, M., and Eguchi, K., "Cold Flow Tests of a Bluff-Body Flame Stabilizer," ASME JOURNAL OF FLUIDS ENGINEERING, Vol. 100, 1978, pp. 323-332.

13 Fujii, S., and Eguchi, K., "A Comparison of Cold and Reacting Flows Around a Bluff-Body Flame Stabilizer," ASME JOURNAL OF FLUIDS ENGINEERING, Vol. 103, 1981, pp. 328-334.

14 Eckbreth, A. C., "Remote Detection of CARS Employing Fiber Optic Guides," *Appl. Optics*, Vol. 18, 1979, pp. 3215-3216.

15 Fujii, S., Gomi, M., and Jin, Y., "Instantaneous CARS Thermometry in Turbulent Flames," *Comb. and Flame*, Vol. 48, 1982, pp. 232-240.

16 Fujii, S., Eguchi, K., and Gomi, M., "Swirling Jets with and without Combustion," *AIAA Jour.*, Vol. 19, 1981, pp. 1438-1442.

17 Gomi, M., Kidawara, S., and Fujii, S., "A Method of Laser Velocimeter Data Processing," Nat'l Aerospace Lab. Tech. Report TR-521, 1978.

18 Fujii, S., Nishiwaki, H., and Takeda, K., "Suppression of Jet Noise Peak by Velocity Profile Reshaping," *AIAA Jour.*, Vol. 19, 1981, pp. 872-877.

19 Ho, C. M., Jakus, K., and Parker, K. H., "Temperature Fluctuations in a Turbulent Flame," *Comb. and Flame*, Vol. 27, 1976, pp. 113-123.

Interaction of an Acoustic Disturbance and a Two-Dimensional Turbulent Jet: Experimental Data

F. O. Thomas

V. W. Goldschmidt

School of Mechanical Engineering,
Purdue University,
West Lafayette, Ind. 47907

An experimental study was performed to determine the effects a periodic acoustic disturbance had upon a two-dimensional turbulent jet in both the initial and similarity regions. Correlation and energy spectra measurements in the initial region indicate that acoustic forcing within a certain frequency range is capable of restructuring the flow in this region. In particular, these measurements suggest the presence of vortical flow structures arranged symmetrically with respect to the jet centerline. Measurements of the mean and turbulent flow structure in the similarity region of the jet indicate strong acoustically induced effects. Evidence suggests that the interaction effects observed in the similarity region are intimately related to those in the initial region.

Introduction

It is a well known fact that the properties of jet flows may be altered by the application of some type of periodic forcing such as acoustic excitation. Early studies of the interaction between sound and jet flows usually involved the documentation of an acoustically induced early transition from laminar to turbulent flow [1–4]. More recently, studies have dealt with the effects of acoustic interaction on the structure of turbulent jets (such as increases in widening rate) [5, 6].

A detailed study of the response of a turbulent plane jet to acoustic excitation was performed by Chambers [7, 8]. It was found that acoustic fields of wide frequency range produced changes in the structure of the mean flow. Certain frequencies were found to increase the turbulent intensities and Reynolds stresses in the main region of the jet. It appeared that the effects of the acoustic interaction diminished with downstream distance. Chambers also concluded from his study that the interaction of the acoustic disturbance with the jet originates in the shear layers in the initial region of the flow.

Along with the recent recognition of quasi-deterministic vortical structures in the initial regions of turbulent jets have come studies of the effects of acoustic forcing upon these structures [9–13]. Evidence suggests that acoustic forcing strongly influences the initial region of jets through an augmentation of coherent structures. In fact some studies have essentially used acoustic forcing as a "tool" by which these structures may be enhanced for study.

The work to be presented describes the response of the planar jet to acoustic excitation. It is demonstrated that two-dimensional jets may be much more sensitive to external disturbances than the work by Chambers or Thompson [14] would suggest. Data are now presented which demonstrate the effect of acoustic forcing on vortical flow structures in the initial region, and the associated effects in the main region of the flow.

Experimental Set-Up

Figure 1 shows a schematic of the set-up. The air to the jet was powered by a large, adjustable centrifugal blower. A heat exchanger, large annular muffler and a chamber lined and partly filled with acoustic absorption material were upstream of the nozzle. The flow was controllable to within 1 percent of the desired operating value.

The plenum chamber contained three turbulence reducing screens and ended in a smooth two-dimensional contraction that accelerated the flow into another rectangular passage that led to the nozzle. This passage contained aluminum honeycomb as well as several turbulence reducing screens of various mesh sizes. Downstream of the final grid the duct formed a gradual two-dimensional contraction to the main nozzle. In all the experiments the jet was operated at a Reynolds number of approximately 6000 which corresponded to an exit velocity of 15.28 m/s (50.15 ft/s). The nozzle was 0.64 cm × 30.48 cm (0.25 in. × 12 in.). The confining plates extended 152 (5 ft) cm in the axial direction and were 91.4 cm (3 ft) wide. The nozzle consisted of a rapidly converging wall, with an additional 0.64 cm (0.25 in.) straight section prior to the point of exhaust. The nozzle exit boundary layers were laminar and agreed well with the Blasius flat plate solution. The free stream turbulence intensity at the jet exit was about 0.2 percent while the momentum thickness of the boundary layer at the nozzle exit was 86 μm. The exit velocity profile was flat away from the boundary layer and, hence, exhibited

Contributed by the Fluids Engineering Division for publication in the JOURNAL OF FLUIDS ENGINEERING. Manuscript received by the Fluids Engineering Division, July 27, 1981.

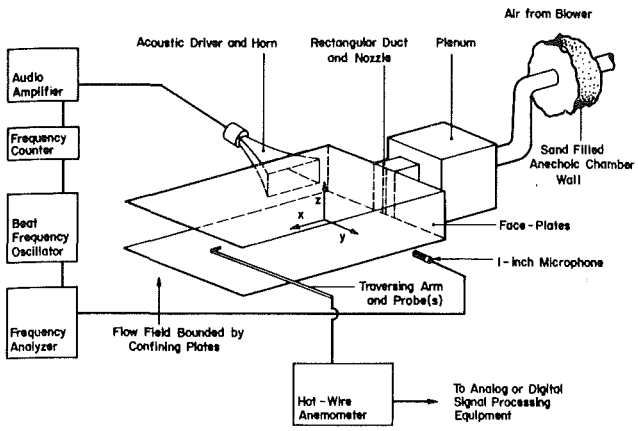

Fig. 1 Experimental apparatus

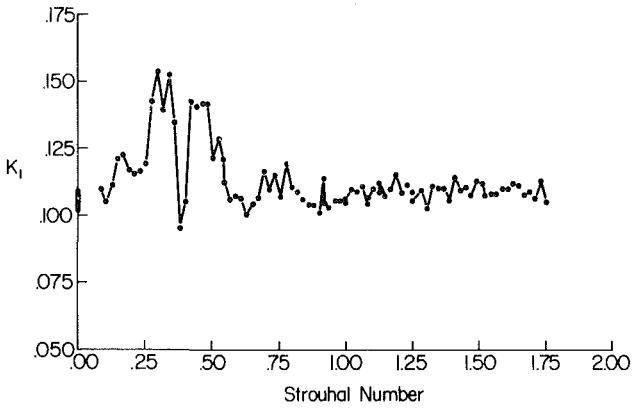

Fig 2 Strouhal number dependence on widening rate, K1 (uncertainty in the order of 7 percent)

the classic "top-hat" shape. The need to perform the acoustic interaction experiments in a quiet environment was met by utilizing a large anechoic chamber with dimensions of 3.66 m (12 ft) on each side.

The acoustic excitation was accomplished by means of a Bruel and Kjaer Beat Frequency Oscillator (type 1022) and an Altec 290E acoustic driver and horn assembly. The exit end of the horn was rectangular in shape with dimensions 18.42 cm (7.25 in.) by 48.26 cm (19 in.) and the width of the horn increased exponentially with distance along an axis perpendicular to its exit. The position of the horn relative to the flow field may be seen in Fig. 1.

In most of the tests the sound pressure level was kept constant. For this reason, a one-inch Bruel and Kjaer microphone was mounted at the edge of the flow field on the opposite side of the jet from the horn to monitor and set the sound pressure level at 105 dB SPL re $20\mu N/m^2$. Checks were made to confirm that the acoustic field was essentially planar. (Weak resonant modes were found, using phase-matched microphones, but sound pressure level profiles indicated that the planar mode, which was dominant throughout the region of primary interest, was primarily of the progressive wave type.) Measurements along the jet centerline from $x/D = 5$ to 75 showed values for the SPL that were essentially constant.

The level used for the disturbing signal was selected somewhat arbitrarily at the beginning of the study. Later checks confirmed that fortunately this level was close to that giving the maximum effects on the flow field. However, levels as low as 70 dB were tested and showed their ability to excite the same modes as now reported, and hence give credence to the generality of the trends observed. The data is submitted in two parts, one for the "similarity" region (for $X/D > 20$), the other for the "initial" region (for $X/D < 20$).

Measurements in the Similarity Region

(a) Widening Rates. The frequency range of the acoustic excitation was from 200 to 4200 Hz, which corresponds to a Strouhal number, St_D, range of 0.083 to 1.745. The widening rate at each excitation frequency was obtained from a series of six profiles (all obtained from pitot tube traverses) at different X/D stations within the similarity region of the jet in which

$$\frac{B}{D} = K_1\left(\frac{X}{D} + C_1\right) \tag{1}$$

The nondimensional widening rate, K_1, is shown as a function of excitation Strouhal number in Fig. 2; large increases in widening rate over the no sound values (those for which $St_D = 0$) are seen and these increases are frequency dependent. In some instances, such as near $St_D = 0.38$, there appears to be a slight suppression from the no-sound level; there is no clear reason for this although similar effects have been observed by others [4, 10]. Little variation in widening rate is observed for Strouhal numbers greater than 1.0. Particularly large increases are noted to be centered at Strouhal numbers of 0.29, 0.34, 0.42, and 0.48. The response of the jet is noted to be quite sensitive to excitation Strouhal number and increases in widening rate of up to 45 percent over no sound levels are observed. The extreme sensitivity of the mean flow to applied acoustic excitation over the indicated realm of frequencies is thus demonstrated.

(b) Turbulence Intensities. The longitudinal turbulence intensity $\sqrt{\overline{u^2}}/U_M$, was measured along the centerline of the jet under different applied acoustic excitation conditons. Conventional "straight wire" DISA 55F11 probes were used in conjunction with TSI 1050 series anemometers. Data were taken along the jet centerline from $X/D = 0$ out to $X/D = 75$ for the excitation conditions of no sound, 700 Hz ($St_D = 0.29$) and 1600 Hz ($St_D = 0.67$). The results of two separate trials of the experiment are shown in Figs. 3 and 4. Figure 4 shows a dramatic departure from the behavior noted in the first trial plotted in Fig. 3. As in the first trial, the 1600 Hz data increases most rapidly and shows values above the no-sound level for regions at least up to $X/D = 20$. However, the 700 Hz case shows different behavior for both trials. The data were repeatable once locking onto one of the modes took place.

In order to answer the question of how two apparently identical trials of the same experiment could yield such disparate results, a straight wire probe was mounted on the jet

Nomenclature

B = jet half-width, defined as the lateral location where $U = U_M/2$
C_1 = jet geometric origin
D = nozzle width
f_c = correlation function frequency
f_e = excitation frequency
St_D = Strouhal number $= Fd/U_0$
u = longitudinal velocity fluctuation
U = local mean velocity
U_M = local centerline mean velocity
U_0 = nozzle exit velocity
v = lateral velocity fluctuation
X = longitudinal coordinate
Y = lateral coordinate

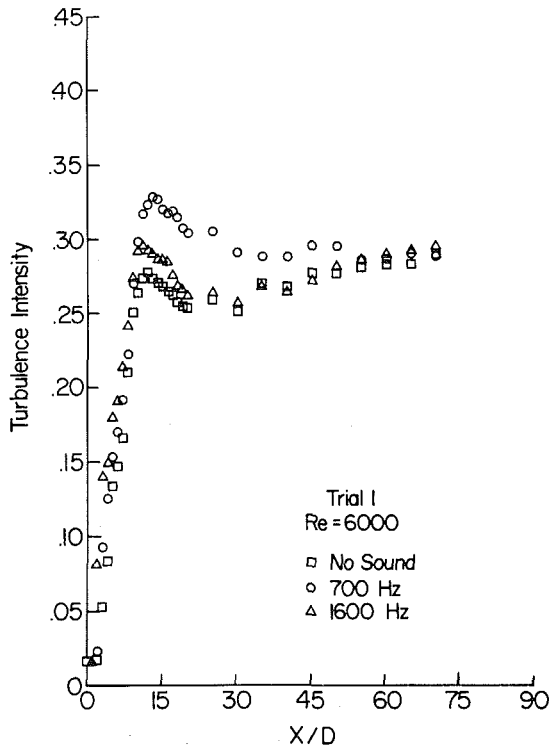

Fig. 3 Distribution of longitudinal turbulence intensity along the jet centerline (uncertainty in the order of 4 percent except for the 700 Hz case)

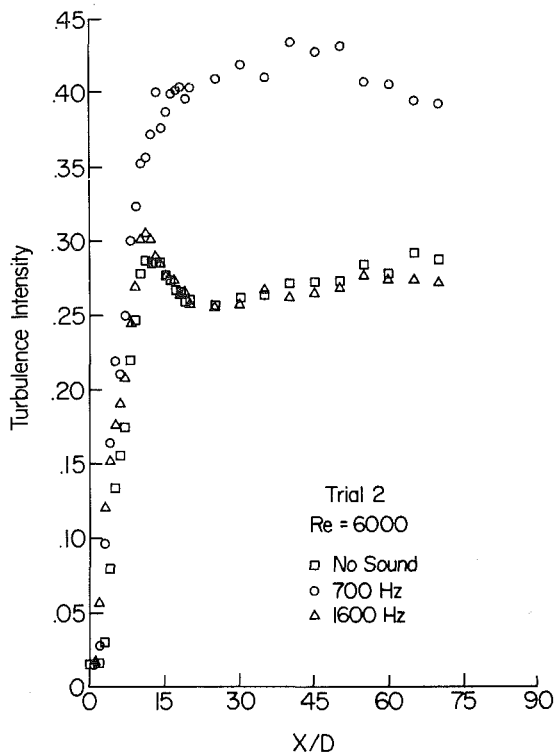

Fig. 4 Distribution of longitudinal turbulence intensity along the jet centerline (uncertainty in the order of 4 percent except for the 700 Hz case)

centerline at a special X/D position and the longitudinal turbulence intensity was measured as a function of excitation Strouhal number. Figure 5 shows the results of such measurements made at $X/D = 20$. It is seen that the application of sound can cause tremendous increases in the turbulence intensity levels. In addition, the response curve of the centerline turbulence intensity is highly correlated with the widening rate data shown in Fig. 2. These data indicate the extreme frequency selectivity of the turbulent structure of the jet. In particular regions of the plotted data it may be seen that small changes in Strouhal number can produce large changes in the corresponding turbulent intensity levels in the flow. This extreme sensitivity to the applied sound may well explain the anomalous behaivor noted in the experimental results plotted in Figs. 3 and 4, where wide variation was observed when the jet was excited at 700 Hz, which is equivalent to a Strouhal number of about 0.29.

Additional measurements of the effect of acoustic interaction of the turbulent structure of the jet were performed. The centerline variation of lateral turbulence intensity, $\sqrt{\overline{v^2}}/U_M$, was measured as well as lateral profiles of longitudinal intensity, lateral intensity, and nondimensional Reynolds stress at $X/D = 20$, 40, and 60. The acoustic excitation conditions were again no sound, 700 Hz and 1600 Hz. The measurements were made by utilizing a DISA 55A38 x-wire probe operated with two DISA 55D10 linearizers and TSI 1050 series anemometers. These measurements showed, in general, increased values of turbulence intensity and Reynolds stress for the 700 Hz excitation condition. Typically there were only small differences between the values obtained for the no sound and the 1600 Hz cases. However, suppression of the 1600 Hz case below no sound levels seemed to be associated with cases of highly enhanced 700 Hz values. Details of these measurements may be found in Thomas [15].

Measurements in the Initial Region

(a) **Space-Time Correlations.** Space-time correlations between the signals from two straight wire probes located at $X/D = 3$, and on opposite sides of the jet centerline at $Y/B = 1$ and -1 were taken. The probes were purposely located in the free shear layers which originated at the nozzle exit. A Saicor Sai-42 Correlation and Probability Analyzer was used to form the correlation function.

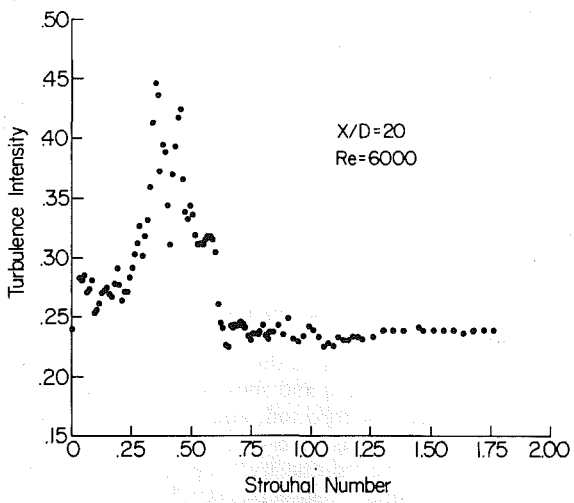

Fig. 5 Strouhal number dependence of centerline longitudinal turbulence intensity at $X/D = 20$ (uncertainty in the order of 4 percent except at highly elevated values)

The correlation functions were found to be periodic over a frequency range from 325 Hz to 1425 Hz which corresponds to a Strouhal number range from 0.135 to 0.592. It was over this range that terminology such as correlation function frequency, f_c as well as phase difference between successive maxima was applicable hinting at an orderly structure in the flow induced by the acoustic excitation. It is interesting to note that the range of excitation where the apparent ordering

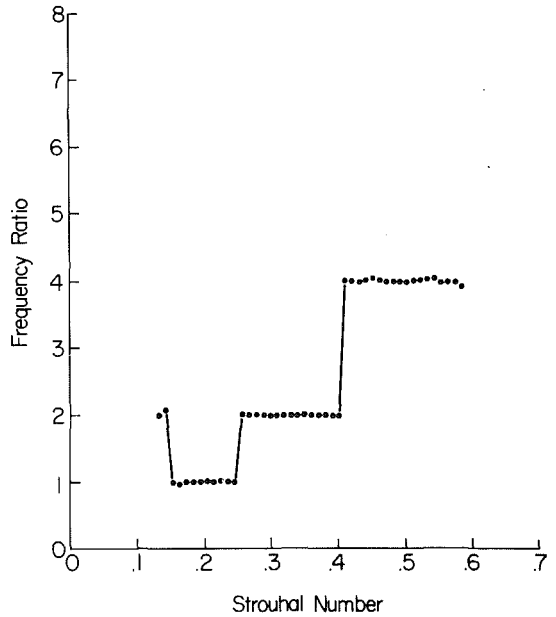

Fig. 6 Strouhal number, dependence of the frequency ratio, f_e/f_c

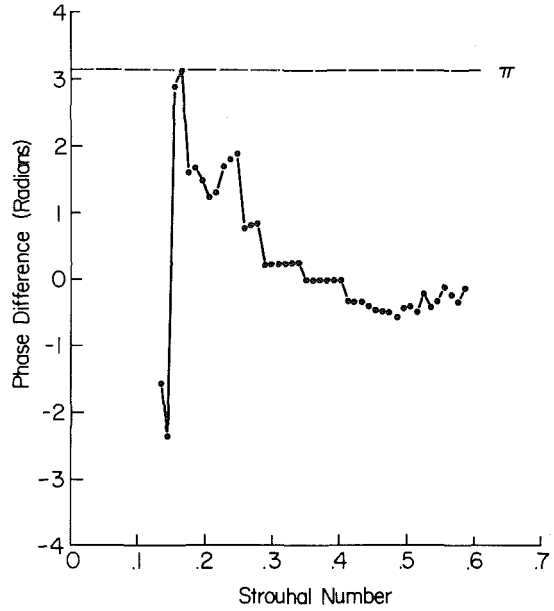

Fig. 7 Strouhal number (excitation) dependence of phase angle

of the flow occurred was the same range where most of the acoustic interaction "activity" was observed in the previous measurements.

The results of the space-time correlation measurements are shown in Figs. 6 and 7. It should be noted that the low frequency limit of the data presented was due to instrumental limitations and the nature of the response of the jet to excitation frequencies lower than the limiting value of this data is open to speculation. The upper limit of the data was determined to be the excitation frequency at which the correlation function was no longer periodic.

Figure 6 shows that the application of acoustic excitation to the jet over the range of frequencies indicated by the data has a profound impact on the organization and rate of creation of eddy structures in the flow. The correlation function exhibits frequencies that are equal to either 1, 1/2, or 1/4 times the excitation frequency. The frequency ratio is observed to vary with excitation Strouhal number in a step-wise manner; the acoustic excitation organizes the flow and regulates the frequency of formation of structures whose passage results in the measured periodic correlation functions. From these data it would appear that there exists a preferred frequency of formation of eddy structures in the initial region of the jet. Forcing the jet acoustically at frequencies other than the preferred frequency results in the jet shifting to a formation frequency that is a harmonic or subharmonic of the preferred frequency (see, also, [11]).

The phase relationship between the two anemometer signals at $X/D = 3$ is plotted as a function of excitation Strouhal number in Fig. 7. From this plot it may be observed that the anemometer signals are initially on the order of $\pm\pi$ radians out of phase. For higher excitation frequencies the data show a tendency toward smaller phase angles. It may be noted that the drop to smaller phase angles tends to occur in rather discrete steps. For a wide range of excitation frequencies, the two hot wire signals are seen to be at least approximately in phase. It appears then, that the application of acoustic excitation to the jet organizes the eddy structures discussed previously in such a way that they are axisymmetrically distributed. It is of interest to note that the region of excitation frequency which displays the near zero phase angles is associated with the greatest jet widening rates and highest longitudinal turbulence intensities displayed in Figs. 2 and 5, respectively. Thus, it appears that the interaction effects that have been measured in the main region of the jet are related to the ordering of the flow in the initial region.

In another experiment the probe pair was moved downstream in an effort to determine how the correlation function for selected excitation frequencies changed with downstream distances. The excitation frequencies of 700 Hz and 900 Hz were chosen for these measurements. The 700 Hz frequency was selected because detailed measurements of widening rate and turbulence intensity were made at this frequency which has also within the range where the correlation function was periodic. The 900 Hz frequency was chosen because it was near the center of the frequency range where the correlation function showed periodicity. The correlation functions in this region of excitation frequency also exhibited the greatest amplitudes.

The measurements were made at selected downstream positions with the probes on opposite sides of the jet centerline, just as they were for the experiments which were done at $X/D = 3$. Downstream correlation measurements were made until further increases in X/D resulted in the loss of periodicity of the correlation function.

The results are shown in Figs. 8 and 9. Figure 8, at least for the higher excitation frequency, shows a sudden change in the correlation frequency with $X/D = 7$. This may understandably correspond to the end of the potential core and the merging of the two shear layers originating at the mouth of the jet. In spite of the high background turbulence developing, there is a measurable periodicity of the pattern excited by the 900 Hz frequency as far downstream as $X/D = 14$. The periodicity for the 700 Hz excitation, however, was either lost in the background noise at around an X/D of 6 or did not surface beyond the merging of the shear layers. The permanence of a symmetric pattern, for at least these two excitation frequencies leading to notable increases in the widening rates, is shown in Fig. 9. This is to be compared with the recognition that for undisturbed jets there is at best a weak correlation corresponding to antisymmetric patterns [11, 12].

(b) **Energy Spectra.** In order to further quantify the nature of the flow in the initial region of the jet, measurements were made of the energy spectra of the longitudinal velocity fluctuations. the measurements were made with a straight wire probe placed at $X/D = 3$, $Y/B = 1$. This probe was operated in conjunction with a Thermo

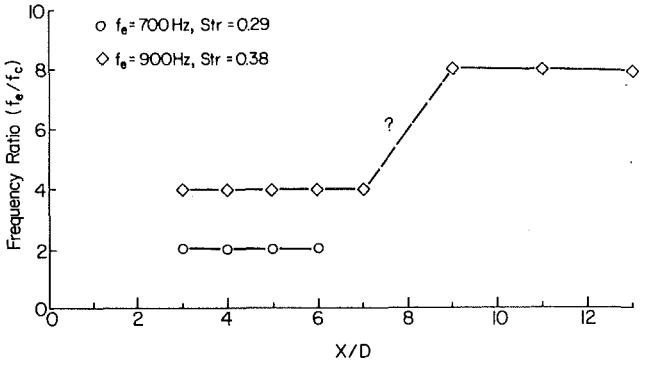

Fig. 8 Dependence of frequency ratio on downstream distance

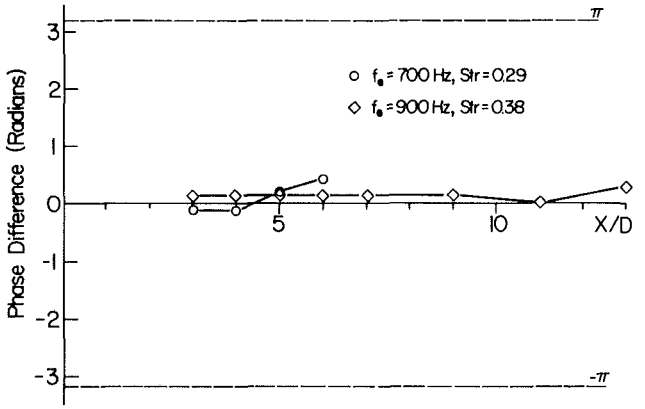

Fig. 9 Dependence of phase angle on downstream distance

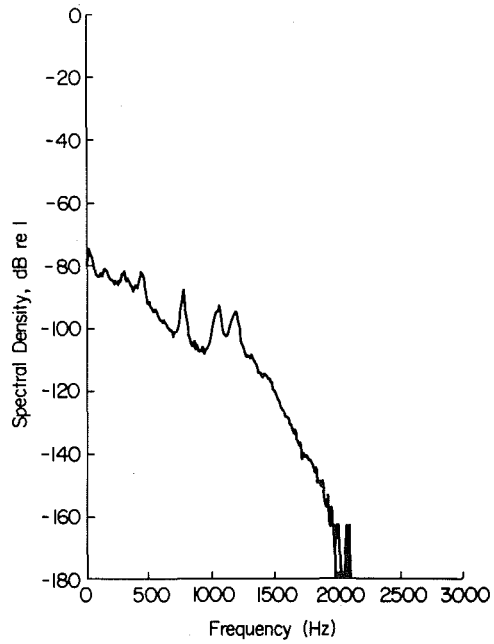

Fig. 10 No sound spectrum at $X/D = 3$, $Y/B = 1$ (frequency resolution is of 10 Hz; ordinate scale is arbitrary)

Systems Model 1050 Anemometer. A Hewlett-Packard 5450A Fourier Analyzer System was used to compute the spectrum. It must be noted that the resulting spectra were not normalized.

The no sound spectrum is shown in Fig. 10. This spectrum is observed to have a broadband appearance with the exception of peaks which are observed at 425, 760, 1040, and 1180 Hz (corresponding to Strouhal numbers of .18, .31, .44, and .49, respectively.). The 700 Hz case spectrum is shown in Fig. 11. It can be seen from this figure that the application of an acoustic disturbance to the jet has altered the nature of the energy spectrum. The general broadhead appearance which characterized the no sound spectrum is observed to give way to a spectrum which contains discrete peaks superimposed on a broadband background. In particular, the peak that occurs at the first subharmonic of the excitation frequency, 350 Hz, is by far the largest. There is also a substantial peak at 700 Hz and higher harmonics are present. Their amplitudes are quite small and they are most likely Fourier components that result from the distorted sinusoidal anemometer signals that characterize the excited flow in this region.

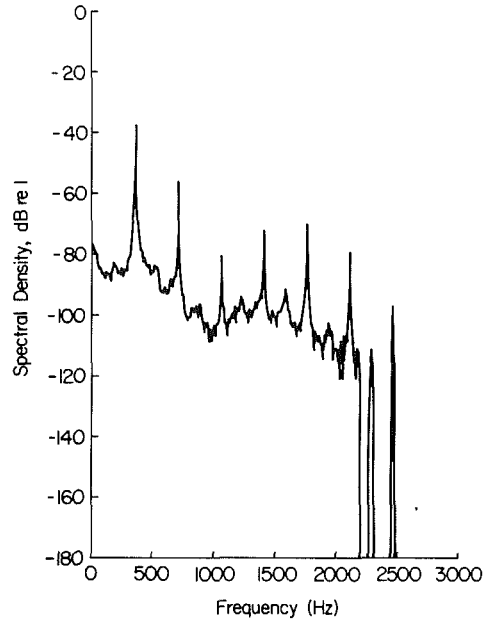

Fig. 11 700 Hz spectrum at $X/D = 3$, $Y/B = 1$ (frequency resolution is of 10 Hz; ordinate scale is arbitrary)

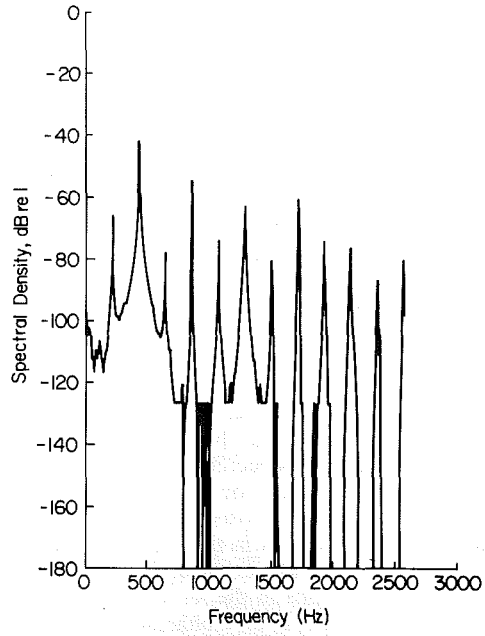

Fig. 12 850 Hz spectrum at $X/D = 3$, $Y/B = 1$ (frequency resolution is of 10 Hz; ordinate scale is arbitrary)

The most dramatic effects are observed when the jet is excited at 850 Hz, (St_D = 0.36), as may be noted from Fig. 12. Nearly all of the fluctuation energy is contained in the first subharmonic of the excitation frequency, 425 Hz (St_D = .18). The broadhead portion of the spectrum is lost and the flow is even more ordered than in the previous case.

Additional spectra showed that the more ordered the flow was (in the spectral sense), the closer it was to having its primary peak near 425 Hz. in other words, the spectra were most ordered when the jet was excited at a frequency close to 850 Hz.

Summary and Conclusions

The widening rate data showed the greatest increases for excitation centered about Strouhal numbers of about 0.34 and 0.42. This compares well with the enhanced jet widening which was observed by Kaiser [6] in a two-dimensional jet at a Strouhal number 0.42 and by Chambers [8] at 0.38. However, the increases noted in this work were generally of far larger amplitude.

The increases in widening rate are accompanied by increases in the measured turbulence intensities which, when plotted as a function of Strouhal number, directly parallel the frequency response of the widening rate data, the largest increases occurring at St_D equal to 0.34 and 0.44.

Measurements in the initial region indicate a restructuring of the flow due to the application of acoustic excitation.

Of significance is the fact that the frequency range over which both the correlation functions and energy spectra obtained in the initial region of the jet show the greatest changes is the same as the range which produces the largest effects on widening rate and turbulence intensity in the main region. The organization imparted to the flow in the initial region is directly related to the effects that are measured downstream in the main region of the flow.

Certain characteristics of the large scale turbulent structures are noted under the presence of acoustic excitation frequencies leading to increased widening rates. These structures appear to move from an antisymmetric array to a symmetric pattern as the excitation frequencies enter the range of notable increases in the widening rate. Simultaneously, the structural frequency in the initial region (seen as a periodicity in the correlation function of the velocity on opposite sides of the jet) is noted to be given as even fractions of the excitation frequency, decreasing as the excitation frequency increases in the sensitive range. There is also evidence that in some instances the structural frequency is halved as the shear layers merge at X/D = 6 to 7. The spatial coherence of the structures was observed to depend strongly upon the excitation frequency. For certain frequencies, the periodic correlation function was lost near the end of the potential core, while at others it was sustained into the nearly self-preserving region.

It was found from the space-time correlation measurements that a characteristic structure passage frequency exists for excitation in the "sensitive region" and corresponds to a Strouhal number of approximately 0.2. The jet always responded to acoustic excitation within this region by forming structures at or near this frequency. Maximum interaction effects were obtained when the jet was excited at frequencies whose first subharmonic was near this structure passage frequency in the initial region. The spectral measurements show that frequencies of excitation in the "sensitive region" lead to the formation of a strong peak at the first subharmonic which dominates the spectrum. The strength of this peak is greatest when it occurs at the preferred passage frequency that was found to characterize the correlation measurements.

Acknowledgments

The work reported was sponsored, in part, by the ONR. Their support is gratefully acknowledged.

References

1 Brown, G. B., "On Vortex Motion in Gaseous Jets and the Origin of their Sensitivity to Sound," *Phys. Soc. of London Proc.*, 47, 1935, pp. 703–732.

2 Sato, H., "The Stability and Transition of a Two-Dimensional Jet," *J. Fluid Mech.*, Vol. 7, No. 1, 1960, pp. 53–80.

3 Sato, H., and Sakao, F., "An Experimental Investigation of the Instability of a Two-Dimensional Jet at Low Reynolds Numbers," *J. Fluid Mech.*, Vol. 20, No. 2, 1964, pp. 337–352.

4 Chanaud, R. C., and Powell, A., "Experiments Concerning the Sound-Sensitive Jet," *J. Acoustical Soc. of Am.*, Vol. 34, No. 7, 1962, pp. 907–915.

5 Becker, H. A., and Massaro, T. A., "Vortex Evolution in a Round Jet," *J. Fluid Mech.*, Vol. 13, No. 3, 1968, pp. 435–448.

6 Goldschmidt, V. W., and Kaiser, K. F., "Interaction of an Acoustic Field and a Turbulent Plane Jet: Mean Flow Measurements," *AICHE, Chem. Eng. Prog. Symp. Series*, Vol. 67, 109, 1971, pp. 91–98.

7 Chambers, P. W., "Acoustic Interaction with a Turbulent Plane Jet," Ph.D. thesis, Purdue University, 1977.

8 Chambers, F. W., and Goldschmidt, V. W., "Acoustic Interaction with a Turbulent Plane Jet - Effects on Mean Flow," AIAA-81-0057, 1981.

9 Crow, S. C., and Champagne, F. H., "Orderly Structure in Jet Turbulence," *J. Fluid Mech.*, Vol. 48, No. 3, 1971, pp. 547–591.

10 Rockwell, D. W., "External Excitation of Planar Jets," *Journal of Applied Mechanics*, Vol. 39, No. 4, 1972, pp. 883–890.

11 Kibens, V., "Discrete Noise Spectrum Generated by an Acoustically Excited Jet," presented at the 5th Aeroacoustic Conference of the American Institute of Aeronautics and Astronautics, Seattle, Wash. 1979.

12 Zaman, K. B. M. Q., and Hussain, A. K. M. F., "Vortex Pairing in a Circular Jet Under Controlled Excitation. Part 1. General Jet Response," *J. Fluid Mech.*, Vol. 101, No. 3, 1980, pp. 449–491.

13 Hussain, A. K. M. F., and Zaman, K. B. M. Q., "Vortex Pairing in a Circular Jet Under Controlled Excitation. Part 2. Coherent Structure Dynamics," *J. Fluid Mech.*, Vol. 101, No. 3, 1980, pp. 493–544.

14 Thompson, C. A., "Organized Motions in a Plant Turbulent Jet Under Controlled Excitation," Ph.D. thesis, University of Houston, 1975.

15 Thomas, F. O., "Effect of Nozzle Geometry on Acoustic Interaction with a Turbulent Plane Jet," M.S. thesis, Purdue University (also prepared as Herrick Laboratories Report HL 80-32), 1980.

16 Cervantes de Gortari, J., and Goldschmidt, V. W., "The Apparent Flapping Motion of a Turbulent Plane Jet - Further Experimental Results," ASME 80-WK/FE 13, 1980.

17 Oler, J. W., "Coherent Structures in the Similarity Region of a Two-Dimensional Turbulent Jet: A Vortex Street," Ph.D. thesis, Purdue University (also prepared as Herrick Laboratories Report HL 80-6), 1980.

Effects of Turbulence on the Pressure Distribution Around a Square Cylinder and Possibility of Reduction

K. C. S. Kwok
Lecturer, School of Civil and Mining Engineering, The University of Sydney, Australia

When a prismatic structure is subjected to air flow, especially at small angle of wind incidence, the separated shear layers may reattach onto the streamwise surface. The turbulent mixing in the shear layers and the extrainment of fluid results in highly fluctuating and strongly negative pressures under the reattaching shear layers. Wind tunnel tests were carried out to determine the pressure distribution around a square cylinder. It was found that an increase in turbulence, in particular fine scale turbulence, significantly altered the pressure distribution, the transverse force characteristic, and hence the galloping behavior of the square cylinder. When small vanes were fitted to the corners of the cylinder, and by maintaining a vent between the vane and the corner, the magnitude of the negative mean and peak pressure coefficients under the shear layer were substantially reduced.

Introduction

The pressure distribution around structures, such as tall buildings and structures and various types of roof structures, has been the subject of numerous studies in recent years. Many of these pressure characteristics appear to be associated with the behavior of the shear layers separating from the leading edge of the structure and in particular the tendency of the separated shear layers to reattach intermittently onto the surface of the structure at small angle of wind incidence. Very high negative pressures could occur in the region near the leading edge under the reattaching shear layer.

A hypothesis relating the high negative pressures and the behavior of the separated shear layer was proposed by Melbourne [1]. The development of this hypothesis was influenced by the work of Gartshore [2] who studied the effects of turbulence on the drag and base pressure of prisms. Melbourne's hypothesis, as shown diagrammatically in Fig. 1, suggested that the separated shear layer and the pressure underneath fluctuate, and for certain conditions of freestream turbulence, angle of wind incidence, (and radius of leading edge curvature) the shear layer commences to occasionally reattach onto the surface. As this occurs, the cavity region under the shear layer, which is often referred to as a separation bubble, is no longer vented to the freestream. As freestream flow over the front of the shear layer accelerates, the increased velocity is accompanied by a decrease in pressure. This decrease in pressure causes the intial radius of curvature of the shear layer to decrease which in turn increases the local freestream velocity outside the shear layer and further decreases the pressure. The freestream turbulence of the flow also produces intense turbulent mixing in the shear layer and entrainment of fluid from inside the bubble into the shear layer. The combined effect of entrainment and a decrease of pressure at the boundary causes the reattached shear layer to move forward towards the leading edge and this produces a reduction in bubble volume and internal pressure. This is an unstable process which proceeds until the shear layer breaks up into a complete separation again and the cavity becomes vented.

The failure of flat roofs on low rise structures and window panels on tall buildings are known to have been caused by the occurrence of very high negative pressures on streamwise surfaces near a leading edge. Some evidence has been

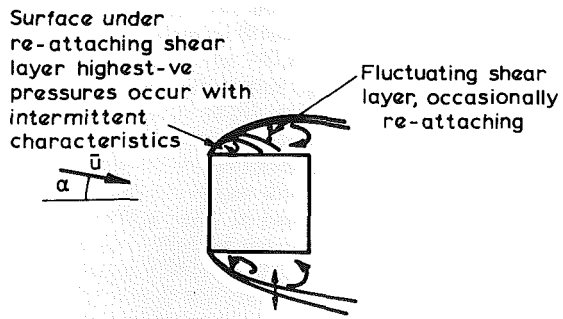

Fig. 1 Region of high negative pressures caused by a reattaching shear layer

Contributed by the Fluids Engineering Division for publication in the JOURNAL OF FLUIDS ENGINEERING. Manuscript received by the Fluids Engineering Division, June 31, 1981.

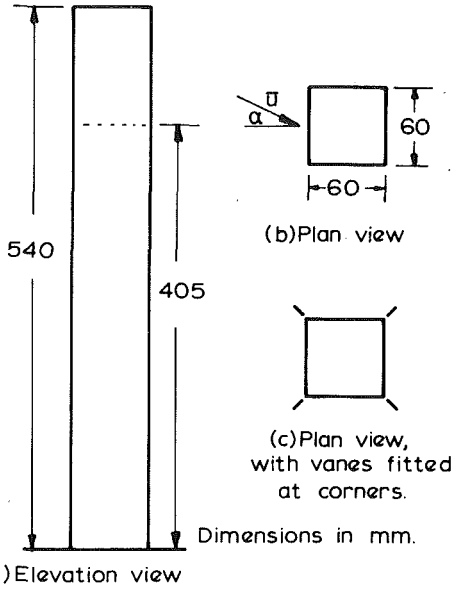

Fig. 2 Sketches of the square cylinder tested in wind tunnel

presented by Melbourne [1] and Sharp [3] that indicate the forward travel of the reattaching shear layer and the occurrence of very high negative pressure peaks near the leading edge. It was also shown that these negative pressure peaks could be substantially reduced (in magnitude) by venting the bubble under the reattaching shear layer.

One of the effects of a reattaching shear layer is to cause galloping, which results in large amplitude cross-wind oscillations for a number of bluff bodies (Parkinson [4, 5]; Novak [6, 7, 8], and others). It can be shown that in the presence of a wind normal to a face, any cross-wind motion of the structure (which effectively creates an angle of wind incidence) will create a pressure distribution around the section which results in a transverse force F_y in the direction of the motion so that the cross-wind displacement increase further. A positive slope of the transverse force coefficient $dC_{Fy}/d\alpha > 0$ is a well known criterion for galloping instability.

It is more convenient to express this aerodynamic force as an equivalent aerodynamic damping. For a vertical structure with a height h, a constant square cross section with sides b, uniform mass distribution, and which is exposed to a turbulent boundary layer flow, as a first approximation in which nonlinearity is neglected, the equivalent aerodynamic damping for the complete structure is, [9]:

$$\zeta_a = -\frac{3\rho}{8\pi\rho_s(3+\gamma)} \cdot \frac{\bar{u}(h)}{n_0 b} \cdot \frac{dC_{Fy}}{d\alpha} \tag{1}$$

the value ρ_s = mass density of the structure, n_0 = natural frequency of the structure, and γ = exponent of a power law expression of the longitudinal velocity profile of the turbulent boundary layer flow. If the equivalent aerodynamic damping is negative so that the resultant damping, that is aerodynamic plus structural damping ζ_s, is zero or negative, the cross-wind response amplitude of the structure will grow until it reaches a steady magnitude governed by the nonlinearity of the aerodynamic damping.

Turbulence intensity and the scale of turbulence of the wind flow have very significant effects on the pressure distribution and hence the galloping behavior of bluff bodies (Laneville and Parkinson [10]; Novak [7]; Barriga et al. [11]; Miyata and Miyazaki [12]; Kwok and Melbourne [13]; and others). To produce these effects, it was suggested by Gartshore [2] and Kwok and Melbourne [13] that an increase in freestream turbulence, and in particular fine scale turbulence, increases the turbulent mixing in the separated shear layer and the rate of entrainment of fluid from the wake, and decreases the radius of curvature of the shear layer, thus promoting earlier reattachment.

Experimental Arrangements

Experiments were carried out in the 2.4m × 2.0m boundary layer Wind Tunnel at the School of Civil and Mining Engineering, the University of Sydney. A rigid "perspex" model 0.54m high and 0.06m square ($h:b = 9:1$), as shown in Fig. 2, was mounted on a turntable in the working section. In some tests, small vanes made of 5mm wide strips of steel were fitted to the corners of the square cylinder. These vanes were adjustable, so that a small gap could be introduced between the vane and the corner.

The surface pressures at a height of 0.405m (3/4 cylinder height) were measured at a number of pressure taps around the square cylinder. These pressure taps consisted of a small length of 1.5mm O.D. stainless steel tubing fitted flush with the surface of the model. These were connected to a Setra 237 Pressure Transducer (a Celesco Pressure Transducer was used in some earlier tests) via 600mm long, 1.5mm I.D. PVC tubing. With restrictors fitted halfway in the tubing, the frequency response was flat (to about ±15 percent) up to 80 Hz.

Three types of flow were generated in the wind tunnel for the test program: uniform smooth flow, turbulent boundary layer flow and rod-generated turbulent flow. The uniform smooth flow has a turbulence intensity of 2 percent. The flow

Nomenclature

b = length of square cylinder side
C_{F_y} = transverse force coefficient
$C_{\bar{p}}$ = mean pressure coefficient
C_{σ_p} = standard deviation of pressure fluctuation coefficient
$C_{\tilde{p}}$ = peak pressure coefficient
F_y = transverse force acting on square cylinder
g = peak factor
h = height of square cylinder
L_x = longitudinal integral length scale of turbulence
n_0 = natural frequency of vibration
p_0 = static pressure in wind tunnel
$\bar{p}$ = mean pressure
$\tilde{p}$ = peak pressure
$\bar{u}$ = mean longitudinal wind velocity
y = cross-wind displacement
α = angle of wind incidence
ζ_a = aerodynamic dumping
ζ_s = structural dumping
γ = power law exponent of longitudinal wind velocity profile
ρ_a = air density
ρ_s = mass density of structure
σ_p = standard deviation of pressure fluctuation
σ_u = standard deviation of longitudinal wind velocity fluctuation
σ_y = standard deviation of dynamic transverse response
π = 3.1416

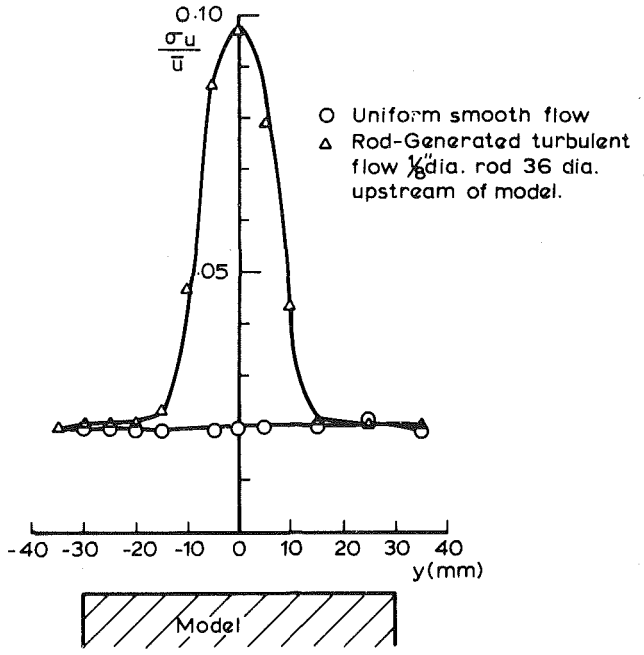

Fig. 3 Longitudinal turbulence intensities of flow behind a thin rod. (Uncertainty in $\sigma_u/\bar{u} = \pm 6$ percent, in $y = \pm 0.1$ mm at 20 : 1 odds)

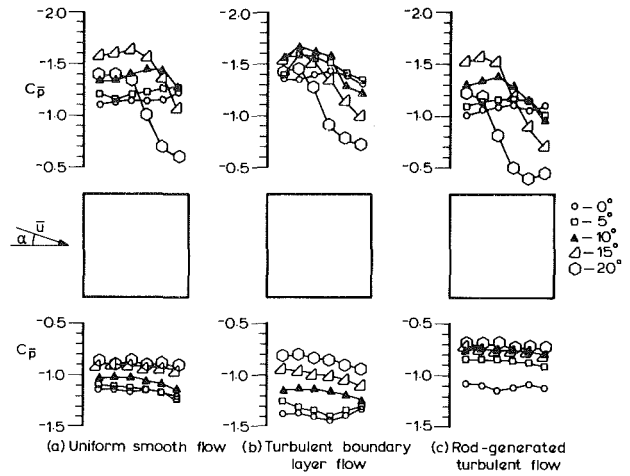

Fig. 4 Variations of mean pressure coefficients in three types of flow. (Uncertainty in $C_{\bar{p}} = \pm 6$ percent, in $\alpha = \pm 1$ deg at 20 : 1 odds)

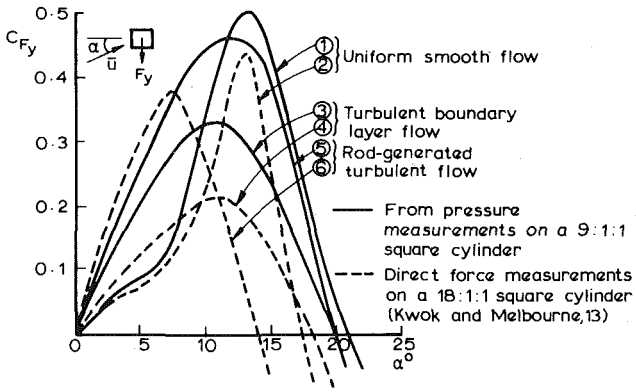

Fig. 5 Transverse force coefficients in three types of flow. (Uncertainty in $C_{Fy} = \pm 11$ percent, in $\alpha = \pm 1$ deg at 20 : 1 odds)

characteristics of the turbulent boundary layer flow were similar to wind flow over a suburban area; with $\gamma = 0.18$ and a turbulence intensity of 11 percent at 3/4 cylinder height. In the rod-generated turbulent flow, the background flow was the same as the uniform smooth flow, but the turbulence near the stagnation streamline of the cylinder, as shown in Fig. 3, was altered significantly by the placement of a 3.2mm diameter rod 36 diameters upstream. The fine scale turbulence generated by the rod has a longitudinal integral length scale L_x/b of 0.27 compared with 6.3 for the turbulent boundary layer flow.

The pressures around the cylinder were measured at angles of wind incidence α from 0 deg up to 25 deg. The mean pressures $\bar{p}$ and standard deviation of pressures σ_p were measured using a computing digital voltmeter. The peak negative pressures $\tilde{p}$ over a period of about 20 seconds were measured using a peak detector. The mean wind velocity at the top of the cylinder and the corresponding dynamic wind pressure $\frac{1}{2}\rho\bar{u}^2(h)$ and the static pressure p_0 in the wind tunnel were also measured by a pitot-static tube and used as references.

Experimental Results and Discussions

The pressure distributions on the two side walls of the square cylinder are expressed in terms of pressure coefficients defined as follows:

$$C_{\bar{p}} = \text{mean pressure coefficient} = \frac{\bar{p} - p_0}{\frac{1}{2}\rho\bar{u}^2(h)} \quad (2)$$

$$C_{\sigma_p} = \text{standard deviation of pressure coefficient} = \frac{\sigma_p}{\frac{1}{2}\rho\bar{u}^2(h)} \quad (3)$$

$$C_{\tilde{p}} = \text{peak pressure coefficient} = \frac{\tilde{p} - p}{\frac{1}{2}\rho\bar{u}^2(h)} \quad (4)$$

The effects of angle of wind incidence on the mean pressure distribution on the two side walls of the square cylinder in the uniform smooth flow are shown in Fig. 4(*a*). As the angle of wind incidence is increased to 5 deg, the mean pressure coefficients on the windward side wall become more negative. As the angle is further increased to 10 deg and then 15 deg, the coefficients near the leading edge become even more negative, while the coefficients become less negative towards the rear. This suggests a forward movement of the reattachment line towards the leading edge. It is thought that the combined effect of a decrease in pressure associated with an accelerating freestream flow over the front of the shear layer, and the entrainment of fluid from inside the separation bubble into the shear layer causes the reattaching shear layer to move forward towards the leading edge and a reduction in bubble volume and internal pressure.

With an increase in freestream turbulence, as in the turbulent boundary layer flow, or with an increase in fine scale turbulence along the stagnation streamline of the square cylinder, as in the rod-generated turbulent flow, the forward travel of the reattachment line and the corresponding increases in negative pressure near the leading edge occur at smaller angles of wind incidence, as shown in Figs. 4(*b*) and 4(*c*). These effects are consistent with the mechanism suggested by Gartshore [2] and Kwok and Melbourne [13] that an increase in freestream turbulence, and in particular fine scale turbulence, increases the turbulent mixing in the separated shear layer and the rate of entrainment of fluid from the wake, and decreases the radius of curvature of the shear layer, thus promoting earlier reattachment.

The negative mean pressure coefficients on the leeward side wall are reduced (i.e., less negative) as the angle of wind

	ζ_s	ζ_a	
		at $\alpha=0°$	at $\alpha=9°$
Uniform smooth flow ○	0.012	−0.0098	−0.022
Turbulent boundary layer flow □	0.0097	−0.015	
Rod-generated turbulent flow △	0.022	−0.034	
Uncertainty at 20:1 odds	±5%	±13%	

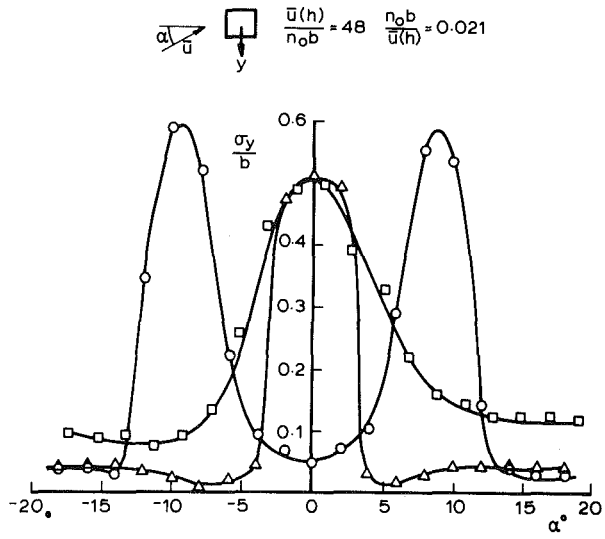

Fig. 6 Transverse response of a slender 18:1:1 square tower model in three types of flow. (From Kwok and Melbourne [13]) (Uncertainty in $\sigma_y/b = \pm 3$ percent, in $\alpha = \pm 1$ deg at 20 : 1 odds)

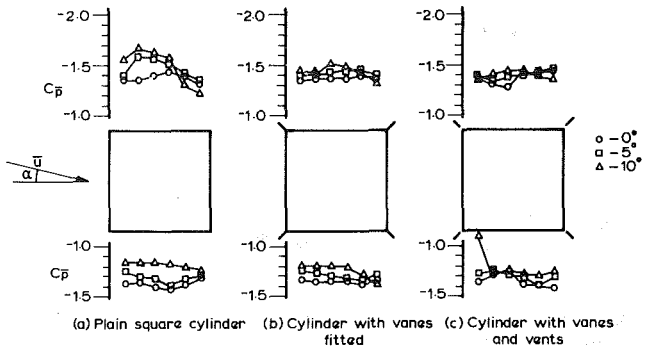

Fig. 7 Variations of mean pressure coefficients of three cylinder configurations. (Uncertainty in $C_{\bar{p}} = \pm 6$ percent, in $\alpha = \pm 1$ deg at 20 : 1 odds)

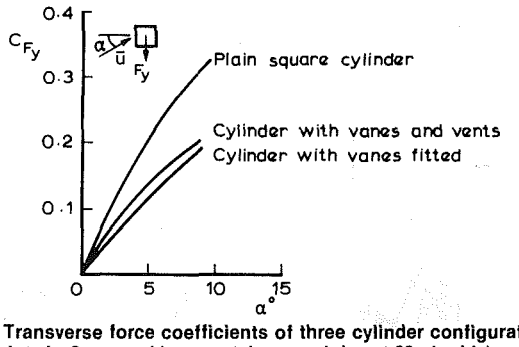

Fig. 8 Transverse force coefficients of three cylinder configurations. (Uncertainty in $C_{F_y} = \pm 11$ percent, in $\alpha = \pm 1$ deg at 20 : 1 odds)

incidence is increased, as shown in Fig. 4. The effects of increase in freestream turbulence on the pressure distribution is much more noticeable in the turbulent boundary layer flow in which the coefficients are generally much more negative than in the other two types of flow at the same angle of incidence.

In all three types of flow, the pressure difference between the windward and leeward side walls of the square cylinder creates a galloping type transverse force F_y which can be determined by numerical integration of the mean pressures and these forces are presented in Figure 5 in coefficient form:

$$C_{Fy} = \frac{F_y}{\frac{1}{2}\rho\bar{u}^2(h)bh} \tag{5}$$

Numerical integrations of mean pressures were carried out at one level only, at 3/4 cylinder height. It was assumed that the pressure distribution does not vary with height in the uniform smooth flow and rod-generated turbulent flow. Although the pressure distribution is likely to vary in height in the turbulent boundary layer flow due to the velocity profile, the pressure distribution at 3/4 cylinder height was assumed to be a reasonable representation of pressure distribution averaged over the height of the cylinder.

The positive slopes of the transverse force coefficients at small angles of wind incidence in all three types of flow satisfy the criterion $dC_{Fy}/d\alpha > 0$ for galloping. One significant feature of the force coefficients is the slope at zero angle of incidence at which the smallest value was registered in the uniform smooth flow. These force coefficient characteristics are consistent with force and displacement response measurements made by Kwok and Melbourne [13] on a slender 18:1:1 square tower model in similar types of flow. It was shown, in Fig. 6, that at zero angle of incidence, there was considerable galloping in both the turbulent flows but no galloping in the uniform smooth flow until the angle of incidence was about 9 deg at which the equivalent aerodynamic damping estimated from the slope $dC_{Fy}/d\alpha$ by using equation (1) was less than the structural damping.

In the turbulent boundary layer flow, by fitting a small vane at the corner of the square cylinder, the negative mean pressure coefficients on the windward side wall, especially near the leading edge, are significantly reduced (i.e., less negative) as shown in Fig. 7(*b*). Up to an angle of wind incidence of 10 deg, there is little evidence to indicate the forward travel of the reattachment line and the corresponding increase in negative pressure towards the leading edge. Although the shear layer separating from the vane may occasionally reattach, it seems that a larger angle of incidence would be required to encourage reattachment and to establish the instability process. It is also thought that the increase in bubble volume underneath the shear layer might help to sustain the fluid entrainment process and to maintain a less negative pressure even if the instability process does become established.

By maintaining a small gap between the vane and the corner, the bubble underneath the reattaching shear layer is vented. This apparently causes the instability process associated with a reattaching shear layer to break down, and prevents the occurrence of the extreme forward travel of the reattachment line and attendance of high negative pressures near the leading edge. It can be seen in Fig. 7(*c*) that the negative mean pressure coefficients on the windward side wall, especially near the leading edge, are significantly reduced compared with those on the plain cylinder.

The fitting of small vanes and vents at the corners has a less significant effect on the pressure distribution on the leeward side wall. The negative mean pressure coefficients over the entire side wall are reduced when the angle of wind incidence is increased, as shown in Figs. 7(*b*) and 7(*c*). It is interesting to note that there is a significant reduction in the pressure difference between the windward and leeward side walls.

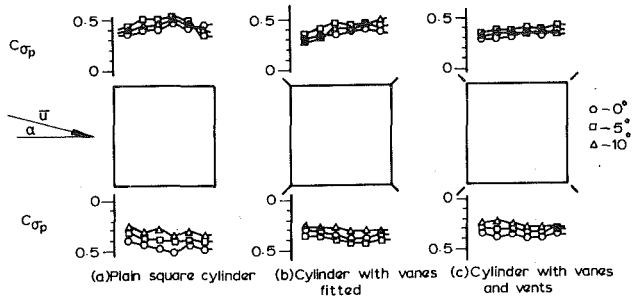

Fig. 9 Variations of standard deviation pressure coefficients of three cylinder configurations. (Uncertainty in C_{σ_p} = ±4 percent, in $\alpha = \pm 1$ deg at 20 : 1 odds)

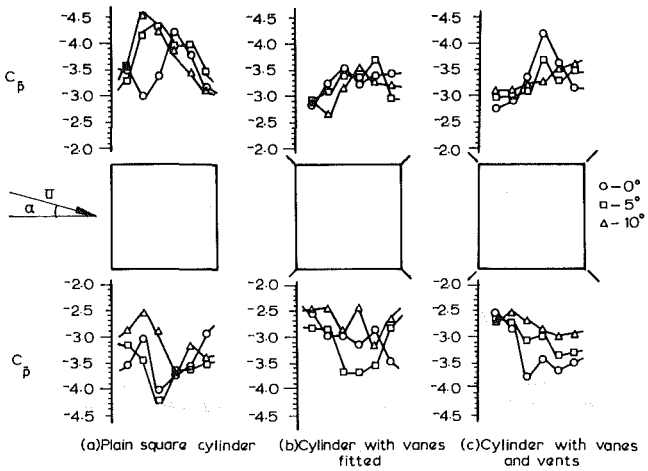

Fig. 10 Variations of peak pressure coefficients of three cylinder configurations. (Uncertainty in $C_{\tilde{p}}$ = ±9 percent, in $\alpha = \pm 1$ deg at 20 : 1 odds)

Therefore, the magnitude of transverse force and the slope of the transverse force coefficient $dC_{Fy}/d\alpha$ causing galloping are also significantly reduced, as shown in Fig. 8. However, in terms of wind-induced dynamic response, the beneficial effects of the fitting of corner vanes would be countered to some extent by the expected increase in drag force acting on the square cylinder.

The pressure fluctuations on the side walls for the three cylinder configurations are presented in Figs. 9 and 10. When small vanes and vents are fitted at the corners, there is a noticeable reduction in the standard deviation of pressure coefficients on both side walls, as shown in Fig. 9. It can be seen in Fig. 10 that reduction in the negative peak pressure coefficients are much more substantial, particularly on the windward side wall and near the leading edge. The percentage reduction in the negative peak pressure coefficients on the windward side wall is presented in Table 1 which shows a reduction of up to 40 percent near the leading edge. These reductions support the earlier suggestions that the fitting of vanes and vents at the corners causes the instability process associated with a reattaching shear layer to breakdown.

The peak pressures are related to the mean and standard deviation pressures as follows:

$$\tilde{p} = \bar{p} + g\sigma_p \tag{6}$$

or in coefficient form,

$$C_{\tilde{p}} = C_{\bar{p}} + gC\sigma_p \tag{7}$$

where g is the peak factor. The peak factor associated with a normally distributed process is about 4.0. The peak factors of most pressure measurements taken in the tests are significantly greater than 4.5, with a maximum value of about 8.0. This indicates that the pressure fluctuations caused by a reattaching shear layer contain very intermittent and sharp pressure peaks.

Table 1 Percentage reduction in negative peak pressure coefficient on the windward side wall when small vanes and vents are fitted at corners

Corners fitted with small vanes	$\alpha = 0$ deg	−20	9	5	−23	−7	10
	5 deg	−12	−25	−22	−17	−6	−13
	10 deg	−19	−41	−27	−9	0	0
Corners fitted with small vanes and vents	$\alpha = 0$ deg	−22	5	−2	−2	−3	−2
	5 deg	−9	−29	−29	−7	−19	0
	10 deg	−13	−34	−27	−17	3	10

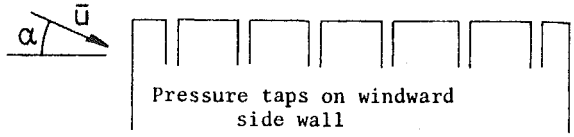

(Uncertainty in percentage reduction = ± 12 percent at 20 : 1 odds)

Conclusions

When a square cylinder is subjected to air flow and especially at small angles of wind incidence, the separated shear layer reattaches onto the windward side wall. It is thought that the combined effect of a decrease in pressure associated with an accelerating freestream flow over the front of the shear layer, and the entrainment of fluid from inside the separation bubble into the shear layer causes the reattaching shear layer to move forward toward the leading edge and a reduction in bubble volume and internal pressure. This results in very high negative pressures on the windward side wall, especially near the leading edge. Increase in freestream turbulence, in particular fine scale turbulence, significantly alters the pressure distribution, the transverse force characteristics and hence the galloping behaviour of the square cylinder.

The fitting of small vanes and vents at the corners of the cylinder apparently causes a breakdown of the instability process. As a result, the negative mean pressure coefficients and peak pressures coefficients are substantially reduced, particularly on the windward side wall and near the leading edge. In practice, the use of such devices could reduce the loads on window panels in tall buildings and the cross-wind galloping excitation of tall buildings and structures. There are also possible practical applications in reducing loads on flat roofs on low rise structures and other types of roof structures.

Acknowledgments

The author wishes to thank Mr. S. J. Palmer and Mr. B. Hindmarsh for their assistance with wind tunnel tests. The study was supported by an URG Special Project Grant from the University of Sydney.

References

1 Melbourne, W. H., "Turbulence Effects on Maximum Surface Pressures a Mechanism and Possibility of Reduction," *Proc. 5th Int. Conf. Wind Engineering*, Vol. 1, Pergamon Press, 1979, pp. 541-551.

2 Gartshore, I. G., "The Effects of Freestream Turbulence on the Drag of Rectangular Two-Dimensional Prism," Boundary Layer Wind Tunnel Laboratory Research Report, BLWT-4-73, Univ. of Western Ontario, 1973, pp. 1-12.

3 Sharp, D. B., "Surface Pressures Under a Re-Attaching Shear Layer in Turbulent Flow," Masters thesis, Dept. of Mech Engg, Monash University, Australia, 1979.

4 Parkinson, G. V., and Brooks, N. P. H., "On the Aeroelastic Instability of Bluff Cylinders," ASME *Journal of Applied Mechanics*, Vol. 28, June 1961, pp. 252–258.

5 Parkinson, G. V., "Wind-Induced Instabilities of Structures," *Phil. Trans. Royal Society of London*, Series A, Vol. 269, 1971, pp. 395–409.

6 Novak, M., "Galloping Oscillations of Prismatic Structures," *Jnl. Eng. Mech. Div., ASCE*, Vol. 98, No. EM1, Proc. Paper 8692, Feb. 1972, pp. 27–46.

7 Novak, M., "Effects of Turbulence on Galloping Instability," *Jnl. Eng. Mech. Div., ASCE*, Vol. 100, No. EMI, Proc. Paper 10338, Feb. 1974, pp. 27–47.

8 Novak, M., and Davenport, A. G., "Aeroelastic Instability of Prisms in Turbulent Flow," *Jnl. Eng. Mech. Div., ASCE*, Vol. 96, No. EM1, Proc. Paper 7076, Feb. 1970, pp. 17–39.

9 Kwok, K. C. S., "Cross-Wind Response of Structures Due to Displacement Dependent Excitations," Ph.D thesis, Dept. of Mech. Engg, Monash University, Australia, 1977.

10 Laneville, A., and Parkinson, G. V., "Effects of Turbulence on Galloping of Bluff Cylinders," *Proc. 3rd Int. Conf. Wind Effects on Buildings and Structures*, Saikon Co. Ltd., 1971, pp. 787–798.

11 Barriga, A. R., Crowe, C. T. and Roberson, J. A., "Pressure Distribution on a Square Cylinder at a Small Angle of Attack in a Turbulent Cross Flow," *Proc. 4th Int. Conf. Wind Effects on Buildings and Structures*, Cambridge Univ. Press, 1977, pp. 89–93.

12 Miyata, T., and Miyazaki, M., "Turbulence Effects on Aerodynamic Response of Rectangular Bluff Cylinders," *Proc. 5th Int. Conf. Wind Engineering*, Vol. 1, Pergamon Press, 1979, pp. 631–642.

13 Kwok, K. C. S., and Melbourne, W. H., "Freestream Turbulence Effects on Galloping," *Jnl. Eng. Mech. Div., ASCE*, Vol. 106, No. EM2, Proc. Paper 15356, Apr. 1980, pp. 273–288.

State College, PA 16801
(814) 865-1741

Bethesda, MD 20084
(202) 227-1578

Artificially Thickened Turbulent Boundary Layers for Studying Heat Transfer and Skin Friction on Rough Surfaces

P. M. Ligrani[1]

R. J. Moffat

W. M. Kays

Department of Mechanical Engineering,
Thermosciences Division,
Stanford University,
Stanford, Calif. 94305

Thermal and hydrodynamic characteristics of boundary layers developing over uniform spheres roughness with momentum thicknesses as large as 1.43 cm are presented. To obtain thick hydrodynamic boundary layers, an artificial thickening device is employed. The normalized velocity and turbulence profiles produced using this device are two-dimensional and self-preserving. The turbulent transport and structural characteristics are representative of normal behavior to the level of spectra of the longitudinal velocity fluctuations. In the artificially thickened layers, the effect of the unheated starting length ($\xi > 0$, $\Delta < \delta$) on thermal boundary layer properties is present. Turbulent Prandtl number profiles are generally unaffected by the magnitude of the unheated starting length, whereas measured Stanton numbers, show different behavior as the unheated starting length varies. In thermal boundary layers which would have the same thickness as the augmented hydrodynamic layers ($\Delta \simeq \delta$), Stanton numbers are shown to be the same as skin friction coefficients, and are then provided for boundary layers much thicker than those previously studied. As fully rough boundary layers develop downstream and δ/k_s increases, $C_f/2$ is proportional to δ_2^{-b} where $b = 0.175$. In order for such U_∞ = constant, thick, rough wall layers to develop far enough downstream to reach smooth behavior where $b = 0.250$, $k_s U_\tau/\nu$ must become small, and b must increase from 0.175 to become greater than 0.250 in the transitionally rough regime.

1 Introduction

Thick turbulent boundary layers developing over rough surfaces are important in many engineering components such as re-entry vehicles, large ocean vessels, and combustion chambers. The wall shear stress, wall heat flux, and overall behavior of the thermal boundary layer are each of interest. In order to study flows with thick boundary layers on an apparatus with only a 2.4 m length of test surface, an artificial thickening device was required. The high cost of the present porous test surface, made of uniformly-packed 1.27 mm diameter spheres and instrumented for heat transfer measurements, made constructing a longer surface impractical.

Thickening devices called elliptic wedge generators [1] have been used to produce thick shear layers in which characteristics of wakes behind two-dimensional surface obstacles have been investigated [2]. Many research institutions also use this or a similar technique to produce simulations of atmospheric boundary layers [3–7] to study a variety of phenomena affected by flow near the earth's surface including pollution dispersal from urban complexes, and wind loading on buildings. Increasing the size of a boundary layer in a short distance also provides a way to produce flow blockage in studies of internal flow through passages such as diffusers [8]. Artificial thickening devices thus allow an investigator to extend the experimental operating domain of a wind tunnel, provided that the flow field produced by the device has properties sufficiently representative of natural behavior.

Techniques to artifically thicken boundary layers can be compared by considering the type of fluid disturbance caused by the thickening device, and how these disturbances interact with shear layers which would be present in a wind tunnel without a thickening device. Three diffeent categories can be defined by considering Townsend's [9] two-layer model for turbulent shear layers near walls. Artificial thickening devices of the first category are the simplest and function either by altering the surface condition to increase the shear (thus accelerating the growth of the already existing turbulent boundary layer), or by producing some other type of abrupt momentum deficit in the inner region. Boundary layer trips or increased surface roughness can be used to accomplish this effect [10]. A second type of device alters both the inner and outer regions of the boundary layer, as, for example, wall jets [6]. A third type of boundary layer augmentation device produces a momentum deficit and derives turbulent energy

[1]Department of Aeronautics, Imperial College of Science and Technology, SW7 2BY London, England

Contributed by the Fluids Engineering Division for publication in the JOURNAL OF FLUIDS ENGINEERING. Manuscript received by the Fluids Engineering Division, November 25, 1981.

from previously irrotational potential flow [1, 5, 7, 11]. With this approach, an array of protrusions is usually employed, extending far from the wall outside the approaching boundary layer. The wakes from these protrusions convect downstream to merge with existing wall boundary layer turbulence, to form an apparent extension of the region influenced by the wall.

Regardless of the approach, it is important to realize that no artificially thickened boundary layer is likely to have completely normal properties if *all* levels of information are considered. The turbulence structure in a normal boundary layer is a result of the development of large scale structures originating from eddies formed by near-wall turbulent bursts. A bursting process consists of the sequence of lifting, oscillatory growth, and breakup of streaks of low momentum fluid which originate in the viscous sublayer. The structures convected away from thickening devices are not likely to be exactly the same as those resulting from such a bursting event. This would be the case except possibly when the flow from a thickening device convected downstream for a time longer than the lifetimes of the largest structures affected by the device.

Consequently, rather than specifying that an artificially thickened shear layer is completely normal, such devices may be considered to produce properties representative of normal behavior up to some specified level of information. If the first four levels of information are considered to be wall-scalar quantities, mean profiles, Reynolds stress component profiles, and spectra, then the degree of normalcy is given by the highest level of information which is correctly simulated by the technique, assuming that all lowered ordered levels are also correct. Lower-ordered flow properties of an artificially thickened boundary layer may then be studied after the higher-order of levels of the flow are demonstrated to be similar to those in boundary layers which developed naturally to the same thickness.

The objectives of the present work are as follows. The first is to show that it is possible to artificially thicken a turbulent boundary layer and obtain behavior similar to normal layers to a high level of information. The second objective is to obtain skin friction coefficients, and Stanton numbers in rough surface boundary layers which are much thicker than those previously studied. These measurements will then be for experimental conditions not previously examined since they are obtained on a test surface which is effectively twice as long as one without a thickening device. The results provide additional understanding of turbulent shear flow, as well as a basis for testing engineering calculation schemes and design procedures for situations where thick, rough-wall boundary layers are present. The Stanton numbers and skin friction coefficients are shown to be representative of natural behavior because three higher levels of information, as well as the turbulent transport of momentum and heat (ie. mixing length and turbulent Prandtl number distributions) are the same as those which would have existed in naturally developed layers of the same thickness.

2 Present Approach

The coordinate system used for the present study is shown in Fig. 1. The effective increase in length due to artificial thickening, L, is shown along with the coordinates x_1 and x_2, which represent actual distance along the test surface, and distance measured from the virtual origin of the hydrodynamic flow field, respectively. In the artificially thickened boundary layer shown in the figure, normal boundary layer properties are considered to be those which would have existed in a boundary layer which developed

Nomenclature

a,b = constants
$C_f/2$ = local skin friction coefficient
C_p = specific heat of fluid
$F_u(k_1)$ = percent of $\overline{u'^2}$ turbulent energy associated with k_1
F = blowing factor, $\rho_w V_0/\rho_\infty U_\infty$
G = Clauser shape factor
k = thermal conductivity
k_s = equivalent sand-grain roughness height
k_1 = one-dimensional wave number
l = mixing length
L = hydrodynamic starting length upstream of test surface, or distance between effective virtual origin of the flow and upstream edge of the test surface, $x_2 - x_1$
n = frequency
Pr_t = turbulent Prandtl number
$\overline{q^2}$ = turbulent kinetic energy, $\overline{u'^2} + \overline{v'^2} + \overline{w'^2}$
$\dot{q}''$ = heat flux
r = radius of spheres comprising test surface
St = Stanton number, $\dot{q}_w''/[\rho_\infty U_\infty C_p (T_w - T_{\infty,0})]$
St_k = rough-wall temperature step Stanton number
T = mean static temperature
u' = longitudinal velocity fluctuation
U = mean longitudinal velocity
U_τ = friction velocity, $U_\infty\sqrt{C_f/2}$
v' = normal velocity fluctuation
V_0 = velocity of transpired fluid at the wall
w' = transverse velocity fluctuation
x = longitudinal coordinate
x_1 = longitudinal coordinate measured from upstream edge of test surface, actual x
x_2 = longitudinal coordinate measured from effective virtual origin of the hydrodynamic flow field, apparent x, $x_1 + L$
y = coordinate normal to surface, measured from velocity virtual origin, $y' + \Delta y$
y^+ = $y\,U_\tau/\nu$
y' = coordinate normal to surface, measured from crests of spherical roughness elements
Δy = distance between ball crests and the virtual origin of the velocity profiles
z = transverse coordinate
Z_0 = corrected roughness size
α = thermal diffusivity, $k/\rho C_p$
δ = hydrodynamic boundary layer thickness, $U/U_\infty = 0.99$
δ_2 = momentum thickness, $\int_0^\infty \frac{\rho U}{\rho_\infty U_\infty}\left(1 - \frac{U}{U_\infty}\right)dy$
Δ = thermal boundary layer thickness, $(T_w - T)/(T_w - T_\infty) = 0.99$
ϵ_H = eddy diffusivity for heat
ϵ_M = eddy diffusivity for momentum
κ = Karman constant
ν = kinematic viscosity
ξ = unheated starting length
ρ = density
τ = shear stress

Subscripts

w = wall
∞ = freestream
° = total or stagnation

Superscripts

$\overline{}$ = mean (time-averaged) value

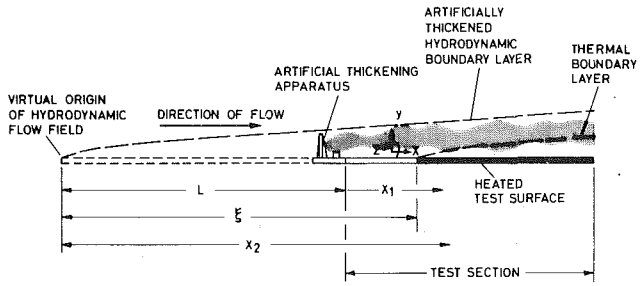

Fig. 1 Coordinate system for artificially thickened turbulent boundary layers

naturally from its virtual origin to the same thickness as that produced by artificial thickening.

Hydrodynamic and Thermal Flow Field Qualification. In order to qualify the hydrodynamic behavior of the artificially thickened boundary layer developing in a zero pressure gradient, the following characteristics are examined: two-dimensionality, growth, structure, equilibrium and turbulent transport of momentum. The behavior of thermal boundary layers is then qualified by demonstrating that the turbulent Prandtl numbers are equivalent to those in naturally developed flows.

The artificially thickened hydrodynamic boundary layer is considered to be at equilibrium when the normalized structural properties are self-preserving. Self preservation is considered at two levels. First, the Clauser shape factor [12, 13] must be independent of downstream distance. Second, the Reynolds stress tensor profiles must be self-preserving [9, 14], when using a single velocity scale for normalization of the stress tensor and a single length scale when normalizing distance from the wall.

The structural characteristics of the rough wall artificially thickened boundary layer are qualified in a way which is different than is possible for smooth-wall flows. In contrast to flows over smooth surfaces which have been extensively documented, no prior studies have been reported concerning thick boundary layers over the type of roughness used for the present experiment. Thus there is no data base available which can be used directly to verify that the flow field is normal. It is necessary to make the proof indirectly, using whatever properties are well known for rough-wall layers. The most sensible properties to be used for this purpose are those which are invariant with downstream development in naturally developing boundary layers. If the artificially thickened boundary layer is in fact an extension of a naturally developed boundary, these should be also invariant in the augmented boundary layer. Flows at different freestream velocities and roughness Reynolds numbers are also to be investigated, hence the flow properties should be independent of these parameters, as well. The law of the wake, the normalized Reynolds shear stress profile, the ratio of Reynolds shear stress to turbulent kinetic energy, and the correlation coefficient for the Reynolds shear stress have the necessary properties.

Stanton Numbers in Artificial Thickened Boundary Layers. With an artificially thickened boundary layer, the thermal layer has developed over a much shorter length than the hydrodynamic layer, as illustrated in Fig. 1. Consequently, the thermal boundary layer is much thinner than the velocity boundary layer and the Stanton numbers show unheated starting length behavior. Thus, it is *not* possible to measure Stanton numbers in thermal layers which are the same thickness as the hydrodynamic layers, and there are no Stanton number data for very thick rough-wall boundary layers. In order to obtain Stanton numbers for temperature boundary layers having the same thickness as velocity

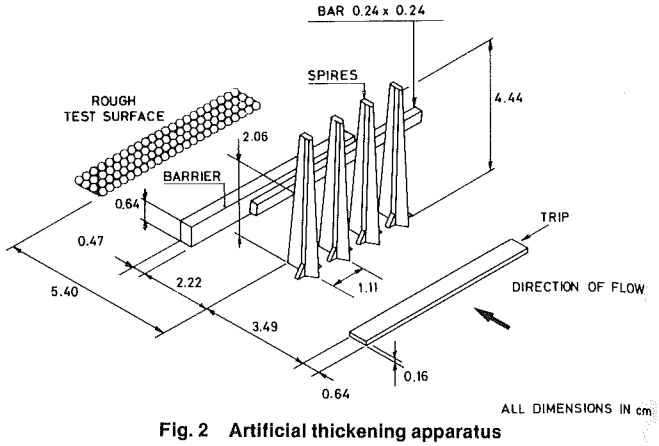

Fig. 2 Artificial thickening apparatus

boundary layers, they must be estimated from measurements of skin friction coefficients.

According to Kays and Crawford [15], the relationship between Stanton numbers and skin friction coefficients in rough-wall boundary layers where the thermal and hydrodynamic layer thicknesses are the same is

$$\mathrm{St} = \frac{C_f/2}{\mathrm{Pr}_t + \sqrt{C_f/2}/\mathrm{St}_k} \tag{1}$$

St_k represents the inverse of a nondimensional temperature difference across which heat is transferred by conduction through what may be a semistagnant fluid in the roughness cavities at the surface. For the uniform spheres roughness of the present study, when fully rough behavior exists and U_∞ = 26.8 m/s, $1/\mathrm{St}_k \simeq 2.0$. When the flows are transitionally rough for U_∞ = 15.8 m/s, and 10.1 m/s, $1/\mathrm{St}_k < 2.0$. $1/\mathrm{St}_k$ is zero when smooth wall behavior is present [16]. Using Pr_t = 0.90 in equation (1), it is then evident that within a few percent

$$\mathrm{St} = C_f/2 \tag{2}$$

for the present experimental conditions when $\xi = 0$ and $\Delta \simeq \delta$.

3 Experimental Apparatus and Procedure

Artificial Thickening Device. The device used to artificially thicken the turbulent boundary layer is shown schematically in Fig. 2. The device consists of an array of spires which extend across the width of the wind tunnel just upstream of the rough test surface. A square bar is located on the downstream side of the spire array and also extends across the width of the wind tunnel. The bar is necessary in order to achieve normal turbulence structure. The final size, shape and location of the bar were determined by trial and error. As the flow approaches the artificial thickening device, a trip is encountered near the wall. Downstream of the array, a barrier is located just before the test surface. This design was developed from a device used for thick smooth-wall boundary layers [17], which in turn, was developed from a technique for atmospheric boundary layers suggested by Peterka and Cermak [7]. The details of the development of the device shown in Fig. 2 are discussed by Ligrani et al. [16]. Two-recurring problems in the development were obtaining a spanwise uniform two-dimensional flow field, and producing a flow field with self-preserving properties.

Wind Tunnel and Measurement Techniques. The wind tunnel used was the HMT roughness rig described by Healzer et al. [18], and by Pimenta et al. [19]. The test surface of the facility is 2.44 meters long and consists of 24 plates, each of which can be electrically heated to maintain a given wall temperature of transpiration boundary condition. Each plate

surface consists of 1.27 mm-diameter uniform spheres, which have an equivalent sandgrain roughness size of 0.79 mm. The tunnel is closed-circuit, and for the present tests, the top wall was adjusted to produce a zero-pressure gradient along the test surface to within 0.5 mm of water for freestream velocities from 10.1 m/s to 27.8 m/s. Stanton numbers were determined by energy balances on each segment of the plate. The power input to each segment was measured and then losses were subtracted to determine the wall heat flux $\dot{q}''_w$. The Stanton number was then calculated using $\dot{q}''_w$, the wall temperature, and freestream total temperature. Measurements of mean temperature profiles and freestream temperatures were made using thermocouples mounted and calibrated as described in reference [16].

Skin friction coefficients were determined from the Reynolds shear stresses and mean velocities, measured in the near-wall region, using

$$C_f/2 = \frac{(-\overline{u'v'})_y}{U_\infty^2} + \frac{\nu}{U_\infty^2}\frac{\partial U}{\partial y}\bigg|_y + \frac{U(y)}{U_\infty^2}\frac{\partial}{\partial x}\int_0^y U\,dy - \frac{1}{U_\infty^2}\frac{\partial}{\partial x}\int_0^y U^2\,dy \tag{3}$$

Equation (3) was derived using the boundary layer equation integrated from the wall to the position y. The value of y' used for determination of $C_f/2$ was 0.330 cm due to limitations on hot wire probe size. For all cases investigated, the measured turbulent shear stress term accounted for 96 to 98 percent of the total magnitude of $C_f/2$.

The mean velocity and six Reynolds stress tensor components were measured using standard hot-wire anemometry techniques [16]. Two types of probes were employed, a DISA 55F04 horizontal wire and a DISA 55F02 slant wire, each with a sensing length of approximately 1.25 mm. The probes were used with TSI Model 1050 bridges operated in constant-temperature / constant-resistance modes with wire overheat ratios of 1.5. The bridges were connected to TSI Model 1052 linearizers, followed by voltmeters for measurement of mean or rms voltages, as appropriate. The directional sensitivity of the hot-wire probes was described using Jorgensen's equations [20]. Five different rotational positions of the slant-wire probe were used in conjunction with horizontal-wire measurements to determine the six Reynolds stress tensor components. The hot-wire measurements were made when the flow field was isothermal at the same temperature as was used for calibration, and thus, no temperature corrections were required. Spectra of the u' signals were measured using digital data sampling techniques and fast Fourier transforms, as described in referenced [16].

Uncertainty estimates of measured quantities based on 20:1 confidence levels are as follows: $C_f/2$, ±10 percent; G, ±0.70; $\overline{q^2}$, ±15 percent; St, ±.0001; T, ±0.1°C; U, ±2.0 percent; U_τ, ±6.5 percent; $\overline{u'^2}$, ±5 percent; $\overline{v'^2}$, ±10 percent; $\overline{w'^2}$, ±10 percent; $-\overline{u'v'}$, ±10 percent; and y', ±.013 mm.

4 Experimental Results

Hydrodynamics. Boundary layer growth can be represented using two different characteristics which are related through the momentum intergral equation: variation of the skin friction coefficient, $C_f/2$, with momentum thickness, δ_2, and variation of momentum thickness with downstream distance, x.

Skin friction is shown in Fig. 3 as a function of momentum thickness in naturally developed [19] and artificially thickened boundary layers for freestream velocities of 10.1 m/s, 15.8 m/s, and 26.8 m/s. The skin friction coefficients were determined independently of the momentum thickness, which

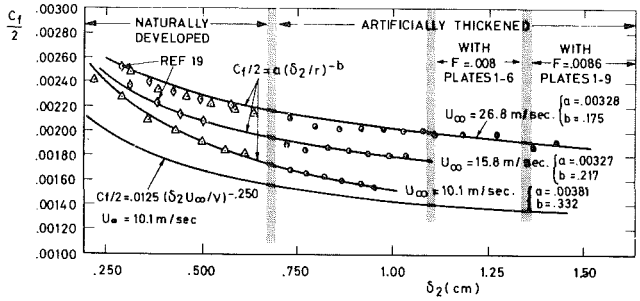

Fig. 3 Skin friction variation as a function of momentum thickness

was calculated from mean velocity profiles. On Fig. 3, the artificially thickened data forms a natural extension of the naturally developed data. As the freestream velocity changes, the values of $C_f/2$ show the same trends in the artificially thickened boundary layer as in those naturally developed, and the rough-wall coefficients are higher than those for a smooth-wall, when compared at the same momentum thickness. Thus, the artificially thickened layer seems to have normal growth characteristics with respect to the variation of $C_f/2$ with δ_2. At a given freestream velocity, data can be represented using

$$C_f/2 = a\left(\frac{\delta_2}{r}\right)^{-b} \tag{4}$$

where the constants a and b are presented in Fig. 3.

At a freestream velocity of 26.8 m/s the thickness of the artificially thickened layer was further augmented by blowing through the upstream portion of the test surface. Data points at the downstream end of the test section are shown in Fig. 3 for two different experimental arrangements: $F = 0.008$ in the first 6 plates and $F = 0.0086$ in the first 9 plates of the wind tunnel. In the later case, a momentum thickness of 1.43 cm was obtained at the downstream end of the rough test surface, compared to approximately 0.60 cm in the naturally developing flow at the same U_∞.

The variation of momentum thickness with downstream distance may be determined using equation (4) and the two-dimensional momentum integral equation

$$C_f/2 = \frac{d\delta_2}{dx} \tag{5}$$

Equating the right-hand sides of equations (4) and (5) and integrating yields

$$\frac{\delta_2}{r} = [a(b+1)]^{\frac{1}{b+1}}\left(\frac{x_2}{r}\right)^{\frac{1}{b+1}} \tag{6}$$

Equation (6) is shown in Fig. 4 using values of a and b for $U_\infty = 26.8$ m/s with data at the same freestream velocity. For each boundary layer augmentation, the momentum thickness for one data point, the "match point," was used in equation (6) to determine the apparent x-location of that data station. The other data points were then plotted knowing their relationship to the "match point." The growth properties of the artificially thickened boundary layers seem normal with respect to variations of δ_2 with x_2 since matching at one point aligns all of the data with the expected growth curve. The wind tunnel length was indicated to be increased as much as 4.13 meters at $U_\infty = 26.8$ m/s by these techniques.

Velocity profiles measured in the artificially thickened layers, at four different freestream velocities, have the universal similarity of shape described by Clauser [12] and also show agreement with Coles' law of the wake [21]. The friction velocities used to non-dimensionalize the profiles were calculated using local skin friction coefficients determined from equation (3). The values of y used for the plots were measured from the virtual wall location, a distance Δy =

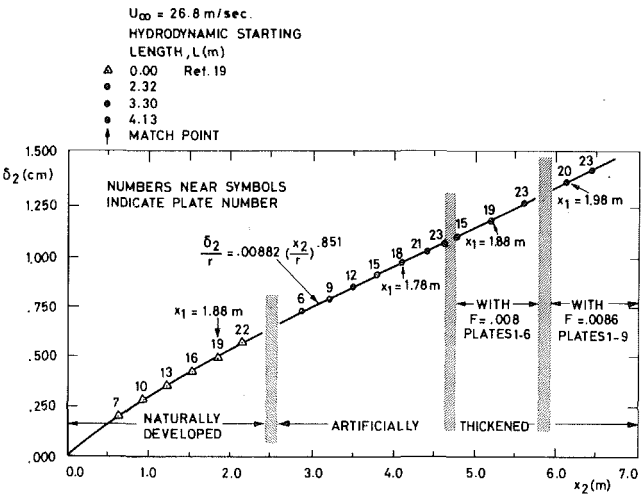

Fig. 4 Variation of momentum thickness with downstream distance

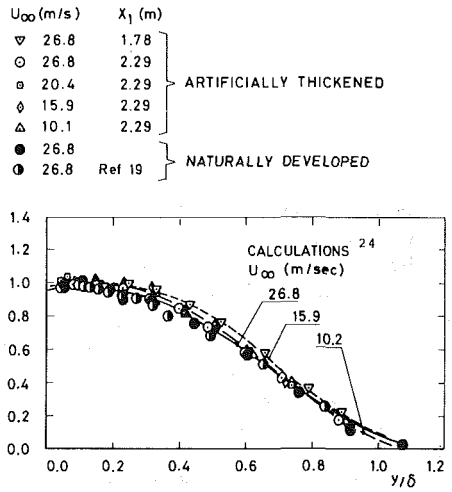

Fig. 5 Normalized Reynolds shear stress profiles

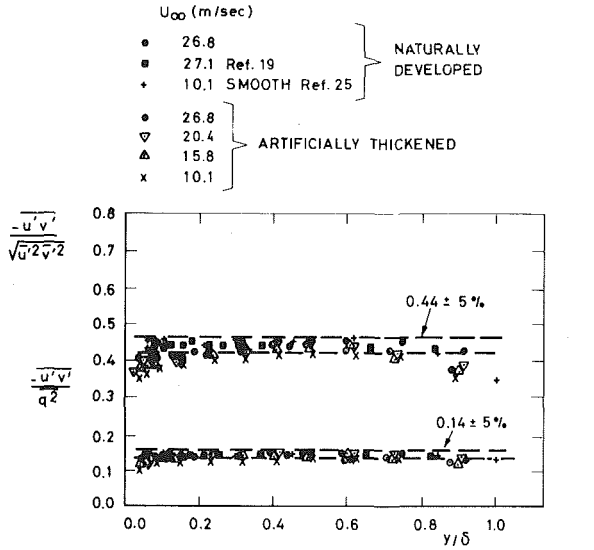

Fig. 6 Cross-correlation coefficient for the Reynolds shear stress, and the ratio of the Reynolds shear stress to the turbulent kinetic energy

0.23 mm below the crests of the roughness elements. The wall shift was determined using the method suggested by Monin and Yaglom [22], in which it is assumed that a corrected roughness size, Z_0, does not change with y near the wall for fully rough flows. Z_0 is defined using

$$U^+ = \frac{1}{\kappa} \ln\left(\frac{y' + \Delta y}{Z_0}\right) \tag{7}$$

The variation of the Clauser shape factor G with downstream distance was determined for artificially thickened boundary layers at freestream velocities of 10.1, 15.8, and 26.8 m/s. The factor is constant at value of 6.3 within ±0.3 units for $x_1 > 1.0$ meters. Such behavior means that velocity profiles in $(U_\infty - U)/U_\tau$ versus y/δ coordinates should be invariant with downstream distance. This conclusion is confirmed by velocity profiles measured in the artificially thickened boundary layers [16].

In Clauser's 1956 paper [12], he indicated that if velocity profiles in the outer parts of turbulent boundary layers are universal in shape, then turbulent shear stress profiles would also be nearly universal when normalized using U_τ and plotted versus y/δ. This conclusion is supported by other work [9, 19, 23], and also may be verified if the momentum and continuity equations are integrated to given y position in the boundary layers in order to calculate shear stress profiles from measured wall shear stress and mean velocity profiles. (See reference [24]). The results of such calculations are shown in Fig. 5 along with measurements from both naturally developed and artificially thickened turbulent boundary layers at different freestream velocities and downstream locations. The agreement between the different profiles in the figure indicates that shear stress distributions in the artificially thickened boundary layers are similar to those which would be expected in boundary layers which developed naturally.

When compared to mean velocity profile behavior, the turbulence structure requires a greater distance downstream from the thickening device in order to reach a self-preserving state. Figure 5 indicates that normalized $-\overline{u'v'}$ profiles for $U_\infty = 26.8$ m/s are the same at $x_1 = 1.78$ m. and at $x_1 = 2.29$ m. When examined with other measured profiles, the measurements from Fig. 5 indicate the normalized shear stress profiles reach self-preservation when $x_1 > 1.4 - 1.5$ meters, as do the normalized normal Reynolds stress profiles. Thus, the two levels of self-preservation discussed in Section 2 are satisfied for about 1.0 meter of test surface length.

In order to check the two-dimensionality of the artificially thickened boundary layers, the $\overline{v'w'}$ and $\overline{u'w'}$ Reynolds stress components were measured at all locations where other stress components were measured. For all measurement locations, these stresses were found to be negligible compared to $-\overline{u'v'}$. Such behavior is consistent with the spanwise uniformity of $\overline{u'^2}$, $\overline{v'^2}$, $\overline{w'^2}$ and $-\overline{u'v'}$ profiles, which was verified within experimental uncertainty for a freestream velocity of 26.8 m/s. Other two-dimensionality checks consisted of measurements of the spanwise uniformity of mean velocity profiles. At the downstream end of the test section over a z-span of 16 cm, the momentum thickness was uniform within ± 4.6 percent of the mean, and at a given y location, spanwise velocity readings were never greater than 1.0 percent different from the centerline value.

The turbulence correlation coefficients

$$\frac{-\overline{u'v'}}{\sqrt{\overline{u'^2}\,\overline{v'^2}}}$$

and

$$\frac{-\overline{u'v'}}{q^2}$$

have been demonstrated to be constant for equilibrium smooth and rough-wall boundary layers by many investigators [9, 14, 16, 19, 24, 25]. These correlations seem to have the same values regardless of surface condition, freestream velocity distribution, and magnitude of wall trans-

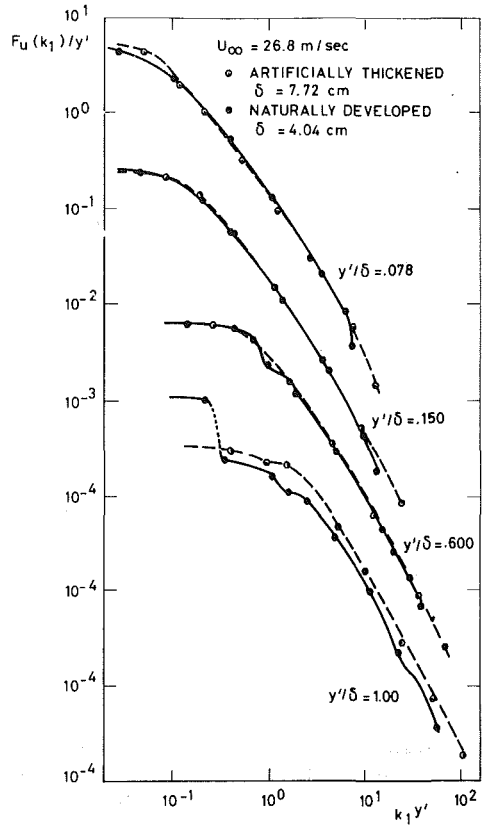

Fig. 7 u' spectra, artificially thickened and naturally developed rough-wall turbulent boundary layers

piration. Figure 6 shows that the values of the correlation coefficients in the rough-wall augmented boundary layers are consistent with values in naturally developing flows within ± 5 percent. The measurements of Orlando et al. [25] and Pimenta et al. [19] are also shown in the figure for comparison.

Qualification of the structural characteristics of the rough-wall, artificially thickened boundary layer can be extended to include spectra of the longitudinal velocity fluctuations. Measurements were made at $x_1 = 1.78$ m in a naturally developing flow for comparison with augmented boundary layer results at the same value of x_1 for a freestream velocity of 26.8 m/sec. Comparison of these measurements at four different values of y'/δ is shown in Fig. 7. In the figure, spectra magnitudes are normalized such that

$$\int_0^\infty \frac{F_u(k_1)}{y'} d(y'k_1) = 1.0 \tag{8}$$

where the one-dimensional wave number, k_1, is determined from frequency using $k_1 = 2\pi n/U$. The nondimensionalization given by equation (8) should be viewed as a normalization with respect to boundary layer thickness, since spectra are compared at the same y'/δ. It should also be mentioned that the dashed and solid lines in Fig. 7 represent a graphical fit to closely spaced data points. The figure shows that the broadband spectral characteristics of the artificially thickened boundary layer show agreement with baseline measurements for $y'/\delta = 0.078$, 0.150, and 0.600. The spectra at $y'/\delta = 1.00$ for the augmented boundary layer and the naturally developing flow show differences which may be related to differences in the intermittency characteristics of the two flows, and/or differences in large-scale eddy structures at the boundary layer edge.

Turbulent Transport of Momentum and Heat. The turbulent transport of momentum and heat in the artificially thickened boundary layers are shown to be normal by showing that the mixing-lengths and turbulent Prandtl numbers are equivalent to those in naturally developed flows. These quantities are determined from measurements of St, $C_f/2$, U and T in the artificially thickened boundary layers. From these measurements, shear stress and heat flux distributions are first obtained through the layers using the energy, momentum, and continuity equations integrated to a position y in the boundary layer. These forms of the boundary layer equations are given in reference [24]. After τ and $\dot{q}''$ versus y are calculated, the eddy diffusivities for momentum and heat are obtained using

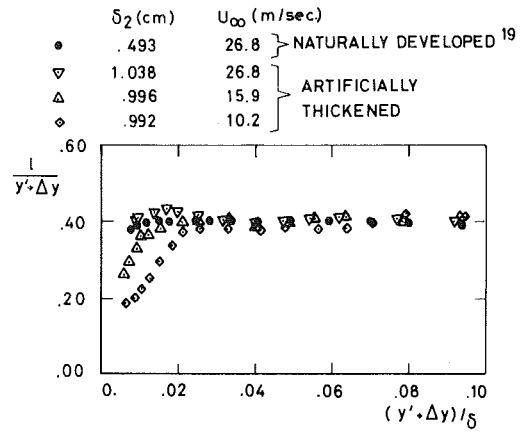

Fig. 8 Mixing-length distributions, rough-wall artificially thickened boundary layers

$$\tau = \rho(\epsilon_M + \nu)\frac{\partial U}{\partial y} \tag{9}$$

and

$$\dot{q}'' = -\rho C_p(\epsilon_H + \alpha)\frac{\partial T}{\partial y} \tag{10}$$

respectively. The turbulent Prandtl number then follows since $\mathrm{Pr}_t = \epsilon_M/\epsilon_H$, and the mixing length may be obtained using $l = (\epsilon_M/|\partial U/\partial y|)^{1/2}$.

Figure 8 shows mixing-length distributions from the artificially thickened boundary layer calculated using this approach. For $y/\delta < 0.10$, except very near the wall, the mixing length distributions follow the equation $l = \kappa y$ where $\kappa = 0.41$. When $y/\delta < 0.03$, the mixing continues to follow this relation for $U_\infty = 26.8$ m/s. However, for freestream velocities less than 26.8 m/s, the magnitudes of the mixing length near the wall decrease. Such behavior indicates that viscous stresses are affecting fluid motion and that the flow is transitionally rough ($U_\infty = 15.8$ m/s, 10.1 m/s) instead of fully rough ($U_\infty = 26.8$ m/s). The augmented layer mixing-length distributions are then similar to those expected in naturally developed flows, where one example from a naturally developed flow at $U_\infty = 26.8$ m/s [19] is included on Fig. 8.

In Fig. 9, turbulent Prandtl number distributions from the inner regions of artificially thickened boundary layers are closely similar to measured and calculated distributions from a naturally developed flow [19]. Differences are apparent between the calculated and measured profiles of reference [19] in the outer parts of the layers as a consequence of large uncertainties in the calculation of $\partial U/\partial y$ and $\partial T/\partial y$. These uncertainties also account for the differences in the layers with unheated starting lengths. However, even though such differences exist in the outer regions, the turbulent transport properties fall within the scatter of existing measurements from flows over rough and smooth surfaces, and would not be expected to affect the overall transport of heat through the boundary layer since it is controlled primarily by inner region behavior.

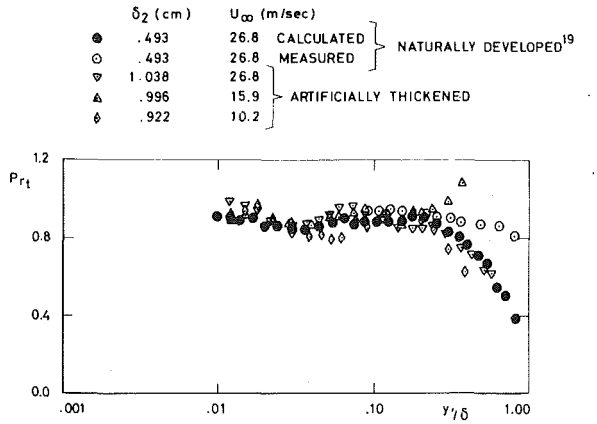

Fig. 9 Turbulent Prandtl number distributions, rough-wall artificially thickened boundary layers

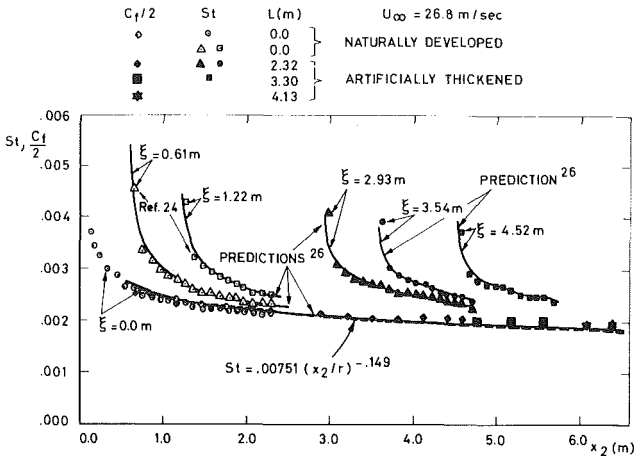

Fig. 10 Variation of Stanton numbers with downstream distance

Thermal Boundary Layers Without Unheated Starting Lengths. The method used to define a reference for the expected behavior of rough-wall Stanton numbers in thermal boundary layers without unheated starting lengths was outlined in Section 2. The details of this argument are now discussed by referring to Fig. 10. Attention is focussed first on the naturally developed data from the thermal layer with $\xi = 0$, shown on the left-hand side of the figure ($x_2 < 2.44$ m). In this case, the thermal and hydrodynamic boundary layers are about the same thickness and the Stanton numbers are in close agreement with the skin friction coefficients. This agreement confirms the validity of equation (2). This equation would then be expected to be valid for thicker thermal boundary layers when $x_2 > 2.44$ m as long as $\Delta \simeq \delta$ for the present experimental conditions. Consequently, Stanton numbers for thick thermal boundary layers when $x_2 > 2.44$ m are the same as artificially thickened $C_f/2$ data, which are shown on the right-hand side of Fig. 10.

The thick thermal boundary layer Stanton numbers shown on the right-hand side of Fig. 10 are verified using two methods: (1) predictions using a mixing-length closure scheme which accounts for roughness in a finite-difference boundary layer program [26], and (2) an empirical result determined from equations (2), (4), and (6). Considering the first of these, the St predictions show excellent agreement with the naturally developed $\xi = 0$ data on Fig. 10. Agreement is also shown with the five cases where $\xi > 0$, for both naturally developed and artificially thickened boundary layers, where the $\xi > 0$ Stanton numbers lie above the $\xi = 0$ Stanton numbers when compared at a given downstream location. The agreement with the $\xi > 0$ data for the artificially thickened cases ($x_2 > 2.44$ m) is important because this strengthens the credibility of $\xi = 0$ predictions at the same x_2 locations. These $\xi = 0$ predictions are further verified since they follow $C_f/2$ data for all artificially thickened boundary layer thicknesses examined.

The empirical result mentioned may be obtained by substituting equation (6) into equation (4) and then replacing $C_f/2$, by St using equation (2). Performing these operations gives

$$\mathrm{St} = C_f/2 = a[a(b+1)]^{\frac{-b}{b+1}} \left(\frac{x_2}{r}\right)^{\frac{-b}{b+1}} \tag{11}$$

which is shown in Fig. 10 using a and b values for $U_\infty = 26.8$ m/s from Fig. 3. The equation agrees with the $\xi = 0$ St measurements and predictions in Fig. 10.

Since the assumptions used in the derivation of equation (11) are also valid at $U_\infty = 15.8$ m/sec and $U_\infty = 10.1$ m/s, Stanton numbers in thermal boundary layers having the same thicknesses as the artificially thickened hydrodynamic layers then seem to decrease with increasing downstream distance according to equation (11) at rates which depend on the freestream velocity. The variation of $C_f/2$, and hence St, with δ_2 are shown in Fig. 3, where the results from the artificially thickened boundary layers at $U_\infty = 10.1$, 15.8, and 26.8 m/s cover the right-hand portion of the figure. From Fig. 3 it is evident that boundary layers with momentum thicknesses as large as 1.43 cm may be obtained using the augmentation service, compared to about 0.60 cm for naturally developed flows.

Thick Rough-Wall Boundary Layers. Even though experimental results from the present study do not provide confirmation, it is believed that a fully rough turbulent boundary layer in a zero pressure gradient will become transitionally rough and eventually smooth, as δ/k_s increases and the layer developes far downstream to become very thick.

Referring to the $U_\infty = 26.8$ m/s data of Fig. 3, δ/k_s is less than about 60 in the naturally developed boundary layer, and increases to 133 in the thickest part of the augmented layer. Even though the roughness becomes contained in a smaller part of the inner regions of this boundary layer as it develops downstream, the roughness remains large enough to suppress the formation of a viscous sublayer near the wall for $\delta_2 < 1.43$ cm. The magnitude of $k_s\ U_\tau/\nu$, the nondimensional roughness height or roughness Reynolds number, varies from 70 to 60 for the $U_\infty = 26.8$ m/s data. These nondimensional k_s values are then greater than the maximum y^+ where viscosity would be expected to contribute to the local shear stress, which is ordinarily at the outer edge of the buffer layer. The $U_\infty = 26.8$ m/s flow is thus considered to be fully rough.

According to calculations [16], fully rough behavior at $U_\infty = 26.8$ m/s would be expected to continue until $\delta/ks \simeq 350$. At this point, the magnitude of $k_s\ U_\tau/\nu$ would be about 55 and the boundary layer would have needed more than 20 meters of test surface to reach a momentum thickness of 3.8 cm. This extremely long distance is required due to the weak dependence of fully rough $C_f/2$ on x_2, as given, for example, by equation (11) for $U_\infty = 26.8$ m/s. As the layer then develops further downstream, a viscous sublayer would begin to form near the wall, and the flow would be transitionally rough. The dependence of $C_f/2$ on x_2/r, and also on δ_2/r, would then be expected to change from fully rough behavior due to an influence of viscosity.

In the thick $U_\infty = 26.8$ m/s transitionally rough boundary layer, the magnitude of $C_f/2$, and hence $k_s\ U_\tau/\nu$ would decrease with downstream distance until roughness elements are contained in a viscous sublayer having the same nondimensional thickness as for a smooth wall flow. When the thick layer then becomes smooth, the variation of $C_f/2$ would then be expected to follow the classic equation given by reference [15]

$$C_f/2 = 0.0125\left(\frac{\delta_2 U_\infty}{\nu}\right)^{-0.250} \tag{12}$$

Referring to Fig. 3, if $C_f/2$ is proportional to $\delta_2{}^{-b}$, then as the flow becomes transitionally rough, the value of b would have to increase from 0.175 and then become greater than 0.250 in order for the $C_f/2$ versus δ_2/r curves to reach equation (12). Otherwise, if the maximum value of b in a transitionally rough flow never exceeds 0.250, the negative slopes of lines in Fig. 3 would never be large enough to reach the smooth line. In this case, a fully rough flow which became thick enough to be smooth would have $C_f/2$ values above equation (12), which seems unlikely. Thus, b must become greater than 0.250 in transitionally rough boundary layers. Such behavior is supported by the $U_\infty = 10.1$ m/s transitionally rough results shown in Fig. 3 where $b = 0.332$ and $C_f/2$ approaches equation (12) as this layer develops downstream.

5 Conclusions

A technique has been developed to produce artificially thickened boundary layers on a uniformly rough surface which have two-dimensional, equilibrium properties representative of normal behavior to the level of spectra of the longitudinal velocity fluctuations. The velocity profiles in wake coordinates, the normalized Reynolds shear-stress profiles, the Reynolds shear stress/turbulent kinetic energy ratio, the correlation coefficient for the Reynolds shear stress, the mixing-length distributions, and the turbulent Prandtl number distributions are the same as in boundary layers which developed naturally to the same thickness. Because these measured properties are shown to be normal, skin friction coefficients, Stanton numbers, and other low-order flow field information may be measured and also considered to be representative of natural behavior.

Stanton numbers are demonstrated to be the same as measured skin friction coefficients in thermal boundary layers which would have the same thickness as the artificially thickened hydrodynamic layers ($\xi = 0$ and $\Delta \simeq \delta$). When $\xi > 0$, turbulent Prandtl number distributions are also largely the same as when $\xi = 0$. These properties are thus provided for experimental conditions not previously studied and contribute to the rough-wall data base since the augmentation service doubles the effective wind tunnel test section length.

The results obtained from the artificially thickened boundary layer contribute to the understanding of turbulent shear flows by providing information as to how boundary layers on rough surfaces behave as δ/k_s increases and the layers develop downstream to become very thick. In fully rough layers, $C_f/2$ is proportional to $\delta_2{}^{-b}$ where $b = 0.175$, compared to $b = 0.250$ in smooth wall flows. As a fully rough layer becomes very thick at constant U_∞, the roughness elements will eventually not suppress the formation of a viscous sublayer and flow behavior will be influenced by viscosity to become transitionally rough and then smooth. In order to do this, transitionally rough values of b must increase from 0.175 to become greater than the value for a smooth-wall flow.

Report HMT-29 [16] is available from University Microfilms International, 300 N. Zeeb Road, Ann Arbor, MI 48106, USA.

Acknowledgment

The authors thank Professor Peter Bradshaw who provided helpful comments on a draft of this paper.

References

1 Counihan, J., "Simulation of an Adiabatic Urban Boundary Layer in a Wind Tunnel," *Atmospheric Environment*, Vol. 7, 1973, pp. 673–689.

2 Counihan, J., Hunt, J. C. R., and Jackson, P. S., "Wakes Behing Two-Dimensional Surface Obstacles in Turbulent Boundary Layers," *Jour. of Fluid Mechanics*, Vol. 64, 1974, pp. 529–563.

3 Cockrell, D. J., and Lee, B. E., "Methods and Consequences of Atmospheric Boundary Layer Simulation," Paper 13-AGARD Conference, Proc. No. 48 on Aerodynamics of Atmospheric Shear Flows, Munich, 1969.

4 Gartshore, I. S., and de Croos, K. A., "Roughness Element Geometry Required for Wind Tunnel Simulations of the Atmospheric Wind," Fluids Engrg. Div., ASME, Winter Annual Meeting, New York, Dec., 1976.

5 Hunt, J. C. R., and Fernholz, H., "Wind-Tunnel Simulation of the Atmospheric Boundary Layer: A Report on Euromech 50," *Journ. of Fluid Mechanics*, Vol. 70, 1975, pp. 543–559.

6 Nagib, H. M., Morkovin, M. V., and Yung, J. T., and Tan-Atichat, J., "On Modelling of Atmospheric Surface Layers by the Counterjet Technique," AIAA Paper No. 74-638, AIAA 8th Aerodynamic Testing Conference, Bethesda, 1974.

7 Peterka, J. A., and Cermak, J. E., "Simulation of Atmospheric Flows in Short Wind Tunnel Test Sections," CER 73-74JAP-JEC32, Fluid Mechanics Program, Colorado State University, 1974.

8 Sajben, M., and Kroutil, J. C., "Effects of Initial Boundary-Layer Thickness on Transonic Diffuser Flows," *AIAA Journal*, Vol. 19, No. 11, Nov. 1981, pp. 1386–1393.

9 Townsend, A. A., *The Structure of Turbulent Shear Flow*, second edition, Cambridge University Press, 1976.

10 Klebanoff, P. S., and Diehl, Z. W., "Some Features of Artificially Thickened, Fully Developed, Turbulent Boundary Layers With Zero Pressure Gradient," NACA Report 1110, 1952.

11 Otten, L. J., III, and Van Kuren, J. T., "Artificial Thickening of High Subsonic Mach Number Boundary Layers," *AIAA Jour.*, Vol. 14, No. 11, 1976, pp. 1528–1533.

12 Clauser, F. H., "The Turbulent Boundary Layer," *Advances in Applied Mechanics*, Vol. IV, Academic Press, New York, 1956, pp. 1–51.

13 Clauser, F. H., "Turbulent Boundary Layers in Adverse Pressure Gradients," *Jour. of Aeronautical Science*, Vol. 21, 1954, pp. 91 –108.

14 Townsend, A. A., "The Properties of Equilibrium Boundary Layers," *Jour. of Fluid Mechanics*, Vol. 1, 1956, pp. 561–573.

15 Kays, W. M., and Crawford, M. E., *Convective Heat and Mass Transfer*, Second Edition, McGraw-Hill, New York, 1980.

16 Ligrani, P. M., Moffat, R. J., and Kays, W. M., "The Thermal and Hydrodynamic Behavior of Thick, Rough-Wall, Turbulent Boundary Layers," Report HMT-29, Thermosciences Division, Dept. of Mech. Eng., Stanford University, Dec. 1979.

17 Ligrani, P. M., and Moffat, R. J., "Artificially Thickening a Smooth-Wall Turbulent Boundary Layer," *AIAA Journal*, Vol. 17, No. 8, Aug. 1979, pp. 907–910.

18 Healzer, J. M., Moffat, R. J., and Kays, W. M., "The Turbulent Boundary Layer on a Rough, Porous Plate: Experimental Heat Transfer with Uniform Blowing," Report No. HMT-18, Thermosc. Div., Dept. of Mech. Engrg., Stanford University, 1974.

19 Pimenta, M. M., Moffat, R. J., and Kays, W. M., "The Turbulent Boundary Layer: An Experimental Study of the Transport of Momentum and Heat with the Effect of Roughness," Report HMT-21, Thermosc. Div., Dept. of Mechanical Engineering, Stanford University, 1975.

20 Jorgensen, F. E., "Directional Sensitivity of Wire and Hot-Film Probes," DISA Information No. 11, 1971.

21 Coles, D., "The Law of the Wake in the Turbulent Boundary Layer," *Jour. of Fluid Mechanics*, Vol. 1, 1956, pp. 191–226.

22 Monin, A. S., and Yaglom, A. M., *Statistical Fluid Mechanics*, Vol. 1, The MIT Press, 1971.

23 Grass, A. J., "Structural Features of Turbulent Flow Over Smooth and Rough Boundaries," *Jour. of Fluid Mechanics*, Vol. 50, Part 2, 1971, pp. 233–255.

24 Coleman, H. W., Moffat, R. J., and Kays, W. M., "Momentum and Energy Transport in the Accelerated Fully Rough Turbulent Boundary Layer," Report No. HMT-24, Thermosc. Div., Dept. of Mechanical Engineering, Stanford University, 1976.

25 Orlando, A. F., Moffat, R. J., and Kays, W. M., "Turbulent Transport of Heat and Momentum in a Boundary Layer Subject to Deceleration, Suction, and Variable Wall Temperature," Report No. HMT-17, Thermsc. Div., Dept. of Mechanical Engineering, Stanford University, 1974.

26 Ligrani, P. M., Kays, W. M., and Moffat, R. J., "A Heat Transfer Prediction Method for Turbulent Boundary Layers Developing Over Rough Surfaces With Transpiration," *IJHMT*, Vol. 24, No. 4, Apr. 1981, pp. 774–778.

Development of Three-Dimensional Turbulent Boundary Layer in an Axially Rotating Pipe

K. Kikuyama
Associate Professor.

M. Murakami
Professor.

K. Nishibori
Research Associate.

Department of Mechanical Engineering,
Nagoya University,
Furocho, Chikusaku,
Nagoya, Japan

The time-mean velocities and turbulent fluctuations inside the turbulent boundary layers which developed in an axially rotating pipe were measured in the case where an undeveloped flow with a rectangular axial velocity distribution was introduced in the pipe. The pipe rotation gives two counter effects on the flow: one is a destabilizing effect due to a large shear caused by the rotating pipe wall and the other is a stabilizing effect due to the centrifugal force of the swirling velocity component of the flow. The destabilizing effect prevails in the inlet region, but the stabilizing effect becomes dominant in the downstream sections. The intensity of turbulence in the rotating pipe decreases ultimately below that in a stationary state of the pipe. Using the experimental results, the relationship between the mixing length and Richardson number proposed by Bradshaw was examined for the turbulent boundary layer that develops in the rotating pipe.

Introduction

When a flow enters an axially rotating pipe, a tangential velocity component is given to the flow by the moving wall and a three-dimensional boundary layer is formed in the rotating pipe. The development of the boundary layer along the pipe is affected by the rotating motion of the pipe. The effect of the pipe rotation on the flow has been studied by several investigators including the present authors [1–4].

The present authors measured the time-mean velocity components and hydraulic losses of the pipe in the case where a fully developed flow was introduced into an axially rotating pipe in a turbulent flow state [4]. Pipe rotation was found to cause a drop in the hydraulic loss in the rotating pipe and to deform the axial velocity profile into a shape similar to that observed in a laminar flow. These changes are due to the stabilizing effect caused by the centrifugal force of the tangential flow component. According to the authors' study [5], when an undeveloped flow is introduced into the rotating pipe, the pipe rotation incurs two counter effects on the developing boundary layer flow: one is a destabilizing effect due to an increase of the relative velocity of the fluid at the surface of the rotating pipe, and the other is a stabilizing effect due to the turbulence suppression caused by the centrifugal force of the swirling flow component. The governing factors for the flow are the axial and tangential Reynolds numbers, and different combinations of two Reynolds numbers bring about different states of stability. But the detailed natures of the boundary layer, especially those of the turbulent intensity and the Reynolds shear stresses, have been left uninvestigated.

This paper describes the experimental results on the time-mean velocities and Reynolds stress components inside the turbulent boundary layer in an axially rotating pipe when an undeveloped flow is introduced into it. Using the experimental results, the relationship between the mixing length and Richardson number proposed by Bradshaw [6] was also examined.

Apparatus and Method of Experiment

A schematic outline of the experimental apparatus is shown in Fig. 1(*a*). Air discharged from a centrifugal blower was introduced into the rectifying tank. After the turbulence was made homogeneous over the inlet section of the rotating pipe by a honeycomb (20 mm square and 100 mm long) and six screens (mesh size: 1.0 ~ 2.62 mm, screen wire dia.: 0.26 ~ 0.56 mm), the air stream was throttled by the nozzle in the ratio of 12.3 : 1, which made the velocity profile at the inlet section of the rotating pipe almost uniform and the intensity of the turbulence was decreased less than 0.3 percent except for the small region near the pipe wall ($z/a \leqq 0.06$ for $\mathrm{Re} = 6 \times 10^4$).

In order to ensure that the flow state inside the boundary layer be turbulent just downstream of the inlet section, a stepring of 1.0 mm height was installed at the exit section of the nozzle as shown in Fig. 1(*a*). The turbulent state was ascertained by a hot-wire probe in the experimental range of the Reynolds number, $\mathrm{Re} = 6 \sim 9 \times 10^4$.

Measurements of the time-mean velocity components and the Reynolds stresses were made using the method of a rotated hot-wire [7, 8]. Two types of hot-wire probes were employed; one was a straight hot-wire type (the wire element was set normal to the stem axis) and the other was a slanted hot-wire type (the wire element was mounted at an angle of about 45 degrees to the axis). The active length of the wires (5 – micron

Contributed by the Fluids Engineering Division and presented at the Symposium on Three-Dimensional Turbulent Shear Flows, St. Louis, Mo., June, 1982.
Manuscript received by the Fluids Engineering Division, August 11, 1982.

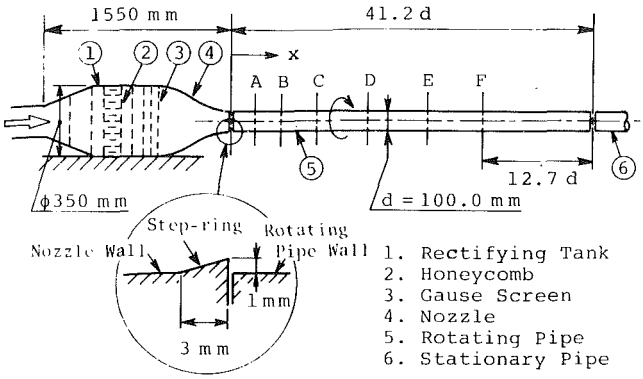

Fig. 1(*a*) Schematic outline of experimental apparatus

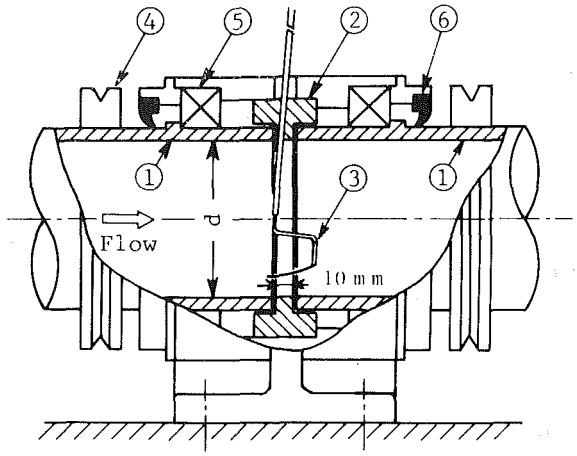

Fig. 1(*b*) Details in measuring section

tungsten) and the distance between the two prongs were 1 mm and 3 mm, respectively. These probes were inserted through a small hole drilled in a narrow stationary ring 10 mm in length placed between two rotating sections. To avoid the effect of this stationary ring on the velocity profile in the boundary layer, the probes were inserted at an angle of 4 degrees from the perpendicular, as shown in Fig. 1(*b*).

Measurements were made at the sections of $x/d = 2.7, 5.7, 9.7, 15.5, 22.5$, and 28.5, respectively, for the axial Reynolds number $\mathrm{Re} = 6\times10^4$ and for the range of rotation rate $0 \leqq N \leqq 0.83$.

Equations

Momentum and Energy Equations. Using the boundary-layer approximation, the equations of mean motion can be written in cylindrical coordinates for the case of an axisymmetric flow as follows:

$$U\frac{\partial U}{\partial x} + W\frac{\partial U}{\partial z} = -\frac{1}{\rho}\frac{\partial P}{\partial x} + \frac{1}{\rho r}\frac{\partial}{\partial z}(r\tau_x) \qquad (1)$$

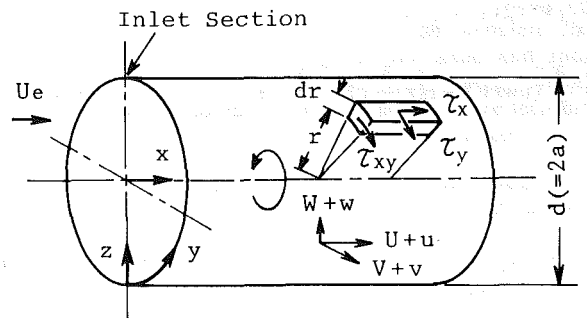

Fig. 2 Cylindrical coordinate system

Nomenclature

a = pipe radius
d = pipe diameter $= 2a$
$F(k)$ = normalized power spectrum in direction of mean flow
k = wave number in direction of mean flow
l = mixing length in rotating pipe
l_0 = mixing length in stationary state of pipe
n = frequency
N = rotation rate $= V_0/U_m$
P = time-mean static pressure
Pr_1 = dimensionless first production term of turbulent energy in equation (13)
Pr_2 = dimensionless second production term of turbulent energy in equation (13)
$q^2/2$ = kinetic energy of turbulence $= (\overline{u^2}+\overline{v^2}+\overline{w^2})/2$
Re = axial Reynolds number $= U_m \cdot d/\nu$
Ri = Richardson number defined by equation (12)
r = radial distance
U,V,W = time-mean velocity components in x, y, and z directions, respectively
u,v,w = fluctuating velocity components in x, y, and z directions, respectively
u',v',w' = rms values of u, v, and w, $(\sqrt{\overline{u^2}}, \sqrt{\overline{v^2}}, \sqrt{\overline{w^2}})$, respectively
$-\overline{uv}, \overline{vw}, -\overline{uw}$ = Reynolds shear stress components
U_e = free stream velocity
U_m = mean axial velocity
V_0 = peripheral speed of rotating pipe
x = axial distance from inlet section of rotating pipe
y = circumferential distance along pipe periphery
z = radial distance from pipe wall $= a-r$
β = parameter in equation (11)
δ = boundary layer thickness
θ_x = momentum thickness of boundary layer in x direction

$$= \int_0^\delta (U/U_e)\{1-(U/U_e)\}(r/a)\,dz$$

θ_{xy} = momentum thickness of boundary layer in y direction

$$= \int_0^\delta (U/U_e)(V/V_0)(r/a)^2 dz$$

τ_x, τ_y = shear stress components in x and y directions, respectively
ρ = density of fluid
μ = dynamic viscosity of fluid
ν = kinematic viscosity of fluid

$$U\frac{\partial V}{\partial x}+\frac{W}{r}\frac{\partial}{\partial z}(rV)=\frac{1}{\rho r^2}\frac{\partial}{\partial z}(r^2\tau_y) \tag{2}$$

$$\frac{V^2}{r}=\frac{1}{\rho}\frac{\partial P}{\partial r}+\frac{1}{r}\frac{\partial}{\partial r}(\overline{rw^2})-\frac{\overline{v^2}}{r} \tag{3}$$

$$\frac{\partial}{\partial x}(rU)+\frac{\partial}{\partial z}(rW)=0 \tag{4}$$

where (U,V,W) and (u,v,w) are the time-mean and turbulent velocity components, respectively, in Fig. 2. The shear stress components in both the axial and tangential directions, τ_x and τ_y, are given by the following equations.

$$\tau_x=-\rho\overline{uw}+\mu\frac{\partial U}{\partial z},\ \tau_y=-\rho\overline{vw}+\mu r\frac{\partial}{\partial z}(V/r) \tag{5}$$

From equations (1) and (2), the energy equations of the time-mean velocities can be obtained as:

$$U\frac{\partial}{\partial x}(U^2/2)+W\frac{\partial}{\partial z}(U^2/2)=-\frac{U}{\rho}\frac{\partial P}{\partial x}+\overline{uw}\frac{\partial U}{\partial z}$$
$$-\frac{1}{r}\frac{\partial}{\partial z}(\overline{uwrU})-\nu\left(\frac{\partial U}{\partial z}\right)^2+\frac{\nu}{2r}\frac{\partial}{\partial z}\left(r\frac{\partial U^2}{\partial z}\right) \tag{6}$$

$$U\frac{\partial}{\partial x}(V^2/2)+W\frac{\partial}{\partial z}(V^2/2)=\frac{V^2W}{r}+\overline{vwr}\frac{\partial}{\partial z}(V/r)$$
$$-\frac{1}{r}\frac{\partial}{\partial z}(\overline{vwrV})-\nu\left\{r\frac{\partial}{\partial z}(V/r)\right\}^2+\frac{\nu}{2r}\frac{\partial}{\partial z}\left\{r^3\frac{\partial}{\partial z}(V/r)^2\right\} \tag{7}$$

In the right-hand sides of equations (6) and (7), the terms including the kinematic viscosity are negligibly small compared with the other terms except for the region of the viscous layer. Using the boundary-layer approximation, the turbulent energy equation can be expressed as:

$$U\frac{\partial}{\partial x}(q^2/2)+W\frac{\partial}{\partial z}(q^2/2)=-\overline{uw}\frac{\partial U}{\partial z}-\overline{vwr}\frac{\partial}{\partial z}(V/r)+D-\epsilon \tag{8}$$

where D and ϵ denote the turbulent diffusion and the viscous dissipation of the energy, respectively. In the above equation the terms on the left-hand side correspond to the convection terms of the turbulent energy, and both the first and second terms on the right-hand side of the equation are the production terms. The second production term does not appear in the stationary state of the pipe.

Mixing Length and Richardson Number. Coefficients of the eddy viscosity both in the axial and tangential directions are defined by:

$$\nu_{tx}=-\overline{uw}/\left(\frac{\partial U}{\partial z}\right),\ \nu_{ty}=-\overline{vw}/\left\{r\frac{\partial}{\partial z}(V/r)\right\} \tag{9}$$

Using the values of the eddy viscosity, the mixing lengths in both directions can be expressed by the reference [9] as:

$$l_i^2=\nu_{ti}/\left[\left(\frac{\partial U}{\partial z}\right)^2+\left\{r\frac{\partial}{\partial z}(V/r)\right\}^2\right]^{1/2},\ i=x,y \tag{10}$$

From the analogy between the buoyancy and centrifugal force, Bradshaw [6] proposed the mixing length l as a function of the Richardson number in the field of a centrifugal force as follows:

$$l/l_0=1-\beta\mathrm{Ri} \tag{11}$$

where l_0 denotes the value of the mixing length in a flow with no swirl component, β is a constant, and Ri is the Richardson number defined by:

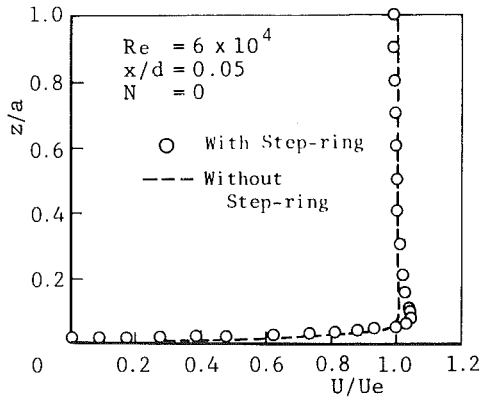

Fig. 3 Velocity profile at the section just downstream from the pipe inlet ($x/d=0.05$) for $N = 0$. (Uncertainties in z/a and U/Ue are ±0.1 percent and ±2 percent, respectively.)

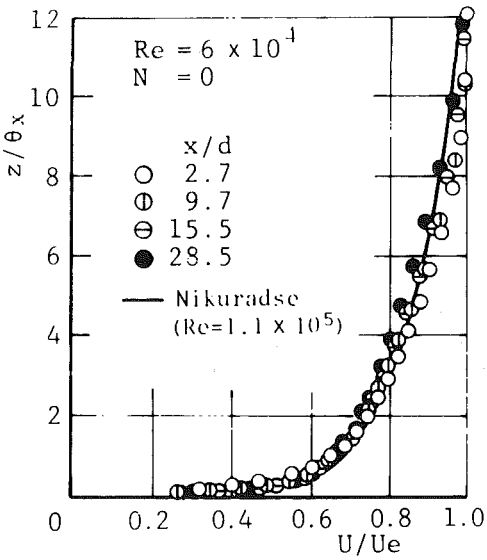

Fig. 4 Velocity profiles for $N = 0$. (Uncertainties in z/θ_x and U/Ue are ±2 percent).

$$\mathrm{Ri}=\frac{2V}{r^2}\frac{\partial}{\partial r}(rV)/\left[\left(\frac{\partial U}{\partial z}\right)^2+\left\{r\frac{\partial}{\partial z}(V/r)\right\}^2\right] \tag{12}$$

The value of the angular momentum, rV, increases with the radial distance r in the rotating pipe, and hence Ri $\geqq$ 0, which shows that the tangential velocity component has a stabilizing effect on the flow when there are no destabilizing effects from other sources.

Experimental Results and Discussion

Time-Mean Velocity Distributions. The time-mean velocity profiles at the section just downstream from the pipe inlet (x/d = 0.05) under the stationary condition of the pipe are indicated in Fig. 3, where the effect of the step-ring at the pipe inlet is also shown. The profiles both with and without the step-ring are almost uniform across the section, except for a narrow region near the pipe wall. The intensity of the turbulence in the uniform velocity zone was measured to be less than 0.3 percent.

The similarity of the velocity profiles of the boundary layer in a stationary pipe when the step-ring is employed are shown in Fig. 4 in which the velocity curve measured by Nikuradse in a fully developed turbulent pipe flow at Re = 1.1 × 10^5 is also indicated. A fairly good coincidence in the velocity curves can be seen in the sections between x/d = 2.7 and 28.5, and it

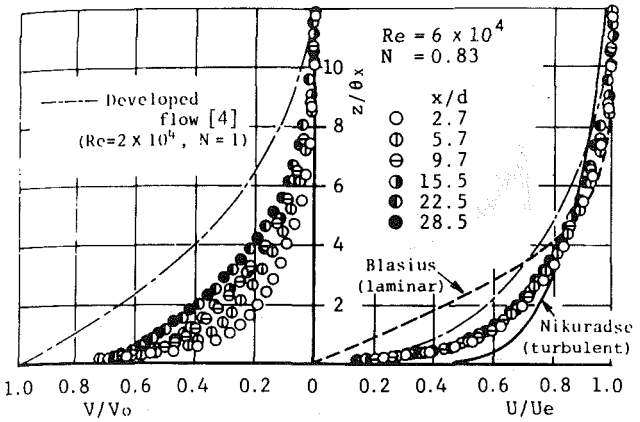

Fig. 5 Changes in velocity profiles for $N = 0.83$. (Uncertainties in z/θ_x and U/Ue are ±2 percent, and in V/V_o ±3 percent.)

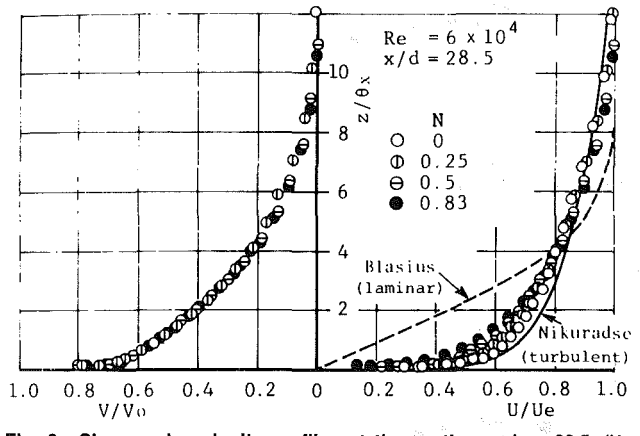

Fig. 6 Changes in velocity profiles at the section $x/d = 28.5$. (Uncertainties in z/θ_x and U/Ue are ±2 percent, and in V/V_o ±3 percent.)

may be considered that the flow in the boundary layer at the section of x/d = 2.7 is already in a turbulent state when the step-ring is installed.

If the pipe is rotated, the velocity profiles are changed, an example of which is shown for $N = 0.83$ in Fig. 5, where the axial and tangential components of the velocities are plotted for different sections situated at $x/d = 2.7 \sim 28.5$. In the same figure, the velocity profiles for a turbulent flow (Nikuradse) and a laminar flow (Blasius) in stationary ducts are also plotted for reference. The axial velocities at the different sections in the rotating pipe show a nearly similar profile, which lies between two reference velocity curves. As the section goes downstream, however, the tangential velocity curves are shifted upward in the inner region by the effect of the rotating wall. The effects of the rotation rate N on the velocity distributions at the section of $x/d = 28.5$ are shown in Fig. 6. As the rotation rate increases, the axial velocity curves approach gradually to that in a laminar state as shown by a broken line. But, the tangential velocity profiles for each value of N remain almost unchanged. The tangential velocity curve can be approximated by the following equation:

$$1 - V/V_0 = \{(z/\theta_x)/10\}^{0.3}$$

The changes in the momentum thickness components along the pipe axis, θ_x and θ_{xy}, are plotted in Fig. 7. As N increases, the curves of θ_x and θ_{xy} are flattened gradually, which displays the suppression of the boundary layer development due to the pipe rotation.

Turbulent Fluctuations and Reynolds Shear Stresses. The distributions of the turbulent fluctuation velocities and

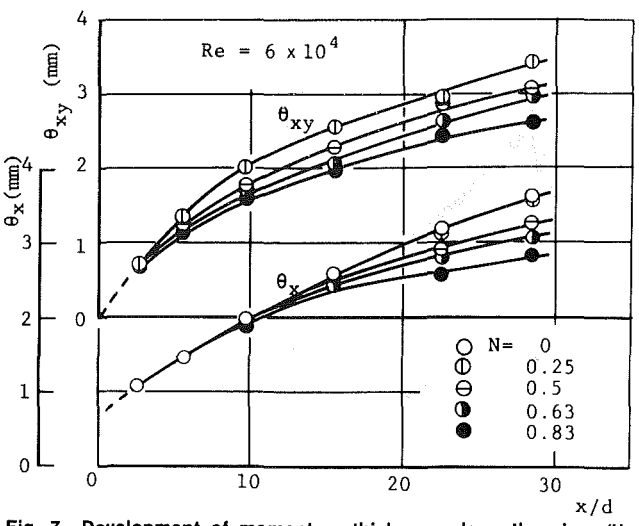

Fig. 7 Development of momentum thickness along the pipe. (Uncertainties in θ_x and θ_{xy} are ±2 percent and ±4 percent, respectively.)

Reynolds shear stresses in a section near the pipe inlet ($x/d = 2.7$) are plotted in Figs. 8(a) and (b), respectively. From Fig. 8(a), it may be seen that the pipe rotation gives a considerable change in the tangential component of the turbulent fluctuations but only a slight change in the axial and radial components. The Reynolds shear stress components $-\overline{uv}$ and $\overline{vw}$ in the stationary state of the pipe in Fig. 8(b) are seen to be zero throughout the boundary layer as is expected from a statistical background. When the pipe is rotated, the stress components of $-\overline{uv}/U_e^2$ and $\overline{vw}/U_e^2$ increase with the increase of N, but the other component $-\overline{uw}/U_e^2$ remains almost unchanged. The increase in the Reynolds shear stress components is caused by an intense shear due to the rotational motion of the pipe wall, which prevails in the inlet region of the pipe.

Figures 9(a) and (b) exhibit three components of the turbulent fluctuations and Reynolds shear stresses at the section of $x/d = 28.5$, respectively. Unlike the results in the section of $x/d = 2.7$, all of the fluctuation components in this section decrease with the increase in the rotation rate N. The drops in u'/U_e and v'/U_e are remarkable in the wall region $z/\theta_x \leqq 1$, but the decrease in w'/U_e is distributed uniformly across the boundary layer. Of the three Reynolds shear stresses, the effect of the pipe rotation on the stress $-\overline{uw}/U_e^2$ is evident, and it decreases with an increase in the rotation rate. The other stresses $-\overline{uv}/U_e^2$ and $\overline{vw}/U_e^2$, however, have only slight values in the rotational state as well as the stationary state.

Distributions of the kinetic energy of the turbulent fluctuation $q^2/U_e^2 (= (\overline{u^2} + \overline{v^2} + \overline{w^2})/U_e^2)$ across the boundary layer are shown in Fig. 10. In the upstream section $x/d = 2.7$, the turbulent energy is seen to increase with the rotation rate. This is due to an intense shear caused by the rotating wall. This destabilizing effect of the tangential shear, however, diminishes gradually as the section goes downstream, and the stabilizing effect due to the swirling flow becomes dominant. At the section $x/d = 9.7$, all of energy curves fall nearly into a single curve because the stabilizing and destabilizing effects of the pipe rotation are well balanced. The drop in the turbulent energies in the downstream sections shows a dominant stabilizing effect caused by the centrifugal force of the swirling flow, and the turbulent energy in the rotating state becomes smaller than that in the stationary state. This fact corresponds well to the results in Fig. 7.

To estimate the contributions of each term in equation (8) to the entire turbulent energy, the values of each term for $x/d = 2.7$ in N = 0.83 are plotted in Figs. 11(a) and (b), in which

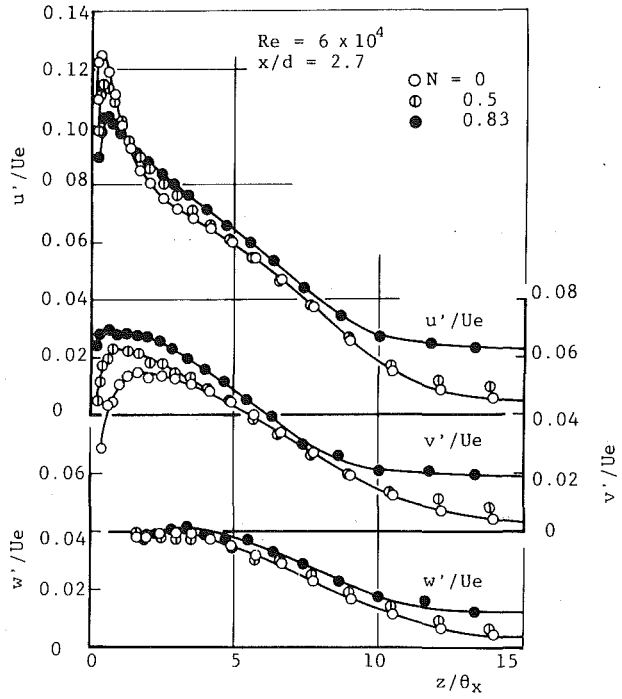

Fig. 8(*a*) Turbulent intensity components. (Uncertainties in *u'/Ue*, *v'/Ue* and *w'/Ue* are ± 3 percent.)

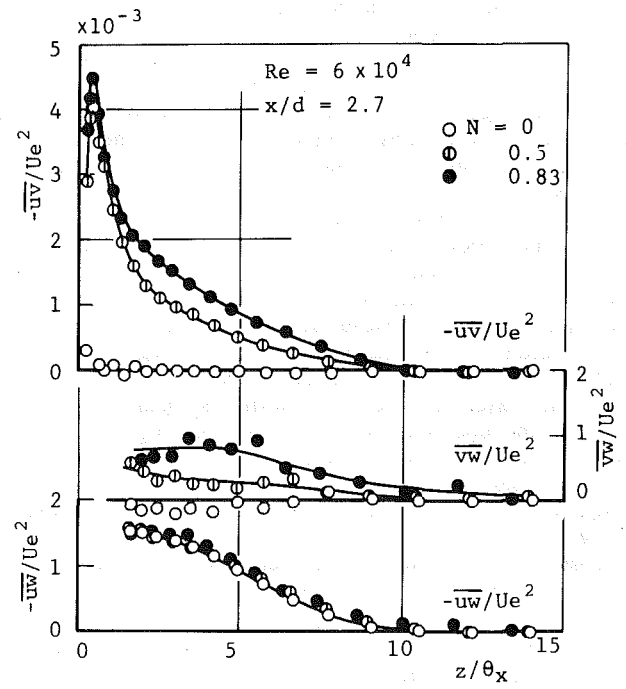

Fig. 8(*b*) Reynolds shear stresses. (Uncertainties in $-\overline{uv}/Ue^2$ and $-uw/Ue^2$ are ±5 percent, and in $\overline{vw}/Ue^2$ ±10 percent.)

Fig. 8 Distributions of turbulent intensity components and Reynolds shear stresses at the section near the pipe inlet x/d = 2.7 (a least-square averaging of data was used)

the first and second terms on the right-hand side of equation (8) are plotted in dimensionless forms as:

$$Pr_1 = -\frac{\delta}{U_e^3}\overline{uw}\frac{\partial U}{\partial z},\quad Pr_2 = -\frac{\delta}{U_e^3}\overline{vwr}\frac{\partial}{\partial z}(V/r) \qquad (13)$$

In these figures, the values of Pr_1, evaluated in this experiment at $N = 0$, as well as those obtained by Klebanoff

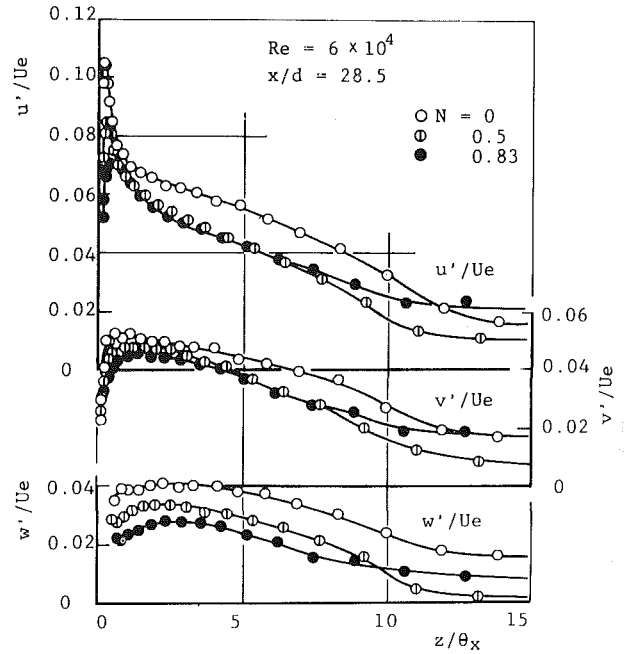

Fig. 9(*a*) Turbulent intensity components. (Uncertainties in *u'/Ue*, *v'/Ue* and *w'/Ue* are ±3 percent.)

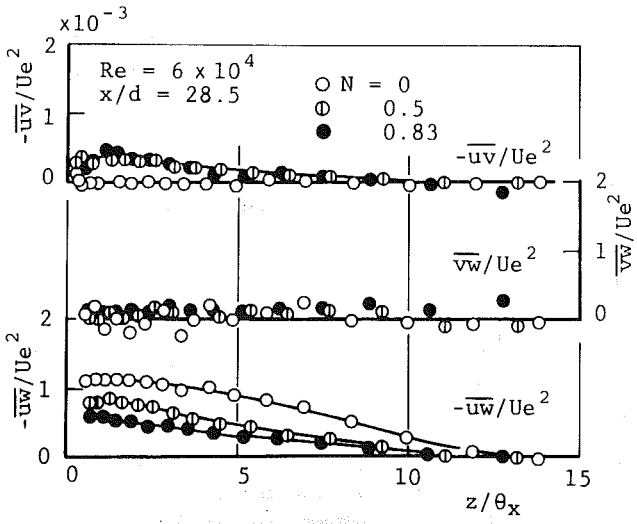

Fig. 9(*b*) Reynolds shear stresses. (Uncertainties in $-\overline{uv}/Ue^2$ and $-uw/Ue^2$ are ±5 percent, and in $\overline{vw}/Ue^2$ ±10 percent.)

Fig. 9 Distributions of turbulent intensity components and Reynolds shear stresses at the downstream section x/d = 28.5 (a least-square averaging of the data was used)

[10] in a turbulent boundary layer on a stationary flat-plate, are plotted for reference. At the section where x/d = 2.7 (Fig. 11(*a*)), the first production term Pr_1 is greater than that observed for $N = 0$, and the second production term Pr_2, which appears only in the rotating state, also has a small positive value. Consequently, the sum of the production terms, $Pr_1 + Pr_2$, becomes much greater than the production term in the stationary pipe.

In the downstream section x/d = 28.5 (Fig. 11(*b*)), the production terms Pr_1 and Pr_2 have decreased greatly and their sum becomes smaller than the production term in the stationary state of the pipe. This decrease in the turbulent energy production in the rotating pipe corresponds well to the decrease in the turbulent fluctuation as shown in Figs. 9(*a*) and (*b*).

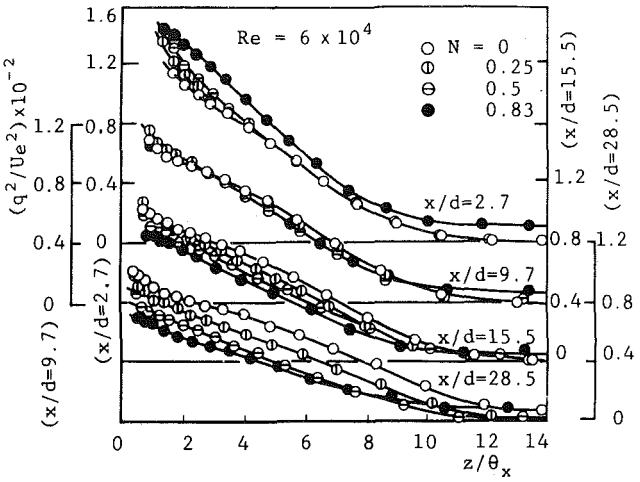

Fig. 10 Distributions of turbulent energy. (Uncertainties in q^2/Ue^2 and z/θ_x are ±3 percent and ±2 percent, respectively.)

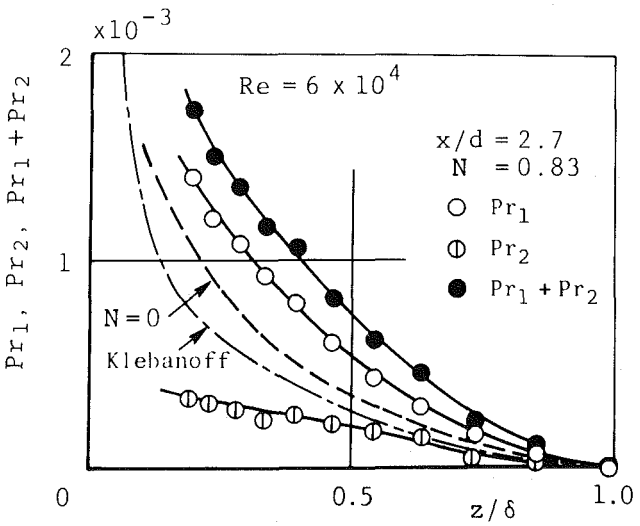

Fig. 11(*a*) At the section $x/d = 2.7$

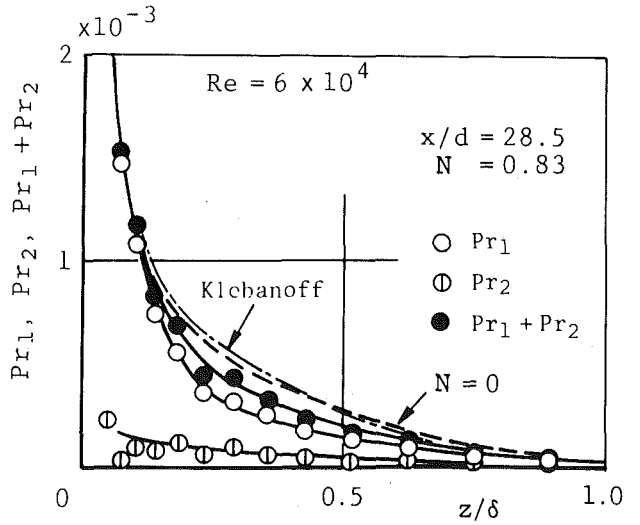

Fig. 11(*b*) At the section $x/d = 28.5$

Fig. 11 Distribution of energy production terms for $N = 0.83$. (Uncertainties in Pr_1, Pr_2 and z/δ are ±5, ±10 and ±5 percent, respectively.)

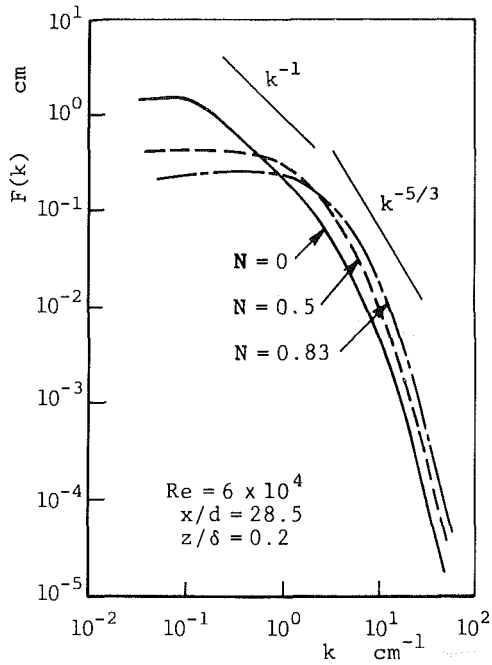

Fig. 12 Power spectra of fluctuating velocity in the direction of mean flow. (Uncertainties in $F(k)$ and k are ±5 percent.)

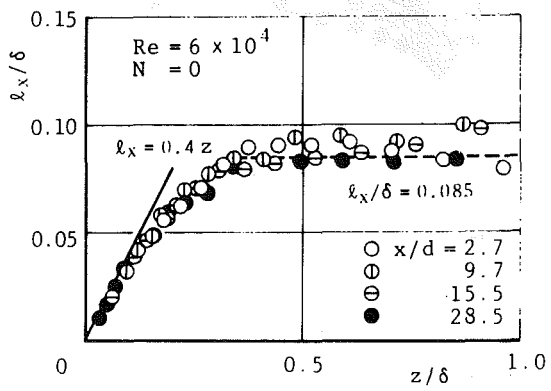

Fig. 13 Distribution of mixing length for $N = 0$. (Uncertainties in l_x/δ and z/δ are ±10 percent and ±5 percent, respectively.)

Figure 12 shows the power spectra of the fluctuating velocity component in the mean flow direction. The data were measured at the point $z/\delta = 0.2$ in the section $x/d = 28.5$. The results in Fig. 12 are normalized as:

$$\int_0^\infty F(k)\,dk = 1$$

where k is the wave number in the mean flow direction, i.e.,

$$k = 2\pi n/(U^2 + V^2)^{1/2}$$

It is seen that the spectrum curves are flattened by an increase in the rotation rate, hence the values of $F(k)$ increase in the range of higher wave number or smaller eddy range.

Mixing Length. Using the mixing length theory, the suppression of the turbulence due to pipe rotation can be equated with the decrease in the mixing length l_x. Figure 13 exhibits the distributions of l_x calculated by equations (9) and (10) for various sections when $N = 0$. Regardless of the axial distance, the mixing length can be expressed by the following relations:

$$l_x = 0.4z, \quad \text{for } z/\delta < 0.1$$
$$l_x = 0.085\delta, \quad \text{for } z/\delta > 0.35$$

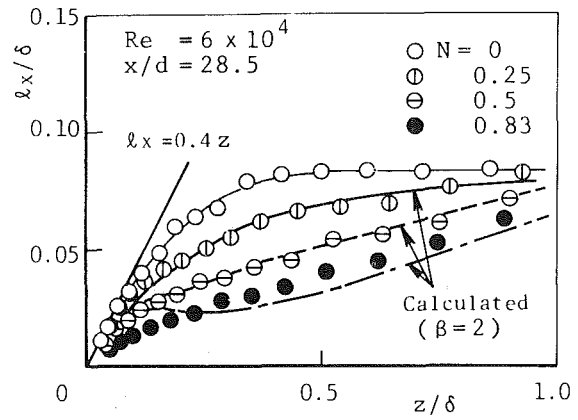

Fig. 14(a) At the section x/d = 28.5

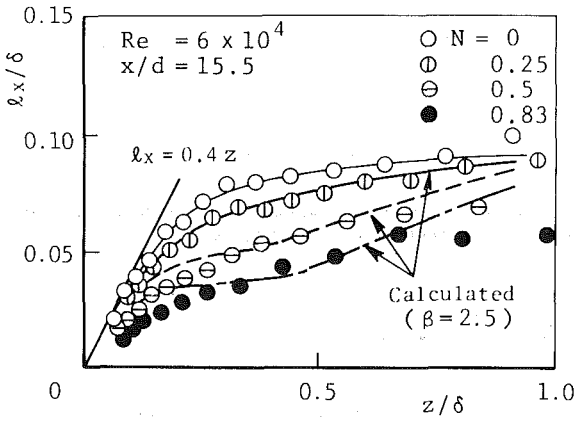

Fig. 14(b) At the section x/d = 15.5

Fig. 14 Changes in mixing length due to rotation. (Uncertainties in l_x/δ and z/δ are ±10 percent and ±5 percent, respectively.)

The distributions of l_x at the sections x/d = 28.5 and 15.5 in rotating states of the pipe are shown in Figs. 14(*a*) and (*b*), respectively. In both sections, the mixing length decreases significantly with an increase in rotation rate, exhibiting the stabilizing effect due to pipe rotation. The gradient of the curves near the pipe wall decreases as N is increased. From an analogy of two forces, the buoyancy and the centrifugal force, Bradshaw [6] has expressed the mixing length in a rotating field as a function of the Richardson number Ri by equation (12). Using the values of Ri calculated by equation (12), the values of l_x in the sections of x/d = 28.5 and 15.5 can be evaluated, and the results are compared with the experiments in Figs. 14(*a*) and (*b*), where in the calculation β is taken as 2 and 2.5 for the two sections, respectively. It is seen that the calculated values agree well with the experiments.

For the discussion of the mixing length change in the curved or rotating flow, Bradshaw [6] has pointed out that the "flux" Richardson number, R_f, given by the following equation may be more appropriate than the "gradient" Richardson number, Ri, defined by equation (12).

$$R_f = 2\overline{vw}(V/r)/\left\{-\overline{uw}\frac{\partial U}{\partial z} + \frac{\overline{vw}}{r}\frac{\partial}{\partial r}(rV)\right\} \qquad (14)$$

The use of equation (14), however, is found not to be adequate in the present flow problem, because the tangential component of the Reynolds stresses, $\overline{vw}$, is much less than the axial component, $-\overline{uw}$, within the boundary layer at the section of x/d = 28.5, as shown in Fig. 9(*b*) and the value of R_f remains substantially zero for the rotation rate of N = 0 ~ 0.83.

Conclusions

(1) The rotation of a pipe generally suppresses development of the turbulent boundary layer in the pipe, and the time-mean axial velocity profile approaches the velocity curve of a laminar state with an increase in the rotational speed.

(2) In the sections immediately downstream from the pipe inlet ($x/d < 10$), the Reynolds shear stress components $-\overline{uv}$ and $\overline{vw}$ are increased by an intensive shear due to the relative motion near the pipe wall.

(3) In the sections further downstream ($x/d \geqq 10$), a stabilizing effect caused by the centrifugal force of the swirling flow develops in the rotating pipe, suppressing gradually the turbulence along the pipe. The turbulence intensity ultimately falls below that of the stationary state of the pipe.

(4) Changes in the mixing length due to the pipe rotation can be estimated by use of the Richardson number.

Acknowledgments

The authors wish to express their appreciation to Mr. T. Yoshimoto, Mr. S. Asai and Mr. S. Hayashi for their experimental work, and also to Prof. I. Nakamura of Nagoya University for discussion and suggestions for this study.

References

1 White, A., "Flow of a Fluid in Axially Rotating Pipe, "*Journal of Mechanical Engineering Science*, Vol. 6, No. 1, 1964, pp. 47–54.

2 Cannon, J. N., and Kays, W. M., "Heat Transfer to a Fluid Flowing inside a Pipe Rotating about its Longitudinal Axis," ASME *Journal of Heat Transfer*, Vol. 91, No. 1, 1969, pp. 135–139.

3 Yamada, Y., and Imao, S., "Swirling Flow in an Axially Rotating Pipe," *Transactions of the Japan Society of Mechanical Engineers*, Vol. 46, No. 409, Ser. B, 1980, pp. 1662–1670 (in Japanese).

4 Murakami, M., and Kikuyama, K., "Turbulent Flow in Axially Rotating Pipes," ASME JOURNAL OF FLUIDS ENGINEERING, Vol. 102, No. 1, Mar. 1980, pp. 97–103.

5 Murakami, M., Kikuyama, K., and Nishibori, K., "Three Dimensional Boundary Layer Development in an Axially Rotating Pipe," *Proc. 3rd Symp. Turbulent Shear Flows*, Calif. Univ., 1981, pp. 2.1–2.6.

6 Bradshaw, P., "The Analogy between Streamline Curvature and Buoyancy in Turbulent Shear Flow," *Journal of Fluid Mechanics*, Vol. 36, No. 1, 1969, pp. 177–191.

7 Bissonnette, L. R., and Mellor, G. L., "Experiments on the Behaviour of an Axisymmetric Turbulent Boundary Layer with a Sudden Circumferential Strain," *Journal of Fluid Mechanics*, Vol. 63, 1974, pp. 369–413.

8 Nakamura, I., Yamashita, S., and Furuya, Y., "Experiments on Turbulence Properties in the Thick Turbulent Boundary Layer on a Rotating Conical Body of Radius Decreasing Toward Downstream," *Turbulent Shear Flows 2*, ed. by L. J. S. Bradbury et al., Springer, 1980, pp. 99–115.

9 Koosinlin, M. L., Launder, B. E., and Sharma, B. I., "Prediction of Momentum, Heat and Mass Transfer in Swirling, Turbulent Boundary Layers," ASME *Journal of Heat Transfer*, Vol. 96, May, 1974, pp. 204–209.

10 Klebanoff, P. S., "Characteristics of Turbulence in a Boundary Layer with Zero Pressure Gradient," NACA Rpt. 1247, 1955, pp. 1135–1153.

M. Arie
President.

M. Kiya
Professor.

Department of Mechanical Engineering,
Hokkaido University,
Sapporo, 060, Japan

M. Moriya
Instructor,
Department of Mechanical Engineering,
Kitami Institute of Technology,
Kitami, 090, Japan

H. Mori
Graduate Student,
Department of Mechanical Engineering,
Hokkaido University,
Sapporo, 060, Japan

Pressure Fluctuations on the Surface of Two Circular Cylinders in Tandem Arrangement

The fluctuating pressures on the surface of two circular cylinders of the same diameter in tandem arrangement were measured in the upper subcritical regime to obtain the distributions of their rms values and the spanwise and circumferential correlations. These pressures were subsequently integrated to yield the spanwise correlation length and the rms values of fluctuating lift and drag as functions of the spacing between the two cylinders. The rms lift and drag were much larger for the downstream cylinder than for the upstream cylinder up to the spacing of 7.0 diameters. At the spacing of 10.0 diameters, they were different from those for a single cylinder by only a small amount.

1 Introduction

The time-mean surface pressures and the vortex-shedding characteristics of two circular cylinders of the same diameter in tandem arrangement have been extensively studied for many years. A critical and extensive review on this subject was written by Zdravkovich [1], who also discussed the cases of parallel and staggered arrangements. The fluctuating component of the surface pressures, on the other hand, is not yet understood to the same extent. Within the authors' knowledge, most previous investigators concentrated directly on the oscillation of two cylinders associated with the vortex shedding (see King & Jones [2]), less attention being paid to the surface-pressure fluctuations.

The properties of the surface-pressure fluctuations, especially the spanwise and circumferential correlations between pressures at two points, are of considerable engineering significance in that they will yield information about the rms values and spanwise coherence of the fluctuating lift and drag forces. Moreover, various statistics of the surface-pressure fluctuations will unveil some aspects of unsteady separated flows around the cylinder during strong interaction.

The rms surface-pressure distributions around two cylinders in tandem arrangement is reported by Igarashi [3] for various intervals between the cylinders. Within the authors' knowledge, no other measurements of the pressure fluctuations seem to be published for this particular flow situation. It may be mentioned in passing that, for two square prisms in tandem arrangement, Reinhold et al. [4] measured instantaneous surface-pressure fluctuations along all the four sides of the prisms, thus approximately obtaining the rms values and the power spectra of the fluctuating forces.

In this paper, properties of the pressure fluctuations on the surface of two circular cylinders in tandem will be presented in some detail for various spacings between the cylinders.

2 Experimental Apparatus and Procedure

The experiments were conducted in an open-return air tunnel with a 48×50 cm, 5 m long working section. Time-mean velocity distributions were measured at several sections along and across the tunnel ahead of the test cylinders by means of a Pitot-static tube. The maximum cross-sectional variations in the approaching velocity, U_∞, were less than 1 percent of the mean over the traversed area except in the boundary layers developing along the tunnel walls. A point where the reference static and total pressures could be measured was chosen on the basis of the longitudinal traverses ahead of the models. The free-stream turbulence intensity (the rms longitudinal velocity fluctuation divided by U_∞) was 0.3 percent at the time-mean velocity of $U_\infty = 54.5 \pm 1.0$ *m/s*, which was the velocity employed in the present experiment.

The circular cylinders tested were machined brass with 4.37 cm diameter with no attempt being made to improve the surface finish. The cylinders were mounted normal to the approaching flow and spanned the 0.5 m side of the tunnel. The resulting aspect ratio 11.4 was considered to be large enough to ensure that the measurements would be representative of infinitely long cylinders. No end plates were

Contributed by the Fluids Engineering Division and presented at the ASME Applied Mechanics, Bioengineering, and Fluids Engineering Conference, Houston, Texas, June 20-22, 1983, of THE AMERICAN SOCIETY OF MECHANICAL ENGINEERS. Manuscript received by the Fluids Engineering Division, February 16, 1981. Paper No. 83-FE-7.

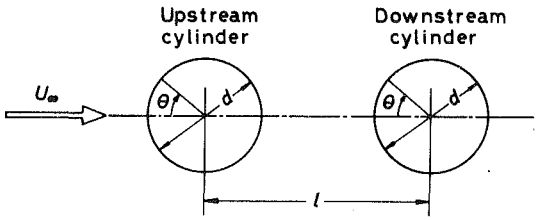

Fig. 1 Two circular cylinders in tandem arrangement

used. The boundary layers along the sides of the tunnel were turbulent and their thickness was 3.7 cm on both sides.

One of the test cylinders was built in two sections to facilitate the construction of the pressure taps whereas another cylinder was not pressure-tapped. The latter cylinder was used solely to realize a required tandem arrangement of the two cylinders. Each of the two sections had a pressure tap of 0.8 mm diameter at each end which was connected to a semiconductor strain-gaged transducer with a small cavity between the opening of the tap and the diaphragm of the transducer.

The two sections were combined by a ball-bearing device so that the angle between the pressure taps could be arbitrarily varied by the rotation about the common axis. This configuration allowed the circumferential correlation of the surface-pressure fluctuations to be measured. The spanwise distance between the pressure taps was 0.14 times the cylinder diameter in this experiment. On the other hand, in order to obtain the spanwise correlation of the surface-pressure fluctuations, spacers of various lengths were separately inserted between the two sections in such a manner that their pressure taps were at the same angle from the leading generator. The center between the two pressure taps was made to coincide with the mid-span position during the measurements of the circumferential and spanwise correlations. The time-mean and rms values and the power spectra of the pressure fluctuations were obtained at the mid-span position.

The pressure transducers responded to the pressure fluctuations up to 500 Hz with a gain factor 1 ± 0.06, the phase lag being negligible. This frequency was well above the frequencies of vortex shedding from the upstream and downstream cylinders. The outputs of the pressure transducers were recorded on an analog tape recorder (KYOWA 520A) and, except a few cases, were later analyzed on a digital correlator (SAICOR 42A) and a digital signal processor (SANEI 7T07A) to obtain the rms values, power spectra, and cross correlations.

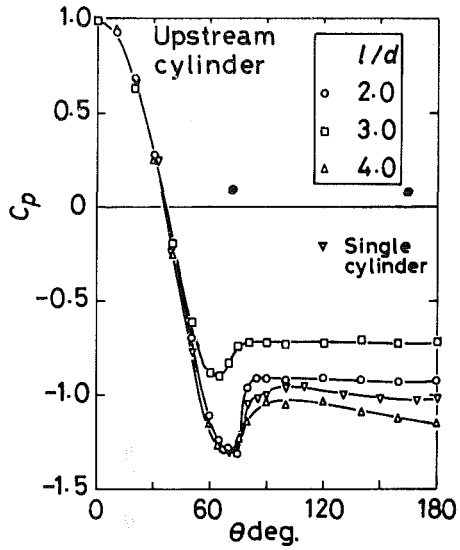

Fig. 2(a)

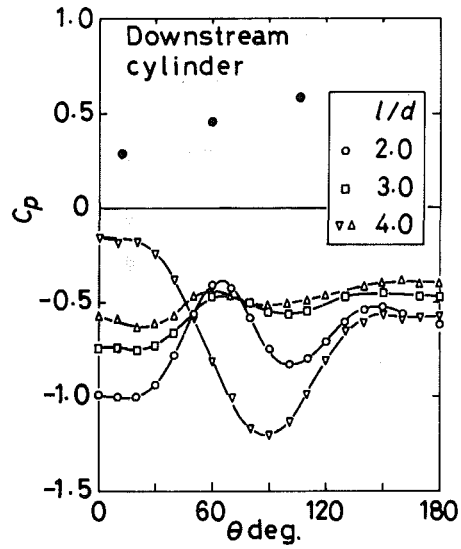

Fig. 2(b)

Fig. 2 Time-mean pressure distribution along the surface of (a) upstream and (b) downstream cylinders for $l/d = 2$, 3, and 4. The uncertainty in the ordinate is ± 0.01 and that in the abscissa is ± 0.2 deg. Lines for visual aid only. •, peaks of C_p' for $l/d = 2$. Ordinate of C_p' is the same to that of C_p.

3 Results and Discussion

A definition sketch of two cylinders in tandem arrangement is shown in Fig. 1. The Reynolds number R was maintained to be 1.57×10^5 throughout this experiment. Moreover, since it was uncertain whether available methods of correction of the tunnel blockage effect could be applicable to the present flow situation, the results will be presented uncorrected. In the interest of space, most of the data for the surface pressure will be shown for the spacings $l/d = 2$, 3, and 4 although the measurements were made until $l/d = 10$. For pressure

Nomenclature

C_D' = rms drag divided by $q_\infty d$
C_{DD} = spanwise correlation coefficient of fluctuating sectional drag coefficients
C_L' = rms lift divided by $q_\infty d$
C_{LL} = spanwise correlation coefficient of fluctuating sectional lift coefficients
C_p = time-mean pressure divided by q_∞
C_p' = rms pressure divided by q_∞
d = diameter of circular cylinder
f = frequency of vortex shedding
l = distance between centers of two cylinders
L_{pz} = spanwise correlation length of surface-pressure fluctuations
q_∞ = free-stream dynamic pressure $= (1/2)\rho U_\infty^2$
R = Reynolds number $= U_\infty d/\nu$
R_{pp} = cross correlation coefficient of surface-pressure fluctuations
U_∞ = time-mean velocity of free stream
α, β = angle measured from leading generator of cylinder
ζ = spanwise distance between pressure taps
θ = angle measured from leading generator of cylinder
ν = kinematic viscosity
ρ = density of fluid

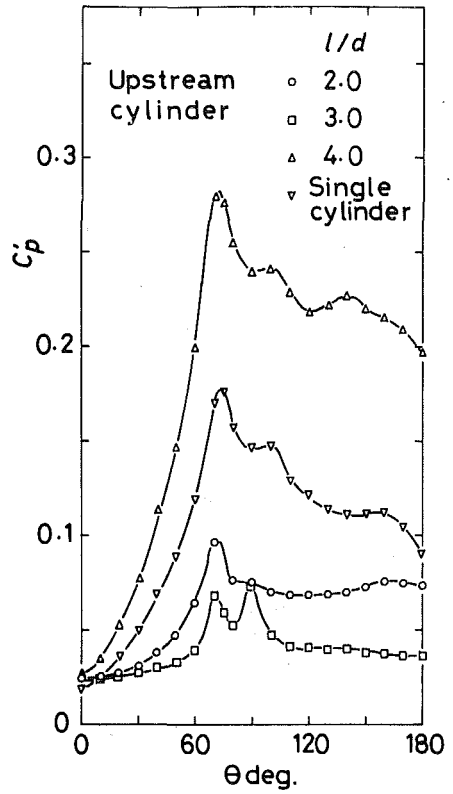

Fig. 3(a)

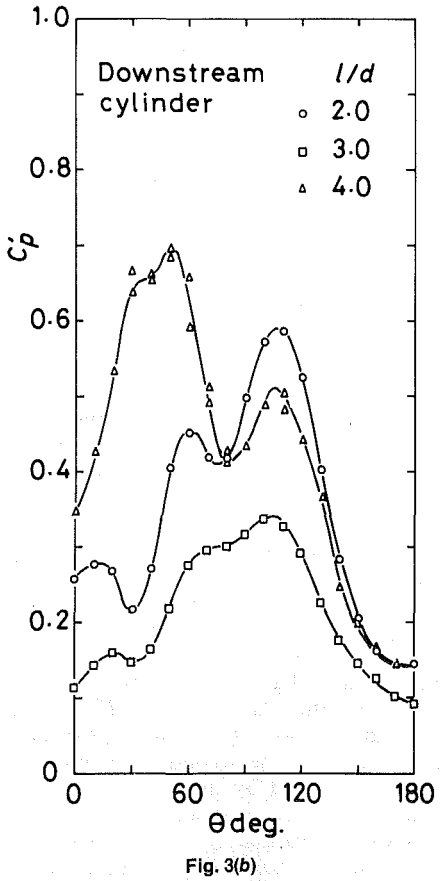

Fig. 3(b)

Fig. 3 Rms pressure distribution along the surface of (*a*) upstream and (*b*) downstream cylinders for $l/d = 2$, 3, and 4. The uncertainty in the ordinate is ± 0.01 and that in the abscissa is ± 0.2 deg. Lines for visual aid only.

distributions in the range $l/d > 4$, Igarashi's [3] paper should be consulted.

3.1 Time-Mean Surface Pressure, Drag and Strouhal Number. The measurement of the time-mean pressure distribution around a single cylinder showed that the flow around it was in the upper subcritical regime at this Reynolds number. The time-mean pressure distributions around the upstream and downstream cylinders are presented in Fig. 2. For the sake of reference, values and locations of peaks of C_p' are also included in these figures for $l/d = 2$. For the spacings $l/d > 4$, the separation of flow occurred well downstream of $\theta = 120$ deg, so that the base-pressure coefficient amounted to -0.6, which is much higher than that for the upstream cylinder. These features are conjectured to be caused by the boundary-layer transition due to the turbulence in the wake of the upstream cylinder. For the case of $l/d = 4$, two pressure distributions are shown for the downstream cylinder in order to show that they appeared one after another with undefined frequencies. The time interval for the distribution denoted by the symbol ▽ was longer than that for the distribution denoted by △. This feature is associated with a jump of the flow pattern which will be described in the following.

It is well established that a sudden change in the flow pattern in the gap between two cylinders occurs when the spacing is increased through a critical spacing (Zdravkovich [1]). Previous measurements (Zdravkovich [1], Okajima [5]) indicate that the critical spacing ranges from 3.5 to 3.8 diameters at a Reynolds number of 1.57×10^5. The authors felt during the pressure measurement that the critical spacing was in the vicinity of $l/d = 4$, so that it is assumed that the critical spacing was $l/d = 3.8$ in the following discussion.

The time-mean drag coefficient for the upstream and downstream cylinders plotted against l/d was in fairly good agreement with Okajima's [5] result taken at approximately same Reynolds numbers, including a discontinuous jump of the drag coefficient at the critical spacing.

The vortex-shedding frequency was determined on the basis of the power spectra of the surface-pressure fluctuations as the frequency corresponding to a spectrum peak. The Strouhal number of the vortex shedding was found to be almost the same for two cylinders. Moreover, they are also in excellent agreement with Okajima's [5] data taken in a Reynolds-number range $R = (1.7 \sim 2.5) \times 10^5$.

3.2 Rms Surface Pressure. The rms pressure distributions around the circumference of both cylinders are shown in Fig. 3 in terms of the rms pressure coefficient C_p'. Similar data available to the authors were those of Igarashi [3] obtained in a lower Reynolds-number range $R = (2.2 \sim 4.4) \times 10^4$.

Previous measurements of C_p' for a single cylinder (Surry [6], Batham [7], Bruun and Davies [8], among others) show that a maximum of C_p' appears in the vicinity of the separation point and its value ranges from 0.28 to 0.5 in the upper subcritical regime when a circular cylinder is smooth and the free-stream turbulence intensity is less than a few percent. The present experiment, however, showed that the maximum rms pressure coefficient was 0.17 at most as seen in Fig. 3(*a*). In this connection, it may be noted that the flow around the single cylinder in this work fell into the region where the surface roughness is of significance in determining the flow and pressure fields. Batham [7] found that the rms surface pressures are so sensitive to the surface roughness that the maximum of C_p' reduces to $0.13 \sim 0.15$ for a roughness height δ of 2.2×10^{-3} times the cylinder diameter in the Reynolds-number range of $(1.11 \sim 2.35) \times 10^5$, the time-mean pressure distribution indicating the flow around the cylinder to be in subcritical regime. Accordingly, the above-mentioned maximum value of C_p' in the present experiment could be

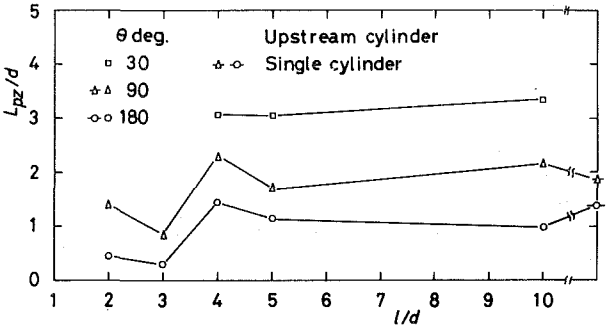

Fig. 4(a)

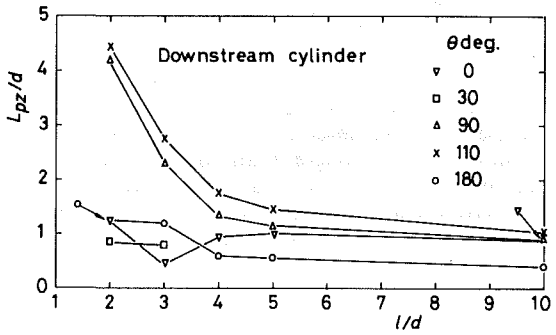

Fig. 4(b)

Fig. 4 Spanwise correlation length plotted against nondimensional spacing l/d for (a) upstream and (b) downstream cylinders. The uncertainty in the ordinate is ±0.2 and that in the abscissa is less than ±0.2 deg. Lines for visual aid only.

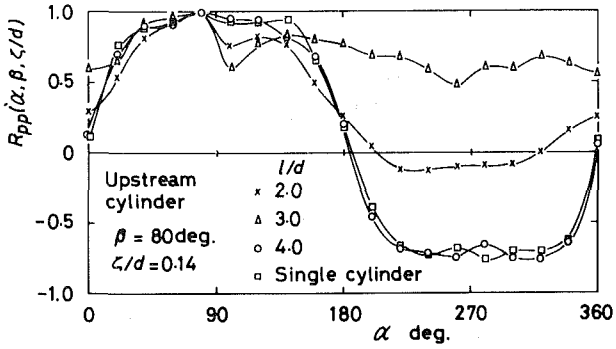

Fig. 5(a)

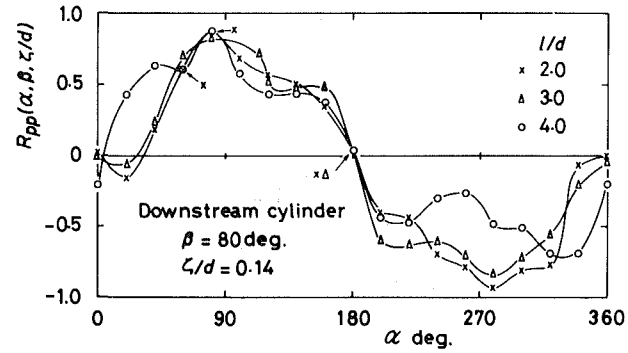

Fig. 5(b)

Fig. 5 Circumferential correlation coefficient for (a) upstream and (b) downstream cylinders at an angle $\beta = 80$ deg. The uncertainty in the ordinate is ±0.02 and that in the abscissa is ±0.2 deg. Lines for visual aid only.

understood if one assumes an effective surface roughness δ/d which is a little smaller than 2.2×10^{-3}. For the downstream cylinder, however, the surface roughness of this order has relatively little effects on the rms surface pressures. The maximum of C_p' appeared to be due to an oscillating movement of the separation point which will produce an effect akin to an oscillating movement of the time-mean pressure distribution.

The rms pressure distributions around the circumference of the upstream cylinder are shown in Fig. 3(*a*). The level of C_p' was much lower than that for a single cylinder and decreased with increasing l/d before vortex shedding from the upstream cylinder occurred, i.e., when $l/d \leqq 3.8$. Immediately after the occurrence of vortex shedding ($l/d = 4$), however, the rms pressures sharply increased to a level much higher than the case of a single cylinder. The low level of C_p' before the jump is associated with a small oscillating movement of the separation point which was mainly caused by the gap-flow fluctuations induced by the vortex shedding from the downstream cylinder. On the other hand, the high level of C_p' for $l/d = 4$ is conjectured to be a result of the switching of the gap flow. For spacings greater than $l/d = 4$, the surface-pressure fluctuations seem to decrease monotonically to those for a single cylinder.

Figure 3(*b*) shows the results for the downstream cylinder. The level of C_p' was much higher than that for the upstream cylinder for all the spacings tested. The rms pressures decreased for $l/d = 2$ and 3 in this order and showed a sharp increase when the jump of the flow pattern occurred. The maximum peak value of C_p' appeared at the spacing $l/d = 5$ (which is not shown in the text) whereas for the upstream cylinder it appeared at $l/d = 4$. It is worth noting that the heat transfer from the cylinders may also attain a maximum value at these spacings.

Three peaks of C_p' were observed for the spacing $l/d = 2$. The location of the second peak ($\theta = 60$ deg) approximately coincided with that of the highest peak of the time-mean surface pressure (see Fig. 2(*b*)), thus being interpreted as the time-mean reattachment point of the shear layer shed from the upstream cylinder. Since the point of the reattachment will oscillate in accordance with the vortex shedding from the downstream cylinder, the rms pressure is expected to attain a maximum at its time-mean position. A part of the reattached fluid will move along the cylinder surface in the direction of the leading generator. The authors imagine that this fluid is eventually decelerated by a positive pressure gradient in the vicinity of the leading generator, thus forming a separation bubble. The existence of the separation bubble is perhaps suggested by a slight increase of the time-mean pressure toward the leading generator. The first peak of C_p' at $\theta \simeq 15$ deg may be interpreted as an oscillating movement of the secondary separation point. Flow-visualization studies, however, are needed in order to prove the existence of the separation bubble. On the other hand, the major part of the reattached fluid will move in the direction of the trailing generator and separate from the surface to yield a periodic vortex shedding from the downstream cylinder. The highest third peak of the rms pressures at $\theta \simeq 110$ deg was brought about by this primary separation.

In the case of $l/d = 3$, the distribution of the time-mean pressure (Fig. 2(*b*)) suggests a weak gap flow, so that the above-mentioned first and second peaks of C_p' were not significant although slight traces of these peaks seem to be still observed. For the spacings $5 \leqq l/d \leqq 10$ (not shown in the text), the distribution of C_p' showed two peaks, the first one being higher than the second. The first peak was conjectured to be produced by the vortices shed from the upstream cylinder. The second peak occurred at the separation point which was approximately estimated from the time-mean pressure distribution, thus being produced by the oscillating movement of the separation point.

3.3 Spanwise Correlation Coefficient. The spanwise correlation coefficient of the surface-pressure fluctuations is a function of two variables, i.e., the angle θ of a generator

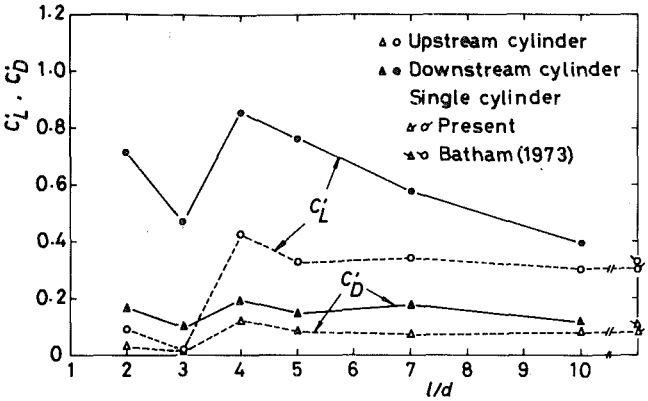

Fig. 6 Rms lift and drag coefficients plotted against nondimensional spacing l/d. The uncertainty in the ordinate is ± 0.03 and that in the abscissa is less than ± 0.005. Lines for visual aid only.

along which the pressure taps are located and the distance ζ between the pressure taps, thus being written as R_{pp} $(\theta, \zeta/d)$. The spanwise correlation length defined by

$$L_{pz}(\theta) = \int_0^\infty R_{pp}(\theta, \zeta/d) d\zeta$$

was evaluated. When the correlation coefficient became negative at a distance, say ζ_n, the above integral was performed in the range $\zeta = 0 \sim \zeta_n$.

In order to examine the behavior of the correlation length through the discontinuous change of the flow pattern, L_{pz} is plotted against the spacing l/d in Fig. 4 for several angles θ. The results for a particular angle $\theta = 90$ deg will be discussed because they seem to be most suggestive of the vortex-shedding properties. For the upstream cylinder, a discontinuous increase (jump) of L_{pz} probably occurred through the critical spacing $(l/d = 3.8)$. After the jump, L_{pz} remained almost unchanged. Contrary to the upstream-cylinder case, the correlation length for the downstream cylinder decreased sharply in the decreasing order of the spacings $l/d = 2$, 3, and 4. The same trend was also observed at the angle $\theta = 110$ deg. Since no measurements were made in the range $3 < l/d < 4$, it is not clear whether a sudden jump of L_{pz} at $\theta = 90$ deg and 110 deg occurred at the critical spacing. The correlation length for other angles showed only insignificant changes with respect to the spacing.

3.4 Circumferential Correlation Coefficient. The distribution of the circumferential correlation coefficient of the surface-pressure fluctuations R_{pp} $(\alpha, \beta, \zeta/d)$ is shown in Fig. 5 as a function of α at an angle of $\beta = 80$ deg. Here β denotes the angle from the leading generator where a pressure tap was temporarily fixed, α the angle of the traversed pressure tap and ζ is the spanwise separation between the pressure taps. As mentioned previously in Section 2, the ratio ζ/d was maintained to be 0.14 in this measurement.

Figure 5(*a*) shows the results for the upstream cylinder together with those for a single cylinder. The correlation coefficients for the spacing $l/d = 3$ were generally of the highest level over the whole surface for the angles β indicated. Since the coefficient was positive, the surface-pressure fluctuations were statistically all in phase. It may be noted, however, that the rms pressures were of the lowest level for this spacing (see Fig. 3(*a*)). Once vortex shedding occurred, the correlation curves (see the data for $l/d = 4$ in Fig. 5(*a*)) showed a marked antisymmetry with high absolute values of the coefficient over a wide range centered at $\alpha = 90$ deg and 270 deg. This will yield a considerable lift fluctuation. Except the case of $l/d = 3$, the correlations between the leading and trailing generators were small, so that drag fluctuations are expected to be also small in the tandem arrangement. When the vortex shedding was present, the correlation curves for the upstream cylinder were similar to those for the single cylinder.

The results for the downstream cylinder are presented in Fig. 5(*b*). The correlation distributions were only weakly dependent on the spacing and similar to those for a single cylinder except that distinct negative lobes appeared for the spacings $l/d = 2$ and 4 when $\beta = 0$ deg. The negative lobes should be attributed to the distortion of vortices shed from the upstream cylinder in front of the downstream cylinder (Durbin & Hunt [9]).

3.5 Rms Lift and Drag Coefficients. The spanwise correlation C_{LL} and C_{DD} of the sectional lift coefficient and the sectional drag coefficient, respectively, between two stations a distance ζ apart are given by

$$\{C_{LL}(\zeta/d), C_{DD}(\zeta/d)\} = \frac{1}{4}\int_0^{2\pi}\int_0^{2\pi} C_p'(\alpha) C_p'(\beta) R_{pp}(\alpha, \beta, \zeta/d) \times \{\sin\alpha\sin\beta, \cos\alpha\cos\beta\} d\alpha d\beta$$

The distributions of the rms surface pressures and the circumferential correlation coefficients permitted an evaluation of the correlations C_{LL} and C_{DD} for $\zeta/d = 0.14$. Surry's [6] data for a single circular cylinder in turbulent streams indicate the rms sectional lift and drag coefficients, i.e. $[C_{LL}(0)]^{1/2}$ and $[C_{DD}(0)]^{1/2}$ to be only slightly (about 5 percent) larger than $[C_{LL}(0.14)]^{1/2}$ and $[C_{DD}(0.14)]^{1/2}$, respectively, so that the values of the latter could approximately be interpreted as the values of the former. In fact for the single cylinder, the present experiment yielded $[C_{LL}(0.14)]^{1/2} = 0.31$ and $[C_{DD}(0.14)]^{1/2} = 0.079$ which compare well numerically with Batham's [7] data $[C_{LL}(0)]^{1/2} = 0.327$ and $[C_{DD}(0)]^{1/2} = 0.105$ obtained at $R = 1.11 \times 10^5$ for a free-stream turbulence of 0.5 percent. Accordingly, $[C_{LL}(0.14)]^{1/2}$ will temporarily be denoted by C_L' and $[C_{DD}(0.14)]^{1/2}$ by C_D'. These quantities are supposed to be sufficient at least to indicate the variation of the exact rms lift and drag coefficients with the spacing.

The results are shown in Fig. 6, where C_L' and C_D' for the upstream and downstream cylinders are plotted against the spacing l/d. The rms lift and drag coefficients were much higher for the downstream cylinder than for the upstream one when the spacing l/d was smaller than 7. In the range $l/d > 10$, they seem to be insignificantly different from the values for a single cylinder.

Extremely small values of C_L' obtained for the upstream cylinder when $l/d = 2$ and 3 were brought about by the absence of organized vortex shedding for these spacings. The small values of C_L' are supposed to be a result of weakly correlated pressure fluctuations in the vicinity of $\theta = 90$ deg and 270 deg, which are perhaps associated with the vortex shedding from the downstream cylinder. Once the vortex shedding occurred from the upstream cylinder, C_L' increased (probably in a steplike manner) to a value which was a little higher than that for a single cylinder. For larger spacings, the rms lift coefficient seems to gradually approach the latter. It is noteworthy that the downstream cylinder experiences a large rms lift when $l/d = 4$. This feature corresponds to the switching of the gap flow (which is shown in Fig. 2(*b*)) for this spacing.

The variation of C_D' with the spacing was very small for both cylinders except that a minimum appeared at $l/d = 3$ for both cylinders.

4 Conclusions

The main results of this study may be summarized as follows:

1 The rms surface pressure was much higher for the downstream cylinder than for the upstream cylinder. For both

cylinders, the rms pressure obtained a highest level just beyond the critical spacing.

2 The spanwise correlation length of the pressure fluctuations at the 90 deg generator of the upstream cylinder increased in a steplike manner through the critical spacing to the level found for a single cylinder.

3 The rms lift and drag were much larger for the downstream cylinder than for the upstream cylinder up to the spacing of 7 diameters. At the spacing of 10 diameters, they were different from those for a single cylinder by only a small amount.

4 For the upstream cylinder, the rms lift was extremely small for the spacings less than critical whereas it was approximately equal to that for a single cylinder beyond the critical spacing.

5 For the downstream cylinder, the rms lift was strongly dependent on the spacing and amounted to as high as 2.8 times the value found for a single cylinder at the spacing of 4 diameters.

6 The rms drag for both cylinders was only weakly dependent on the spacing.

Acknowledgments

The authors express their sincere thanks to Mr. H. Tamura and Dr. Y. Suzuki for their assistance in the manipulation of the data-processing apparatus and discussions on the experimental results, and to Mr. T. Yamazaki and Mr. T. Sampo for their assistance in the construction of the experimental apparatus. The present research was supported by the Grant-in-Aid for Scientifc Research from the Ministry of Education, Science and Culture of Japan, and later by Hatakeyama Foundation.

References

1 Zdravkovich, M. M., "Review of Flow Interference Between Two Circular Cylinders in Various Arrangements," ASME JOURNAL OF FLUIDS ENGINEERING, Vol. 99, No. 4, 1977, pp. 618-633.

2 King, R., and Jones, D. J., "Wake Interaction Experiments with Two Flexible Circular Cylinders in Flowing Water," *Journal of Sound and Vibration*, Vol. 45, No. 2, 1976, pp. 259-283.

3 Igarashi, T., "Flow Characteristics Around Two Circular Cylinders in Tandem Arrangement (Part I)," *Transactions of the JSME*, Vol. 46, No. 406, 1980, pp. 1026-1036.

4 Reinhold, T. A., Tieleman, H. W., and Maher, F. J., "Interaction of Square Prisms in Two Flow Fields," *Journal of Industrial Aerodynamics*, Vol. 2, No. 3, 1977, pp. 223-241.

5 Okajima, A., "Flows Around Two Tandem Circular Cylinders in Very High Reynolds Numbers," *Bulletin of the JSME*, Vol. 22, No. 166, 1979, pp. 504-511.

6 Surry, D., "Some Effects of Intense Turbulence on the Aerodynamics of a Circular Cylinder at Subcritical Reynolds Number," *Journal of Fluid Mechanics*, Vol. 52, Part 3, 1972, pp. 543-563.

7 Batham, J. P., "Pressure Distributions on Circular Cylinders at Critical Reynolds Numbers," *Journal of Fluid Mechanics*, Vol. 57, Part 2, 1973, pp. 209-228.

8 Bruun, H. H. and Davies, P. O. A. L., "An Experimental Investigation of the Unsteady Pressure Forces on a Circular Cylinder in a Turbulent Cross Flow," *Journal of Sound and Vibration*, Vol. 40, No. 4, 1975, pp. 535-559.

9 Durbin, P. A., and Hunt, J. C. R., "Fluctuating Surface-Pressures on Bluff Structures in Turbulent Winds: Further Theory and Comparison with Experiment," *Proceedings of the Fifth International Conference on Wind Engineering*, Fort Collins, Colo., USA, July 1979, Vol. 1, 1980, pp. 491-507.

cylinders, the rms pressure obtained a highest level just beyond the critical spacing.

2 The spanwise correlation length of the pressure fluctuations at the 90 deg generator of the upstream cylinder increased in a steplike manner through the critical spacing to the level found for a single cylinder.

3 The rms lift and drag were much larger for the downstream cylinder than for the upstream cylinder up to the spacing of 7 diameters. At the spacing of 10 diameters, they were different from those for a single cylinder by only a small amount.

4 For the upstream cylinder, the rms lift was extremely small for the spacings less than critical whereas it was approximately equal to that for a single cylinder beyond the critical spacing.

5 For the downstream cylinder, the rms lift was strongly dependent on the spacing and amounted to as high as 2.8 times the value found for a single cylinder at the spacing of 4 diameters.

6 The rms drag for both cylinders was only weakly dependent on the spacing.

Acknowledgments

The authors express their sincere thanks to Mr. H. Tamura and Dr. Y. Suzuki for their assistance in the manipulation of the data-processing apparatus and discussions on the experimental results, and to Mr. T. Yamazaki and Mr. T. Sampo for their assistance in the construction of the experimental apparatus. The present research was supported by the Grant-in-Aid for Scientifc Research from the Ministry of Education, Science and Culture of Japan, and later by Hatakeyama Foundation.

References

1 Zdravkovich, M. M., "Review of Flow Interference Between Two Circular Cylinders in Various Arrangements," ASME JOURNAL OF FLUIDS ENGINEERING, Vol. 99, No. 4, 1977, pp. 618-633.

2 King, R., and Jones, D. J., "Wake Interaction Experiments with Two Flexible Circular Cylinders in Flowing Water," *Journal of Sound and Vibration*, Vol. 45, No. 2, 1976, pp. 259-283.

3 Igarashi, T., "Flow Characteristics Around Two Circular Cylinders in Tandem Arrangement (Part I)," *Transactions of the JSME*, Vol. 46, No. 406, 1980, pp. 1026-1036.

4 Reinhold, T. A., Tieleman, H. W., and Maher, F. J., "Interaction of Square Prisms in Two Flow Fields," *Journal of Industrial Aerodynamics*, Vol. 2, No. 3, 1977, pp. 223-241.

5 Okajima, A., "Flows Around Two Tandem Circular Cylinders in Very High Reynolds Numbers," *Bulletin of the JSME*, Vol. 22, No. 166, 1979, pp. 504-511.

6 Surry, D., "Some Effects of Intense Turbulence on the Aerodynamics of a Circular Cylinder at Subcritical Reynolds Number," *Journal of Fluid Mechanics*, Vol. 52, Part 3, 1972, pp. 543-563.

7 Batham, J. P., "Pressure Distributions on Circular Cylinders at Critical Reynolds Numbers," *Journal of Fluid Mechanics*, Vol. 57, Part 2, 1973, pp. 209-228.

8 Bruun, H. H. and Davies, P. O. A. L., "An Experimental Investigation of the Unsteady Pressure Forces on a Circular Cylinder in a Turbulent Cross Flow," *Journal of Sound and Vibration*, Vol. 40, No. 4, 1975, pp. 535-559.

9 Durbin, P. A., and Hunt, J. C. R., "Fluctuating Surface-Pressures on Bluff Structures in Turbulent Winds: Further Theory and Comparison with Experiment," *Proceedings of the Fifth International Conference on Wind Engineering*, Fort Collins, Colo., USA, July 1979, Vol. 1, 1980, pp. 491-507.

DISCUSSION

M. M. Zdravkovich[1]

The authors are to be complimented for systematic and comprehensive measurements of fluctuating pressure around two circular cylinders in tandem arrangement at $R_e = 1.57 \times 10^5$. They stated that the cylinder surface was not polished so some minor effect of surface roughness might be expected. An early precritical regime might be inferred from a rather low spanwise correlation coefficient of 1.8 behind the single cylinder at the same Reynolds number (Fig. 4*a*). The precritical regime could also be inferred from the value of pressure drag coefficient for the single cylinder. It will be helpful if the authors could provide the value of drag coefficient (either uncorrected or corrected for the blockage effect).

Another important issue is the possible existence of the laminar separation bubble(s) on the downstream cylinder. The bubble usually formed a kink beyond $Cp_{\min}$ on the mean pressure curve for the single cylinder. The kinks were absent on the second adverse pressure gradient parts of all Cp curves in Fig. 2(*b*).

The reattaching shear layers separated from the upstream cylinder were fully turbulent before they impinged on the downstream cylinder and it was unlikely that the relaminarization took place before separation at 110°. Oil film visualization was carried out at $R_e = 5 \times 10^5$ by Okajima [5] and the trace of the separation bubbles was found only on the upstream cylinder. It might be expected that either a single or both separation bubbles were obliterated on the downstream cylinder by the turbulence produced by the upstream cylinder. Similar obliteration of separation bubbles was found on the single cylinder submerged in turbulent free stream.

The most interesting and intriguing finding was the variation of two $C'_{p_{\max}}$ in Fig. 3(*b*) with the spacing between the cylinders. The first peak which was caused by the reattachment of turbulent shear layers was less than the second one produced by the separation for $1/d = 2$ and 3. However, for $1/d = 4$ when the vortex shedding was established behind the upstream cylinder the "reattachment" peak was the dominating one. It will be revealing if the authors could provide separately the contribution of periodic and turbulent fluctuations for each $C'_{p_{\max}}$ shown in Fig. 3(*b*).

An unexpected significant increase in the spanwise correlation length behind the downstream cylinder at $1/d = 2$ indicated strong and well correlated vortex shedding behind the downstream cylinder. This was confirmed by the high C'_L in Fig. 6 for $1/d = 2$. Similar increase in $C'_{p\max}$ was found by Igarashi [3] at $R_e = 3.5 \times 10^4$ with the absolute maximum of $C'_{p_{\max}}$ at $1/d = 2.35$. However, for both $1/d = 2$ and 3 the reattachment peak was greater than the separation peak and also the overall fluctuations were greater for spacing $1/d = 3$ than for $1/d = 2$. These differences were presumably caused by different Reynolds numbers i.e., medium subcritical and precritical regimes. The authors comments on this peculiar nature of $C'_{p_{\max}}$ peaks will be most valuable.

[1] Reader, University of Salford, Salford, U.K. Mem. ASME

Authors' Closure

We would like to thank Dr. Zdravkovich for his valuable comments.

As the discusser suggests, the flow around the single cylinder was in the precritical regime. The uncorrected time-mean drag coefficient C_D was 1.06. If this is corrected for the wind-tunnel blockage by Allen and Vincenti's [10] formula, we obtain $C_D = 0.93$. This value of the drag coefficient suggests that the flow was in the precritical regime.

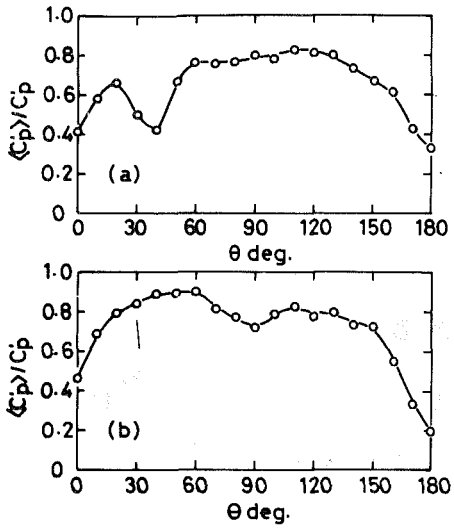

Fig. 7 Circumferential distribution of the r.m.s. periodic pressure fluctuation divided by C_p' at the same position for (a) $l/d=2$ and (b) $l/d=4$. The uncertainty in the ordinate is ± 0.05 and that in the abscissa is ± 0.2 deg.

The time-mean pressure profiles for the downstream cylinder showed no kink in the tested range of l/d. The authors agree to the discusser in that the separation bubbles were obliterated by the turbulence produced by the upstream cylinder.

With regard to Fig. 3(*b*), Dr. Zdravkovich expresses his concern about the changes in the relative magnitude of the reattachment and separation peaks of C_p' with l/d. In this connection, he suggests to provide separately the contribution of periodic and turbulent fluctuations for each peak shown in Fig. 3(*b*). Figure 7 presents the circumferential distribution of the r.m.s. periodic pressure fluctuation $<C_p'>$ divided by C_p', i.e., the overall r.m.s. pressure fluctuation at the same position, for $l/d=2$ and 4 (Sakata and Kiya [11]). The experimental condition was the same to the present one. At both reattachment and separation peaks, the r.m.s. periodic fluctuation is seen to be roughly 80 percent of the overall r.m.s. value.

The last point raised by the discusser concerns with the differences in the reattachment and separation peaks of C_p' between the present results and those of Igarashi [12]. As Dr. Zdravkovich suggests, these differences were possibly caused

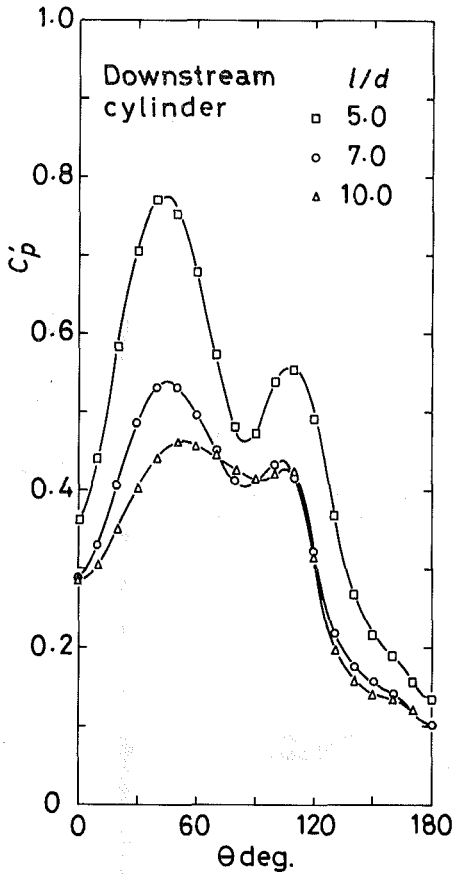

Fig. 8 R.m.s. pressure distribution for the downstream cylinder at $l/d=5$, 7, and 10. The uncertainty in the ordinate is ± 0.01 and that in the abscissa is ± 0.2 deg.

by the different flow regimes. At present the authors have no clear idea about this feature. It should be noted that in this experiment the reattachment peak was always greater than the separation peak in the range $l/d=4$–10, as shown in Fig. 8.

Additional References

10 Allen, H. J., and Vincenti, W. G., NACA Rep. no. 782, 1944.

11 Sakata, I., and Kiya, M., to be published in *Transactions of the JSME* (in Japanese).

12 Igarashi, T., *Transactions of the JSME*, Vol. 46, No. 406, 1980, pp. 1026–1036 (in Japanese).

Gas Flow Resistance Measurements Through Packed Beds at High Reynolds Numbers[1]

D. P. Jones
Graduate Research Assistant,
Department of Aeronautical and Astronautical Engineering.

H. Krier
Professor,
Department of Mechanical and Industrial Engineering.

University of Illinois at Urbana-Champaign, Urbana, Ill. 61801

This research study indicates that the classical Reynolds number dependency of the coefficient of drag for gases forced into packed beds is not correct at high Reynolds numbers. Care must also be taken to account for boundary layer wall effects that occur when the ratio of test chamber diameter to bead particle diameter is too small. Included is a review of the literature pertaining to gaseous flow resistance in packed beds. An existing test facility used in a previous study was found unsatisfactory, and necessary corrections were made to obtain normalized pressure gradient measurements at increasingly high Reynolds numbers. The resultant data was organized into a new correlation for the coefficient of drag, that is

$$Fv = 150 + 3.89\left(\frac{Re}{1-\phi}\right)^{0.87}$$

This formula was developed for air flowing over spherical particles at Reynolds numbers ranging from 10^3–10^5.

Introduction

The resistance of gaseous flow through packed beds of various sized particles is a problem of fundamental concern for the viscous interaction and the resulting pressure drop. This phenomenon has been investigated by numerous researchers, extending back to the work of Orborn Reynolds in the early 1900's. One attempts to determine a fundamental coefficient of drag based on properties of the fluid and the solid. The factors which determine the energy loss (or pressure loss) are numerous, and the analysis requires many simplifying assumptions.

Reference [1] gives a review of the important literature on the reported functions for $\Delta P/L$ (pressure gradient) as a function of the steady flow properties. A more recent review was made in the report by Wilcox and Krier [2]. The work reported by previous investigators can be catalogued by a coefficient of drag, Fv, defined as

$$Fv = \frac{\Delta P}{L}\frac{D_b^2}{\mu U_{\text{avg}}}\left(\frac{\phi}{1-\phi}\right)^2 \tag{1}$$

where ϕ represents the porosity of the packed bed, and $(1-\phi)$ is the solids loading, D_b is the (spherical) particle diameter, μ is the gas viscosity, and U_{avg} is the average gas velocity, determined from the mass flow in a channel of area, A_p. That is

$$U_{\text{avg}} = \dot{m}/\rho_g A_p \phi \tag{1a}$$

Table 1 is a summary of the work that deals specifically with flow resistance measurements of gases through packed spherical particles. The table lists the investigators (including the reference), the range of the flow Reynolds number (defined in equation (3)), the range of porosities and the bead sizes tested. The earliest systematic work in which a coefficient of drag was determined was based on the experiments as correlated by Ergun (3). This classical work specifies that the pressure losses in a packed bed are caused by simultaneous kinetic and viscous energy losses, and the coefficient of drag may be presented as

$$Fv = 150 + 1.75\left(\frac{\text{Re}}{1-\phi}\right) \tag{2}$$

where

$$\text{Re} = \rho U_{\text{avg}} D_b \phi/\mu \tag{3}$$

More recently other researchers have attempted to verify Ergun's correlation and extend the range of the correlation validity. Kuo and Nydegger [4], in an attempt to verify the Ergun equation, developed a correlation for an extended Reynolds number range. Their correlation was

$$Fv = 276.23 + 5.05\left(\frac{\text{Re}}{1-\phi}\right)^{0.87} \tag{4}$$

Robbins and Gough [5] also performed experiments to determine coefficient of drag at high Reynolds numbers. Although they did not propose a correlation for the coefficient of drag, they did acquire a large amount of data which they presented in terms of an inverse coefficient of drag defined as

[1]Work supported by Air Force Office of Scientific Research under grant AFOSR 77-3336; Dr. Leonard H. Caveny was contract monitor.

Contributed by the Fluids Engineering Division and presented at the ASME Applied Mechanics, Bioengineering, and Fluids Engineering Conference, Houston, Texas, June 20–22, 1983. Manuscript received by the Fluids Engineering Division, January 11, 1982. Paper No. 83-FE-8.

Table 1

Investigator	Re (range)	Porosity ϕ	Spherical (mm) bead size range	Max air pressure	Range D_c/D_b
Ergun [3]	0.4–1380	0.40–0.65	----	----	----
Kuo/Nydegger [4]	460–14,600	0.38–0.39	0.83 (one size)	14 MPa	9.3 (one ratio)
Robbins/Gough [5]	778–79,200	0.39–0.40	1.25–8	20 MPa	9.6–60
Jones/Krier	440–76,000	0.38–0.44	1–6	2.5 MPa	8.5–50

$$\hat{f}_s = \frac{\Delta P}{L}\,\frac{D_b\rho}{(\rho U_{\text{avg}}\phi)^2}\,\frac{\phi^3}{1-\phi} \tag{5}$$

Utilizing equation (5), Ergun's correlation, equation (2) becomes

$$\hat{f}_s = 1.75 + \frac{150(1-\phi)}{\text{Re}} \tag{6}$$

while eqution (6) developed by Kuo and Nydegger is

$$\hat{f}_s = \frac{276.23}{\text{Re}}(1-\phi) + 5.05\left(\frac{\text{Re}}{1-\phi}\right)^{-0.13} \tag{7}$$

Motivation

The final column of Table 1 shows the ratio of test chamber diameter to bead diameter, D_c/D_b. It should be noted here that the experiments of Kuo and Nydegger were carried out inside a very small diameter tube, while Robbins and Gough (and this study) used a relatively large diameter test section. Based on Benenati and Brosilow (6), it seems logical that the boundary layer effects are minimal, as well as the best averaged uniform porosity occurs when D_c/D_b is large. The work that follows indicates that this ratio of D_c/D_b must be sufficiently large so that frictional effects on the walls do not interfere with the measurement of the fundamental resistance properties through the packed bed. Experiments were carried out to acquire data to check on the validity and to extend the range of the correlations stated above.

In order to investigate the gas-particle drag interaction, a cold flow experimental apparatus was developed at the University of Illinois by Wilcox and Krier [2] to perform experiments which would substantiate existing correlations for a coefficient of drag through a packed bed or which would develop a new correlation at high Reynolds numbers approaching 10^5. It was this test apparatus which was modified by the present study so that one could accurately compare drag measurements to ascertain the wall confinement effects which have been briefly discussed above.

Test Facility

Figure 1 gives a detailed schematic of the modified Wilcox/Krier experimental apparatus. The 20 cm long test section which contains the packed bed is 5.08 cm in diameter. The 20 cm length of the test section was similar to that used by the other researchers, and allows enough distance from the ends of the test section to the first and last pressure transducer so that the entrance and exit flow patterns do not bias the pressure data. Also the length chosen would diminish any errors that may occur due to nonuniformity in packing.

A Grove Pressure Reducing Regulator, Model 82-829 (4.96 MPa max inlet), regulates the compressed air source to the desired test pressure. This regulator could handle the source pressure of 3.1 MPa, required mass flow, and in addition, regulate itself so that the desired test pressure in the plenum tank would not fluctuate.

The regulated compresses air enters a plenum tank with an inner diameter of 7.60 cm. This enlarged diameter, from 3.22 cm in the pipe, to 7.60 cm in the plenum, was designed to bring the gas to a low velocity. The straightening vanes smooth the flow of air in the plenum. The Bourdon Pressure Gauge indicates the test pressure, equal to the stagnation pressure, P_0. The Bourdon gauge is a Solfrunt 4.5 inch test gauge with a range of 0-1000 psig and a plus or minus 0.25 percent of span accuracy. Temperature is monitored using three Omega thermocouples located along the test apparatus length as shown. There are chromel-alumel, CASS-186-12, gounded junction probes that are designed to provide fast response under high pressures. These thermocouples measure the stagnation temperature, T_0.

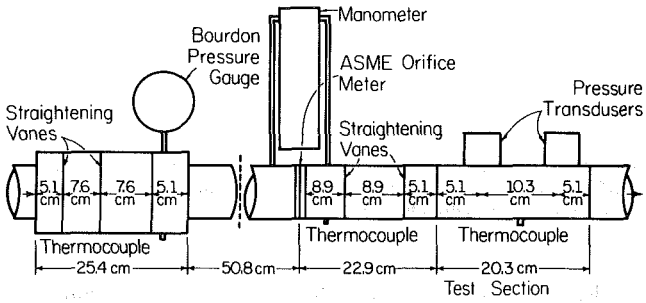

Fig. 1 Schematic of test facility to measure friction factor in packed beds. (Bed is located in the section below the two pressure transducers.)

The plenum opens into a 50.8 cm section of pipe which further stabilizes the flow before it reaches the standard ASME orifice meter which is used to measure mass flow. A Meriam manometer, Model 20AA25 WM is used to measure the pressure drop across the orifice meter. On the downstream side of the orifice the flow enters a straightening vane section. Based on the recommended minimum lengths of pipe preceding and following the orifice, a 23 cm long expansion-straightening section is used.

The 20 cm long and 5.08 cm diameter test section is directly mounted to the straightening section. This section has a screen mesh as the entrance and a metal stainless steel grid at the exit to secure the packed bed in the test section. There are two rapid response pressure transducers mounted on the test section to measure the pressure drop of the gas as it flows through the packed bed. They are Setra Systems, Model 205, with a pressure range of $0-3.45\times10^6$ Pa, a one millisecond response time and an accuracy of 0.11 percent at full scale. This type of transducer provides output signals for detection of any fluctuation in the steady-state air flow.

Appendix A provides additional details of how the data was recorded. The uncertainty for the measurements are given there.

Specific Experiments Performed

Flow resistance experiments were performed using the 5.08 cm diameter test section in which spherical glass beads of 0.96, 1.5, 2, 3, 4, and 6 mm diameter were packed.

The pressure gradient data was reduced, analyzed, and compared to the theoretical correlation of Ergun, Kuo, and

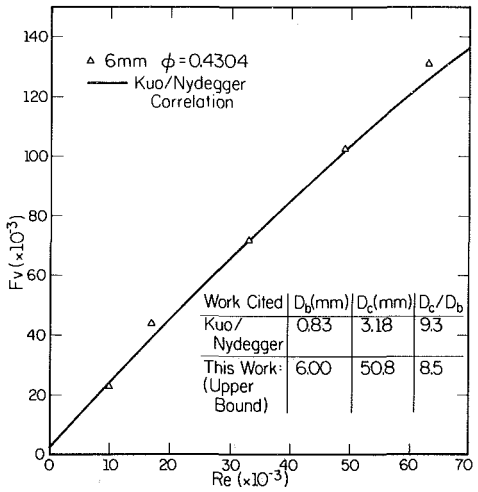

Fig. 2 Coefficient of drag: comparison of data for lowest value of *Dc/Db* with Kuo/Nydegger correlation. (uncertainty in F_v = ± 6 percent and in Re = ± 4.5 percent; see Appendix)

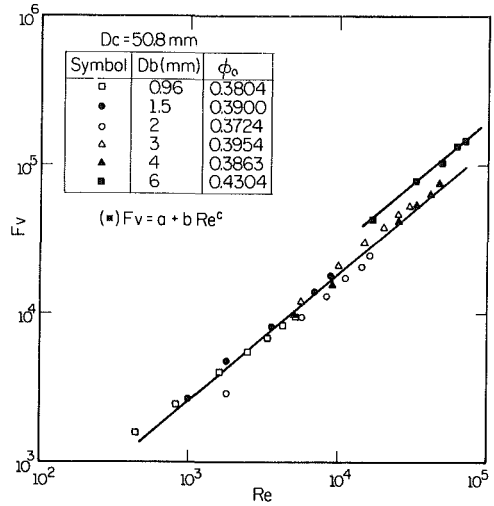

Fig. 3 Coefficient of drag plotted versus Reynolds number. Top line shows data for *Dc/Db* < 10 and bottom line shows data for *Dc/Db* > 20. (uncertainty in F_v = ± 6 percent and in Re = ± 4.5 percent; see Appendix)

Nydegger, as well as to the experimental data of Robbins and Gough.

Coefficient of Drag Correlation

Figure 2 represents data obtained in this work for the normalized pressure gradient as a function of Reynolds number for 6 mm beads at a loading porosity of 0.43, loaded in the 5.08 cm diameter cylindrical tube. The data indicates that the correlation of Kuo and Nydegger [4] matches fairly well to the data obtained in this study.

It is interesting to note that the ratio of the container diameter to bead diameter, D_c/D_b in the experimental data shown in Fig. 2, is approximately equal to the ratio used by Kuo and Nydegger. It is believed that this ratio is actually too small and that a larger test section diameter should have been used. This is made clear in subsequent data presented below.

Figure 3 represents the coefficient of drag plotted versus Reynolds number. The data, plotted on log-log paper, indicate that Fv is proportional to Re, where the exponent is identical to the value as reported by Kuo and Nydegger, c = 0.87. Note that the data for the 6 mm beads (in which the D_c/D_b ratio was below 10) shows a translation to higher values of Fv for equal Reynolds number compared to the majority of tests where the ratio of D_c/D_b was greater than 20. As seen in this figure, the 6 mm bead coefficient of drag in fact has the same slope when plotted versus Re but a different intercept value than the more correct higher D_c/D_b ratio cases.

In order to obtain a correlation of Fv versus Re′ (i.e., Reynolds number divided by $(1-\phi)$) the data presented in Fig. 3 were replotted in order to obtain our new correlation. The results are shown in Fig. 4. Based on the large number of tests carried out for conditions in which the ratio of chamber diameter to bead diameter was at least 20 or greater, our correlation is

$$Fv = 150 + 3.89\left(\frac{\mathrm{Re}}{1-\phi}\right)^{0.87} \tag{8}$$

For comparison, the correlation of Kuo and Nydegger and the correlation of Ergun are listed on the figure. As has been pointed out, the data for the 6 mm bead are satisfied quite accurately by the Kuo/Nydegger correlation.

Table 2 summarizes the coefficient of drag correlation and the range of Re′ in which those experiments have been carried out. It should be noted that in the current study the range of the Reynolds number has been extended significantly. Subsequent figures comparing our correlation for the coefficient of drag with the Robbins/Gough data are presented later.

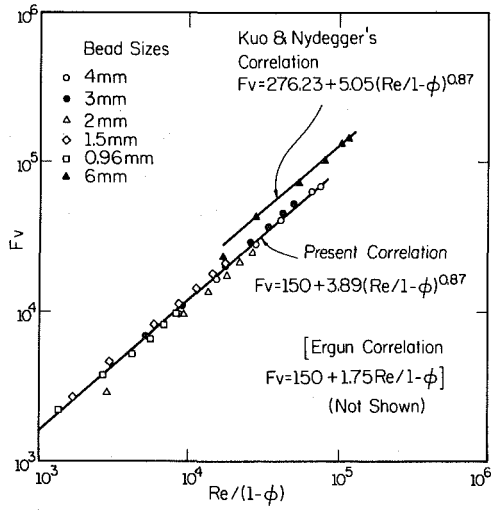

Fig. 4 Comparison of coefficient of drag: present correlation uses data for 1, 1.5, 2, 3, and 4mm spherical beads (all data obtained with *Dc/Db* > 20). (uncertainty in F_v = ± 6 percent and in Re = ± 4.5 percent; see Appendix)

Table 2

Investigators [a]	Fv (coefficient of drag)	Ré ≡ Re/(1 − φ)
Ergun [3]	$Fv = 150 + 1.75$ (Ré)	0.67 < Ré < 2300
Kuo and Nydegger [4]	$Fv = 276 + 5.05\ \mathrm{Ré}^{(0.87)}$	767 < Ré < 24330
Jones, Krier (this study)	$Fv = 150 + 3.89\ (\mathrm{Ré})^{0.87}$	733 < Ré < 126670

[a] Robbins/Gough [5] presented data of $\hat{f}_s$ versus Re; their data correlates very well with Jones/Krier correlation.

Although it may appear that the present correlation, as shown in Fig. 4 (and also in Table 2) does not vary appreciably from those published by the other researchers; the calculation of the pressure gradient $\Delta P/L$ at two specific Reynolds numbers will bear out that the differences are in fact significant. Table 3 presents such a comparison. In order to make the comparison meaningful, we have chosen a constant bead diameter of 1 mm packed at a porosity of 0.39. Nominal

Table 3

Pg (KPa)	ρ_g (Kg/m^2)	$\frac{Re}{1-\phi}$	Correlation	Fv	$\Delta P/L$
687	8.12	2911	Ergun	5244	2.31 (MPa/m)
			Kuo/Nydegger	5488	2.43
			Jones/Krier	4165	1.83
2061	24.6	8733	Ergun	15,433	6.80
			Kuo/Nydegger	13,831	6.09
			Jones/Krier	10,591	4.66

Given: $D_b = 1$ mm; $\phi = 0.39$; $U_{avg} = 10$ m/s; $\mu_g = 1.8 \times 10^{-5}$ kg/ms

Since $\Delta P/L = Fv\left(\frac{\mu_g U_g}{D_b{}^2}\right)\left(\frac{1-\phi}{\phi}\right)^2 = 440.4\,Fv\ (nt/m^3)$

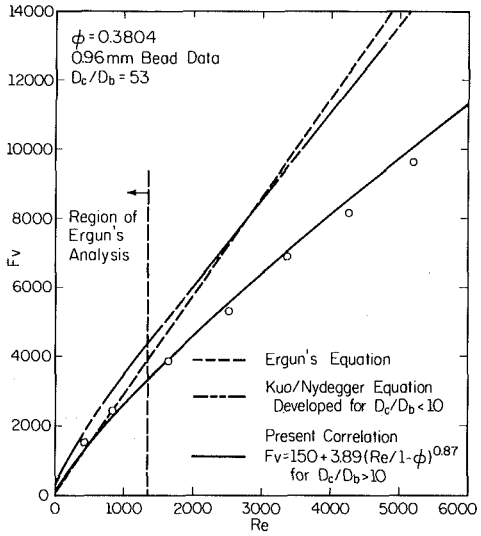

Fig. 5 Coefficient of drag (1mm spherical beads in 50mm diameter pipe): comparison with three correlations.

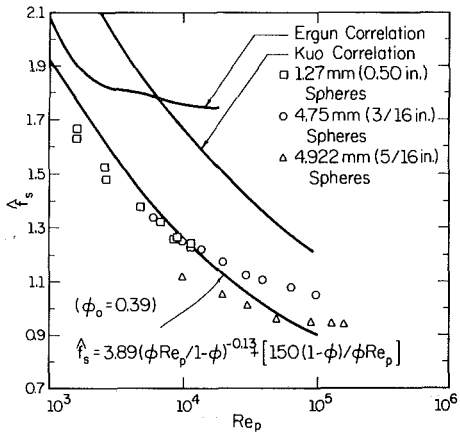

Fig. 6 Comparison of the data of reference [5] with Kuo/Nydegger correlation and with present correlation. (Data from reference [5]; no uncertainty given)

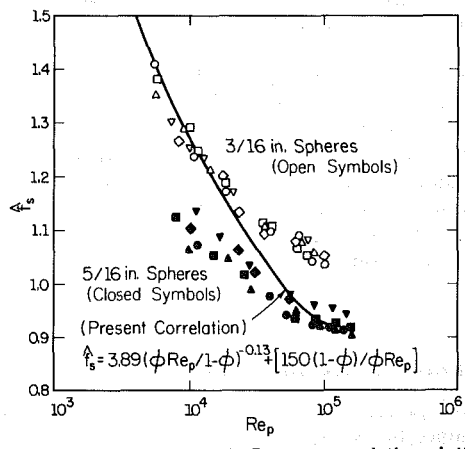

Fig. 7 Data by Robbins and Gough. Present correlation plotted for ϕ_0 = 0.39. (Data from reference [5]; no uncertainty given)

values of gas viscosity are used and more importantly the gas velocity is assumed to be fixed at 10 m/s. Fixing the velocity requires a given value of the mass flow per unit area, the pressure of the system and the temperature. Table 3 lists in the last two columns predicted values for $\Delta P/L$ for two different Reynolds numbers based on the input value discussed in the above sentence. The first normalized Reynolds number, Re′, was calculated to be 2911, a nominal value which was obtained by using a value of 8.2 Kg/m^3 for the gas density. Such a density is achieved for room temperature air at a pressure of 687 KPa. The calculated values for the coefficient of drag and the pressure gradients are listed in Table 3. Clearly the present correlation provides the smallest pressure gradient (units of MPa/m).

At a significantly high Reynolds number, Re′ exceeding 8700, and with a density of almost 25 Kg/m^3 the new correlation presented in this work provides a significantly lower coefficient of drag. One can make the general conclusion that at Reynolds numbers greater than 10,000 the present correlation provides a pressure gradient that is about half as large as that predicted by Ergun and about 85 percent that of the Kuo/Nydegger correlation. It should be added that tests carried out at these high Reynolds numbers verify the present correlation. In fact, it is through the measurement of the pressure gradient, $\Delta P/L$, that one obtains the formula for Fv. Until tests are carried out at Reynolds numbers that are even higher than those tested and presented here, the upper limit Reynolds number for using equation (8) should be about 10^5.

Another way to compare the three coefficients of drag as the function of Reynolds is to plot the three equations shown in Table 3 directly as a function of Reynolds number. This is done in Fig. 5. The data superimposed on the present correlation was for 1 mm diameter bead confined in our 50 mm diameter test section. Again, it is clear that had one utilized either the Kuo/Nydegger correlation at Reynolds numbers exceeding 5000, the coefficient of drag would have been clearly over estimated by the other correlations.

Further Substantiation for New Fv

The data of Robbins/Gough [5], was presented in terms of

Table A1

Parameter	Meaning	Range of parameter tested	% of uncertainty range
L	Distance in packed bed separating pressure transducers	10.2 cm (fixed)	None
ΔP	Pressure drop in packed bed	50 to 550 KPa	±2 to ±0.4%
D	Particle bead diameter	0.96 to 6.0 mm	±2 to 1.5%
ϕ	Bead porosity	0.372 to 0.436	±1.5% to ±1%
T_g	Gas temperature	13°C to 27°C	±3% to 1.6%
P_g	Gas pressure in bed	200 KPa to 2.5 MPa	±1.8% to ±1.2%
$\dot{m}$	Air mass flow rates	0.02 to 1.1 $\frac{\text{Kg}}{\text{sec}}$	±1.5% to ±0.5%
A_p	Port diameter	2.54 cm to 5.08 cm	None
μ_g	Air viscosity	1.82×10^{-5} Kg/s-m	None assumed
Re	Reynolds number	440 to 76,000	±4.5% to ±2.8%
F_v	Coefficient of drag	$1.5(10^3)$ to $145(10^3)$	±5.8% to 4.5%

a friction factor, $\hat{f}_s$. Recall one can express the coefficient of friction Fv as an inverse function of $\hat{f}_s$. Rewriting the present correlation (equation (8)) as an inverse coefficient of drag, one obtains

$$\hat{f}_s = \frac{150(1-\phi)}{\text{Re}} + 3.89\left(\frac{\text{Re}}{1-\phi}\right)^{-0.13} \tag{9}$$

Figure 6 compares equation (9) (the present correlation for $\hat{f}_s$) with the pressure drop data obtained by Robbins and Gough. It is not surprising that the data fits fairly accurately with the present correlation. It has been mentioned that Robbins and Gough noted (reference [4]) that their data did not satisfy the Kuo and Nydegger correlation. Such a correlation is shown in Fig. 6 for comparison. Also shown is the correlation of Ergun.

The conclusion is striking. The data obtained in the tests by Robbins and Gough verify fairly completely the present correlation, and thereby calling into question the accuracy of the other two correlations. Figure 7, taken from reference [5], shows additional data presented by Robbins and Gough for two specific sizes. Again, the present correlation for $\hat{f}_s$ (equation (9)) has been inserted and indicates a very acceptable correlation of that data.

Conclusions and Recommendations

The work presented above has shown that the correlation of Ergun cannot be extended beyond Reynolds numbers of 10^3. The correlation for the coefficient of drag developed by Kuo and Nydegger, although properly identifying a Reynolds number exponent, is of limited value because the data was obtained for a test chamber diameter that is too small for the bead diameter. Having carried out hundreds of tests in cold flow high pressure gases, we have obtained a correlation that is universal and extends to Reynolds numbers approaching greater than 10^5. It has also been shown that the correlation presented here adequately describes the data reported by Robbins/Gough.

References

1 Bird, R., Stewart, W., and Lightfoot, E., *Transport Phenomena*, New York, Wiley, 1966.

2 Wilcox, S. F., and Krier, H., Technical Report AAE 80-1, University of Illinois at Urbana-Champaign (UILU-Eng 80-0501), Mar. 1980.

3 Ergun, S., "Fluid Flow Through Packed Columns," *Chemical Engineering Progress*, Vol. 48, No. 2, Feb. 1952, pp. 89–94.

4 Kuo, K. K., and Nydegger, C. C., "Flow Resistance Measurements and Correlation in a Packed Bed of WC 870 Ball Propellants," *Journal of Ballistics*, Vol. 2, No. 1, 1978, pp. 1–25.

5 Robbins, R., Gough, P. S., "Experimental Determination of Flow Resistance in Packed Beds of Gun Propellant," *Proceedings of 15th JANNAF Combustion Meeting*, CPIA pub. 297, Sept. 1978.

6 Benenati, R., and Brosilow, C., "Void Fraction Distribution in Beds of Spheres," *A.A. Industrial Engineering Chemistry*, Vol. 41, 1949, p. 1179.

APPENDIX

Estimates of Uncertainty of Experimental Data

Our data are shown in Figs. 2–5, as coefficient of drag, F_v versus Reynolds number. Now F_v is deduced from equation (1), with the average gas velocity determined from equation (1*a*). The Reynolds number is calculated from equations (3) and (1*a*). Thus

$$F_v \equiv \left(\frac{\Delta P}{L}\right)\frac{D_b^2}{\mu U_{\text{avg}}}\left(\frac{\phi}{1-\phi}\right)^2 \tag{A1}$$

$$U_{\text{avg}} = \dot{m}/\rho_g A_p \phi \tag{A2}$$

$$\text{Re} = \frac{\dot{m} D_b}{A_p \mu_g} \tag{A3}$$

Measurements of the mass flow, $\dot{m}$, were made using a standard ASME orifice meter with a large monometer to measure pressure drop across the orifice. Porosity was calculated by measuring the weight of all particles taking up the measured bed volume. Thus

$$\phi = 1 - \frac{\text{mass of beads/density of bead material}}{\text{volume of test section including beads}}$$

The gas density was calculated by taking the two pressure measurements (where $\Delta P/L$ was recorded) averaging and then dividing by RT_g, where T_g was measured by thermocouples imbedded in the bed.

Table A1 summarizes the average percent uncertainty in the parameters measured that were used to calculate F_v and Re. The last two lines indicate estimates in uncertainty for F_v and Re.

DISCUSSION

E. J. Henley[2]

Professor Krier and Mr. Jones have made a contribution in extending current pressure-drop-through-packed-bed correlations to the realm of higher Reynolds numbers. Reliable, new data in this field are always welcome, and improved correlations with empirical constants which fit the data a little better than the old ones will be useful to the design engineer.

The Ergun equation for predicting pressure drop through packed-bed gas absorbers is widely used by chemical engineers. Unfortunately, in this low-Reynold's-number-chemical-engineering application, the packing does not consist of smooth, round glass spheres, and one of the most difficult variables for the designer to conjur is the "effective diameter" of the particles which, typically, consist of saddles, or oddly punched-out meshes. Empirical parameters whch are particle-specific are frequently used in conjunction with the Ergun equation.

Higher-Reynold's number-flow packed beds are of interest primarily to chemical reactor engineers. Here the flow is through particles of catalysts. Typically, these are irregular particles; many have very rough surfaces.

It is unfortunate that the area of flow through packed beds has, for decades, been considered intractable by theoreticians, and abandoned by experimentalists. Perhaps this paper will help revive interest in this field.

[2]Department of Chemical Engineering, University of Houston, Houston, Tex. 77004.

K. W. Ragland
Professor of Mechanical Engineering.

M. A. Mason[1]

W. W. Simmons
Graduate Student.

Department of Mechanical Engineering,
University of Wisconsin-Madison,
Madison, WI 53706

Effect of Tumbling and Burning on the Drag of Bluff Objects

The drag on various tumbling, nonburning wooden plates, cubes, rods, and wood chips was determined by measuring the free-fall velocity. The drag coefficient was reduced by a factor of 0.46 to 0.72 compared to the drag coefficient with the largest flat surface oriented perpendicular to the flow. The drag coefficient of burning wooden cubes and disks which are not tumbling was half that of identical nonburning, nontumbling cubes and disks. The drag coefficient of burning wooden cylinders with axes normal to the flow was slightly larger than nonburning cylinders with the same orientation. The information was obtained in order to better model the trajectory of solid fuel particles in furnaces.

I Introduction

The aerodynamic drag on fuel particles which are fed into a boiler is a key parameter in modeling the residence time of the fuel, and hence the combustion efficiency and particulate emissions, for suspension burners, stoker spreaders and fluidized beds. The fuel may, for example, be crushed coal, hog-wood fuel, refuse-derived-fuel or agricultural waste. Typically the fuel may range in size from 2-50 mm, and have shapes ranging from chunks to flat plates to rod-like stringers.

When the fuel particles are injected from the top or side of the boiler, the fuel falls if the weight is greater than the drag, and rises if the drag is greater than the weight. The particles accelerate and tumble as they are carried by the flow. The particles lose weight and change shape as they burn. A complete data set which considers these factors in a manner useful for alternative solid fuels is not currently available in the literature. Hence the purpose of this paper is to present experimental drag data on a set of variously shaped objects, and to present correlations of these data in a manner useful for modeling trajectories of irregularly-shaped particles. Freely-falling, tumbling, non-burning objects along with stationary, burning objects are investigated.

A review of the literature suggests that the drag coefficient (C_D) of an object is a function of Reynolds number, shape, acceleration, turbulence, spacing between neighboring particles, particle rotation, and vaporization/combustion of the particle.

Drag coefficients of inert, nonrotating spheres and cylinders are well known over a Reynolds number (Re) range of 10^{-2} to 10^7 for steady flow [1]. For bluff bodies C_D for a wide variety of shapes is known for Re greater than 1000 since the flow separates at the corners of the body and C_D is essentially independent of Re. However, for Re less than 10^3, C_D depends on Re. For a circular disk normal to the flow, C_D essentially approaches that of a sphere for Re less than 20, and is known over the full Re range [2, 3]. The drag coefficient of spheres, infinite cylinders and thin disks over a Reynolds Number of 1 to 20,000 is shown in Fig. 1. For other bluff bodies C_D is not available for Re less than 1000.

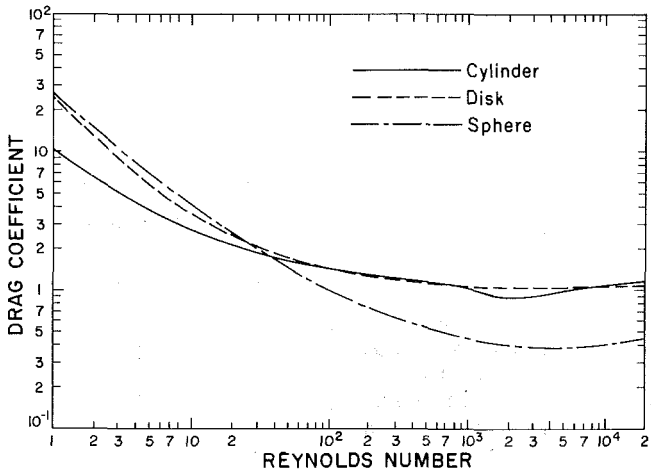

Fig. 1 Drag coefficient versus Reynolds number for infinitely long smooth cylinders, thin disks, and smooth spheres, all nonburning, nonrotating

Many authors have sought to define universal shape factors which can relate the drag of nonspherical particles to that of a sphere. No entirely satisfactory or universally accepted shape factor has yet been developed [4]. Degree of sphericity, equivalent projected area, equivalent surface area, and other parameters have been tried.

Acceleration appears not to have any effect on the drag coefficient of solid spheres and cylinders in a gaseous fluid [5, 6]. For disks in the face-on orientation there is a steady decrease in drag coefficient of about 10 percent as the acceleration increases from 0 to 10 m/s^2 [5]. Roberson [7] has shown that increased turbulence increases the drag on disks and square plates, and decreases the drag on cubes, cylinders, and rods for $5000 < \text{Re} < 70{,}000$. In some instances the change is up to 50 percent.

[1] Now employed at Briggs and Stratton Corp., Milwaukee, Wisc.

Contributed by the Fluids Engineering Division for publication in the JOURNAL OF FLUIDS ENGINEERING. Manuscript received by the Fluids Engineering Division, February 24, 1982.

Freely-falling bluff objects such as a disk tend to fall with the largest flat surface perpendicular to the direction of motion, once a steady state condition is reached. If Re is above 100 the object will oscillate about the longest axis due to the turbulent wake and a zig-zag motion is produced which depends on the moment of inertia of the object as well as Re [8]. The distance required to reach a steady-state free-fall condition, independent of the initial starting orientation, is short for liquid media but rather long for gaseous media. Christiansen and Barker [8] used a 125 m drop in air, for example. For objects such as wood and refuse which are injected into a boiler, the initial injection will cause the particles to tumble and the rotations are not likely to damp-out inside the furnace except for very lightweight objects such as paper. The drag data and correlations given in [8] are not applicable to tumbling objects.

Experimental drag coefficient studies of burning kerosene drops have been done by Bolt and Wolf (see [9]) for $Re < 1$. These results indicate a decrease in drag coefficient due to burning. Rabin et al. [see 9] determined the drag coefficient of burning and non-burning liquid fuel drops accelerating due to the convective flow behind a shock wave. Rabin's data also indicated a decrease in the drag coefficient due to burning for $100 < Re < 10{,}000$. Similarly, Crowe [6] found that the drag on 250 μm solid spheres was reduced 15 percent due to burning.

First, the experimental results on the aerodynamic drag of nonburning irregularly-shaped objects, which are freely falling and tumbling in still air, are presented, and then drag data for stationary, burning cubes, and cylinders are presented and discussed.

II Nonburning Objects

Experimental Technique and Analysis Procedure. The drag on irregularly-shaped particles was determined by dropping individual particles in quiescent air and measuring their velocity as a function of distance.

Light from three light bulbs operating with direct current was passed through three 20.3 cm wide by 0.16 cm slits spaced 20.3 cm apart. Each plane of light was focused to a photodiode by means of a Fresnel lens. The photodiodes were connected to operational amplifiers which started and stopped two electronic time interval counters. The counters were adjusted so that an object blocking only 1.5 percent of the light striking the photodiode would trigger the counter.

The target area through which the objects must fall was limited to 20 by 30 cm in order to minimize error due to drifting particles which could actually travel farther than the vertical distance between the planes of light. The vertical distance between light planes was 20.3 cm, which is large compared to the size of the objects so as to limit the effect of tumbling on the time interval measurement. Nevertheless a certain error in the apparent transit time was introduced by tumbling. This necessitated repeating each drop 10 times. If the separation distance is too large, then error due to acceleration becomes significant.

Each object was dropped from 6 different heights up to 4.7 m above the light plane. In this way a curve of velocity versus distance was obtained. Greater heights could not be used, in order to achieve terminal velocity, because of particle drift due to tumbling. One drop gave two velocities from the two time interval counters. These velocities were assumed to be midway between the planes of light, which is correct if the acceleration is small.

Before each test session, the sensitivity of each counter was adjusted until a 3.1 mm diam. ball bearing just triggered the counters. A ping-pong ball was used repetitively as a check, also.

As the objects fell they tended to rotate or tumble rather rapidly. Typically several turns were made in the space of traversing the light planes. The measured velocity was essentially independent of initial orientation of the particle. No initial rotation was given to the particles.

A curve fit of the velocity versus distance data for each object was made using a linear equation of the following form:

$$V^{1/9} = \alpha/x + \beta$$

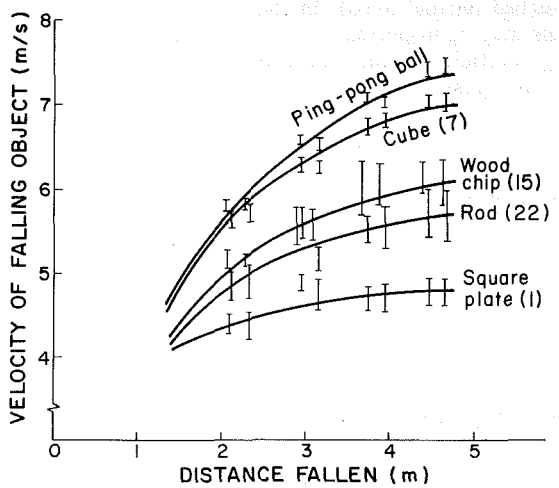

Fig. 2 Velocity of falling objects versus distance travelled. Each curve represents 10 repetitions at four initial heights; range of data shown by vertical lines.

Table 1 Characteristics of nonburning objects tested

Object	Shape	Weight (mg)	Size (cm)
1	Square plate	418	2.00 wide, 2.00 long, 0.15 thick
2	Rectangular plate	315	1.00 wide, 3.00 long, 0.15 thick
3	Rectangular plate	207	0.52 wide, 4.04 long, 0.15 thick
4	Rectangular prism	616	0.85 wide, 2.03 long, 0.85 thick
5	Square plate	95	0.93 wide, 0.94 long, 0.16 thick
6	Rectangular plate	875	2.00 wide, 4.00 long, 0.16 thick
7	Cube	343	0.88 wide, 0.98 long, 1.00 thick
8	Triangular rod	964	0.78 altitude, 1.48 base, 3.25 long
9	Triangular plate	210	1.38 altitude, 2.69 base, 0.16 thick
10	Cylindrical rod	205	0.23 diameter, 6.75 long
11	Wood chip	933	2.5 wide, 2.1 long, 0.24 thick
13	Wood chip	475	1.7 wide, 2.6 long, 0.16 thick
14	Wood chip	112	0.66 wide, 1.8 long, 0.14 thick
15	Wood chip	630	1.5 wide, 2.4 long, 0.26 thick
20	Ping-pong ball	2500	3.75 diameter
22	Cylindrical rod	100	0.20 diameter, 2.56 long

Table 2 Analysis of drag coefficients for tumbling objects

Object	Length / width	Max fixed C_D	Max fixed C_DA (cm^2)	Falling C_DA (cm^2)	Falling C_DA / Fixed C_DA
Plate-like					
Square plate (1)	1	1.18	4.71	3.10 ± .14	0.66
Square plate (5)	1	1.18	1.03	0.64 ± .03	0.62
Rectangular plate (6)	2	1.19	9.35	6.06 ± .40	0.65
Rectangular plate (2)	3	1.19	3.55	2.02 ± .10	0.58
Rectangular plate (3)	7.8	1.26	2.65	1.23 ± .09	0.46
Triangular plate (9)	2	1.19	2.19	1.16 ± .07	0.53
Thin wood chip (11)	1.2	1.19	6.19	4.26 ± .21	0.69
Thin wood chip (15)	1.6	1.19	4.26	2.65 ± .21	0.62
Thicker wood chip (13)	1.5	1.19	5.22	2.71 ± .14	0.52
Thicker wood chip (14)	2.7	1.19	1.48	0.71 ± .05	0.48
Cube-like					
Cube (7)	1	1.1	1.41	1.01 ± .02	0.72
Rectangular prism (4)	2.4	1.1	2.67	1.81 ± .06	0.68
Rod-like					
Cylindrical rod (22)	18	.91	0.71	0.48 ± .03	0.68
Cylindrical rod (10)	30	.95	1.45	0.90 ± .09	0.62

where α and β are constants determined by the method of least-squares. This curve fit was chosen to prevent any inflection points in what should be a monotonic curve.

The drag force was obtained from the velocity versus distance curve in the following way. The mass times the acceleration of the object equals the weight minus the drag, minus the buoyancy, plus the inertial force of the fluid being disturbed (virtual mass). In these experiments the latter two terms may be neglected. The drag force is represented by the drag coefficients times the projected frontal area times the dynamic pressure:

$$\text{drag} = \frac{C_D A\, \rho_a V^2}{2} \tag{2}$$

The equation of motion for the falling object is

$$\frac{dV}{dt} = g - K\, C_D\, A\, V^2. \tag{3}$$

where

$$K = \rho_a / 2M. \tag{4}$$

M = particle mass

and solving for C_D in equation (3) we obtain

$$C_D = \frac{g + \left(\frac{\alpha}{x} + \beta\right)^8 \left(\frac{9\alpha}{x^2}\right) V}{KAV^2}. \tag{5}$$

Thus the drag coefficient (and drag) may be obtained from a curve fit of the velocity versus distance data, provided the appropriate area to be discussed below is specified.

For a given object the measured velocity V and the curve fit coefficients α and β will exhibit some variability. The velocity V was measured 10 times at each distance x for each object, and is a random variable independent of α and β. The error in the determination of C_D may be obtained from the combined errors associated with V, α, and β according to

$$\text{Var}(C_D) = C_1^2 \text{Var}(V) + C_2^2 \text{Var}(\alpha) + C_3^2 \text{Var}\,\beta + 2C_2C_3\, \text{Cov}(\alpha, \beta). \tag{6}$$

Var is the variance and Cov is the covariance and where the coefficients are obtained by differentiating equation (5) as follows:

$$C_1 = \frac{\partial C_D}{\partial V} = \frac{-9VZ^8\, \alpha/X^2 - 2g}{KAV^3}, \tag{7}$$

$$C_2 = \frac{\partial C_D}{\partial \alpha} = \frac{144\, Z^7\, \alpha/X^3 + 18\, Z^8/X^2}{KAV}, \tag{8}$$

$$C_3 = \frac{\partial C_D}{\partial \beta} = \frac{72\, Z^7\, \alpha}{KAV\, x^2} \tag{9}$$

$$Z = \frac{\alpha}{x} + \beta \tag{10}$$

The most probably error associated with the drag coefficient, P, is used in the tables of experimental results and is given by

$$P = 0.675\, [\text{Var}(C_D)]^{1/2}. \tag{11}$$

Results for Nonburning Objects. The objects tested may be grouped as plate-like, cube-like, and rod-like. The size, shape, and weight of each object is given in Table 1. The objects were made of wood except for the ping-pong ball which was used for validation purposes. Objects 1, 2, 3, 5, and 6 were thin rectangular plates with various length to width ratios; object 9 was a thin triangular plate. Object 4 was a rectangular cube, 7 a square cube and 8 a prism. Objects 10 and 22 were cylindrical rods. Objects 11, 13, 14, and 15 were actual wood chips with various length to width ratios.

The velocity (as obtained from the time to fall the 20.3 cm distance between slits) versus distance traveled curves are presented for a few representative objects in Fig. 2. The error bars represent the extremes of the data after the highest and lowest values were discarded. The solid lines are curve fits of the data using equation (1). The curves are fit through the origin. Considerable scatter is expected because the objects are rotating and break the planes of light in different orientations. The velocities, which approached terminal velocity but were not quite at terminal velocity, ranged from 4.5 to 7.5 m/s, and the Reynolds numbers (based on the largest characteristic distance of the object) ranged from 1500 to 18,000.

First, the drag coefficient for the ping-pong ball was obtained from equation (5) as a check on the technique, as shown in Fig. 3. The drag coefficient is 0.53 at the large distances. The generally accepted value for a smooth sphere with this Re = 1.8×10^4 is 0.45. The difference is believed to be due to surface roughness and also analysis error due to acceleration. For this method to be accurate the acceleration must be small or otherwise an error is introduced into the assignment of the position x associated with the mean velocity between the two planes of light. Hence only the flat part of the curve can be used for determination of the drag coefficient.

Fortunately, the irregularly-shaped particles approach terminal velocity more rapidly than smooth spheres.

When working with tumbling objects the projected surface area is not known, and hence we have determined C_DA using equation (5) rather than C_D. A plot of C_DA versus distance is given in Fig. 3 for representative objects. It is seen that reasonably constant values are obtained after 3 m of travel.

The values of C_DA which were measured for the various falling particles are summarized in Table 2. The maximum fixed orientation values of C_D are obtained from the literature. The maximum fixed C_DA values are based on the largest projected frontal area of the objects. For cubes the area of the largest face is used. In the last column of Table 2 the ratio of the measured parameter C_DA to the maximum fixed orientation value of C_DA is given. The particles have been grouped into three categories: plate-like, cube-like and rod-like. Plate-like objects have a falling drag to fixed drag ratio of about 0.58, whereas cube-like average 0.70 and rod-like average 0.65. In addition, within each category the falling drag to fixed drag ratio decreases slightly with increasing length to width ratio.

As a generalization then, the drag on a tumbling, nonburning, bluff body may be calculated by calculating the drag on a fixed particle oriented in the position of maximum drag and then multiplying by 0.6 to account for the tumbling. A more accurate value (ranging from 0.46 to 0.72) for the tumbling correction factor may be obtained by using Table 2.

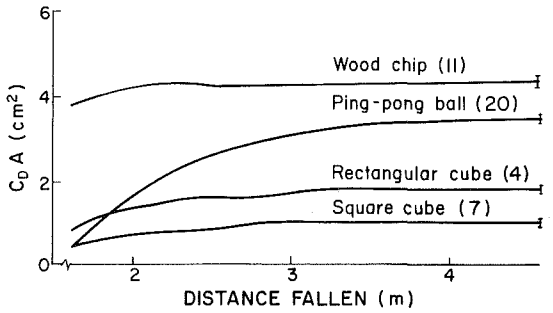

Fig. 3 Drag coefficient times frontal area versus distance travelled for several representative objects

Further details on the technique and data obtained regarding the nonburning experiments are given in the thesis by Mason [10].

III Burning Particles

Experimental Technique. The drag on burning objects was obtained by suspending the object from an electronic balance in a heated air stream. The combustion occurred in a vertical, insulated, circular duct, 51 mm in diameter, with electrically heated air flowing upwards around the object. The test object was fixed to a thin glass rod extending out of the furnace away from the heated area and attaching to the balance above. A solenoid valve in the air line was used to allow rapid shutoff of air flow.

The drag measurements were made by placing the object in the furnace under flowing conditions and continually monitoring the weight minus the drag. The flow was periodically shut off to determine the instantaneous weight. The drag was then obtained by subtracting the two readings.

Room-dried oak in the shape of cubes (10 mm and 20 mm), disks, and cylinders (10 mm dia) were tested. The cubes were burned in three orientations: flat with the bottom surface perpendicular to the flow, rotated 45 degrees along the central axis such that the leading edge appears as a wedge, and oriented such that the leading and trailing edges are points.

Results for Burning Objects. The difference between the drag coefficient for burning and non-burning cubes is very dramatic as shown in Table 3. In nearly all cases the drag coefficient is reduced by at least a factor of two when the cube is ignited. Even with the limited number of samples tested this trend is very consistent despite the relatively large error bands in the burning drag analysis. These error bands were obtained by evaluating the variance of the experimental measurements and then calculating most probable error. The values of the drag coefficients for the 10 mm cubes versus the 20 mm are not directly comparable because wall effects are more strongly felt by the larger particles. No significant trends can be established as to the effect of Re or particle orientation on the drag coefficient in this test configuration due to the limited data available; however, the drag reduction with burning is apparent.

Table 3 Drag coefficients for nonburning and burning cubes, disks and cylinders in 51 mm tube

Cube size (mm)	Orientation	Re	Nonburning C_D	Burning
		— Cubes —		
10	Flat	700	0.97 ± .03	0.26 ± .07
	Wedge	700	0.69 ± .02	0.33 ± .09
	Point	700	0.56 ± .02	0.34 ± .09
10	Flat	1100	0.53 ± .03	0.23 ± .06
	Wedge	1100	0.50 ± .02	0.39 ± .07
	Point	1100	0.53 ± .01	0.19 ± .03
20	Flat	1400	1.4 ± .08	0.91 ± .15
	Wedge	1400	1.7 ± .09	1.0 ± .20
	Point	1400	1.6 ± .04	0.88 ± .17
20	Flat	2100	1.3 ± .08	0.65 ± .11
	Wedge	2100	1.6 ± .09	0.72 ± .09
	Point	2100	1.5 ± .05	0.56 ± .07
		— Disk ($l/d = 1$) —		
10	End-on	670	3.4 ± .11	1.9 ± .38
10	End-on	1000	2.3 ± .16	1.3 ± .22
10	End-on	1300	1.3 ± .11	0.85 ± .11
		— Cylinder ($l/d = 2$) —		
10	Normal	450	1.5 ± .04	1.5 ± .33
10	Normal	670	0.9 ± .05	1.3 ± .26
10	Normal	890	0.7 ± .06	1.3 ± .22
10	Normal	1100	0.8 ± .04	0.91 ± .13

The results of the disk and cylinder tests are also shown in Table 3. For the disk a reduction in drag coefficient with ignition was again observed. However, for the cylinder with its axis perpendicular to the flow, the drag coefficient tended to increase slightly.

IV Discussion

The free-falling, nonburning wooden objects were within 70 to 95 percent of their terminal velocity and were tumbling. There was generally no significant difference in results due to initial orientation of the object. The drag coefficients of the bluff objects were independent of distance fallen over the range of 2-4 m as indicated in Fig. 3.

Rather than attempt to introduce shape factors for the nonspherical objects in order to generalize the data, we have used C_DA in combination where A is the frontal area of the object associated with the maximum fixed orientation drag coefficient. In order to compute the drag on a tumbling, nonburning bluff object, the suggestion here is to calculate the drag on a fixed particle using the maximum drag coefficient, and then multiply by a tumbling correction factor (found in Table 2). If Re $<$ 1000 the fixed C_D for bluff bodies other than a disk is not available, since the flow may not be separated. However, it is reasonable to assume that the C_D curve for a bluff body, such as a cube or plate, follows the curve of a disk, as given in Fig. 1, for low Re.

The use of the suggested tumbling factor for computing the drag is not the same as computing the average drag force based on each of the fixed orientations through which the object passes. The latter approach yields a drag which is too low by a factor of 10 to 40 percent compared to the observed data.

For burning, nonrotating objects there appear to be two factors which influence the drag. During devolatilization of the particle, mass flows from the particle into the boundary layer causing (i) movement of the flow separation point and (ii) change in the effective aerodynamic form of the particle. Also, skin friction is reduced by the mass addition but skin friction drag is small compared to pressure drag for the objects discussed here and cannot explain the effect observed.

For the cubes and disks the major influence appears to be change in the aerodynamic form of the particle. The ignited boundary layer causes the particle to behave more as an elipsoid. Elipsoids have drag coefficients nearly an order of magnitude less than cubes or disks, which supports the direction of change in drag coefficients observed after ignition. For the cylinders oriented with the axis perpendicular to the flow, movement of the separation point seems to be the more dominant effect. As separation progresses towards the leading edge, the particle wake becomes larger increasing the drag coefficient as observed in the tests.

In a furnace the fuel particles would in general be tumbling and burning. Although for bluff bodies the drag is reduced both due to the tumbling and burning, it is doubtful that the effects are multiplicative. During the preignition stage the drag can be modeled as a nonburning, tumbling particle, and after ignition the particle can be modeled as a nontumbling, burning particle because, as the particle gets lighter, the particle will tend to stabilize its orientation.

V Conclusions

The drag coefficient of bluff objects is decreased significantly due to tumbling and burning. For nonburning, tumbling objects the drag coefficient equals the maximum fixed orientation value times a tumbling factor which depends on particle shape. The tumbling factor averages 0.58 for plate-like objects, 0.70 for cube-like objects, and 0.65 for rod-like objects. For burning, nontumbling cubes and disks the drag coefficient is decreased by a factor of two compared to the same nonburning particles. Burning cylinders with the axis perpendicular to the flow exhibited a slight increase in drag coefficient. Drag reduction of burning, bluff objects is due to mass addition into the flow around the particle from the burning particle, which has a streamlining effect. For streamlined objects mass addition into the boundary layer accentuates flow separation and increases drag.

Acknowledgments

The authors wish to thank Edward Gisske for designing the photodiode setup. MAM was supported by a fellowship from the Graduate School, University of Wisconsin. WWS was supported by a fellowship from the Weyerhaeuser Corporation. A grant from the U.S. Forest Products Laboratory was used in part to build the burning particle setup.

References

1 White, F. M., *Fluid Mechanics*, McGraw-Hill, New York, 1979.

2 Massey, B. S., *Mechanics of Fluids*, Van Nostrand Reinhold, New York, 1979.

3 Roos, F. W., and Willmarth, W. W., "Some Experimental Results on Sphere and Disk Drag," *AIAA Journal*, Vol. 9, 1971, pp. 285-291.

4 Zenz, F., *Fluidization and Fluid-Particle Systems*, Reinhold, New York, 1960.

5 Marchildon, E. K., and Gauvin, W. H., "Effects of Acceleration, Deceleration and Particle Shape on Single-Particle Drag Coefficients in Still Air," *AIChE Journal*, Vol. 25, 1979, pp. 938-948.

6 Crowe, C. T., Nicholls, J. A., and Morrison, R. B., "Drag Coefficients of Inert and Burning Particles Accelerating in Gas Streams," *Ninth Symposium (International) on Combustion*, Academic Press, New York, 1963.

7 Roberson, J. A., Lin, C. Y., Rutherford, A. M., and Stine, M. D., "Turbulence Effects on Drag of Sharp-Edged Bodies," *J. Hydraulics Division of the ASCE*, Vol. 98, 1972, pp. 1187-1203.

8 Christiansen, E. G., and Barker, D. H., "The Effect of Shape and Density on the Free Settling of Particles at High Reynolds Numbers," *AIChE Journal*, Vol. 11, 1965, pp. 145-151.

9 Selburg, B. P., and Nicholls, J. A., "Drag Coefficient of Small Spherical Particles," *AIAA Journal*, Vol. 6, 1968, pp. 401-507.

10 Mason, M. A., "Drag on Freely-Falling Wood Chips and Other Irregularly-Shaped Bodies," M. S. thesis, University of Wisconsin-Madison, 77 p., 1980.

O. Güven
Istanbul Technical University,
Emergan, Istanbul, Turkey

C. Farell
St. Anthony Fall
Hydraulic Laboratory,
University of Minnesota,
Minneapolis, Minn. 55414

V. C. Patel
Institute of Hydraulic Research,
The University of Iowa,
Iowa City, Iowa

Boundary-Layer Development on a Circular Cylinder With Ribs

An integral method for the calculation of the boundary layer development on a circular cylinder with external meridional ribs is presented. The calculation method, which takes into account the effect of the ribs on the laminar and turbulent boundary layers and on transition, gives results which are in qualitative agreement with experimental data. Analytical results obtained with this method shed some light on the influence of rib roughness on boundary-layer development and support earlier arguments and conclusions derived from experimental data on the effect of external ribs or stakes on the mean flow around rounded structures at large Reynolds numbers.

I Introduction

The effects of external roughness elements – either uniformly distributed random-shaped or regular elements, or geometrically regular configurations of ribs or strakes – on the mean pressure distributions on cooling towers and circular cylinders have been discussed in a number of recent publications [14, 1, 7, 15, 11, 6]. The present paper provides additional information on the effect of meridional ribs on the flow around circular cylinders at large Reynolds numbers. The work reported included boundary layer measurements and an analytical study in which an attempt was made to calculate the characteristics of the boundary layer over rib roughnesses using a simple integral method. A similar method was used by the authors [12] in an analytical model for high-Reynolds-number flow past circular cylinders with distributed roughness.

The calculation method and the major results of the experimental study of boundary-layer development are presented herein. Comparison with experimental data shows that while quantitative agreement is not quite achieved by the present calculations, the method is at least qualitatively correct, and may be used to demonstrate the effects of rib roughnesses at high Reynolds numbers. Results obtained with this method shed some light on the influence of rib roughness on the development of the boundary layer at high Reynolds numbers and on the relative importance of certain roughness parameters, and support earlier arguments and conclusions [6] based on experimental data on ribbed rounded structures.

II Calculation Method

We consider the development of the boundary layer on a circular cylinder fitted with external meridional ribs. It is assumed that the cylinder is placed in a uniform stream of velocity U and relative turbulence intensity $T_u = u'/U$ (u' = r.m.s. longitudinal turbulent velocity fluctuation), and that the mean flow past the cylinder is two dimensional. The meridional ribs are rectangular in section, of width b and height k, and are placed symmetrically about the forward meridian at an equal circumferencial (linear spacing s). The Reynolds number, $\mathrm{Re} = Ud/\nu$, where d is the cylinder diameter and ν is the kinematic viscosity of the fluid, is assumed to be sufficiently large so that boundary-layer transition is completed sufficiently upstream of the location of minimum pressure on the cylinder and that therefore the complexities associated with the so-called laminar separation-turbulent reattachment "bubbles" observed on circular cylinders with relatively small roughness over the critical Reynolds number range (see, e.g., [2, 1, 6]) are not present. Furthermore, the relative rib height, k/d, is assumed to be sufficiently small so that the local velocity and pressure variations due to the ribs (see e.g., [14, 13]) are also small, at least over most of the cylinder surface, and the usual boundary-layer assumptions are applicable.

It is obvious that in such an attempt to calculate the boundary layer development one should take into account the influence of rib roughness on the laminar and turbulent boundary layers as well as on transition. While a substantial amount of information is available concerning turbulent boundary-layer flow over rib-type roughness, especially for small values of the spacing parameter s/k (see Dvorak [4]), no information seems to exist either about laminar boundary layer flows over rib roughnesses or about transition due to a train of rectangular ribs. Only recently Kiya and Arie [5] have reported an analytical study concerning the flow past single semi-circular and semi-elliptical, two-dimensional, elements attached to a wall and immersed deeply in a laminar boundary layer. In this study, Kiya and Arie have calculated, among other things, drag-coefficients of such elements over a Reynolds number ($U_k k/\nu$) range up to 100, U_k being the velocity of the approaching shear flow at the tip of the element. As may be inferred from this study, knowledge of laminar flows over rib-type roughness is very limited at the present time. The same observation is also true regarding

Contributed by the Fluids Engineering Division and presented at the Winter Annual Meeting, Washington, D.C., November 15-20, 1981, of The American Society of Mechanical Engineers. Manuscript received by the Fluids Engineering Division, May 25, 1982. Paper No. 81-WA/FE-28.

transition. The influence of circular wires on transition has been extensively studied (see, for example, Schlichting [16] or Tani [17]). A recent experimental study of the effect of symmetrically placed trip wires on the boundary layer around a circular cylinder has been reported by Groehn [9]. This study included data on transition and the separation regions behind the wires. However, a criterion for transition applicable to single rectangular ribs or trains of rectangular elements does not seem to be available. Several as yet untested assumptions are therefore made in the present analysis in order to consider the laminar boundary layer and transition. One should point out that even an approximate analysis of the boundary-layer flow is of interest so as to identify the important parameters and to demonstrate their relative effects. The results of this analysis may then be used to give qualitative, and perhaps quantitative, support to the experimental observations and to make extrapolations to those cases where experiments are difficult to perform (such as ribs of small height for which Reynolds-number independent conditions are difficult to obtain in laboratory facilities). The present attempt should be viewed in this context.

The boundary-layer development is calculated by integrating the momentum-integral equation for a prescribed pressure distribution on the cylinder. The calculation procedure employed here is similar to the one used before by the authors [12] for distributed roughness, with the following differences:

1. The boundary-resistance coefficent, C_{fL}, for the laminar boundary layer is assumed to be given by

$$C_{fL} = \begin{cases} 4/(3R_{\delta_1}) + [(k/\delta)(2-k/\delta)]^2/(s/k) & ;k/\delta \le 1 \\ 4/(3R_{\delta_1}) + 1/(s/k) & ;k/\delta > 1 \end{cases} \quad (1)$$

where R_{δ_1} is the displacement-thickness Reynolds number $U_e\delta_1/\nu$; U_e is the velocity at the edge of the boundary layer; δ_1 is the displacement thickness; and δ is the boundary-layer thickness. This relation is based on the assumption of a parabolic velocity profile and a drag coefficient of 1.0 for the ribs based on the tip velocity. (The parabolic velocity distribution is expressed as $u/U_e = 2(y/\delta) - (y/\delta)^2$, where u is the velocity in the boundary layer and y is the normal distance from the cylinder surface.) The first term in equation (1) is due to the smooth surface between the ribs, and the second term represents the apparent boundary resistance arising from the drag of the ribs "distributed" over the area between adjacent ribs.

When the calculation is started at the stagnation point, the displacement thickness there is assumed to be equal to that which would obtain on a smooth surface (i.e., $\delta_1/d = 0.324/\mathrm{Re}^{1/2}$). If k/δ_1 is less than 0.1, the cylinder surface is assumed to be smooth and the laminar boundary layer is calculated using Thwaites' method, as has been done in [12]. In this case, equation (1) is not needed.

2. The transition criterion is similar to the one used before in [12] for distributed roughness. That is, transition is assumed to take place abruptly when R_{δ_1} exceeds a critical value, $R_{\delta_1\,\mathrm{cri}}$, given by

$$R_{\delta_1\,\mathrm{cri}} = \text{minimum of } \{R_{\delta_1 cs}, R_{\delta_1 ck}\} \quad (2)$$

where $R_{\delta_1 cs} = 416 + 2555\ \exp(-103\ \mathrm{Tu})$, as before, but $R_{\delta_1 ck} = \text{maximum of } (416{,}826/(k/\delta_1))$ based on the assumption that the critical Reynolds number for the rib roughnesses is the same as that for a cylindrical wire. According to Gibbings (see reference [17]), transition takes place at the wire if $U_e k/\nu$ exceeds 826, k being the wire diameter in this case.

3. Due to the uncertainty in Dvorak's [4] skin-friction formula for large values of s/k, the turbulent boundary-layer calculations are performed using both the Dvorak relation as well as a simple relation involving an apparent surface-resistance coefficient C_{fR} due to the drag of the ribs, developed in [10] on the basis of Good and Joubert's [8] data for the drag of an isolated fence in a turbulent boundary layer. In the latter case the total resistance coefficient, C_{fT}, for the turbulent boundary layer is assumed to be given by

$$C_{fT} = C_{fS} + C_{fR} \quad (3)$$

where C_{fS} is the smooth-wall value obtained by the Ludwieg-Tillman formula, and C_{fR} is given by

$$C_{fR} = 0.91 + 0.37 \log_{10} k/\delta)/(s/k) \quad (4)$$

over the range $0.05 < k/\delta < 0.60$.

Dvorak's skin friction equation contains an additive term specifically to represent pressure gradient effects, as derived essentially by Arndt and Ippen [3]. The reader is referred to Ref. [4] for a discussion of relevant experimental data and applications to other turbulent-boundary-layer calculations.

4. The smoothed "overall" pressure distributions are used in the calculations. This means that the local influence of the ribs on the pressure distribution is ignored.

III Calculation Results and Comparison With Experiment

The results of a series of calculations performed for two

Nomenclature

b = rib width
C_d = drag coefficient
C_{fL} = laminar boundary-resistance coefficient
C_{fR} = apparent boundary-resistance coefficient due to ribs
C_{fS} = smooth-wall boundary-resistance coefficient
C_{fT} = turbulent boundary-resistance coefficient
C_p = pressure coefficient, $(p-p_0)/[(1/2)\rho U^2]$
C_{pb} = base pressure coefficient
C_{pm} = minimum pressure coefficient
d = cylinder diameter
k = rib height
l = cylinder length
p = pressure
p_0 = pressure in undisturbed stream
$\mathrm{R_e}$ = Reynolds number, Ud/ν
R_k = Uk/ν
R_{δ_1} = displacement-thickness Reynolds number
$R_{\delta_{1\,\mathrm{cri}}}$ = critical value of R_{δ_1}
s = rib spacing
T_u = relative turbulence intensity
U = velocity of uniform stream
U_e = velocity at edge of boundary layer
U_k = approach velocity at tip of element
u = r.m.s. longitudinal velocity fluctuation
y = normal distance from cylinder surface
δ = boundary-layer thickness
δ_1 = boundary-layer displacement thickness
δ_2 = boundary-layer momentum thickness
δ_m = boundary-layer thickness at pressure minimum
ϕ = circumferential angle
ϕ_T = angular location of transition
ν = kinematic viscosity of fluid
ρ = mass density of fluid

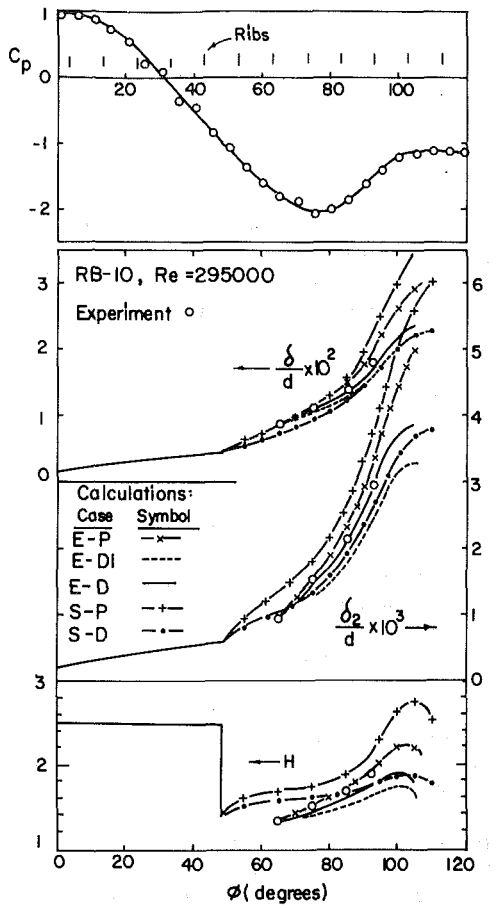

Fig. 1 Pressure distribution and boundary layer development on the test cylinder RB = 05 ($k/d = 1.97 \times 10^{-3}$, $s/k = 22.1$). Re = 2.95×10^5, Tu = 0.2 percent. (Uncertainty in $C_p = \pm 0.015$; in $\delta/d = \pm 0.001$; in $\delta_2/d = \pm 0.001$; in $H = \pm 0.12$; with at least 95 percent confidence)

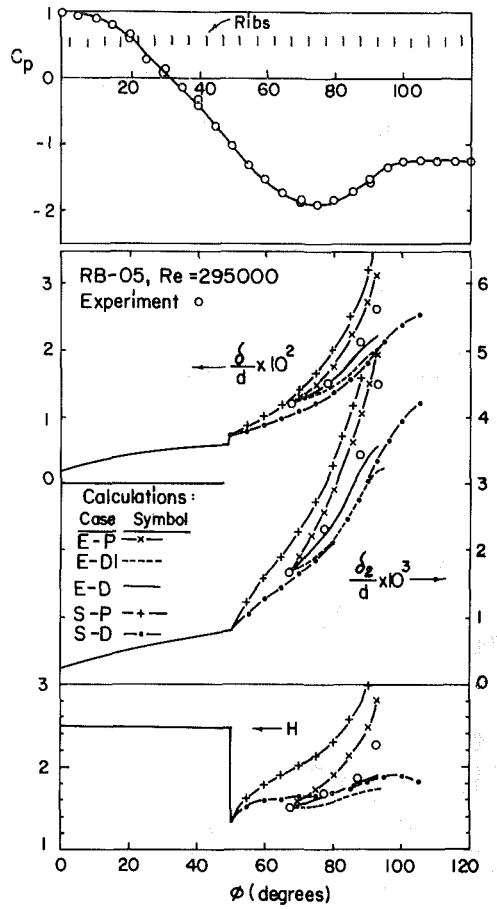

Fig. 2 Pressure distribution and boundary-layer development on the test cylinder RB-10 ($k/d = 1.97 \times 10^{-3}$, $s/k = 44.2$). Re = 2.95×10^5; Tu = 0.2 percent. (Uncertainty in $C_p = \pm 0.015$; in $\delta/d = \pm 0.001$; in $\delta_2/d = \pm 0.001$; in $H = \pm 0.12$; with at least 95 percent confidence)

cases of cylinders with ribs are shown in Figs. 1 and 2 together with the experimental pressure distributions and the δ/d, δ_2/d, and H developments, where δ_2 is the momentum thickness and H is the shape factor, $H = \delta_1/\delta_2$. The location of the ribs is also shown in the figures. Here, ϕ is the meridional angle measured from the forward stagnation point and C_p denotes the pressure coefficient, $C_p = (p - p_0)/\frac{1}{2}\rho U^2$, where p is the pressure on the cylinder surface, p_0 is the static pressure of the undisturbed uniform stream and ρ is the fluid density. (Other symbols in the figures are defined in the next two paragraphs.) In the two cases presented here the relative rib height is 1.97×10^{-3} and the cylinder Reynolds number is 2.9×10^5. The spacing of the ribs is different in each case.

The experiments were conducted in a closed circuit wind tunnel with a rectangular test section 60 inches wide and 32.9 inches high, with free-stream turbulence intensity less than 0.2%. The aluminum cylinder models were 10.65 inches in diameter and were fitted with 53 pressure taps at their midsections. Additional taps were provided at 4.0 inches and 8.0 inches above and below the midsections to assess the degree of two-dimensionality of the flow. All taps were 0.040 inch in diameter. The pressures (including the reference static and dynamic pressures) were transmitted by means of plastic tubing to a Scanco Scanivalve and measured with a Statham differential pressure transducer. The mean pressure data were obtained automatically using an IBM data aquisition system, scanning in succession the Scanivalve terminals at prescribed time intervals. The pressure measuring system was calibrated statically before and after each run. For the boundary layer

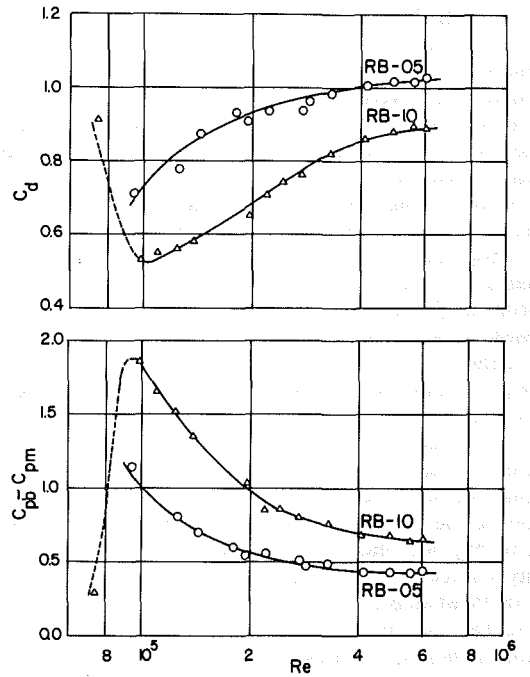

Fig. 3 Variation of C_d and $C_{pb} - C_{pm}$ with Re for the test cylinders RB-05 ($k/d = 1.97 \times 10^{-3}$, $s/k = 22.1$) and RB-10 ($k/d = 1.97 \times 10^{-3}$, $s/k = 44.2$). (Uncertainly in $C_d = \pm 0.015$, in $C_{pb} - C_{pm} = 0.015$; with at least 95 percent confidence)

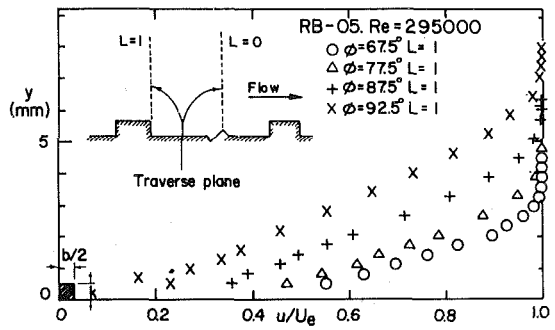

Fig. 4 Boundary-layer velocity profiles. Ribs RB-05. (Uncertainty in $u/U_e = \pm 0.02$, with at least 95 percent confidence)

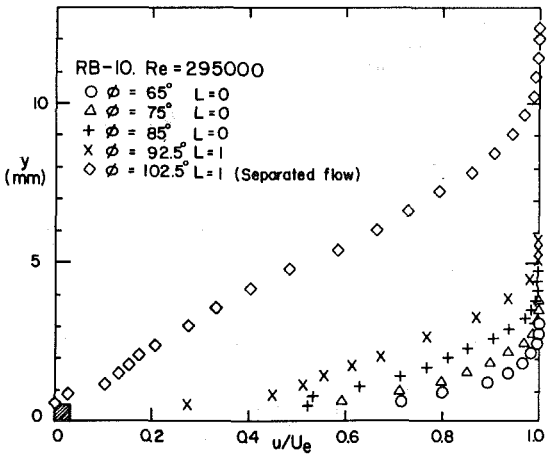

Fig. 5 Boundary-layer velocity profiles. Ribs RB-10. (Uncertainty in $u/U_e = \pm 0.02$, with at least 95 percent confidence)

measurements, flattened hypodermic needles (tip size after flattening 0.037 inch) were used, supported on a traversing mechanism which allowed adjustment of the normal distance from the cylinder to within 0.001 foot. The stagnation pressures were measured by means of an alcohol micromanometer with a resolution of 0.001 inch alcohol. The rib roughnesses were obtained by means of rectangular commercial flat wires. For some experiments, a gap was provided on the midsection to analyze the local rib effects on the mean pressures measured. Since the main purpose of this paper is to present the calculation technique, the reader is referred to [13] for a complete account of the experiments and to [7], [10] and [11] for additional discussions of the experimental method.

In order to give an idea about the flow regime of the present test cases, and about the measured boundary-layer velocity profiles, the curves of drag-coefficent, C_d, and pressure-rise, $C_{pb} - C_{pm}$, versus Reynolds number corresponding to each test cylinder are presented in Fig. 3; the measured velocity profiles are given in Figs. 4 and 5. In Fig. 3, C_{pb} is the average pressure coefficient in the wake region and C_{pm} is the minimum pressure coefficient. In Figs. 4 and 5, L denotes the location of the velocity traverse plane relative to a rib (see sketch in Fig. 4). The experimental evaluation of the boundary layer thicknesses δ_2 and δ_1 in the case of cylinders with ribs is difficult due to errors in the velocity profiles close to the ribs, discussed in detail in [10, 13]. In order to obtain an estimate of these quantities in the present cases a power-law velocity distribution was assumed and the power-law exponent was evaluated on the basis of the velocity distribution measured in the outer region away from the ribs. The experiments with the smallest rib height tested ($k/d = 1.97 \times 10^{-3}$) have been chosen for comparison with theory since it is expected that the application of the usual boundary-layer concepts should gain an increased validity with decreasing rib height.

Several tests of the present calculation method are displayed in Figs. 1 and 2. In the cases denoted by E-P, E-D1, and E-D, the calculations were started with experimental values of H and δ_2. In E-P the present simple skin-friction relation (equation (3)) was employed, while in E-D1 and E-D, Dvorak's skin-friction law with $\lambda = s/k$ and $\lambda = 0.5(s/k)$, respectively, was used. Here, λ is the roughness-density parameter defined by Dvorak as the ratio of total surface area to that of the normal projection of the roughness elements on the surface. For rib roughness, this definition is equivalent to s/b. However, all the rib-type roughnesses considered by Dvorak were square rods so that λ may also be taken as s/k. Actually, for large values of s/k and small values of b/k (say, less than 3) for which there is very little flow-pattern interaction between the ribs, the more significant parameter should be s/k and not b/k (see also reference [7]). In the cases considered here $b/k = 1.71$, so that, according to Dvorak's original definition, $\lambda = 0.585(s/k)$. In view of the foregoing arguments, however, it is more reasonable to use $\lambda = s/k$, if Dvorak's skin-friction law, derived on the basis of experiments with square rods only, is to be compared with the present experiments where the relative rib spacing is quite large. Furthermore, the general applicability of this skin-friction law is doubtful for values of λ greater than about 5. Therefore, two different values of λ have been used in these calculations for comparison. It is seen from Figs. 1 and 2 that the case E-P shows good agreement with experiment. This may be considered as further support for the validity of equation (4) used earlier in reference [7] for discussion of experimental results on ribbed cylinders and cooling towers. It is also seen that the best overall agreement with experiment (including the H development) is given by the case E-D ($\lambda = 0.5s/k$) while case E-D1 ($\lambda = s/k$) underestimates the boundary-layer thicknesses.

In cases S-P and S-D, shown in Figs. 1 and 2, the calculations were started at the stagnation point. In S-P the present resistance formula was used in the turbulent boundary-layer calculation while Dvorak's skin-friction law with $\lambda = 0.5\ (s/k)$ was used in S-D. It is seen that, in general, the developments of δ and δ_2 are at least qualitatively reproduced in either case. The quantitative agreement with experiment may be considered reasonable in the case of S-P for the δ development shown in Fig. 2. While none of these calculations can adequately reproduce all the important characteristics of the boundary layer at the same time, it is seen that the best overall agreement with experiment (including the H development) is obtained in the case S-D. It may also be observed that the prediction of transition appears to be reasonable. Indirect support for this observation may be found in the pressure distribution shown in Fig. 2 for the test cylinder RB-10. It will be seen that the local pressure variations shown by the data for the pressure taps at $\phi = 25$, 30, 35, 40 deg are not observed beyond $\phi = 45$ deg. This is apparently due to a decrease in the length of the separation pocket behind a rib as the boundary layer becomes turbulent beyond $\phi = 40$ or 45 deg which is close to the location of transition shown in the same Fig. 2.

The good qualitative agreement observed between calculations and experiment for the δ and δ_2 developments and for transition in the foregoing cases suggests that the present calculation procedure may be used to demonstrate analytically the influence of the important roughness parameters k/d and s/k on the development of the boundary layer. This is done in the next section. In view of the better agreement with experiment shown by the cases of E-D and S-D, and also because the present simple resistance formula

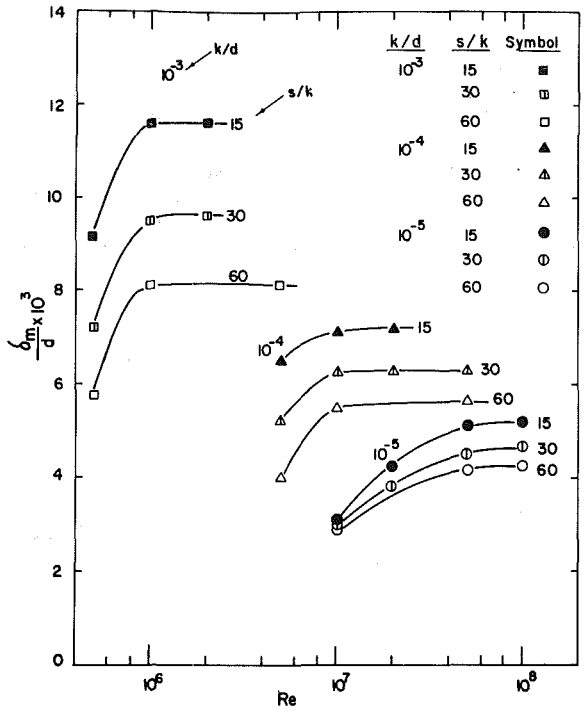

Fig. 6 Calculated variation of δ_m/d with k/d, s/k, and Re. (Tu – 0.5 percent)

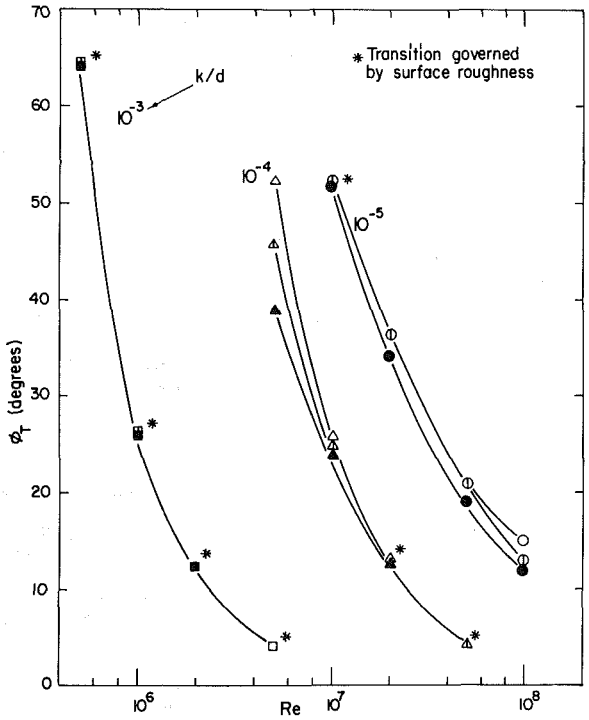

Fig. 7 Calculated variation of ϕ_T with k/d, s/k, and Re. (Tu = 0.5 percent). Symbols as in Fig. 6.

cannot be used for $k/\delta < 0.05$ (see equation (4)), Dvorak's friction law is used with $\delta = 0.5$ (s/k) in the calculations in the next section.

IV Effect of Rib Roughness on Boundary-Layer Development

In the calculations of this section, the pressure distribution

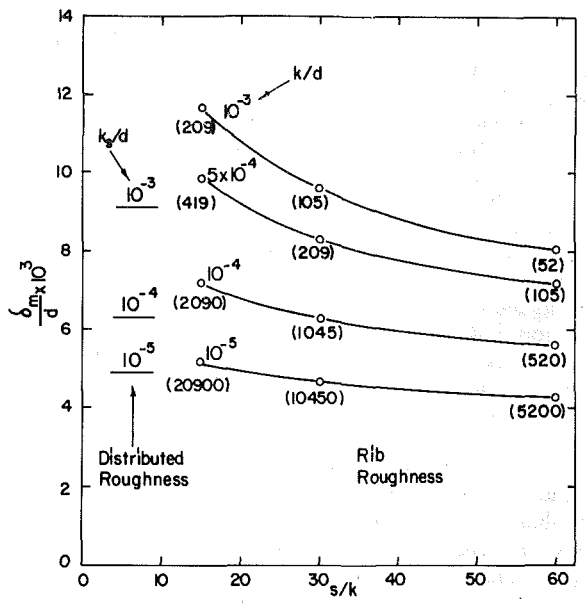

Fig. 8 Variation of δ_m/d with k/d and s/k in the range of Reynolds-number independence. The numbers in parantheses are the total number of ribs corresponding to each case.

shown in Fig. 2 for the test cylinder RB-10 has been used throughout and the freestream turbulence intensity has been assigned a value of Tu = 0.5 percent. This distribution is in the range of Reynolds number independence for the k/d and s/k values indicated in the figure. The more important results of these calculations are summarized in Figs. 6, 7, and 8.

Figure 6 shows the variation of the boundary-layer thickness, δ_m, at the location of the pressure minimum with Re, k/d and s/k over a range of large Reynolds numbers, for k/d values in the range 10^{-5} – 10^{-3} and s/k values in the range 15 – 60. The similarity of the curves shown in Fig. 6 with those of earlier curves [7, 11] depicting the experimental variation of characteristic pressure-distribution parameters with Reynolds number and surface roughness may be taken as additional evidence of the relationship between the boundary-layer development and the pressure distribution. It is also seen that a Reynolds-number independent condition is obtained as the Reynolds number is increased, consistent with the previous experimental observations, and that the boundary-layer thickness is larger for larger roughnesses and smaller spacings. A definite influence of both k/d and s/k on the boundary-layer development is seen. The changes with s/k are relatively larger for the largest roughness and become small as both the Reynolds number and the relative rib height are decreased. In particular, practically no influence of s/k is seen at $\mathrm{Re} = 10^7$ with $k/d = 10^{-5}$. For this small relative rib height the relative rib spacing appears to affect only slightly the boundary-layer development as the Reynolds number is increased. The effects of s/k and k/d in the range of Reynolds-number independence are discussed further later on.

Figure 7 shows the variation of the angular location of transition, ϕ_T, with Re and with the roughness parameters k/d and s/k. Here we observe that transition is generally insensitive to the value of s/k, as one would expect in view of the transition criterion (2) assumed. As indicated in the figure, it is governed by the rib height for $k/d = 10^{-3}$, and by the freestream turbulence for $k/d = 10^{-5}$ at large Re. The variations in ϕ_T with s/k exhibited for $k/d = 10^{-4}$ at $\mathrm{Re} = 5 \times 10^6$ arise from the influence of roughness on the early laminar boundary-layer development. The results shown in Figs. 6 and 7, when examined together, indicate that if transition occurs sufficiently upstream the characteristics of the boundary layer at ϕ_m, for a given k/d and s/k, are very similar independent

of Reynolds number, as has been also observed with distributed roughness [11, 12]. When Reynolds-number independence has been achieved, the transition is seen to take place prior to $\phi = 20 - 30$ deg.

It is of particular interest to examine the influence of k/d and s/k on the boundary-layer development in the range of Reynolds-number independence, especially for relatively small rib heights, since it is difficult to obtain Reynolds-number independent conditions with these roughnesses in experiments in most presently available wind tunnels. Furthermore, the construction of the actual physical models is also difficult due to the very small roughness. The calculated variation of δ_m/d with k/d and s/k in the range of Reynolds-number independence is shown in Fig. 8. Also included in this figure are the results obtained for distributed roughness [12] at large Reynolds numbers. (These are indicated by short lines centered at $s/k = 6.35$, since $\lambda = 3.175$ for distributed roughness if the equivalent Nikuradse roughness k_s is used instead of k (see Dvorak [4]), and we have used $\lambda = 0.5\ s/k$ for the calculation with ribs).

Several important conclusions may be drawn from Fig. 8. One of these is that a cylinder with $k/d = 10^{-5}$ behaves practically (in the Reynolds-number-independent range) as if the surface were smooth even though the calculations indicate that the ribs pierce the viscous sublayer for all the values of s/k shown in the figure. The boundary-layer flow is fully rough in all these cases. Under these conditions, the increase in the boundary resistance over that of a smooth surface is very small for these small ribs, and consequently very small changes are seen with s/k (with the number of ribs). As k/d is increased, the boundary-layer thickness also increases. At the same time the influence of s/k becomes larger. Although it is not possible in the present cases to assess the quantitative influence of the changes in δ_m/d (depicted in Fig. 8) on the pressure distributions, the qualitative similarity of these changes with those shown by the pressure-distribution parameters, and the relationship between pressure distribution and boundary layer characteristics demonstrated by earlier investigations, imply that the results shown in Fig. 8 may also be used to derive conclusions, qualitatively valid at least, as to the effects of s/k and k/d on the mean pressures. Thus, it may be suggested that the pressure distributions obtained with rib roughness will be similar to those with distributed roughness for similar relative roughness heights of the order of $k/d = 10^{-5}$ and 10^{-4}, provided s/k is in the range shown in the figure. Therefore, ribs of such small height ($k/d \sim 10^{-4}$) cannot be expected to cause significant reductions in the magnitude of cooling tower minimum pressure coefficients $|C_{pm}|$, even if a very large number of ribs is employed. This result has been used already in the discussion of experimental data regarding the influence of rib roughnesses on the mean pressure distributions on cooling towers [7].

Conclusions

Main conclusions of the present study are summarized below.

1. Comparisons with experimental data show that the present calculations of boundary-layer development on a circular cylinder with external ribs are at least qualitatively correct and may be used to demonstrate the effects of rib roughnesses at high Reynolds number. The study indicates also that present knowledge of laminar and turbulent boundary-layer flows and transition over rectangular rib trains is rather limited.

2. The present analytical results support earlier conclusions derived from experimental data about the effects of rib roughness at large Reynolds numbers, in particular the reduction in the pressure rise to separation with increasing relative roughness height, k/d, or decreasing relative rib spacing, s/k, over a range of values of these parameters. The significant effects of both parameters s/k and k/d are demonstrated by the calculations.

3. A cylinder with $k/d = 10^{-5}$ behaves practically as if the surface were smooth and ribs of small height ($k/d < 10^{-4}$) cannot be expected to cause significant reductions in the value of the pressure rise $C_{pb} - C_{pm}$ even if a very large number of ribs is employed.

Acknowledgments

This paper is based upon research sponsored by the National Science Foundation under Grants No. GK-35795, ENG 76-08849 and ENG 78-22092.

References

1 Achenbach, E., "Influence of Surface Roughness on the Cross Flow Around a Circular Cylinder," *Journal of Fluid Mechanics*, London, England, Vol. 46, 1971, pp. 321–335.

2 Achenbach, E., "Distribution of Local Pressure and Skin Friction Around a Circular Cylinder in Cross Flow up to R = 5 × 10^6," *Journal of Fluid Mechanics*, London, England, Vol. 34, 1968, pp. 625–639.

3 Arndt, R. E. A., and Ippen, A. T., "Cavitation near Surfaces of Distributed Roughness," Report No. 104, Hydrodynamics Laboratory, M. I. T., 1967.

4 Dvorak, F. A., "Calculation of Turbulent Boundary Layers on Rough Surfaces in Pressure Gradient," *AIAA Journal*, Vol. 7, 1969, pp. 1752–1759.

5 Kiya, M., and Arie, M., "Viscous Shear Flow Past Small Bluff Bodies Attached to a Plane Wall," *Journal of Fluid Mechanics*, Vol. 69, Part 4, 1975, pp. 803–823.

6 Farell, C., "Flow Around Fixed Circular Cylinders: Fluctuating Loads," *Journal of the Engineering Mechanics Division*, ASCE, Vol. 107, No. EM3, 1981, pp. 565–588.

7 Farell, C., Güven, O., and Maisch, F., "Mean Wind Loading on Rough-Walled Cooling Towers," *Journal of the Engineering Mechanics Division*, ASCE, Vol. 102, No. EM6, Proc. Paper 12647, 1976, pp. 1059–1081.

8 Good, M. C., and Joubert, P. M., "The Form Drag of Two-Dimensional Bluff Plates Immersed in Turbulent Boundary Layers," *Journal of Fluid Mechanics*, Vol. 31, Part 3, 1968, pp. 547–592.

9 Groehn, H. G., "Über Der Einfluss Von Stolperdrähten Auf Die Umströmung Eines Kreiszylinders," Berichte Der Kernfors Chungsanlage Jülich, No. 1237, Institut Für Reaktokbauelemente, Germany, September 1975.

10 Güven, O., "An Experimental and Analytical Study of Surface-Roughness Effects on the Mean Flow Past Circular Cylinders," thesis presented to the University of Iowa at Iowa City, Iowa, 1975, in partial fulfillment of the requirements for the degree of Doctor of Philosophy.

11 Güven, O., Farell, C., and Patel, V. C., "Surface Roughness Effects on the Mean Flow Past Circular Cylinders," *Journal of Fluid Mechanics*, London, England, Vol. 98, 1980, pp. 673–701.

12 Güven, O., Patel, V. C., and Farell, C., " A Model for High Reynolds Number Flow Past Rough-Walled Circular Cylinders," ASME JOURNAL OF FLUIDS ENGINEERING, Vol. 99, No. 3, 1977, pp. 486–494.

13 Güven, O., Patel, V. C., and Farell, C., "Surface Roughness Effects on the Mean Flow Past Circular Cylinders," IIHR Report No. 175, Institute of Hydraulic Research, The University of Iowa, Iowa City, Iowa, May 1975.

14 Nieman, H. J., "On the Stationary Wind Loading on Axisymmetric Structures in the Transcritical Reynolds Number Region," Report No. 71-2, Institut für Konstructiven Ingenierbau, Ruhr-University, Bochum, Germany, 1971.

15 Propper H., "Zur Aerodynamischen Belastung Grosser Kühlturme," Report No. 77-3, Institute für Konstructiven Ingenierbau, Ruhr-University, Bochum, Germany, 1977.

16 Schlichting, H., *Boundary Layer Theory*, 6th Ed., McGraw-Hill, 1968.

17 Tani, I., "Boundary Layer Transition," *Annual Review of Fluid Mechanics*, Vol. 1, 1969, pp. 169–196.

T. T. Yeh

Baldwin Robertson

National Bureau of Standards,
Washington, D.C. 20234

W. M. Mattar

Research Associate,
The Foxboro Co.,
Foxboro, Mass.

LDV Measurements Near a Vortex Shedding Strut Mounted in a Pipe

The velocity field around vortex shedding strut mounted in a circular pipe has been in detail with a laser Doppler velocimeter (LDV) at a pipe Reynolds number equal to 90,000. The instantaneous velocity is decomposed into mean, periodic, and random components. Only the first two harmonics are large enough to be detected; the large-scale structure can be characterized by just these two these and the mean. Profiles of the different velocity terms are given upstream of, downstream of, and close to the strut. The two-dimensional velocity vector field of the mean flow on the transverse diametral plane of symmetry is presented along with its streamlines. Finally, for each spatial component, profiles of vortex visibility, the ratio of the energy of a periodic component to the total fluctuating energy in a narrow frequency band, are given.

Introduction

A cylindrical obstacle placed in a flowing fluid produces a regularly oscillating wake at a frequency roughly proportional to the fluid velocity. The majority of the available data concerning this vortex shedding phenomenon is for an obstacle either in unbounded flow or in a flow confined by parallel channel walls [1, 2, 3]. Also, most data are limited to global results such as the shedding frequency, the associated drag or lift forces, the flow-induced resonant-structure vibration, or the spacing of the vortex street. Little quantitative data describing the detailed velocity fields are available, especially when the vortex shedding is bounded by a circular cross-section conduit.

Velocity measurements in the literature include those by Kovaszny [1] who studied the velocity field in free wake flow behind a circular cylinder. Durgin and Karlson [2] studied vortex street breakdown phenomenon in the wake of a small shedding cylinder placed in front and perpendicular to a larger circular cylinder. Both measurements were made at low Reynolds number in unbounded flows. Baker, et al. [3] measured the mean velocity profile at large Reynolds numbers. Recently, Perry and Watmuff [4] used a phase-average technique to eliminate small-scale structures and turbulence and the effects of "vortex jitter" from hot-wire signals, they successfully drew the large-scale vortex structures in a three-dimensional turbulent wake.

Vortex shedding from a cylinder is largely a two-dimensional phenomenon. However, the boundary conditions for a circular pipe and the turbulence in the flow are both three-dimensional and hence may be expected to modify the two-dimensional properties of shedding. Measurements with the circular boundary condition are of particular interest for developing the understanding necessary for improving the design of vortex-shedding flow meters. This geometry precludes hope of exact analytical calculations for comparisons with experiment. Hence there is no advantage in using a strut with a cross section that can be described by an analytic formula. On the other hand, a strut having a bluff forward face with sharp edges precisely defines the lines of separation of the flow. Furthermore, a strut with a downstream-facing splitter plate gives a relatively constant Strouhal number over a broad range of Reynolds number [5]. Also, the splitter plate is a convenient place to install a differential pressure transducer, which could be useful for future meausurements. For these reasons, the T-shaped strut of Fig. 1, mounted in a circular pipe, was used to generate the vortices studied in this paper.

Measurements of the velocity field upstream, at the side of, and downstream of the strut are reported for a pipe Reynolds number equal to 90,000. Profiles of the visibility of the oscillations in the flow are also given. This measure of the ease of detecting the oscillations may also be useful for improving the design of vortex shedding flowmeters.

Definitions

For high Reynolds number flow, the total instantaneous velocity around an obstacle is an extremely complicated function of both time and space. However, one obvious characteristic is the almost periodicity of the wake. This suggests decomposing the flow field into a sum of mean, periodic, and random velocity components [1]. The axial or x component of the velocity is

$$U(t) = \bar{U} + \sqrt{2} \sum_{n=1}^{\infty} u_n \cos(2\pi f_n t + \phi_n) + u'(t),$$

where t is the time. The transverse or y component of the velocity is

$$V(t) = \bar{V} + \sqrt{2} \sum_{n=1}^{\infty} v_n \cos(2\pi f_n t + \psi_n) + v'(t).$$

Contributed by the Fluids Engineering Division for publication in the JOURNAL OF FLUIDS ENGINEERING. Manuscript received by the Fluids Engineering Division, June 4, 1982.

The decomposition of the z component of velocity is not given because velocity measurements in that direction were not performed. Here $\bar{U}$ and $\bar{V}$ are the mean velocities, u_n and v_n are the rms amplitudes of the velocity components occuring at the nth harmonic f_n of the frequency f_1 of the shedding from one side, ϕ_n and ψ_n are the corresponding phases, and u' amd v' are the remaining turbulence velocities which are random. All velocities and the phases are understood to be functions of position (x,y,z). Other definitions are: the turbulence intensities $u_t = <(u')^2>^{1/2}$ and $v_t = <(v')^2>^{1/2}$, and the total velocity fluctuations $u_T = (\Sigma u_n^2 + u_t^2)^{1/2}$ and $v_T = (\Sigma v_n^2 + v_n^2)^{1/2}$.

Also the pipe Reynolds number is $R_e = U_b D/\nu$, where $U_b = \dot{Q}/A$ is the bulk of area-averaged velocity, D is the pipe diameter, ν is the kinematic viscosity, $A = \pi D^2/4$ is the pipe cross-sectional area, and $\dot{Q}$ is the total volume of bulk flow rate.

At low Reynolds numbers, the velocity field is very periodic in time and in space. However, at high Reynolds numbers, the vortex formation is not perfectly regular, so that the amplitudes and especially the phases are randomly modulated in both time and space. Furthermore, there is always some small-scale random turbulent velocity superposed on the large-scale velocity field. To handle this, the velocity power spectrum was used to obtain the amplitude of the time-dependent velocity components. These also were measured everywhere in the vicinity of the vortex shedding strut.

Apparatus and Technique

The flow system used consists of a recirculating water flow loop with a centrifugal pump driven by a 2,200 W (3 hp) motor, which is capable of delivering water flow of 3.2×10^{-3} m^3/s (50 GPM) at a 340 kPa (50 psi) pressure head. A heat exchanger was used to maintain the water temperature at 21.1 ±0.3 °C (70 ± 0.5°C), and a ditigal thermometer mounted just downstream of the test section was used to record the water temperature.

Measurements were made at a bulk flow near the maximum capacity of the flow loop. Although the bulk flow rate was kept constant during each test, it was not possible to ensure exactly the same flow rate on different days. To correct for this, an electromagnetic flowmeter was mounted in-line and downstream of the test section, calibrated by a static weigh technique, and used to normalize the velocity measurements in terms of the bulk flow velocity.

To insure a fully developed incoming pipe flow, a straight pipe about 118 diameters long was installed upstream of the test section with a cross-shaped swirl-removing flow straightener at the pipe entrance and another one 12 diameters downstream of the entrance.

The test section used is shown in Fig. 1 along with the vortex shedding strut. This test section allows easy installation of the strut and has glass sides for the laser beams to enter and the scattered light to exit. The strut is installed inside a thin-walled (3 mm) glass tube having a 52.1 mm (2.067 in.) inside diameter, which is equal to the inside diameter of the stainless steel pipe upstream. The tube and strut assembly is housed within a stainless steel box of square cross-section with opposite sides made of 19 mm thick glass, which is thick enough to contain the water pressure. To reduce the effects from the different indices of refraction of the media on either side of the curved tube walls, small slits at the upstream end of the glass tube are provided so that the region between the tube and the box fills with the loop water. The downstream end of the glass tube is mounted with a gasket so that flow leakage through the surrounding region is minimized. The useful length of the test section is 60 cm (24 in.).

The instantaneous point velocity measurements were made with a laser-Doppler velocimeter (LDV). The LDV consists of

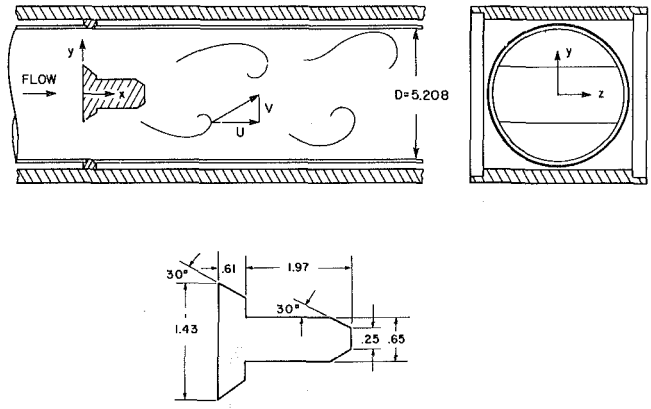

Fig. 1 Test section and test strut. Dimensions are in millimeters.

a 2-watt argon-ion laser and TSI Inc.[1] optics and frequency-tracking signal processors. It is equipped with Bragg-cell frequency shifters and so is capable of measuring very low velocites with flow reversals, including the transverse velocity component, which had a mean equal to zero at the center of the pipe. The 514.5 nm (green) beam from the laser was used at a total (multicolor) power of 250 mW, and lenses with a 250 mm focal length were used in the dual-beam forward-scatter mode, which gives a measuring volume of about 1.5 mm × 0.15 mm. At the highest velocity measured, the LDV tracker validated at least 120,000 particles per second in unseeded tap water that was filtered with a 10 micron filter.

The laser is mounted on a granite slab, and the remaining optical components are mounted on a three-dimensional dovetail-slide traversing mechanism mounted on the slab. This allows continuous movement of the measuring volume along each of the three perpendicular coordinate axes with a resolution of 5 μm. Positioning of the measuring volume at any point in the test section is accomplished by three computer-controlled stepping motors, which move the dovetail slides. The light beam is directed from the stationary source to the movable LDV optics by a mirror system that maitains the beam path parallel to the dovetail slides.

Before the LDV could be used correctly, the position of the measuring volume inside the pipe and the spacing of the fringes had to be determined. The bending of light beams, due to differences in the indices of refraction of the water and the curved glass, changes both the position of the beam crossing point and the angle between the beams, and hence the fringe spacing. These effects were studied both experimentally and theoretically using Snell's law. Although the equations are nonlinear in form, the final result was an approximately linear relation for predicting the position of the measuring point inside the round glass tube. This relation is the same as the well known one that would apply if the glass were not curved. Also the theory predicted that the fringe spacing would be approximately constant for both longitudinal and transverse velocities. Both approximations were fairly good for most of the pipe cross section, except near the uppermost and lowermost parts of the cross section, where the laser beams were far from perpendicular to the pipe walls.

The theoretical predictions were checked experimentally with a calibration device, which used a No. 28 (0.35 mm diameter) Chromel C wire inside the water filled pipe. The wire travelled longitudinally at a constant velocity parallel to the pipe axis. A photo detector, which measured the time required for a point on the wire to travel a known distance, was used to determine the wire speed. The calibration wire

[1] Manufacturer's names and model numbers are cited only to give a complete description of the instruments used. Their use is not to be construed as an endorsement or recommendation.

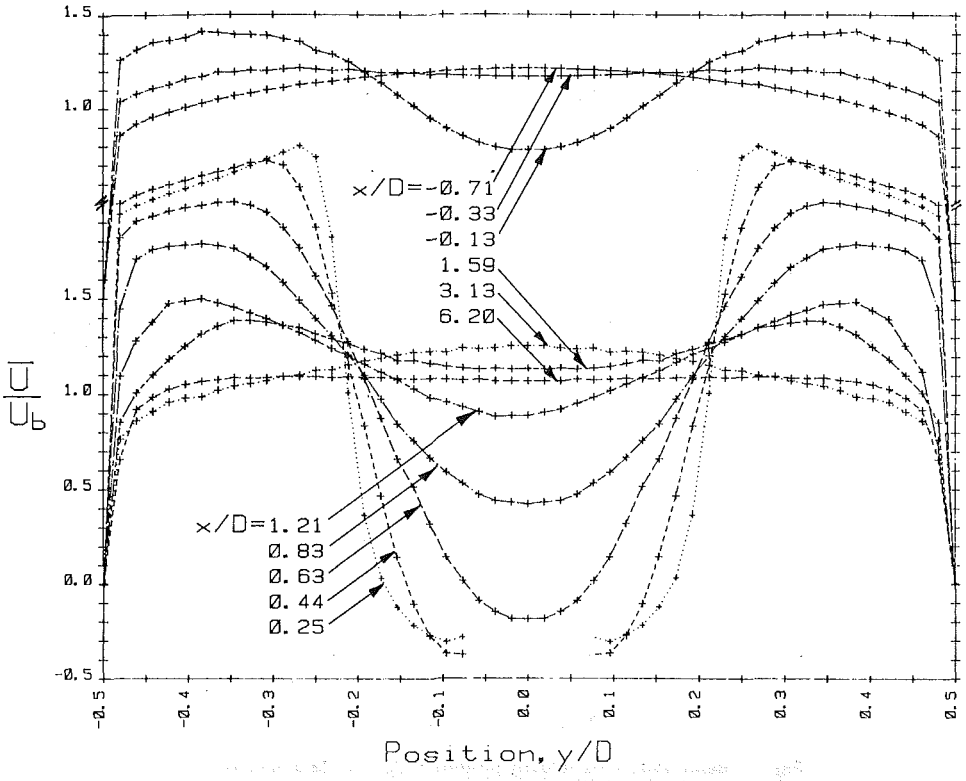

Fig. 2 Mean axial velocity profiles $\bar{U}/U_b$. Note that the top three curves have a different scale than the others. The data presented for y < 0 were obtained from data measured for y > 0. (Uncertainty in x/D = + .02, in y/D = ± .01 and in $\bar{U}/U_b$ = ± .01 $\bar{U}/U_b$ for $|\bar{U}/U_b| > \bar{I}$ and ± .01 for $|\bar{U}/U_b| < 1$)

could be moved to any position in the pipe cross section by two stepping motors interfaced to the same computer that operates the LDV system. The calibration system confirmed the predictions of the approximate theory to the expected uncertainty. Throughout most of the pipe, the nonlinearity of the position was smaller than the length of the measuring volume and the variation in the fringe spacing for the longitudinal velocity was less than 0.5 percent.

Another effect is due to the nonuniformity of the fringe spacing that occurs in a dual bean LDV when the beam waist does not coincide with the beam-crossing point, as mentioned by Hanson [6]. When the fringe spacing is not uniform across the measuring volume, the Doppler frequency will be broadened giving rise to an apparent velocity fluctuation which is not real. The effect can be reduced by using a collimator to make the beam waist occur at the beam crossing point. However, the adjustment cannot be done perfectly for all positions of the measuring volume when the latter is traversed while the laser remains stationary. This is true because the waist is located at a fixed optical path distance from the laser while the cross point is located at a fixed distance from the focusing lens, which is traversed. Nevertheless, a traveling distance of plus or minus 15 cm results in a fringe variation of less than plus or minus 0.5 percent provided the waist coincides with the crossing point at the center of the test section. This gives a sufficiently uniform fringe spacing for the entire test region.

A computer-controlled digital voltmeter measures the mean voltage from the tracker while a digital signal processor (DSP) analyzes the unsteady fluctuations. The DSP digitizes and computes the power spectral density of a block of 1024 12-bit measurements. Twenty-five of these spectra are averaged for each spatial point.

Results and Discussion

The nominal bulk flow velocty was U_b = 175 cm/s, which corresponds to a pipe Reynolds number of 90,000, a fundamental frequency f_1 of 26 Hz, and a Strouhal number $f_1 D/U_b$ of 0.744. Unless specified, velocities and lengths are normalized by the area averaged or bulk mean velocity U_b and the pipe diameter D, respectively. All data except where specifically stated are from locations on the diametral symmetry plane (z = 0) that is perpendicular to the span of the strut (see Fig. 1). Profiles of the longitudinal and transverse, mean and periodic velocities were measured at axial locations x/D = −0.71, −0.33, −0.13, 0.25, 0.44, 0.63, 0.83, 1.21, 1.59, 3.13, and 6.20 with data taken at 1 mm increments along the tube diameter (y axis). In view of the symmetry or antisymmetry of the velocities about y = 0, which was verified, most of the data were collected on only half the diameter with $y \geq 0$. The symmetry or antisymmetry was used to extend the graphs to $y < 0$ so they will be more easily understood.

Mean Velocity Components. The mean velocities, $\bar{U}$ and $\bar{V}$ were measured by connecting the LDV signals from the tracker directly to a ditigal voltmeter. The computer averaged 1500 of these voltage measurements, which required a total time of about two minutes, for each spatial point.

The distributions of the normalized mean axial and transverse velocity components are shown in Figs. 2 and 3, respectively. The values of $\bar{V}$ for three profiles (at x/D = −.71, 3.13, and 6.20) all have magnitudes smaller than 0.04 U_b and hence are not shown in Fig. 3 in order to keep the figure clear.

As the flow approaches the upstream face of the strut, the mean longitudinal velocity $\bar{U}$, as expected, decreases at the

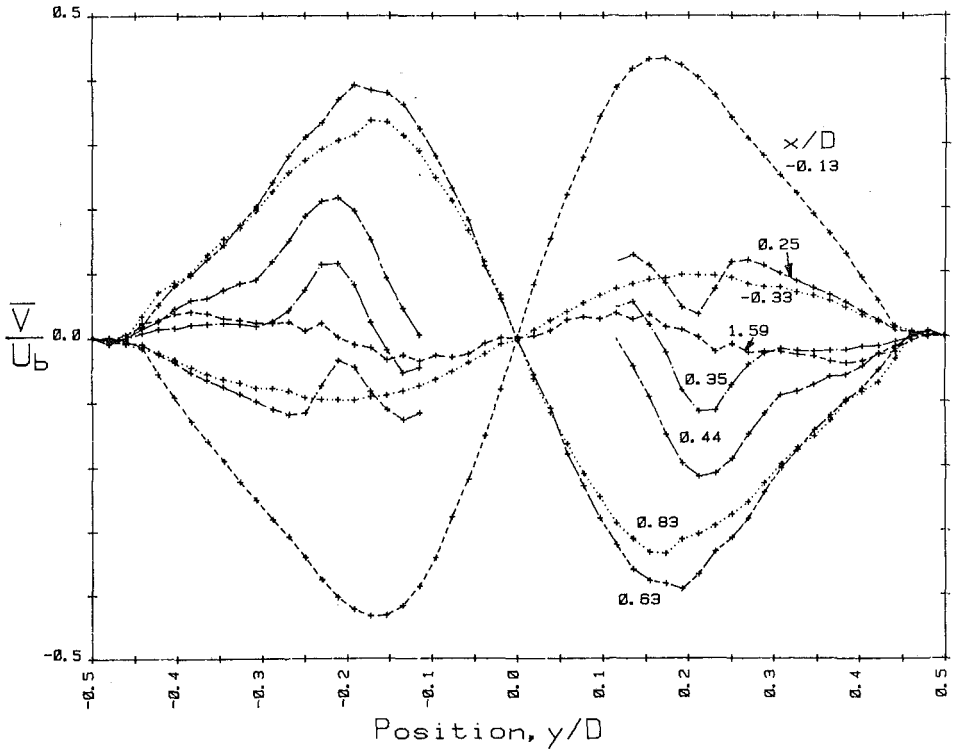

Fig. 3 Mean transverse velocity profiles $\bar{V}/U_b$. The data presented for $y < 0$ were obtained from data measured for $y > 0$. (Uncertainty in $x/D = \pm 0.02$, in $y/D = \pm .01$ and in $V/U_b = \pm .01$)

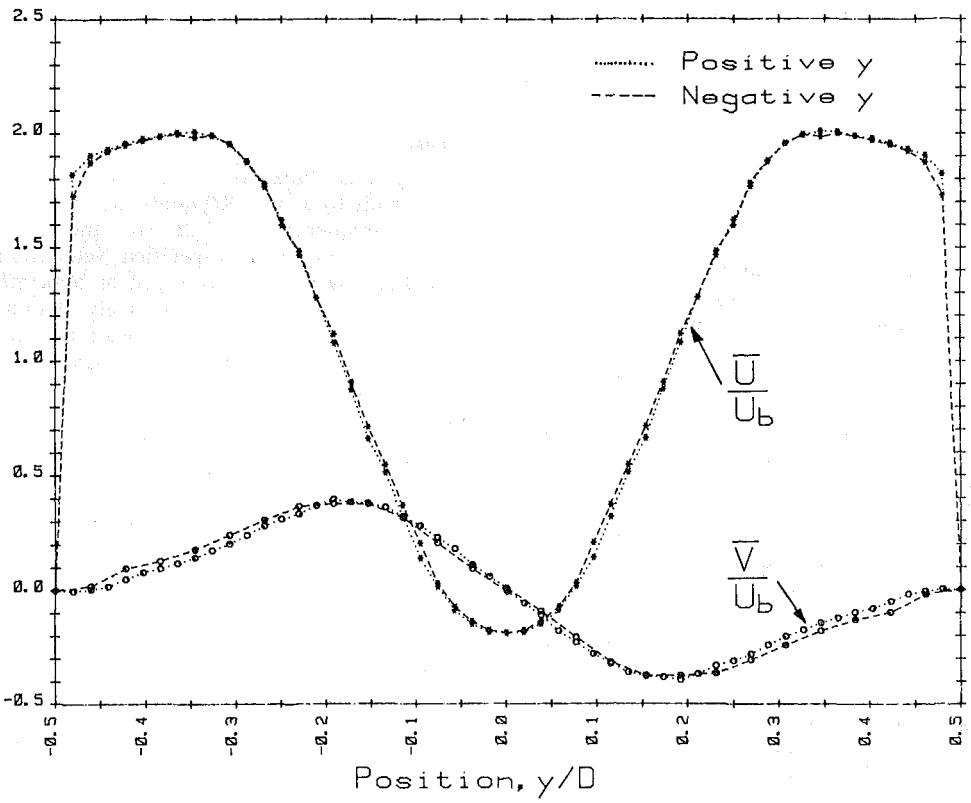

Fig. 4 Comparison of the mean velocity profile between positive and negative y at $x/D = 0.63$. (Uncertainty in $y/D = \pm .01$, in $\bar{U}/U_b = \pm .01$ $\bar{U}/U_b$ for $\bar{U}/U_b > 1$ and $\pm .01$ for $\bar{U}/U_b < 1$, and in $\bar{V}/U_b = \pm .01$)

center ($y = 0$) and increases along each side. The mean transverse velocity profile $\bar{V}$ is antisymmetric about $y = 0$ with a zero value on the walls at $y/D = \pm 0.5$ and has a positive maximum in the region of positive y. This indicates that the flow divides into two equal streams, one on either side of the strut. The magnitude of $\bar{V}$ gets larger and the division

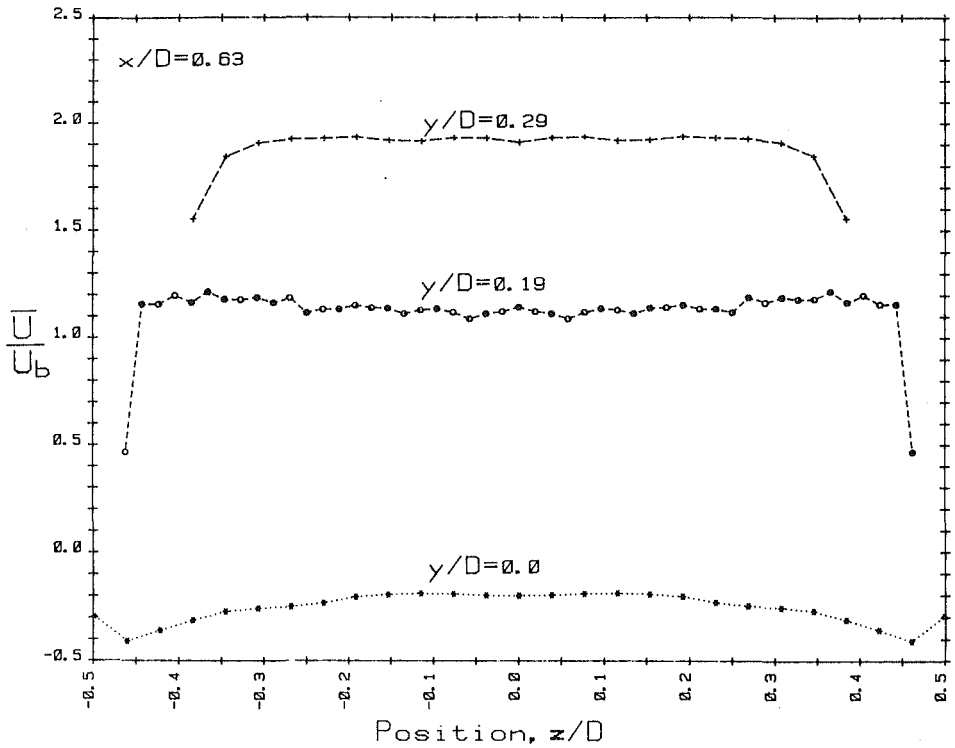

Fig. 5 Profiles of $\bar{U}/U_b$ along the span of the strut at $x/D = 0.63$. The data presented for $z < 0$ were obtained from data measured for $z > 0$. (Uncertainty in $x/D = \pm .02$, in $y/D = \pm .02$, in $z/D = \pm .02$, and in $\bar{U}/U_b = \pm .01\ \bar{U}/\bar{U}_b$ for $\bar{U}/U_b > 1$ and $\pm .01$ for $|\bar{U}/U_b| > 1$).

becomes more apparent as the flow approaches the upstream face of the strut.

As the flow passes the front surface and moves along the side of the strut, there is a shear layer where a large transverse gradient of $\bar{U}$ occurs. This layer separates two flow regions, the outer flow region, $|y|/D \gtrsim 0.2$, which has high speed flow, and the inner wake region, $|y|/D \lesssim 0.2$, which has low speed and even reverse flow. On either side of the splitter plate (i.e., for $0.25 < x/D < 0.44$) in the outer region, $\bar{U}/U_b$ maintains a value of about 2, independent of x and roughly independent of y. In this region, as expected, the rate of divergence of the outer flow away from the strut decreases, and as x increases the outer flow then converges back toward the strut. In the range $0.25 < x/D < 0.35$, the profile of $\bar{V}/U_b$ near the shear layer has two maxima for positive y and two for negative y. And, as expected from the incompressible condition, the $\bar{U}/U_b$ curves for $x/D = 0.25$ and 0.44 intersect near local maxima or minima of the $\bar{V}/U_b$ curves. In general $\partial\bar{V}/\partial y > 0$ where $\partial\bar{U}/\partial x < 0$ and vice versa as expected since $\partial\bar{W}/\partial x$ vanishes everywhere at the $z = 0$ plane where the measurements were made. The intersections occur where all three derivatives are zero.

The shear layer grows in width and slowly moves outward as it travels downstream. Downstream of the strut for $x/D > 0.5$, the mean velocity $\bar{U}$ increases in the inner wake region and decreases in the outer flow region. Immediately downstream of the strut at $x/D = 0.63$, the mean velocity $\bar{U}$ is still negative near the center region. Also, in the region $\bar{V}$ reaches its maximum converging magnitude, and the convergence decreases as x increases downstream. For $x/D > 0.83$, the mean velocity $\bar{U}$ is positive everyhere, the transverse gradient of $\bar{U}$ becomes smaller, and the shear layer is no longer very visible. At the largest values of x/D, the mean velocity profiles begin to return to their upstream fully-developed condition.

To check the symmetry, measurements for both positive and negative y were made. A typical comparison of the mean velocity at $x/D = 0.63$ for both positive and negative y is shown in Fig. 4. This shows that $\bar{U}$ is indeed quite symmetric and $\bar{V}$ is quite antisymmetric. Data obtained at other axial locations show similar results.

Profiles along the z-direction were also measured to investigate the homogeneity of the flow field along the span of the shedding strut. Figure 5 shows the profiles of $\bar{U}/U_b$ along z for $x/D = 0.63$ at $y/D = 0$, 0.19, and 0.29. The data indicate that the flow field is approximately two-dimensional and uniform along the z-axis and that the effects of the circular boundary condition may be neglected in a first approximation. Similar results were obtained at $x/D = 0.44$ and 0.25 for the same three values of y/D.

Figure 6 shows the profiles of $\bar{U}$ and $\bar{V}$ at the two extreme locations, one far upstream at $x/D = -0.71$, and one far downstream at $x/D = 6.20$. For comparison, the velocity was normalized by the center line velocity $\bar{U}_0$, and an 1/8 power law profile was also included. At $x/D = -0.71$, the velocity profile of $\bar{U}/\bar{U}_0$ was approximately fully developed, having a 1/8 power law. On the other hand, at the farthest downstream location ($x/D = 6.20$), the longitudinal velocity profile $\bar{U}$ has not yet returned to the fully developed shape. However, at both positions, $\bar{V}$ appears negligibly small.

The mean-velocity vector field is easily generated using the velocities $\bar{U}$ and $\bar{V}$ shown in Figs. 2 and 3. The result is shown in Fig. 7, which clearly shows the flow division and the flow reversal. On careful examination, vortices in the mean velocity field can be seen on either side of the splitter plate. These mean vortices are an artifact of the averaging; there are no steady vortices in the full time-dependent velocity field.

Since the mean flow field is approximately two-dimensional and uniform along the span of the strut, a stream function can be defined. The two-dimensionality is a particularly good approximation at the plane of symmetry $z = 0$, where the measurements were made. The stream function $\psi(x,y)$ for this

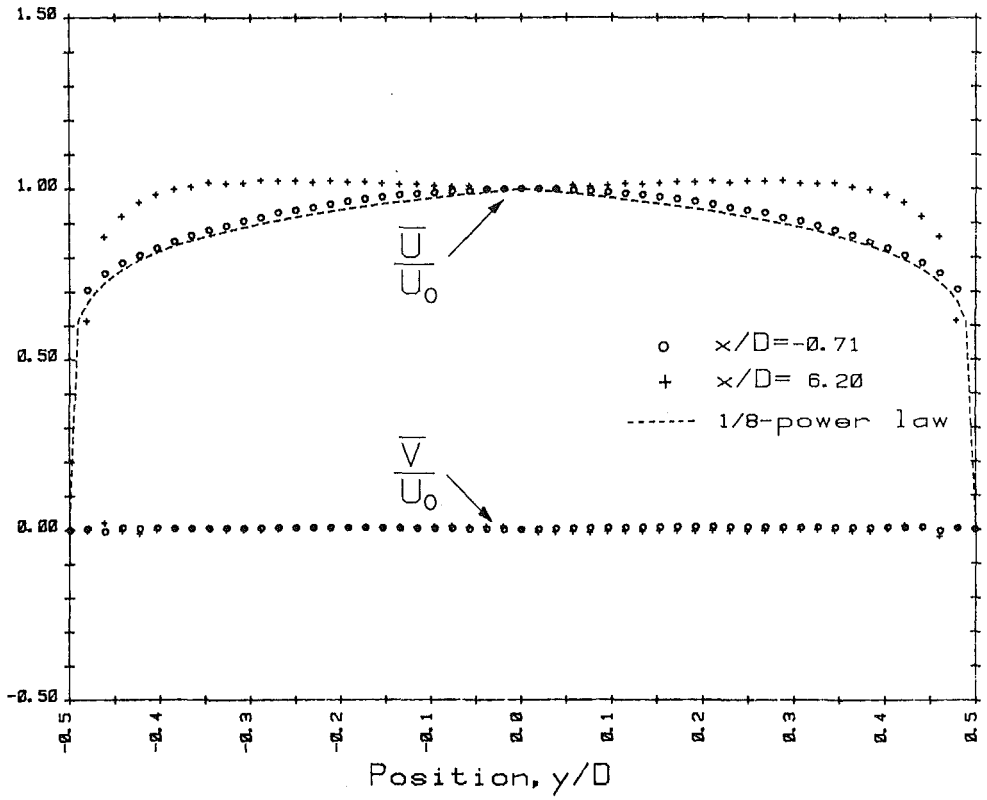

Fig. 6 Mean velocity profiles at two extreme axial locations compared with a 1/8 power law. The data presented for $y < 0$ were obtained from data measured for $y > 0$. (Uncertainly in $x/D = \pm .02$, in $y/D = \pm .01$, in $\bar{U}/\bar{U}_0 \pm .01$, and in $\bar{V}/\bar{U}_0 = \pm .01$)

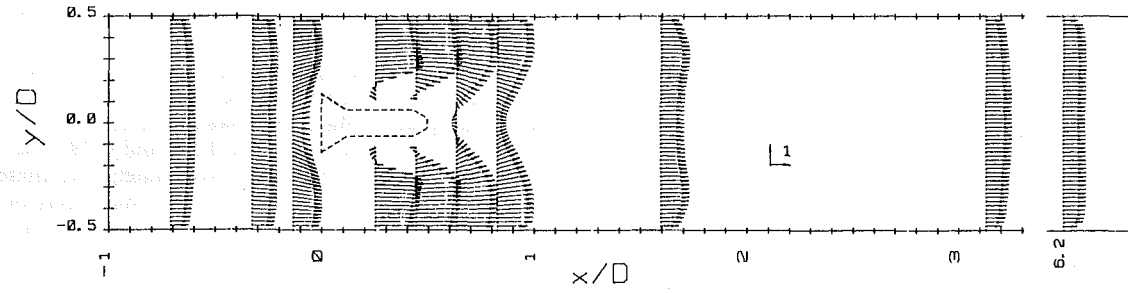

Fig. 7 Mean velocity vectors. The time averaging makes the field symmetric. (Uncertainty in $x/D = \pm .02$, in $y/D = \pm .01$, in $|U| = \pm .01$ $|U|$ for $|U| > 1$ and $\pm .01$ for $|U| < 1$, where $|U|$ = mean velocity magnitude/U_b. The arrows indicate $|U| = 1$)

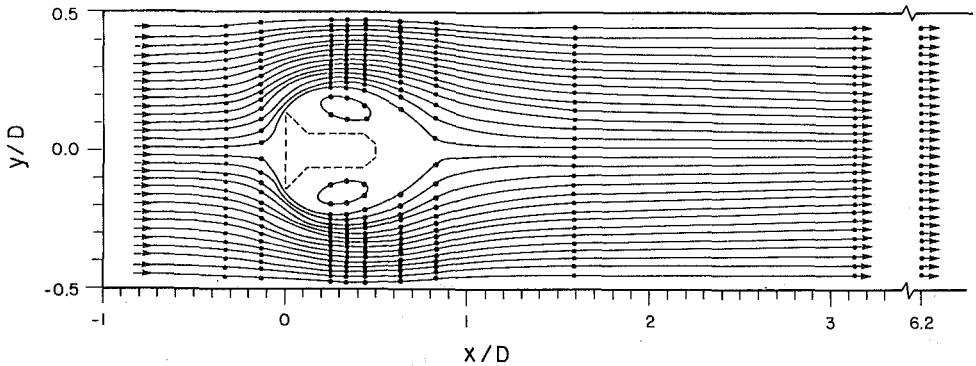

Fig. 8 Mean flow streamlines. The time averaging makes them symmetric. (Uncertainty of each point in $x/D = \pm .02$, and in $y/D = \pm .01$ and the curves drawn freehand)

incompressible flow is defined to satisfy $\bar{U} = \partial\psi/\partial y$ and $\bar{V} = -\partial\psi/\partial x$. By using the incompressibility condition, one can easily see that

$$\psi(x,y) = \int_{-D/2}^{y} \bar{U}(x,y')\,dy'.$$

satisfies both of the previous equations. The mean streamlines of Fig. 8 are constructed with this formula. At each value of x for which data is available, the integral is computed for $y = D/2$ and divided by 31 to get $\Delta\psi = \psi(x, D/2)/31$. Then the value of y is found for which the integral equals $n\Delta\psi$ for $n =$ 1 to 30. For a given n, each such point for a given x is connected to the corresponding point for the next x by a smooth curve drawn freehand. This is not possible for the groups of six points on each side of the splitter plate, they do not connect to points upstream or downstream of the strut. The streamline that runs from upstream, then below the strut almost touching it, and finally continues downstream has $n =$ 15, and the opposite streamline above the strut has $n = 16$. On the other hand the six points immediately below the strut have $n = 16$, and the six above have $n = 15$. Thus the group of six points below the splitter plate must form one closed streamline, and the six above, another. With a finer resolution than 1/31, more concentric, close streamlines are found on either side of the splitter plate, with reverse flow extending down to about $x/D = 0.8$. These are the mean vortices mentioned previously.

The streamlines clearly show the flow pattern around the shedding strut as discussed before. However, it now appears as if the mean vortices act like additional obstacles or blockages to the flow that push the incoming outer flows away from the strut.

Time-Dependent Velocity Components. At the same time the steady velocity components were measured, the time-dependent velocity components were obtained. The analog signal from the tracker was connected to the digital signal processor, which computed the power spectral density (psd) of the velocity. A maximum frequency of 100 Hz was selected for most of the analysis. This corresponds to a frequency resolution or bin size of 0.25 Hz, a sampling frequency of 256 Hz, a sampling time interval of 3.91 ms, and a real time window of 4 seconds. Twenty-five of these individual spectra

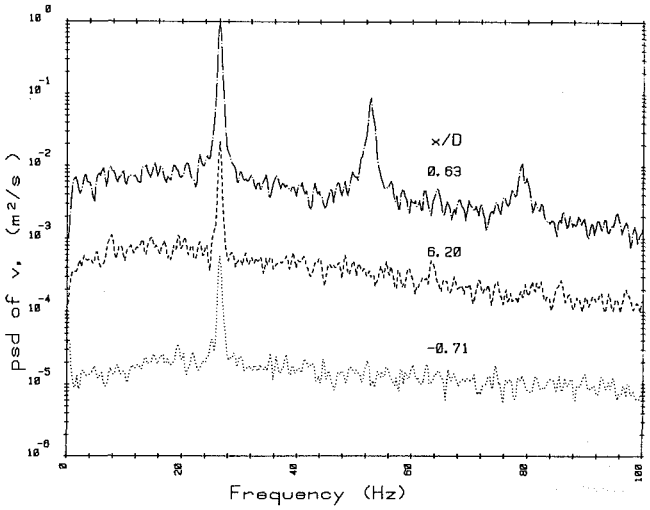

Fig. 9 Typical power spectral density of the fluctuating transverse velocity. (Uncertainty in $v^2 = \pm .02\,v^2$, in frequency = ± .1 Hz, and in $x/D = \pm .02$)

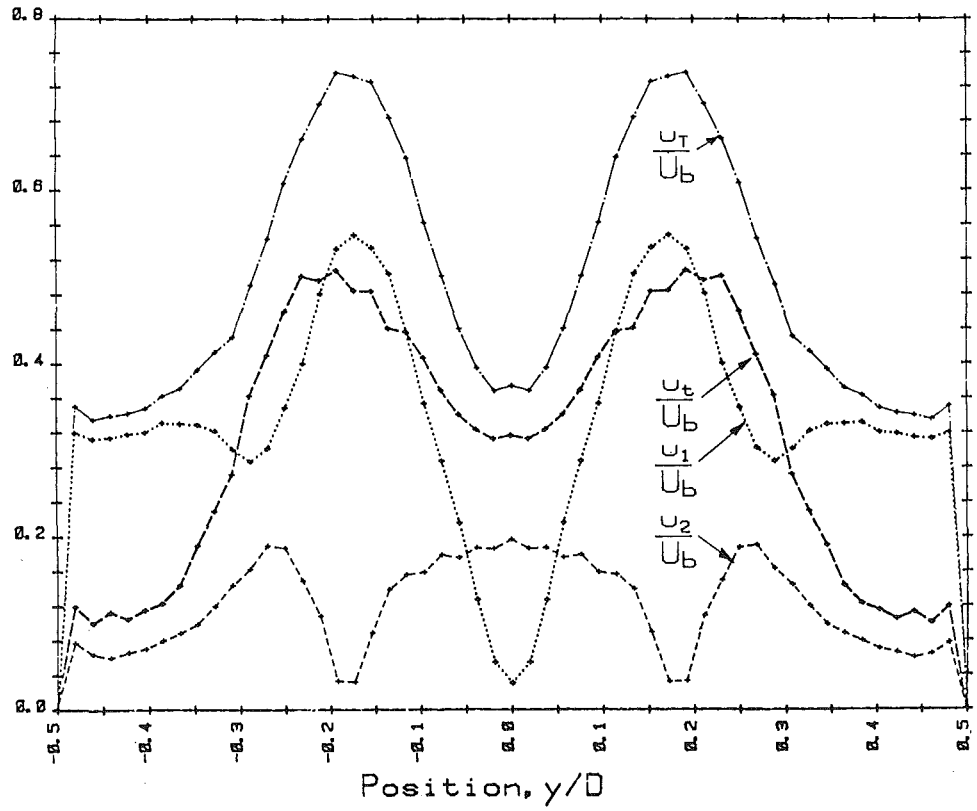

Fig. 10 Normalized profiles of the magnitudes of the unsteady velocity components at $x/D = 0.63$. The data presented for $y < 0$ were obtained from data measured for $y > 0$. (Uncertainty in $y/D = \pm .01$, and in $u/U_b = \pm .02\,u/U_b$ for $u/U_b > .01$ and $\pm .002$ for $u/U_b < .1$)

were averaged to obtain the power spectral density. From time to time during the test, different maxima frequencies were also used for examining the velocity spectral contents, but the 100 Hz range was found to reveal the most information of interest.

Figure 9 was the power spectral density of the transverse velocity component at three locations. As expected, the spectra clearly exhibit amplitude peaks around the fundamental frequency (27 Hz) and its harmonics. The non-zero width of these peaks indicates that the velocity signals are not perfectly periodic. This is the "vortex wandering" or phase jitter that occurs at high Reynolds number flow, as discussed by Baker, et al. [3], and by Perry and Watmuff [4].

The energies contained in the different periodic velocity components at each measuring position are obtained from the power spectal density. The area under the peak at a given frequency gives the amplitude at that frequency once the random signal is subtracted out. The number of frequency bins used for computing the area is 21, which corresponds to a 5.25 Hz total bandwidth. In general the periodic components of both U and V consist predominantly of the first two harmonic terms. Usually, no higher harmonic was detected, with the exception of a very small third harmonic velocity at a few places. The uppermost curve in Fig. 9 is a worst case in which the third harmonic is as large as it ever gets. In all cases the third and higher harmonics had less than one percent of the energy of the lower harmonics. The first two harmonics are apparently sufficient to characterize vortex shedding flow, and the second harmonic is usually much smaller than the fundamental.

The total kinetic energy was determined from the total area under the entire spectrum up to 100 Hz, and the random turbulent energy was obtained by subtracting the sum of the energy of the two periodic velocity terms from the total energy. The root mean square value determined from the energy contained in each velocity component was interpreted as the amplitude of that velocity term.

For comparison, the profiles of the magnitudes of the time-dependent velocity components u_1, u_2, u_t, and u_T, all normalized by the bulk mean velocity U_b, are shown in Fig. 10 at $x/D = 0.63$ just downstream of the strut. Here u_1, u_t, and u_T show maxima at the shear layer regions and a minimum at the center ($y = 0$), while the second harmonic u_2 shows a maximum at the center and minima in the shear layers.

The turbulence intensity profiles u_t and v_t at the two extreme axial locations with $x/D = -0.71$ and 6.20 are shown in Fig. 11. The turbulence intensities obtained by Laufer [7] in fully developed pipe flow are also presented for comparison. The velocities are normalized by the center mean velocity $\bar{U}_0$. At $x/D = -0.71$ upstream of the strut, $u_t/\bar{U}_0$ is fairly close to, and $v_t/\bar{U}_0$ is somewhat lower than Lauafer's. At $x/D = 6.20$, both $u_t/\bar{U}_0$ and $v_t/\bar{U}_0$ are much larger than upstream. Like the mean velocity profiles shown in Fig. 6, the turbulence intensities indicate again that the upstream flow is fully developed, and the downstream flow is still in a state of highly turbulent mixing and not yet returned to the upstream condition, even at $x/D = 6.20$.

The velocity distributions of the total fluctuations u_T and v_T, the fundamental components u_1 and v_1, the second harmomics u_2 and v_2, and the turbulence intensities u_t and v_t, all normalized by the mean bulk velocity U_b, are given on Figs. 12, 13, 14, and 15, respectively. In each figure, (*a*) is the axial component, and (*b*) is the transverse component. A discussion of the unsteady velocity components is given below.

At $x/D = -0.71$, the influence of the obstacle is minimal, with turbulence intensity profiles close to values typical of a fully-developed turbulent pipe flow, and very little periodic

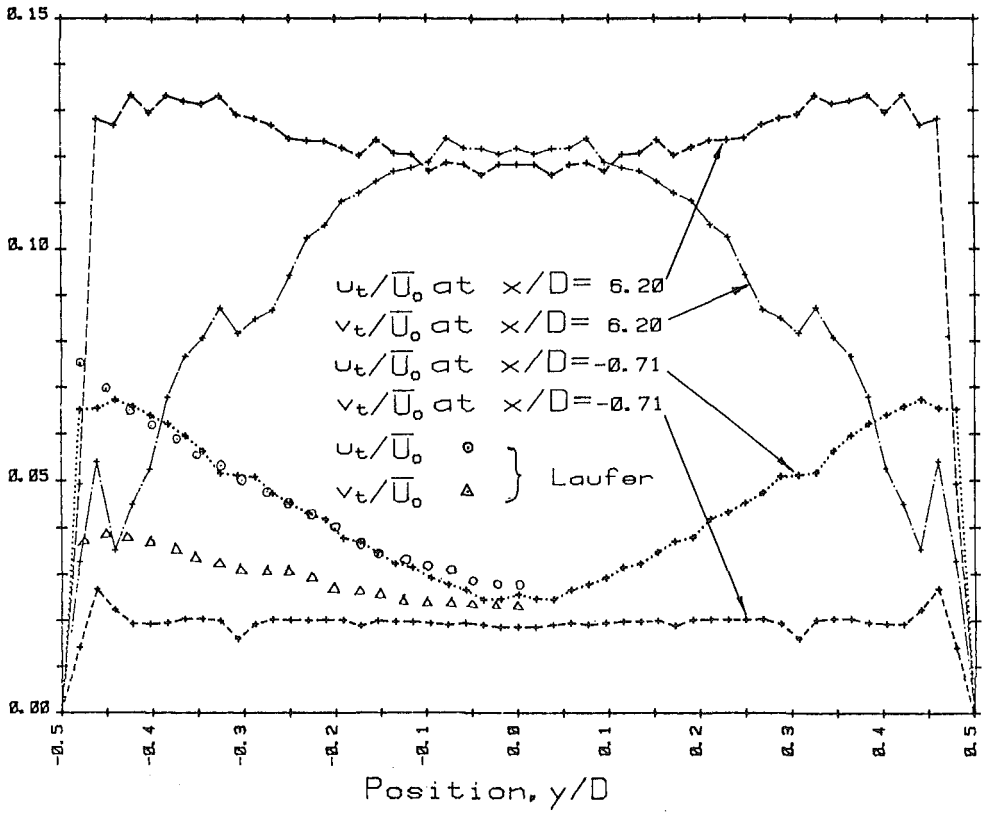

Fig. 11 Normalized turbulence intensity profiles at two extreme locations. The data presented for $y < 0$ were obtained from data measured for $y > 0$. (Uncertainty in $y/D = \pm .01$, and in $u_t/U_0 = \pm .02$ u_t/U_0 for $u_t/U_0 > .1$ and $\pm .002$ for $u_t/U_0 < .1$)

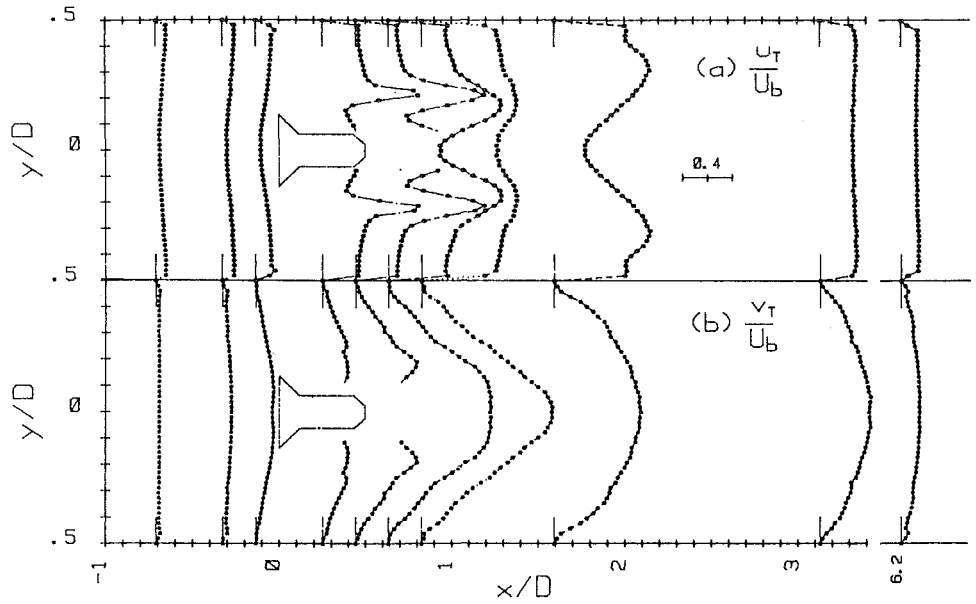

Fig. 12 Normalized total-fluctuating-velocity magnitude profiles. The data presented for $y < 0$ were obtained from data measured for $y > 0$. The bar indicates a change of .4 in u_T/U_b or v_T/U_b. (Uncertainty in $x/D = \pm .02$, in $y/D = \pm .01$ and in $u_T/U_b = \pm .02\, u_T/U_b$ for $u_T/U_b > .1$ and $\pm .002$ for $u_T/U_b < .1$. Same uncertainty for v_T/U_b)

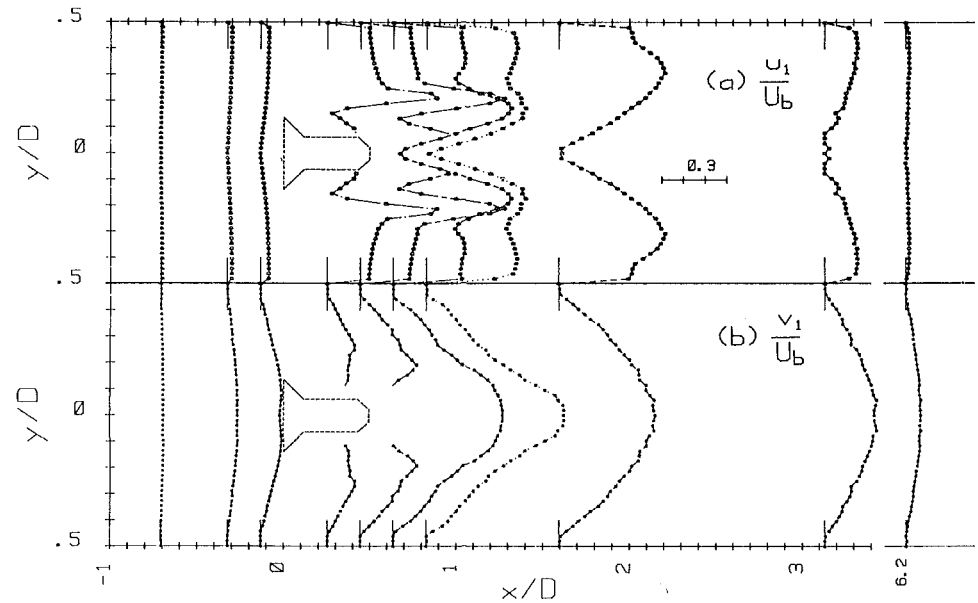

Fig. 13 Normalized fundamental-frequency velocity-component magnitude profiles. The data presented for $y < 0$ were obtained from data measured for $y > 0$. The bar indicates a change of .3 in u_1/U_b or v_1/U_b. (Uncertainty in $x/D = \pm .02$, in $y/D = \pm .01$, and in $u_1/U_b = \pm .02\, u_1/U_b$ uncertainty in v_1/U_b)

velocity is seen. As the flow approaches the upstream face of the strut (i.e., at $x/D = 0.33$ and 0.13), the fundamental velocity components become more visible although they are still small in magnitude. The second harmonics are negligibly small upstream of the strut.

As expected, just downstream of the front face of the strut, large periodic and turbulence terms are observed. At $x/D = 0.25$ and 0.44, all these unsteady terms take on large values in a narrow transverse region apparently close to the shear layer where a large mean velocity gradient exists and large turbulence is created. In this region, the magnitudes and gradients of the axial components are significantly larger than those of the transverse components. All unsteady axial components exhibit both a maximum and minimum on each side of the strut, while the unsteady transverse components show only one local maximum there. At $x/D = 0.63$ just downstream of the strut, all terms are similar to those at the previous station except the shear layer diffuses, the velocity gradient decreases, and the two wakes, one from each side of the strut, begin to merge. The axial components u_1, u_t and u_T show a minimum at the center of the pipe, while the transverse terms v_1, v_t and v_T exhibit a maximum there. On the other

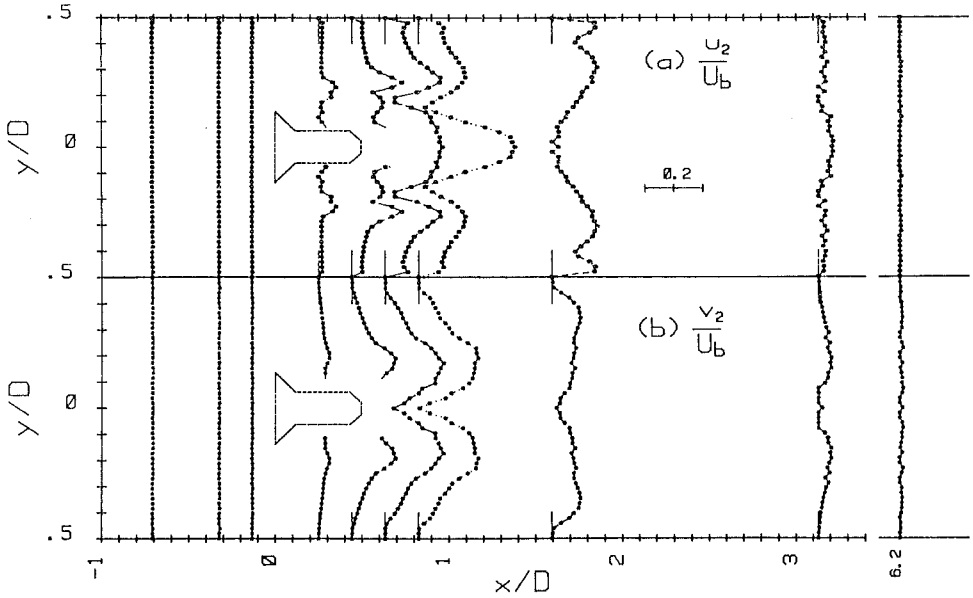

Fig. 14 Normalized second-harmonic velocity-component magnitude profiles. The data presented for $y < 0$ were obtained from data measured for $y > 0$. The bar indicates a change of .2 in u_2/U_b or v_2/U_b. (Uncertainty in $x/D = \pm .02$, in $y/D - \pm .01$, and in $u_2/U_b = \pm .02$ u_2/U_b for $u_2/U_b > .1$ and $\pm .002$ for $u_2/U_b < .1$. Same uncertainty for v_2/U_b)

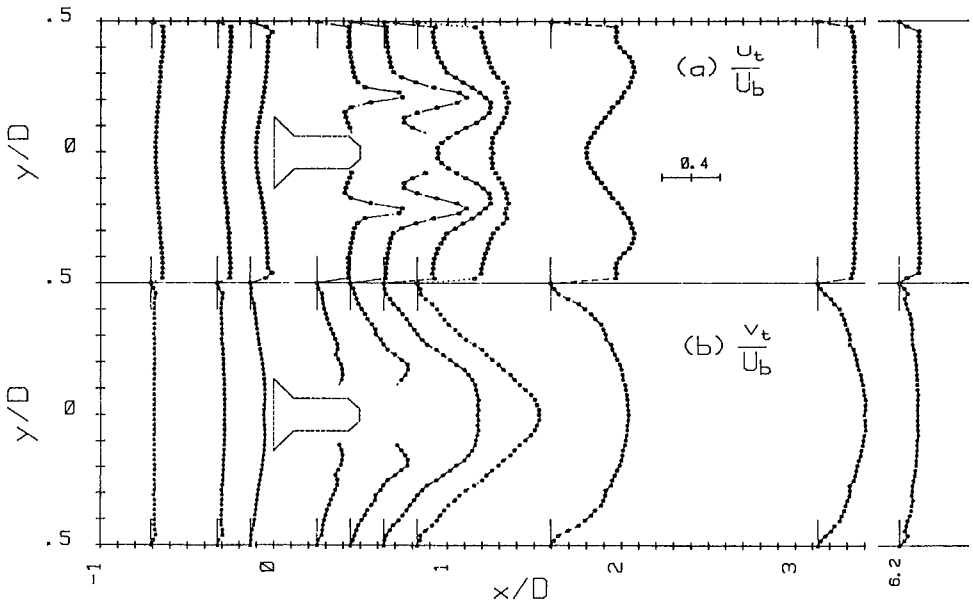

Fig. 15 Normalized turbulence-velocity component profiles. The data presented for $y < 0$ were obtained from data measured for $y > 0$. The bar indicates a change of .4 in u_t/U_b or v_t/U_b. (Uncertainty in $x/D = \pm .02$, in $y/D = \pm .01$, and in $u_t/U_b = \pm .02$ u_t/U_b for $u_t/U_b > .1$ and $\pm .002$ for $u_t/U_b < .1$. Same uncertainty for v_t/U_b)

hand, the axial component u_2 has a large value and the transverse v_2 shows a mimimum close to the center of the pipe.

The longitudinal velocity profiles downstream of the strut can be interpreted as follows. At the center of the pipe, vortices pass by on both sides, and they do so at twice the rate vortices are shed from one side alone. Thus vortices pass by at twice the fundamental frequency. Successive vortices rotate in opposite directions and pass by on opposite sides of the pipe. Thus their relative longitudinal velocities at the center of the pipe are always in the same direction (upstream). As a vortex passes by, the longitudinal velocities at the center of the pipe increases and decreases in time in the same way for all vortices, no matter on which side they pass. Hence, at the center of the pipe, u_1 must be zero, and u_2 must be nonzero.

To understand the transverse velocity profiles, consider the flow between adjacent vortices on opposite sides of the pipe. Because, these rotate in opposite directions, the transverse velocity due to the earlier vortex adds to that due to the later vortex. For the flow between the later vortex and the next one

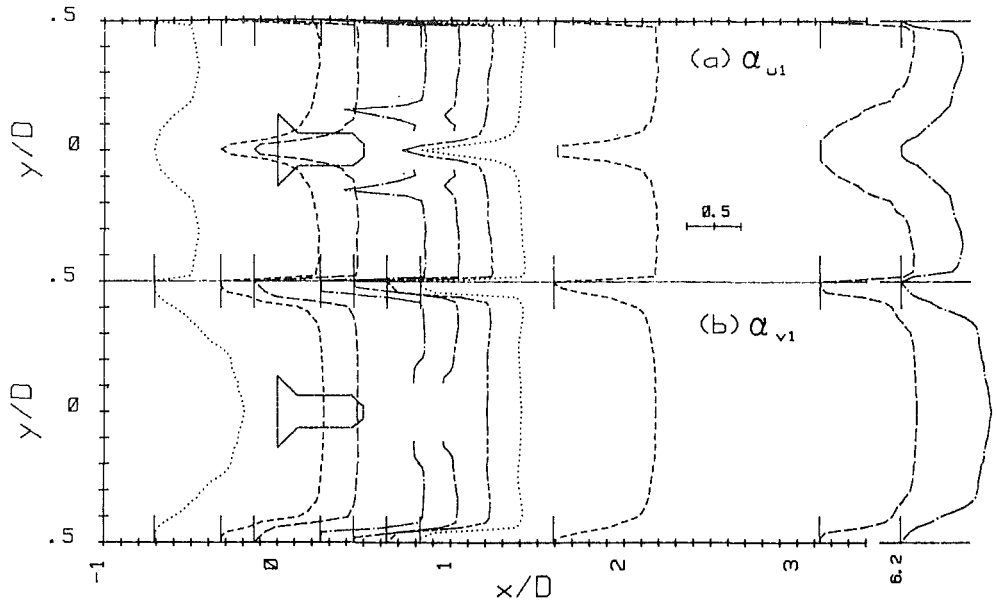

Fig. 16. Visibility profiles of the fundamental-frequency velocity components. The data presented for $y < 0$ were obtained from data measured for $y > 0$. The bar indicates a change of .5 in α. (Uncertainty in $x/D = \pm .02$, in $y/D = \pm .01$, and in $\alpha = \pm .05$ with $0 < \alpha < 1$ and the curves drawn freehand)

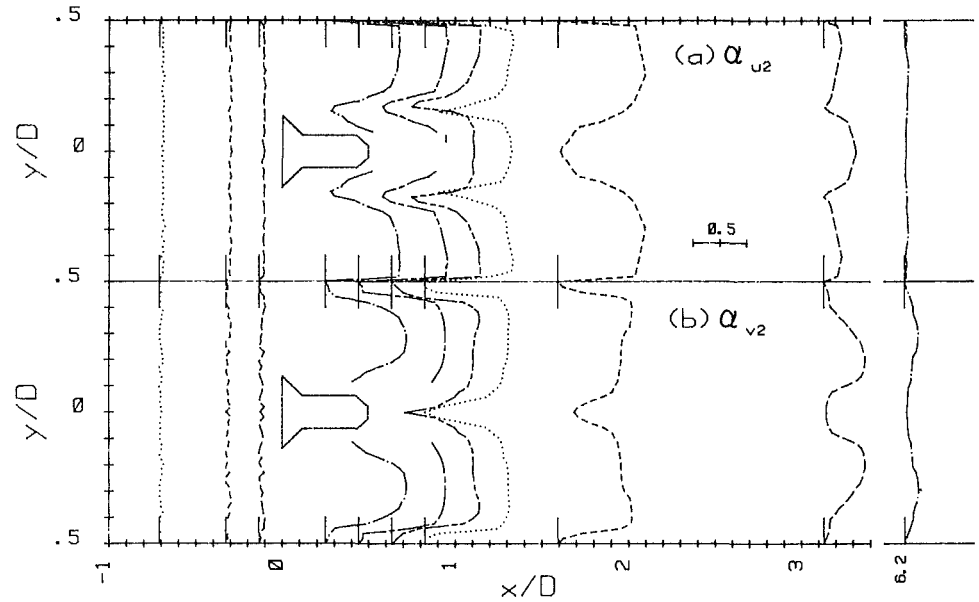

Fig. 17 Visibility profiles of the fundamental-frequency velocity components. The data presented for $y < 0$ were obtained from data measured for $y > 0$. The bar indicates a change of .5 in α. (Uncertainty in $x/D = \pm .02$, in $y/D = \pm .01$, and in $\alpha = \pm .05$ with $0 < \alpha < 1$) and the curves drawn freehand)

after it, the transverse velocity goes in the opposite direction. The cycle is completed with the next pair. Since pairs go by at the fundamental frequency, the reversing of the transverse velocity occurs at that rate, so v_1 must be nonzero. Also, since vortices on opposite sides of the pipe have equal strength, v_2 must be zero at the center of the pipe.

Near $x/D = 0.83$, the periodic velocity components reach their maximum and subsequently start to decay. For $x/D > 0.83$, the shear layers diffuse further with the periodic and turbulence components spreading out transversely. For $x/D > 1.59$, the random turbulent wake broadens to cover the width of the pipe and the turbulence level begins to return to its free stream value, although it is still much larger than it was upstream of the strut.

In addition to knowing the absolute values of the periodic velocities, it is sometimes useful to know their relative amplitudes with respect to a reference. For a given spatial direction, the visibility of a periodic velocity component is defined as the ratio of the energy of that component to the energy of the total velocity fluctuation contained in the same frequency band (5.25 Hz in this paper). As the name implies, the visibility gives an indication of how visible a periodic term

is. It is related to the signal-to-noise ratio of the vortex flow. This information is valuable for vortex flowmeter design.

The visibilities α_{u1}, α_{v1}, α_{u2}, and α_{v2}, of u_1, v_1, u_2, and v_2, respectively are shown in Figs. 16 and 17. Although the amplitudes of the fundamental terms in the region upstream of the strut are small as shown in Fig. 13, their visibilities α_{u1} and α_{v1} shown in Fig. 16 are very large. This occurs because the turbulent distrubance upstream of the strut is small. However, the visibilities of the second harmonic terms are very small everywhere upstream of the strut.

For $x/D > 0$, although the values of α_{u1} and α_{v1} decrease slightly as x/D increases for large x/D, these values are high throughout the test region, with the exception of small value of α_{u1} near the center of the pipe and at the two recirculation regions on each side of the strut. The value of α_{v1} normally shows a maximum near the center where α_{u1} has a minimum. In contrast to the fundamental component, α_{v2} shows a mimimum, and α_{u2} a maximum near the center, with the exception that α_{u2} shows a minimum at $x/D = 1.59$. Finally, for $x/D > 3.13$, the visibilities of the second periodic terms all diminish to a very small value.

Summary

In a high Reynolds number flow, the velocity field around a vortex shedding strut mounted in a circular pipe has been measured in detail with a laser Doppler velocimeter system. The velocity field consists of three components: mean, periodic, and random or turbulent. The mean velocity shows two recirculation eddies or vortices on either side of the splitter plate. These vortices are separated from the outer flow by thin shear layers, where large periodic and random components are produced. The periodic velocity consists predominantly of the first two harmonic terms with the fundamental being much larger than the second harmonic. No higher harmonic was observed with the exception of very small third harmonic velocity fields at a few places. Far downstream of the strut, the periodic terms evolve into highly turbulent motions that cover the entire pipe.

The visibility, defined as the ratio of the energy of a periodic component to the total fluctuation energy contained in the same narrow frequency band, is also graphed. The graphs show that the vortex shedding oscillations could be detected not only downstream of the strut, but also upstream of it. The visibility of the fundamental velocity component is very high in regions upstream of the strut, even though the periodic velocity amplitude is small there.

Acknowledgments

The authors would like to thank Mr. G. Paul Baumgarten for helping to design the test section and set up the apparatus.

References

1 Kovaszny, L. S. G., "Hot-Wire Investigation of the Wake Behind Cylinders at Low Reynolds Numbers," *Proc. Royal Society*, A198, 1949.

2 Durgin, W. W., and Karlson, S. K. F., "On the Phenomenon of Vortex Street Breakdown," *Journal of Fluid Mechanics*, Vol. 48, Part 3, 1971, pp. 507–527.

3 Baker, G. R., Barker, S. J., Bofah, K. K., and Saffman, P. G., "Laser Anemometer Measurements of Trailing Vortices in Water," *Journal of Fluid Mechanics*, Vol. 65, Part 2, 1974, pp. 325–336.

4 Perry, A. E., and Watmuff, J. H., "The Phase-Average Large-Scale Structures in Three-Dimensional Turbulent Wakes," *Journal of Fluid Mechanics*, Vol. 103, 1981, pp. 33–51.

5 Miller, R. W., DeCarlo, J. P., and Cullen, J. T., "A Vortex Flowmeter—Calibration Results and Application Experiences," *Proceedings of the Symposium on Flow in Open Channels and Closed Conduits* held at NBS, Gaithersburg, MD, Feb. 23–25, 1977, NBS Special Publication 484, pp. 549.

6 Hanson, S., "Broadening of the Measured Frequency Spectrum in a Differential Laser Anemometer Due to Interference Plane Gradients," *Journal of Phys. D: Applied Physics*, Vol. 6, 1973, pp. 164.

7 Laufer, J., "The Structure of Turbulence in Fully Developed Pipe Flow," NACA Report 1174, 1954.

Aerodynamic Studies on Swirled Coaxial Jets From Nozzles With Divergent Quarls

T. F. Dixon[1]
J. S. Truelove
T. F. Wall

Department of Chemical Engineering,
University of Newcastle, NSW. 2308,
Australia

The aerodynamic characteristics of strongly swirled coaxial jets issuing from a divergent nozzle into stagnant-air surroundings have been studied. Maps of the central reverse-flow zone and detailed measurements of mean velocity have been obtained in the region close to the exit of the nozzles and the effects of varying the level of swirl and the ratio of the momenta in the central and annular jets have been examined. The level of swirl and the momentum flux ratio are found to influence significantly the flow type and stability. The measurements are compared with calculations obtained by numerical solution of the time-averaged equations governing conservation of mass and momentum. The calculation procedure is also used to examine the effects of burner geometry and heat release on flow type.

1 Introduction

1.1 Flows in Swirl Burners. Swirl is often used in burners to control the mixing between fuel and hot combustion products, and consequently the heating of the fuel to its ignition temperature.

Early investigations [1, 2] at the International Flame Research Foundation (IFRF) on oil burners reported the formation of a swirl-induced central reverse-flow zone which could greatly enhance flame stability by recirculating hot combustion products to the root of the flame.

Later studies [3] at the IFRF on swirling natural gas flames identified the two flow types illustrated in Fig. 1: type 2 flows characterized by a large central reverse-flow zone and type 1 flows characterized by an annular zone of recirculation. Type 2 flows were observed at relatively low primary-gas velocities and gave short high-intensity flames, while type 1 flows were observed at high primary-gas velocities and gave long flames.

Swirl burners designed for pulverized coal have a higher proportion of the nozzle area occupied by the primary jet than oil and gas burners and although swirl is known to have a pronounced effect on burner and combustion performance [4], flow and mixing have not been examined in detail.

1.2 Present Investigation. The wide range of geometries for pulverized-coal burners is illustrated in Fig. 2. The present experimental and theoretical investigations examine in detail the aerodynamics of an unconfined air model of a typical brown-coal burner, the geometry of which is shown in the lower half of Fig. 2. In practice, the burner is confined in a furnace, however the expansion ratio of the burner in the furnace is typically five or more and so the use of an unconfined experiment to study the near-burner flow is justified.

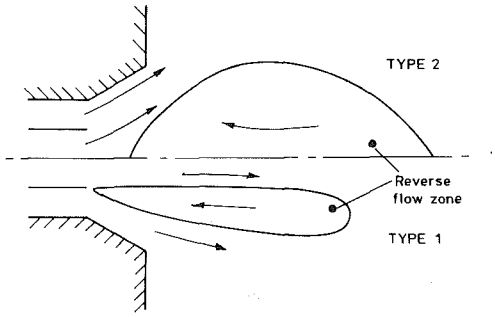

Fig. 1 Flow patterns for type 1 and type 2 flows

The measurements are intended to give an improved understanding of the aerodynamics of isothermal swirling flows and provide a basis for understanding the mechanism of flame stabilization in related combusting flows. In the theoretical investigation the measurements are used to evaluate a mathematical model for calculating turbulent flows. The calculation procedure is also used to examine the aerodynamics for a geometry typical of a black-coal burner, viz. lower primary-to-secondary radius ratio and quarl length-to-diameter ratio, and to examine the effect of operational variables on flow type.

2 Experimental Facility and Instrumentation

2.1 Model Burner. The experiments were conducted on a 1/9th-scale air model of a brown-coal burner with the experimental apparatus illustrated in Fig. 3. The scale factor fixed the diameter at the throat of the divergent quarl (D) at 102mm, the ratio of primary to secondary nozzle radii (R_p/R_s) at 0.68, the half-angle of the quarl at 30 deg, and the ratio of quarl length to throat diameter (L/D) at 1.0. Air was supplied to the burner nozzles by two centrifugal fans gated

[1] Presently, Sugar Research Institute, Mackay, Qld.4740, Australia.

Contributed by the Fluids Engineering Division for publication in the JOURNAL OF FLUIDS ENGINEERING. Manuscript received by the Fluids Engineering Division, February 24, 1982.

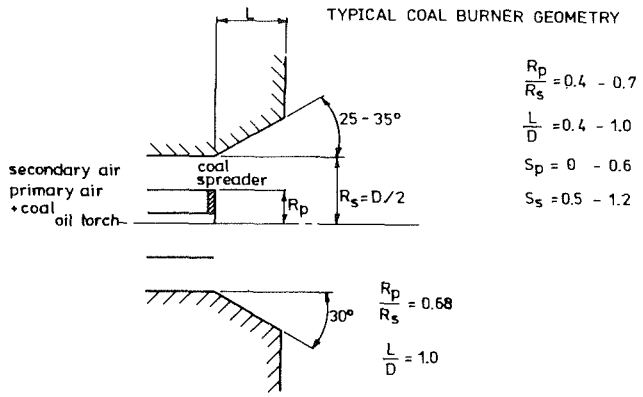

Fig. 2 Geometries for pulverized-coal burners

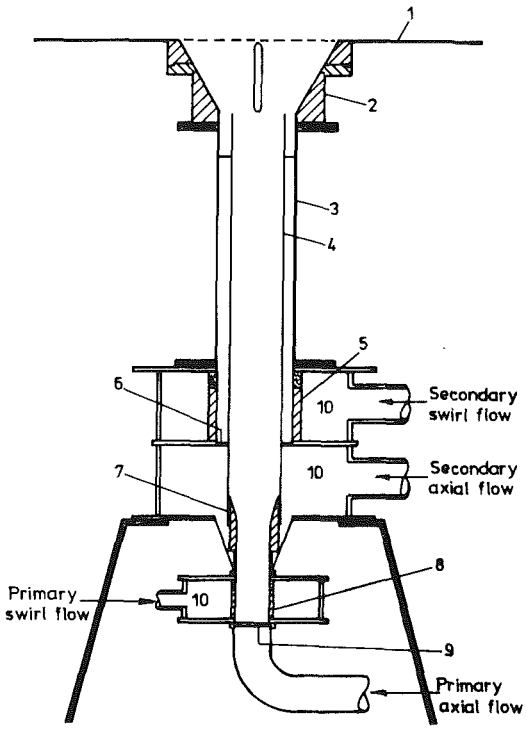

Fig. 3 Diagrammatic arrangement of the model swirl burner: 1—burner exit wall; 2—divergent quarl; 3—flow straightener section; 4—primary nozzle; 5—secondary tangential swirl generator; 6—secondary axial distribution plate; 7—primary nozzle adaptor; 8—primary tangential swirl generator; 9—primary axial distributor plate; 10—annular supply chamber

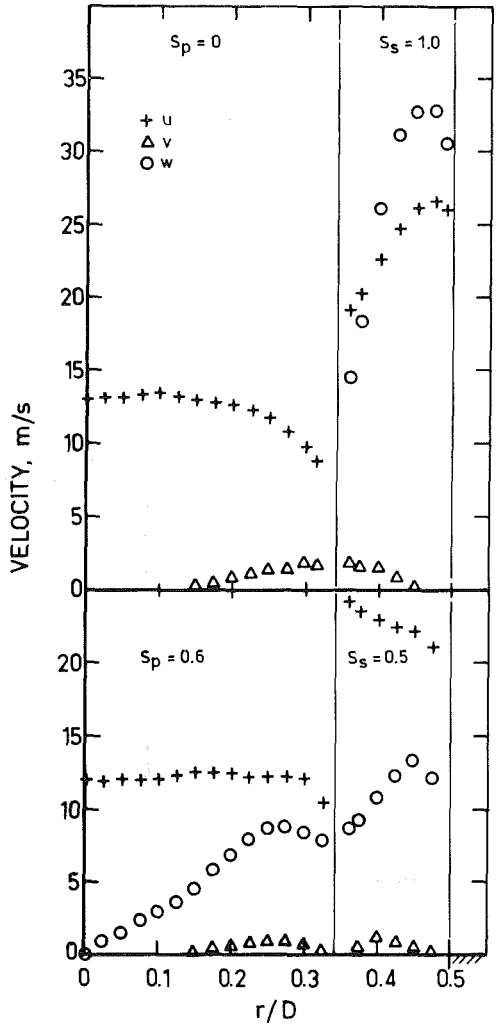

Fig. 4 Radial distributions of axial, radial and tangential components of velocity at the nozle exit of the burner

through a series of control values to the axial and tangential air inlets of the primary and secondary swirl generators. Swirl was generated by a number of tangential slot entries located well upstream of the burner exit and varied by varying the proportions of the air flow introduced tangentially and axially into the swirl generator. The flow at the burner exit was substantially axisymmetric and the jet flow beyond the burner-exit wall was unconfined.

Measurements were obtained with a secondary-flow space-mean exit velocity ($U_{s,av}$) of approximately 23 m/s, secondary swirl numbers (S_s) of 0.5 and 1.0, primary-flow space-mean

Nomenclature

$C\mu$ = constant in turbulence model
D = diameter at throat of divergent quarl
E = constant in wall function
G = momentum flux ratio, equation (2)
k = kinetic energy of turbulence
l_{mix} = mixing length
L = quarl length
$\dot{m}$ = mass flowrate
P = time-mean static gauge pressure
r = radial co-ordinate
R = nozzle radius
S = swirl number, equation (1)
S_ϕ = source term for dependent variable ϕ
U = time-mean axial velocity
V = time-mean radial velocity
W = time-mean tangential velocity
x = axial co-ordinate
y = normal distance from wall
Γ_ϕ = turbulent exchange coefficient for dependent variable ϕ
ϵ = dissipation rate of turbulence energy
κ = constant in wall function
μ = laminar viscosity
ρ = density
τ_w = resultant wall shear stress
ϕ = dependent variable
ψ = streamfunction, equation (3)

Superscript

$+$ = dimensionless variable

Subscripts

av = space mean
in = inlet
max = maximum
p = primary
r = recirculation
s = secondary
t = total or turbulent

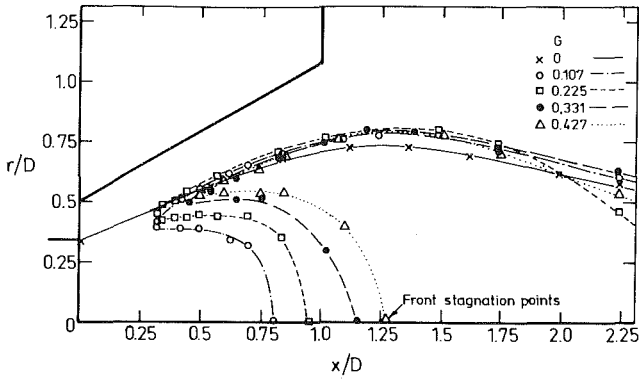

Fig. 5 Variation of the reverse-flow boundary with momentum flux ratio for the type 3 flow

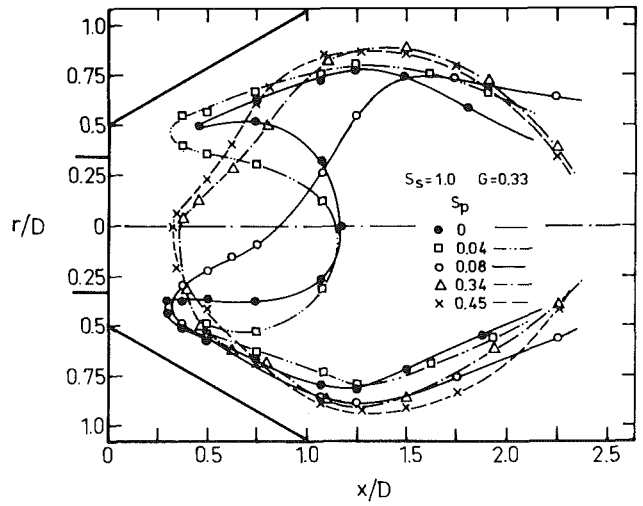

Fig. 6 Variation of the reverse-flow boundary with primary swirl number at high secondary swirl

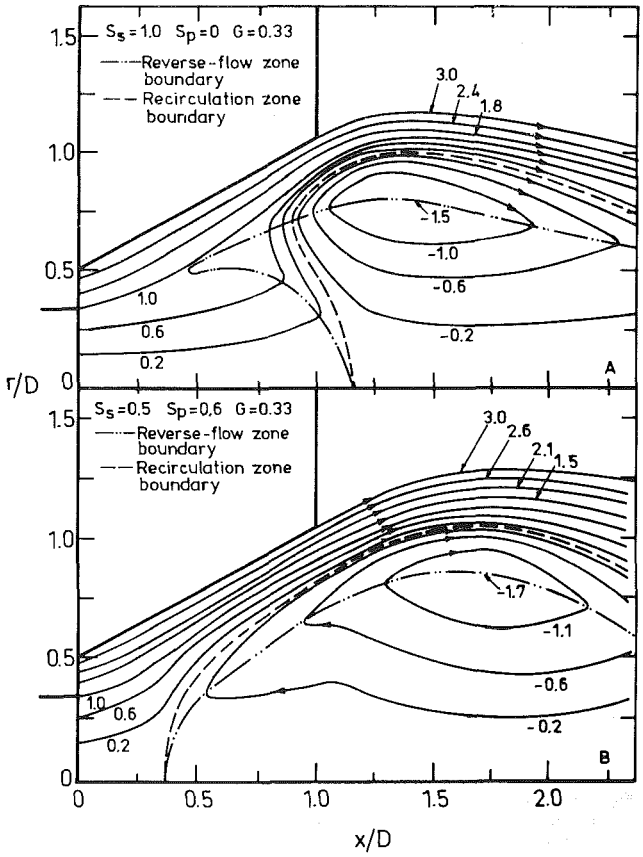

Fig. 7 Flow streamlines for (*a*) type 3, and (*b*) type 2 flows computed from the measured axial velocity profiles. Errors in streamfunction values estimated to be ± 10 percent

exit velocities ($U_{p,av}$) up to 14 m/s and swirl numbers of the coswirling primary flow (S_p) up to 0.6.
Here the swirl number is defined as

$$S = \frac{\int_{R_1}^{R_2} \rho UW r^2 dr}{R_2 \int_{R_1}^{R_2} (\rho U^2 + P)\, r\, dr} \tag{1}$$

where R_1 and R_2 are the inner and outer radii of the nozzle in question. The total swirl number for the combined primary and secondary flow is obtained from the above definition with R_1 as zero and R_2 the outer radius of the secondary annulus. The swirl numbers were calculated from the integration of measured time-mean velocity and static gauge pressure distributions at the nozzle exit.

Typical radial distributions of axial, radial and tangential components of velocity at the nozzle exit of the burner are shown in Fig. 4.

2.2 Probes. Probe access to the quarl region was through a narrow slot in the quarl wall. During measurements the slot was covered with thin adhesive tape to prevent inleakage of air.

2.2.1 Directional Pitotmeter. The boundary of the reverse-flow zone (U = 0 contour) was determined with a two-hole pitotmeter with opposed sensing holes. In operation, the sensing holes were aligned parallel to the burner axis and were predominantly sensitive to the axial component of velocity. Flow reversal was indicated by a change in sign of the pressure differential as the probe was traversed radially. Spatial resolution was typically ± 1.0mm in regions of low turbulence, but degraded at very high levels of turbulence (e.g., near stagnation points) to ± 10mm.

2.2.2 Spherical Five-Hole Pitotmeter. The three components of velocity and the static pressure were measured with a standard five-hole pitotmeter with an 8mm diameter spherical sensing head. The probe was calibrated in the potential core of a round jet at a velocity of 8.8 m/s for the full range of pitch and yaw angles, and subsequently checked by comparison with a total-head probe for velocities in the range 2-32 m/s. Measurement errors are to be expected due to the turbulent nature of the burner flow and these were estimated at ± 4 percent, except in regions of low velocity ($\lesssim$ 1 m/s) where an errror of ± 20 percent was estimated. The latter figure applied particularly to the radial component of velocity since it was small over large regions of the flow. As a further check on the precision of the probe the total flowrate calculated from the measured nozzle-velocity profiles was compared with that measured directly by an orifice flowmeter: the discrepancy was less than 5 percent.

3 Experimental Results

3.1 Boundary of the Reverse-Flow Zone. Figure 5 shows, at a secondary swirl number of 1.0 and no primary swirl, the boundary of the reverse-flow zone (U = 0 contour) for a range of primary-flow velocities. The curves are labelled in terms of the momentum flux ratio, G, defined as

$$G = \frac{\rho_p U^2_{p,av}}{\rho_s U^2_{s,av}} \tag{2}$$

which has been used previously [5] as a parameter for recirculation in brown-coal burners. Comparison with Fig. 1 reveals that the present flow cannot be classified as either a type 1 or type 2 flow, since the primary jet does not penetrate completely the reverse-flow zone (type 1) nor is it deflected radially at the nozzle exit (type 2). Instead, the primary jet is deflected radially at some distance downstream from the nozzle after partially penetrating the reverse-flow zone to a degree which increases with increasing momentum flux ratio. Hereinafter this flow type is referred to as type 3. At momentum flux ratios above 0.67 the flow became asymmetric and at the highest momentum flux ratio examined

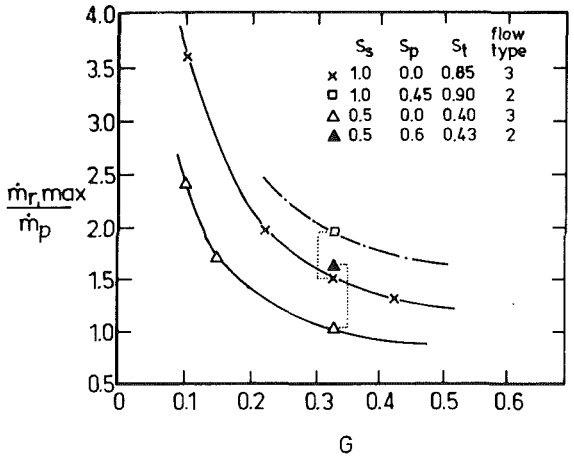

Fig. 8 Maximum recirculated-mass flowrate as a function of momentum flux ratio for various swirl conditions. Errors estimated to be ± 10 percent

(1.19), for which a type 1 flow with complete penetration might be expected, the flow was strongly asymmetric with the primary jet deflected to one side of the reverse-flow zone. The difficulty in maintaining a stable, symmetric flow at high momentum flux ratios arises due to the relatively large primary nozzle.

At the lower secondary swirl number (0.5) and no primary swirl the boundary of the reverse-flow zone was similar to that shown in Fig. 5 (i.e., type 3 flow) but, as expected, the degree of primary jet penetration for a given momentum flux ratio was slightly greater. Furthermore, the onset of flow asymmetry occurred at a lower momentum flux ratio of 0.2.

Figure 6 shows, at a secondary swirl number of 1.0 and momentum flux ratio of 0.33, the effect of primary swirl on the boundary of the reverse-flow zone. With no primary swirl a stable type 3 flow is produced. However, at low primary swirl numbers, in the range of $0.04 < S_p < 0.27$, the flow is strongly asymmetric and unstable. At higher primary swirl numbers, greater than 0.3, the primary jet is deflected radially close to the nozzle exit and a stable, axisymmetric, type 2 flow is established. At swirl numbers above 0.34 the boundary of the reverse-flow zone is essentially unchanged (although the recirculated mass flowrate is increased).

At a secondary swirl number of 0.5 the effect of primary swirl on the boundary of the reverse-flow zone was similar to that depicted in Fig. 6, but the mimimum primary swirl number for stable, axisymmetric flow increased to 0.6.

3.2 Streamline Patterns. The detailed streamline patterns for typical type 2 and type 3 stable, axisymmetric flows are presented in Fig. 7. Here the streamfunction is normalized by the primary-nozzle mass flowrate:

Table 1 Definition of Γ_ϕ and S_ϕ for conservation equations

Equation	ϕ	Γ_ϕ	S_ϕ
Mass	1	0	0
Axial momentum	U	μ_{eff}	$-\frac{\partial P^*}{\partial x}+\frac{\partial}{\partial x}\left(\mu_{\text{eff}}\frac{\partial U}{\partial x}\right)+\frac{1}{r}\frac{\partial}{\partial r}\left(r\mu_{\text{eff}}\frac{\partial V}{\partial x}\right)$
Radial momentum	V	μ_{eff}	$-\frac{\partial P^*}{\partial r}+\frac{\partial}{\partial x}\left(\mu_{\text{eff}}\frac{\partial U}{\partial r}\right)+\frac{1}{r}\frac{\partial}{\partial r}\left(r\mu_{\text{eff}}\frac{\partial V}{\partial r}\right)-2\mu_{\text{eff}}\frac{V}{r^2}+\frac{\rho W^2}{r}$
Tangential momentum	W	μ_{eff}	$-\left[\frac{\rho V}{r}+\frac{1}{r^2}\frac{\partial}{\partial r}(r\mu_{\text{eff}})\right]W$
Turbulence energy	k	$\frac{\mu_{\text{eff}}}{\sigma_k}$	$G-\rho\epsilon$
Turbulence energy Dissiptation rate	ϵ	$\frac{\mu_{\text{eff}}}{\sigma_\epsilon}$	$\frac{\epsilon}{k}(C_1G-C_2\rho\epsilon)$

$$\mu_{\text{eff}} \equiv \mu+\mu_t=\mu+C_\mu\rho k^2/\epsilon$$

$$P^*=P+\frac{2}{3}\rho k$$

$$G=\mu_{\text{eff}}\left\{2\left[\left(\frac{\partial U}{\partial x}\right)^2+\left(\frac{\partial V}{\partial r}\right)^2+\left(\frac{V}{r}\right)^2\right]+\left(\frac{\partial W}{\partial x}\right)^2+\left[r\frac{\partial}{\partial r}\left(\frac{W}{r}\right)\right]^2+\left(\frac{\partial U}{\partial r}+\frac{\partial V}{\partial x}\right)^2\right\}$$

C_μ	C_1	C_2	σ_k	σ_ϵ	κ	E
0.09	1.44	1.92	1.0	1.22	0.42	9.79

$$\psi(r) = \frac{2\pi \int_0^r \rho U r'\, dr'}{\dot{m}_p} \tag{3}$$

The flow boundaries shown on the figure are the boundary of the reverse-flow zone ($U = 0$ contour) and the boundary of the recirculation zone ($\psi = 0$ contour).

For the type 3 flow ($S_s = 1.0$, $S_p = 0.0$), Fig. 7(*a*) shows that approximately 90 percent of the primary flow penetrates the reverse-flow zone at a momentum flux ratio of 0.33. At momentum flux ratios of 0.23 and 0.43 the primary-flow penetrations were 80 percent and 100 percent, respectively. For all three momentum flow ratios the eye of the recirculation zone was located at an axial distance of 1.43D. By comparison, for the type 2 flow ($S_s = 0.5$, $S_p = 0.6$), Fig. 7(*b*) shows that a moderate level of primary swirl causes the primary flow to diverge strongly downstream of the nozzle exit. Also, the eye of the recirculation zone is located further from the burner nozzle at an axial distance of 1.78D.

For both flows the central recirculation zone is seen to occupy a considerable volume of the jet flow within a few nozzle diameters of the burner exit. Also, the mass flowrate of fluid recirculated in both flows is considerable, being 1.5 $\dot{m}_p$ and 1.7 $\dot{m}_p$ for the type 3 and type 2 flows, respectively.

The estimates of the maximum error given in the figure caption include measurement errors in the velocity (see Section 2.2.2) and errors arising from flow asymmetry (see Fig. 6).

3.3 Maximum Recirculated Mass Flowrate. Figure 8 shows the maximum recirculated-mass flowrate (at the eye of the recirculation) plotted as a function of momentum flux ratio for four swirl conditions. As can be seen, the maximum recirculated-mass flowrate decreases with increasing momentum flux ratio. The effect of primary swirl on the recirculated-mass flow at a momentum flux ratio of 0.33 is indicated by the vertical broken lines, from which it can be seen that the addition of only a small amount of primary swirl (in terms of its effect on the total swirl number of the nozzle flow) significantly increases recirculation. That such a large increase in recirculation can result from such a small increase in total swirl is presumably a consequence of the fact that a large change in flow pattern results from the addition of a small amount of primary swirl, as shown in Fig. 6. For the flow configuration investigated here, the recirculation at a total swirl number of 0.48 ($S_s = 0.5$, $S_p = 0.6$) was slightly greater than that at a much higher total swirl number of 0.85 ($S_s = 1.0$, $S_p = 0.0$).

4 Calculations

The predictions were obtained by numerical solution of the time-mean equations governing conservation of mass and momentum, supplemented by a two-equation ($k-\epsilon$) effective viscosity turbulence model. The general form of the equations for isodensity axisymmetric flow in cylindrical geometry is:

$$\frac{\partial}{\partial x}(\rho U \phi) + \frac{1}{r}\frac{\partial}{\partial r}(r\rho V \phi) - \frac{\partial}{\partial x}\left(\Gamma_\phi \frac{\partial \phi}{\partial x}\right) - \frac{1}{r}\frac{\partial}{\partial r}\left(r\Gamma_\phi \frac{\partial \phi}{\partial r}\right) = S_\phi \tag{4}$$

value ϕ represents one of the dependent variables U (axial component of velocity), V (radial component of velocity), W (tangential component of velocity), k (turbulence energy) and ϵ(dissipation rate of turbulence energy). The turbulent exchange coefficients, Γ_ϕ, and source terms, S_ϕ, for each dependent variable are given in Table 1.

The boundary conditions were obtained from the measurements wherever possible. Thus, the inlet velocities and turbulence levels were taken from the measurements at the nozzle exit. The turbulence energy dissipation rate at the inlet was estimated from an assumed mixing length:

$$\epsilon_{in} = \frac{k_{in}^{3/2}}{l_{mix}} \tag{5}$$

where l_{mix} was taken as 0.33 times the supply duct dimension (radius for the primary nozzle and annulus width for the secondary nozzle). At the external entrainment boundary ($r/D = 4.3$) the axial and tangential velocities and the turbulence energy were taken as zero and the radial velocity was calculated from the radial gradient of pressure. At the outflow boundary, which was located beyond the recirculation zone in a region of forward flow ($x/D = 10.5$), the axial derivatives of tangential velocity, turbulence energy and turbulence energy dissipation rate and the second axial derivative of axial velocity ($\partial^2 U/\partial x^2$) were taken as zero. (In practice, the calculation of the flow within the burner quarl proved to be relatively insensitive to the conditions imposed at the entrainment and outflow boundaries.) The flow was assumed to be axisymmetric. At solid surfaces the velocity was set to zero and so-called wall functions, based on logarithmic velocity profiles, used to bridge the turbulent boundary layer:

$$U_t^+ = \frac{1}{\kappa}\ln(Ey^+) \tag{6}$$

$$\frac{\partial k}{\partial y} = 0 \tag{7}$$

$$\epsilon = C_\mu^{3/4} k^{3/2}/(\kappa y) \tag{8}$$

where

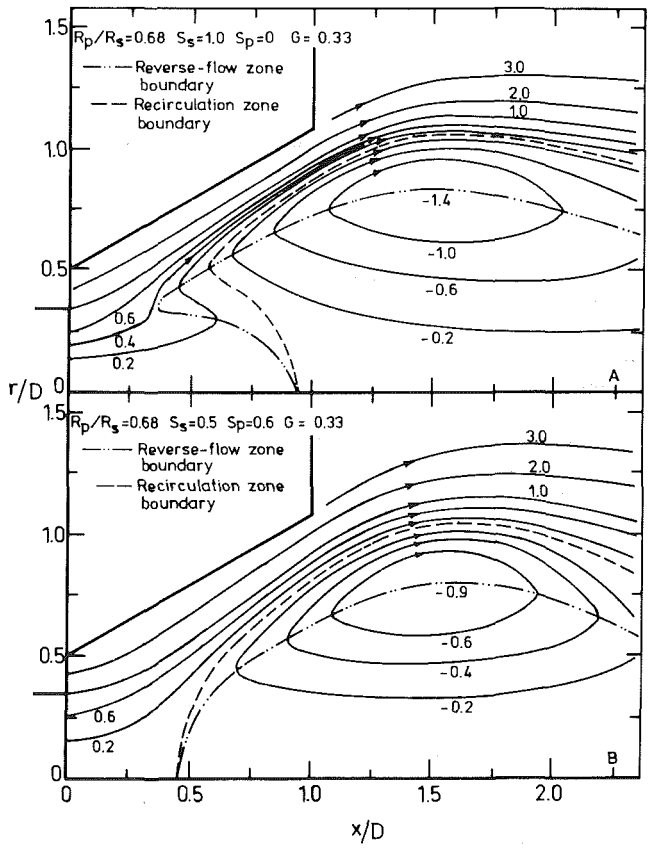

Fig. 9 Predicted flow streamlines for (*a*) type 3, and (*b*) type 2 flows in the brown-coal-burner geometry

$$U_t^+ = (C_\mu^{1/4} \rho k^{1/2}/\tau_w)\, U_t \quad (9)$$

$$y^+ = (C_\mu^{1/4} \rho k^{1/2}/\mu) y \quad (10)$$

and U_t is the resultant velocity parallel to the wall, τ_w the resultant shear stress at the wall and y the normal distance from the wall.

The differential equations were reduced to a conservative finite-difference form using the control-volume method over a rectangular grid covering one half-plane of the axisymmetric flow domain. Staggered grids were employed for the U and V equations. The pressure was calculated from a Poisson-like equation derived from the finite-difference form of the mass conservation equation. The physical boundaries of the flow domain were located midway between the scalar grid lines except for the sloping quarl wall which passed through the gird nodes. A hybrid central/upwind difference scheme was used everywhere except adjacent to the quarl where skew-upwind differences were used for the north and west faces of the U and V control volumes. The boundary conditions were introduced in the usual way via modifications to the linearized source terms. The finite-difference equations were solved by a line-by-line iterative procedure with under-relaxation. Further details of the computational method may be found in reference [6].

The final computations were carried out on a nonuniform 30 × 30 grid with a concentration of nodes within and near the quarl. The results were checked for grid independence, within reasonable limits, by comparison with results obtained on a 22 × 22 grid and a second 30 × 30 grid with a different distribution of nodes. The differences in the calculated velocities were typically less than four percent of the maximum velocity. Clearly, the grid dependence, although non-zero, is small. A VAX 11/780 computer was used, the run times being about 15 minutes for 400 iterations with a convergence criterion that the normalized sum of the absolute residual mass sources be less than 10^{-4}.

Figure 9 shows the calculated streamline patterns for the type 2 and type 3 flows discussed in section 3.2 above. A comparison of Figs. 9 and 7 reveals that the measured and calculated streamline patterns are qualitativley in good agreement. The axial distances to the forward stagnation point agree to within 20 percent which is acceptable considering the high measurement errors due to the complex and highly turbulent nature of the flows in this region. For both flows the calculated location of the eye of the recirculation and the maximum width of the reverse-flow zone are within 7 percent of the measurements.

The calculated and measured maximum recirculated-mass flow rates are in very good agreement for the type 3 flow, but differ by a factor of two for the type 2 flow. No satisfactory explanation for this large discrepancy was found. Although the $k-\epsilon$ turbulence model is known to be deficient for swirling recirculating flows, due to the neglect of anisotropy in the turbulent viscosity and additional turbulence generation terms arising from streamline curvature, it is unlikely to lead to an error of such magnitude, particularly in view of the good agreement for the high swirl type 3 flow. Also, it is not considered likely that measurement errors account for the discrepancy.

In the type 3 flow the recirculation zone is predicted to extend further into the quarl region than shown by the measurements and less of the primary stream is predicted to penetrate the reverse-flow zone. These related discrepancies are possibly attributable to inaccurate measurements of the radial component of velocity at the primary nozzle exit, leading to an erroneous boundary condition for the calculation. As expected, the detailed flow of the primary stream immediately downstream of the nozzle before penetrating the reverse-flow zone is sensitive to the radial component of velocity at the nozzle exit.

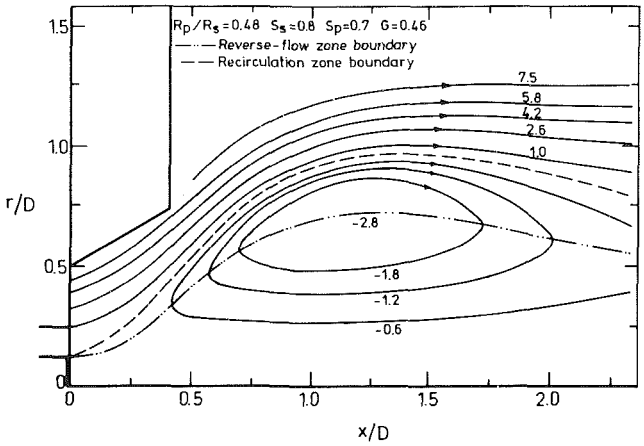

Fig. 10 Predicted flow streamlines for black-coal-burner geometry with a center-line blockage to simulate an oil gun

5 Effect of Burner Geometry and Operational Variables on Flow Type

The calculation method was used to examine the effect of changes in burner geometry and operating conditions on the flow patterns. The results are too numerous to be given in detail and only the more important and practically relevant findings are presented.

5.1 Quarl Length and Angle. For both type 2 and type 3 flows a reduction in quarl length, from an L/D of 1.0 to 0.41, resulted in a narrower reverse-flow zone and a significant reduction in recirculation. In the case of the type 3 flow the penetration of the reverse-flow zone by the primary stream increased only slightly. Similarly, a reduction in quarl angle, from 30 to 25 deg, also resulted in a narrower reverse-flow zone and a reduction in recirculation. In all cases the basic flowpattern type remained unchanged.

5.2 Black-Coal-Burner Geometry. Calculations were performed for a nozzle and quarl geometry typical of a black-coal burner, viz. nozzle radius ratio of 0.48, quarl length-to-diameter ratio of 0.41 and quarl half-angle of 30 deg. The secondary mass flowrate was fixed at its previous value, giving a secondary-flow mean velocity averaging 16 m/s. The secondary swirl number was 0.8.

At a typical momentum flux ratio of 0.46 the flows with primary swirl ($S_p = 0.7$) and without primary swirl were qualitatively similar to the type 2 and type 3 brown-coal-burner flows shown in Fig. 9. For the type 3 flow the penetration of the reverse-flow zone by the primary stream was greater than for the corresponding brown-coal-burner flow, with the forward stagnation point predicted to lie beyond the eye of the recirculation zone. Under these conditions it is doubtful whether, in practice, the recirculation zone would remain stable and axisymmetric. A potentially more stable type 3 flow was produced at the lower momentum flux ratio of 0.36. At the high momentum flux ratio of 1.5 the primary stream completely penetrated the reverse-flow zone resulting in a type 1 flow. However, in view of the experimental results for the brown-coal-burner geometry it is doubtful whether, in practice, the toroidal recirculation zone would remain stable and symmetric, although the smaller primary-nozzle diameter in the black-coal-burner geometry will enhance the stability of the type 1 flow.

The effect of a central oil gun on the black-coal-burner flows has been simulated by adding a bluff body on the axis of the primary nozzle to give a blockage ratio typical of that used in existing black-coal burners. In practice, the oil gun is only fired during burner start-up. The calculated streamline pattern for the flow with primary swirl ($S_p = 0.7$, $G = 0.46$)

is presented in Fig. 10, and shows the expected large reverse-flow zone created by the swirling flow emerging from the divergent quarl. An interesting feature of the flow is the merging of the small bluff-body-induced reverse flow with the large swirl-induced reverse flow to form a single, large recirculation zone attached to the burner nozzle.

The flow so formed is essentially an attached type 2 flow. For the flow without primary swirl the predicted flowpattern was very similar to that shown in Fig. 10, with no evidence of primary stream penetration into the reverse-flow zone. Thus, without primary swirl the addition of a central oil gun may significantly modify the flowpattern, causing a transition from a type 3 flow to an attached type 2 flow. Of course, the precise effect of the oil gun will depend upon the blockage ratio and the momentum flux ratio: for a low blockage ratio and high momentum flux ratio the flow may be of type 3.

6 Conclusions

The following main conclusions can be drawn from the present investigation:

1 A stable, symmetric central recirculation zone within the divergent quarl of a swirl burner can be produced for a range of flow conditions.

2 The range of momentum flux ratios over which the central recirculation zone remains stable and symmetric without primary swirl support is relatively narrow and decreases with decreasing swirl number. Without primary swirl a portion of the primary flow partially penetrates the reverse-flow zone before being deflected radially, resulting in a type 3 flow. Complete penetration of the reverse-flow zone – a type 1 flow – is not expected with the range of radius ratios and momentum flux ratios used in existing coal burners.

3 At a fixed momentum flux ratio a minimum level of primary swirl is required to establish a stable, symmetric type 2 flow previously observed for oil- and gas-burner geometries. This mimimum level of primary swirl depends on the secondary swirl and decreases with increasing secondary swirl. Once a stable type 2 flow is established further increases in primary and secondary swirl produce relatively small changes to the reverse-flow boundary, although the recirculated-mass flowrate increases.

4 The recirculated mass flowrate is increased by a decrease in momentum flow ratio and/or an increase in swirl. Furthermore, the measurements suggest that the overall swirl number of the flow at the burner nozzle is not sufficient to characterize completely the effect of swirl on recirculation and that the interaction between swirl, in particular primary swirl, and flowpattern type must be taken into account.

5 The measured flow patterns are adequately represented by a calculation procedure based on numerical solution of the equations governing conservation of mass, momentum, turbulence energy and turbulence energy dissipation rate. However, differences still remain to be explained and further improvements to the calculation method are desirable. A substantial part of the difference between the calculations and measurements is thought to be attributable to the turbulence model. Despite the discrepancies, the present investigation suggests that the calculation method is adequate for many engineering purposes.

References

1 Chigier, N. A., and Beér, J. M., "Velocity and Static-Pressure Distributions in Swirling Air Jets Issuing From Annular and Divergent Nozzles," ASME *Journal of Basic Engineering*, Vol. 86, 1964, pp. 788–796.

2 Beér, J. M., "On the Stability and Combustion Intensity of Pressure Jet Oil Flames," *Combustion*, Vol. 37, 1965, pp. 27–34.

3 Leuckel, W., and Fricker, N., "The Characteristics of Swirl-Stabilized Natural Gas Flames, Part 1: Different Flame Types and Their Relation to Flow and Mixing Patterns," *J. Inst. Fuel*, Vol. 49, 1976, pp. 103–112.

4 Beér, J. M., Chigier, N. A., "Stability and Combustion Intensity of Pulverized-Coal Flames - Effect of Swirl and Impingement," *J. Inst. Fuel*, Vol. 42, 1969, pp. 443–450.

5 Pleasance, G. E., "The Isothermal Aerodynamics of Swirling Double-Concentric Jets," State Electricity Commission of Victoria, Scientific Division Preprint, 1975.

6 Gosman, A. D., and Pun, W. M., "Calculation of Recirculating Flows," Imperial College, Mechanical Engineering Department Report HTS/74/2, 1974.

Flow in a Rectangular Diffuser With Local Flow Detachment in the Corner Region

F. B. Gessner
Professor,
Mem. ASME

Y. L. Chan
Research Assistant.

Department of Mechanical Engineering,
University of Washington,
Seattle, Wash. 98195

An experimental study was conducted in order to examine the nature of flow within a high-inlet-aspect-ratio rectangular diffuser with locally detached flow in the corner region, but attached flow elsewhere in the diffuser. The results include flow visualization data corresponding to tuft and oil flow patterns observed on the diffuser walls and flow angle data taken in the immediate vicinity of the corner. Axial mean velocity distributions and local wall shear stress profiles are also presented. Analysis of the results provides new insight into the structure of separated, three-dimensional corner flows, wherein combined attached and detached flow conditions exist simultaneously at each streamwise location.

Introduction

In certain design applications, a rectangular diffuser is sometimes used as a means of decelerating the flow. For turbulent flow in high-inlet-aspect-ratio rectangular diffusers (AS $\geq$ 4), the state-of-the-art has now progressed from a knowledge of basic flow regimes [1,2] and overall pressure recovery behavior [3], to integral methods which can predict the onset of flow separation [4], and local pressure recovery for unstalled [5] and partially stalled [6] flow conditions, to a zonal integral method [7] which can be applied to predict local flow behavior in the unstalled flow, transitory stall, and fully-developed stall regimes defined by Fox and Kline [2]. The two-dimensional predictive code reported in [7] has recently been extended to accommodate diffuser flows with unsteady inlet flow conditions [8]. Data are also presently available which demonstrate the effects of inlet blockage [9], inlet profile nonuniformity [10], and wall shape [11] on the performance of high-inlet aspect ratio diffusers. More recent experimental studies have focused on the nature of diffuser exit velocity profiles with transitory stall present [12], details of the transitory stall cycle for both undisturbed and periodically disturbed inlet conditions [12], the sensitivity of the line of first appreciable stall to "wake-like" inlet flow conditions [13], and the nature of flow direction intermittency along the diverging walls of a diffuser [14].

All of these studies have increased our physical understanding and predictive capabilities in the area of high-inlet-aspect-ratio rectangular diffuser flows. With the exception of limited flow visualization data available from the studies by Fox and Kline [2] and Waitman, et al. [9], however, no data are available from the above references on corner flow separation patterns or on flow characteristics in the corner region under locally detached flow conditions. This same comment applies for studies which have been conducted to date in low-inlet-aspect-ratio rectangular diffusers (AS $\leq$ 0.5), which generally focus on overall diffuser performance, as influenced, for example, by a uniformly sheared [15, 16] or fully-developed [17] inlet flow condition.

Previous investigations of rectangular diffuser flows have included some studies for which the inlet aspect ratio was identically unity and mean flow behavior was investigated to a limited extent [18, 19]. In more recent work, novel measurement techniques have been applied to determine the local flow structure within rectangular diffusers having an inlet aspect ratio at or near two [20–22]. In most of these studies, data are restricted to the midplane region of the diffuser [19–22], and only limited data are included in one reference [20] which show the change that occurs in the axial mean velocity component near a wall as the corner is approached.

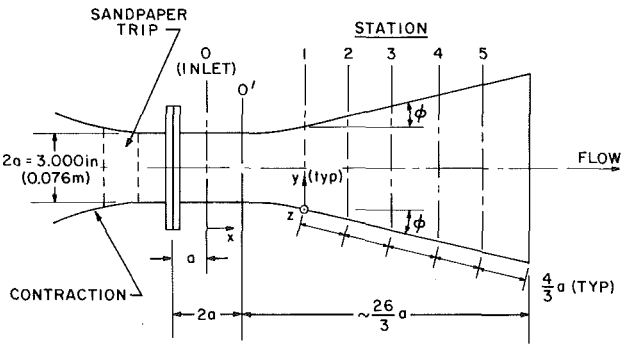

Fig. 1 Schematic diagram of rectangular diffuser

Contributed by the Fluids Engineering Division and presented at the AIAA/ASME 3rd Joint Thermophysics, Fluids, Plasma and Heat Transfer Conference in St. Louis, Missouri, June 7–11, 1982, of The American Society of Mechanical Engineers. Manuscript received by the Fluids Engineering Division, June 16, 1982.

On the basis of the above considerations, it is apparent that our knowledge of local flow behavior in the corner region of a rectangular diffuser for various operating conditions is incomplete. The purpose of this paper is to present results which demonstrate flow development within a rectangular diffuser when locally detached flow exists in the corner region, but the flow is attached elsewhere. The data are based on a low Mach number, high Reynolds number, uniform core, thin-inlet-boundary-layer flow which develops symmetrically within a high-inlet-aspect-ratio rectangular diffuser. The results include flow visualization data corresponding to tuft and oil flow patterns observed on the diffuser walls and flow angle data taken in the immediate vicinity of the corner. Axial mean velocity distributions and local wall shear stress profiles are also presented.

Experimental Program

Flow Facility. The overall flow facility is an open-circuit configuration with air flow provided by means of a variable-speed axial flow fan (General Electric Model 7A5 A1). Air discharges from the fan into a plenum chamber and then passes into an aluminum contraction which reduces the flow area from 4 ft × 4 ft (1.2 m × 1.2 m) to 3 in. × 24 in. (0.076 m × 0.61 m). These outlet dimensions are compatible with the inlet dimensions of the rectangular diffuser, which is directly coupled to the contraction and exhausts to the atmosphere, as shown in Fig. 1. The diffuser consists of two variable-divergence-angle, aluminum walls (0.25 in. or 4.0 mm thick) and two parallel, plexiglas end walls of the same thickness. For prediction purposes, the curved contour of each diverging wall edge (four edges) was mapped between the station where the wall began to curve (Station 0′) and the first station (Station 1) where the wall became flat again. These positions are tabulated in a thesis [23] which forms the basis of the present paper. That reference also includes complete details of the measurement techniques and probe configurations used in this study. Additional information and results appear in an extended version of the present paper [24].

Flow Visualization Techniques. Flow in the near-wall region was observed by means of: (1) a wool tuft attached to a hand-held wooden dowel inserted upstream of the flow, (2) an array of tufts located on the left side of the lower diverging wall, and (3) a mixture of oil and fluorescent dye which coated the diffuser walls. The oil-dye mixture consisted of 10 ml of silicon oil, 10 drops of oleic acid, and 20 drops of fluorescent dye (oil dye #50, Morton Chemical Company, Chicago) and was used to observe limiting wall streamline patterns in the corner region. The mixture was sprayed onto the surface by means of an air brush (Badger Model 200-1), and an ultraviolet light (Magnaflux Model ZB22) was used to illuminate the fluorescent dye.

Operating Conditions. Flow visualization studies were conducted over a range of inlet core flow velocities ($20 \leq U_{c,0} \leq 50$ m/s) and diffuser divergence angles ($4 \leq 2\phi \leq 12$ deg). For the velocity and wall shear stress measurements reported in this paper, the total divergence angle was set at 8 deg and the inlet core flow velocity was maintained at 20 m/s (± 0.05 m/s). For this operating condition, the inlet Reynolds number, $\mathrm{Re}_0 \equiv 2aU_{c,0}/\nu$, was 9.7×10^4 and the midplane displacement thicknesses evaluated at the diffuser inlet were $2\delta^*_{y,0}/W_1 = 0.0259$ (at $z/a = 8$) and $2\delta^*_{z,0}/(2b) = 0.0025$ (at $y/a = 1$). The above conditions correspond to a high Reynolds number, thin inlet-boundary-layer operating condition, for which the inlet blockage is less than 3 percent of the throat area and the Reynolds number is sufficiently high to ensure sustained turbulent flow at the diffuser inlet [3].

Experimental Results

Inlet Station Profiles (Station 0). Initial velocity profile data were taken at the inlet station by means of a circular pitot tube referenced to a wall tap in order to examine the spanwise

Nomenclature

a = throat half-width (Fig. 1)
AS = inlet aspect ratio
C = law-of-the-wall constant
d_i = inside diameter
d_0 = outside diameter
$D_{\max}$ = outside diameter of largest Preston tube
$D_{\min}$ = outside diameter of smallest Preston tube
$D^+_{\max,y}$ = normalized y location of $D_{\max}$ ($D^+_{\max,y} \equiv D_{\max} u_{\tau,y}/\nu$)
$D^+_{\max,z}$ = normalized z location of $D_{\max}$ ($D^+_{\max,z} \equiv D_{\max} u_{\tau,z}/\nu$)
$D^+_{\min,y}$ = normalized y location of $D_{\min}$ ($D^+_{\min,y} \equiv D_{\min} u_{\tau,y}/\nu$)
$D^+_{\min,z}$ = normalized z location of $D_{\min}$ ($D^+_{\min,z} \equiv D_{\min} u_{\tau,z}/\nu$)
Re_0 = core flow Reynolds number ($\mathrm{Re}_0 \equiv 2aU_{c,0}/\nu$)
U = mean velocity in x-direction
U_c = local core flow velocity
$U_{c,0}$ = mean axial centerline velocity at Station 0 (Fig. 1)
U^+_y, U^+_z = dimensionless velocities ($U^+_y \equiv U/u_{\tau,y}$, $U^+_z \equiv U/u_{\tau,z}$)
$u_{\tau,y}, u_{\tau,z}$ = friction velocities on diverging and parallel end walls, respectively, ($u_{\tau,y} \equiv \sqrt{\tau_{w,y}/\rho}$, $u_{\tau,z} \equiv \sqrt{\tau_{w,z}/\rho}$)
x = axial coordinate (Fig. 1)
y,z = local transverse coordinates (Figs. 1 and 2)
y_{c1} = centerline position on end wall
y_r = reattachment line location (Fig. 4)
y_0, z_0 = zero velocity line locations (Fig. 4)
y^+, z^+ = dimensionless coordinates ($y^+ \equiv yu_{\tau,y}/\nu$, $z^+ \equiv zu_{\tau,z}/\nu$)
Δy = incremental y distance
z_s = detachment line location (Fig. 4)
Δz = incremental z distance
δ = boundary layer thickness ($\delta \equiv \delta_{0.995}$)
$\delta^*_{y,0}, \delta^*_{z,0}$ = displacement thicknesses at $z/a = 8$ and $y/a = 1$, respectively, at Station 0
θ = yaw angle (Fig. 6)
θ_w = yaw angle of limiting wall streamline on diverging wall (Fig. 6)
κ = von Karman's constant
ν = kinematic viscosity
ϕ = diffuser half angle (Fig. 1)
ρ = density
τ_w = axial wall shear stress component
$\tau_{w,y}, \tau_{w,z}$ = axial wall shear stress components on diverging and parallel end walls, respectively, ($\tau_{w,y} \equiv \mu \partial U/\partial y|_{y=0}$, $\tau_{w,z} \equiv \mu \partial U/\partial z|_{z=0}$)

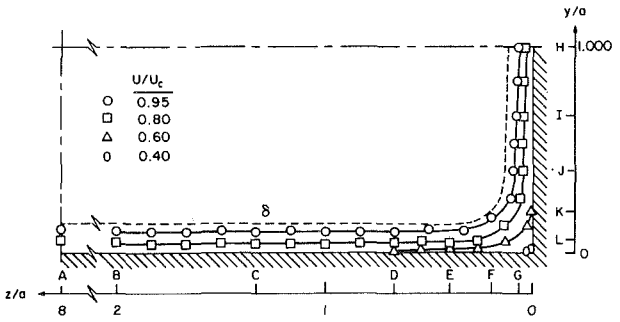

Fig. 2 Isotach contours and velocity profile locations (A-L) at the inlet station (Station 0)

uniformity of the flow and the sensitivity of inlet flow profiles to the diffuser divergence angle setting. The results indicated that flow at the inlet station was not influenced by downstream effects, which ranged from a wholly attached flow condition for $2\phi = 0$ deg to locally detached flow in the corner region, with attached flow elsewhere, when $2\phi = 8$ deg. Inlet flow symmetry was also examined by measuring lines of constant axial mean velocity (isotachs) within the entire cross section of the diffuser. The pattern measured within one quadrant is shown in Fig. 2 and is indicative of a distortion-free flow at the inlet. The y/a, z/a position of the points for $U/U_c = 0.95$ are estimated to be accurate to within $\Delta y/a = \pm 0.04$, $\Delta z/a = \pm 0.03$, as determined by comparing indicated positions measured with the circular pitot tube first referenced to a single wall tap, and then to the wall tap in closest proximity to the probe. These deviations decrease as isotach values decrease, until $\Delta y/a = \pm 0.01$, $\Delta z/a = +0.01$ for points corresponding to the lowest isotach value shown in Fig. 2 ($U/U_c = 0.040$).

In order to determine the extent of local law-of-the-wall behavior at the inlet plane, additional boundary layer profile measurements were made with a flattened pitot tube at the lettered locations shown in Fig. 2 (Positions A through L). Local wall shear stress measurements were also made at these positions, and at the interim positions, by means of Preston tubes. The use of a Preston tube presumes, of course, that a wall-defined log-law region exists at each transverse location. This presumed behavior was confirmed by the results, which indicate that log-law behavior exists well into the corner region (e.g., at positions G and L in Fig. 2). These results are shown explicitly in the related paper by Gessner and Chan [24].

Flow Visualization Results. Initial probing of the peripheral near-wall flow indicated that locally detached flow in the corner region, when present, always occurred simultaneously in all four corners of the diffuser. For the smallest diffuser divergence angle setting ($2\phi = 4$ deg), it was apparent from visual observation of the tuft array on the lower diverging wall that the flow remained wholly attached. For $2\phi = 8$ deg the flow detached locally in the near-corner region, as indicated by tuft motions which were interpreted as being indicative of intermittent transitory stall [9]. When the total divergence angle was increased to 12 deg, there was a definite transverse variation in the stall pattern at a given streamwise location, ranging from local transitory stall in the immediate vicinity of the corner, to intermittent transitory stall in the adjacent wall region, to unstalled flow in the central wall region. The patterns which formed were relatively insensitive to inlet core flow velocity variations within the range $20 \leq U_c < 40$ m/s, and are described in detail by Chan [23].

Oil flow visualization of limiting wall streamline patterns indicated that time-averaged flow behavior in the near-corner region could still be discerned in the presence of gross unsteadiness in the flow. Figure 3 show typical limiting wall streamline patterns observed near the diffuser exit plane on the diverging wall (Fig. 3(*a*)) and on the end wall (Fig. 3(*b*)) bounding the quadrant shown in Fig. 2 with the total divergence angle set at 8 deg. The irregular ribbon of dye near the corner line in Fig. 3(*a*) (which is reflected on the end wall) is an artifact caused by the downward movement of oil on the vertical end wall over the time period required for a stable pattern to form (20 to 30 min). The results shown in Fig. 3 indicate that limiting wall streamlines do not form a symmetric pattern about the corner line, but form, instead, an antisymmetric "S"-shaped pattern about this line. This result was unexpected, inasmuch as wholly attached flow in the vicinity of a streamwise corner generally exhibits a high degree of local symmetry about the corner bisector.

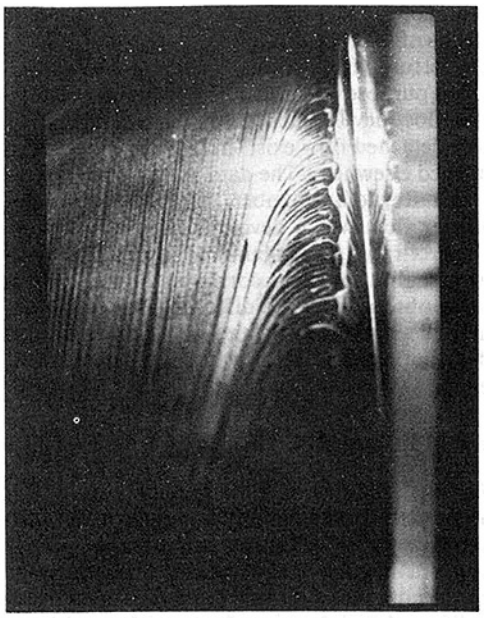

Fig. 3(*a*) Diverging wall

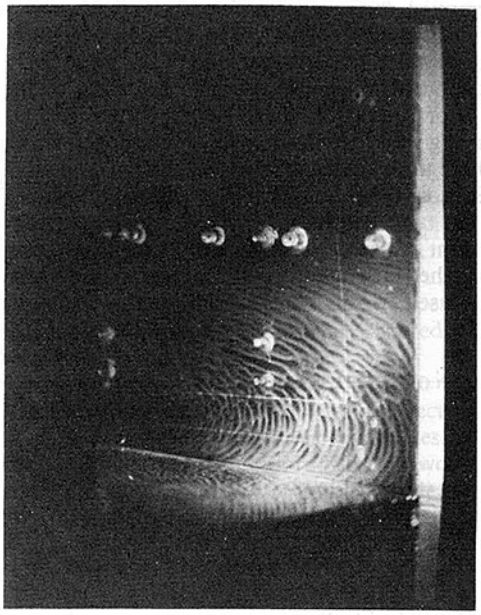

Fig. 3(*b*) End wall

Fig. 3 Observed limiting wall streamlines near the diffuser exit plane ($2\phi = 8$ deg)

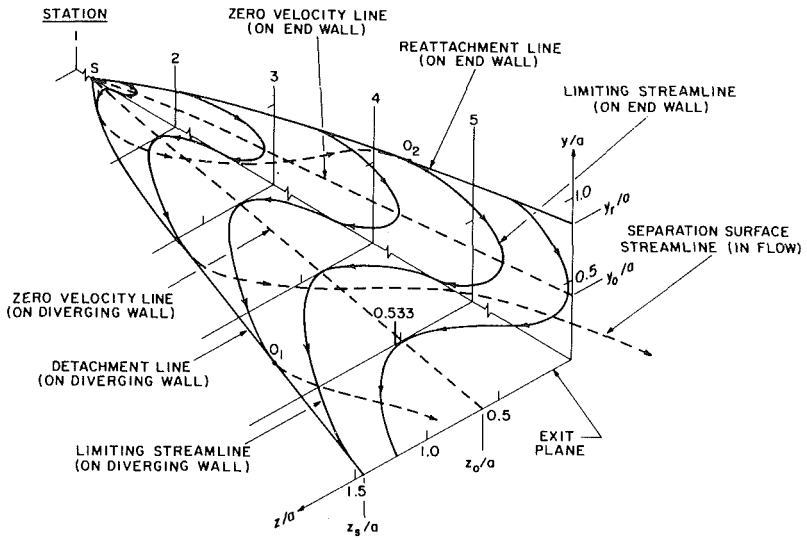

Fig. 4 Structure of the separation bubble in the corner region (2ϕ = 8 deg)

The results shown in Fig. 3 can be interpreted more fully by referring to Fig. 4, which shows details of the separation bubble inferred from the patterns in Fig. 3. The limiting wall streamlines in Fig. 4 bound the lower portion of a separation bubble which emanates from an isolated singular point, S, on the corner line between Stations 1 and 2. The exact position of this singular point could not be discerned in the present study. It was also not possible to discern whether limiting wall streamlines on the diverging wall, for example, actually coalesce to form a locus of points along which local flow detachment occurs (following Maskell's [25] interpretation) or whether limiting wall streamlines approach the detachment line asymptotically, as Lighthill [26] conjectures. In the present study, Maskell's point of view was adopted, so that the streamline pattern shown in Fig. 4 reflects his interpretation of detachment and reattachment behavior in three-dimensional, bubble-type separating flows. The limiting wall streamlines on the diverging wall thus terminate along a locus of points which can be interpreted as a detachment or separation line, along which fluid must leave the surface to avoid a build-up on this line. Similarly, limiting wall streamlines on the end wall emanate from a line along which fluid on the outer surface of the bubble must reattach to avoid fluid depletion on this line. The detachment and reattachment lines shown in Fig. 4 are thus lines along which ordinary separation and reattachment occur (typically at points 0_1 and 0_2), and flow on the outer surface of the bubble must be spiral-like in nature to accommodate the detachment-reattachment pattern which has been observed. On the basis of an analysis by Mojola [27], the detachment and reattachment lines should emanate from the singular point on the corner line in cusp-free fashion (normal to the corner line). This behavior was not observed in the present study, however, because of resolution difficulties in the vicinity of the separation point.

The zero velocity lines shown in Fig. 4 correspond to the locus of points where the limiting wall streamlines are everywhere tangent to lines normal to the corner line, so that the streamwise component of the time-averaged wall shear stress is identically zero on these lines. In the region between these lines and the detachment or reattachment lines, the time-averaged fluid motion is forward facing, and the local wall shear stress varies markedly in both magnitude and direction. A similar comment applies for wall shear stress behavior in the region between the zero velocity lines and the corner line, except that the flow is locally reversed (on a time-averaged basis) in this region. In Fig. 4, the position of the zero velocity lines (typically at y_0/a and z_0/a) and the position of the detachment line (typically at z_s/a) correspond to the observed positions of these lines (to within an estimated uncertainty of $\Delta y/a = \pm 0.07$ or $\Delta z/a = \pm 0.07$). The nominal position of the reattachment line shown in Fig. 4 (typically at y_r/a) is only approximate, inasmuch as the position of this line could not be distinguished by visual observation.

Before discussing hot-wire and pressure probe measurements in the flow, it should be noted that the limiting wall streamline pattern in the corner region of a symmetrically expanding square duct must be radically different from the pattern shown in Fig. 4. In this case, the only admissible pattern is one which is symmetric about the corner line. A plausible pattern would consist of limiting wall streamlines on each wall bounding the corner similar to those shown on the diverging wall of Fig. 4. Under these conditions, limiting wall streamlines on each wall would emanate from an "attachment" line coincident with the corner line, and fluid downstream of the expansion would serve wholly as the source of fluid within the region of locally reversed flow bounded by the zero velocity lines and the corner line. The exact nature of the separation bubble under these conditions merits further study.

Downstream Station Profiles (Stations 1-5). The streamwise development of the axial mean flow is shown in Fig. 5, which indicates that the diverging and end wall boundary layers develop at approximately the same rate. This behavior is in contrast to that observed by Norbury [18] in a rectangular diffuser having an inlet aspect ratio of unity, wherein the diverging wall boundary layers developed approximately twice as fast as the end wall boundary layers. The distortion which appears in the isotach contours shown in Fig. 5 (especially near the end wall at Station 5) is due primarily to a displacment effect induced by formation of the separation bubble, rather than corner generated secondary flows. The relative position of the $U/U_c = 0$ isotach at Stations 3 and 5 is in remarkably good agreement with the zero velocity points determined by means of oil flow visualization, even though the sensing element (a circular pitot tube) was subject to large-scale fluctuations and intermittent flow reversal in the near-corner region.

In order to examine the extent of local law-of-the-wall

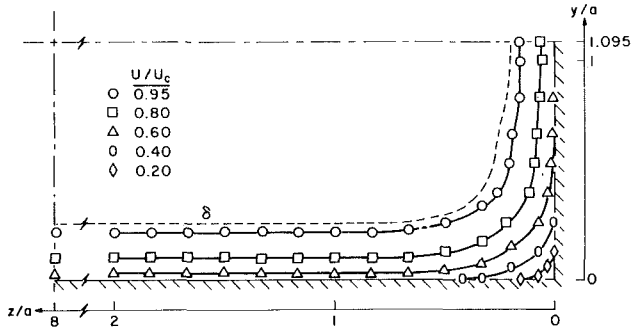

Fig. 5(*a*) Station 1

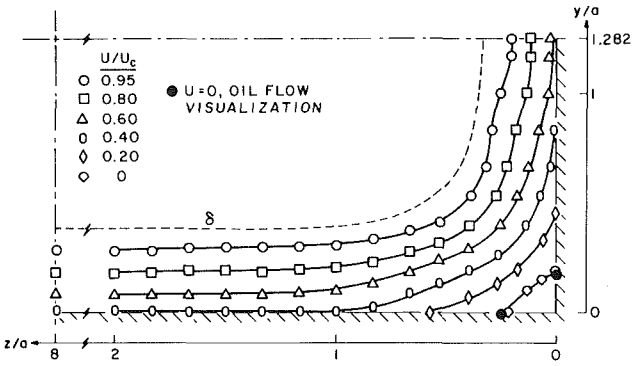

Fig. 5(*b*) Station 3

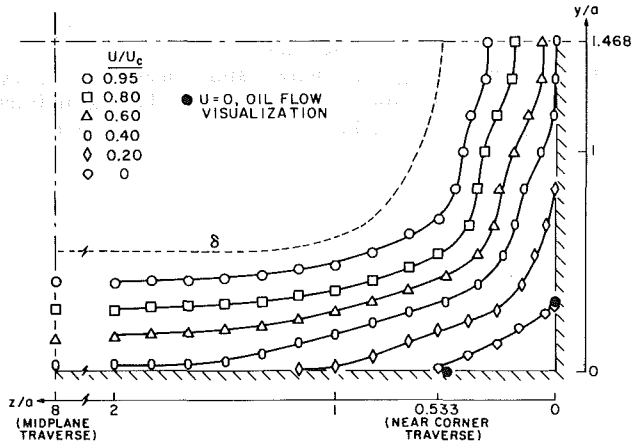

Fig. 5(*c*) Station 5

Fig. 5 Isotach contours (2ϕ = 8 deg)

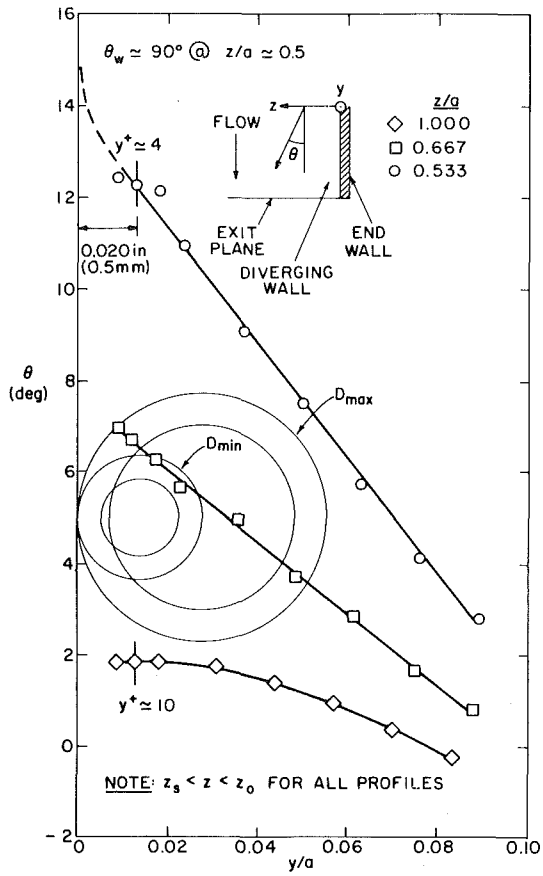

Fig. 6 Flow angle profiles near the diverging wall (2ϕ = 8 deg)

behavior at downstream stations with locally detached flow present in the corner region, it was first necessary to determine, or at least estimate, skewness characteristics of flow in the near-wall region. Between the diffuser mid-plane positions and the detachment or reattachment line locations shown in Fig. 4 ($y_r/a \le y/a \le y_{cl}/a$ or $z_s/a \le z/a \le 8$), local flow angles along traverses normal to the diverging wall and end wall were assumed to be less than 10 deg, which corresponds to the maximum observed angle of inclination of the detachment line relative to the corner line. For traverses within the forward-facing-flow portions of the separation bubble ($y_0/a \le y/a \le y_r/a$ or $z_0/a \le z/a \le z_s/a$) a more accurate determination of skewness levels had to be made, inasmuch as the near-wall flow undergoes a turning angle of approximately 90 deg between the zero velocity lines and the detachment and reattachment lines.

Figure 6 shows yaw angle profiles measured at Station 5 along traverses normal to the diverging wall at z/a locations between the zero velocity line (z_0/a) and the detachment line (z_s/a). Along the traverse closest to the zero velocity line (z/a = 0.533; refer to Fig. 4), measured yaw angles at points beyond the first point where velocity profile data were taken (y/a = 0.0067) are less than 13 deg, and are even less along the adjacent two traverses (z/a = 0.667 and z/a = 1.000). Along all of these traverses, measured yaw angles in the immediate vicinity of the wall are likely to be 2 to 3 deg below actual values by virtue of aerodynamic interference effects induced by probe proximity to the wall [28]. Even if this correction is applied, however, local yaw angles are still less than 10 deg along the traverses at z/a = 0.667 and 1.000, and do not exceed 15 deg along the traverse at z/a = 0.533. In view of this behavior, all pressure and hot-wire probe data at the downstream stations were taken with probes aligned with the axial flow direction. Under these conditions, the maximum deviation in measured axial mean velocity component values caused by probe misalignment was estimated to be less than 1-1/2 percent along all diverging and end wall traverses, with the exception of traverses closest to the zero velocity lines, where the maximum deviation was estimated as 3 percent for the first few data points closest to the wall.

The use of Preston tubes within the forward-facing-flow portions of the separation bubble also required close scrutiny before their actual application to measure local wall shear stress values. The outside diameter and tube wall thickness of the largest and smallest diameter Preston tubes selected for measurements at Station 5 are shown to scale in Fig. 6. The most severe operating condition occurs when the smallest probe is positioned at z/a = 0.533, where the flow is inclined at an angle of approximately 12 deg relative to the probe axis.

For these operating conditions, Prahlad [29] has shown that the total pressure indicated by a Preston tube aligned with the axial flow direction differs by less than 2 percent from the true total pressure. On the basis of this result, all Preston tube data at the downstream stations were taken with probes aligned with the axial flow direction, and two-dimensional calibration data were used to reduce the readings. The latter approach again assumes that log-law behavior exists along each diverging and end wall traverse, and at least applies approximately along traverses within the forward-facing-flow regions of the corner separation bubble. The validity of this assumption will be demonstrated shortly.

Figure 7 shows distributions of the streamwise component of the local wall shear stress measured at three downstream stations (Stations 1, 3, and 5) relative to the distribution measured at the inlet station (Station 0). Each distribution measured on the end wall (y/a variable) terminates at the horizontal midplane of the diffuser. In general, values measured by the different diameter Preston tubes at a given point are in good agreement, and the limiting behavior of distributions measured at Stations 3 and 5 is compatible with the zero values determined by means of oil flow visualization. The tendency of wall shear stress distributions on the diverging and end walls at Station 1 to approach the corner line normally is also in accord with the corner flow separation criterion developed by Mojola [30].

In high intensity flows with intermittent flow reversal, it is not possible to state *a priori* whether flattened pitot tube or hot-wire probe readings will be inherently more accurate. In order to determine the preferred method of measurement within the forward-facing-flow regions of the separation bubble, comparative measurements were made at Station 5 at the same z/a location noted earlier where operating conditions are particularly severe ($z/a = 0.533$; refer to Fig. 4). Axial mean velocity profiles measured at this location by four different methods are shown in Fig. 8. In general, all methods agree well in the outer portion of the boundary layer ($y/a > 0.2$). In the inner region, however, values based on linearized and nonlinearized hot-wire data exceed flattened pitot tube values by 100 percent or more. Similar behavior has been noted in the high intensity region of a pressure driven, three-dimensional turbulent boundary layer [28]. An opposite effect has been observed, however, in a nominally two-dimensional turbulent boundary layer near incipient separation [31], which serves to illustrate the complexity of the problem.

In order to reconcile the differences observed in the present study, the profiles shown in Fig. 8 were plotted in terms of law-of-the-wall coordinates, as shown in Fig. 9. From the figure it is apparent that only flattened pitot tube values exhibit correct behavior in the viscous sublayer, which presumably still exists at $z/a = 0.533$. It should be noted that the elevated hot-wire values shown in Fig. 9 are not attributed to probe offset or wall proximity effects, inasmuch as comparable distributions measured at the vertical midplane ($z/a = 8$) both agreed well with the viscous sublayer distribution at this location. The elevated U_y^+ values based on non-linearized hot-wire data would tend to follow the viscous sublayer distribution if the friction velocity were increased by a factor of approximately two. This would require, however, a four-fold increase in the measured wall shear stress at $z/a = 0.533$, which is considered implausible and would distort the overall wall shear stress distribution from the limiting form shown in Fig. 7. For compatibility between U_y^+ values based on linearized hot-wire data and the viscous sublayer distribution shown in Fig. 9, an even greater (six fold) increase in the local wall shear stress value at $z/a = 0.533$ would be required. These results were interpreted to mean that the local wall shear stress distributions shown in Fig. 7 are reasonably

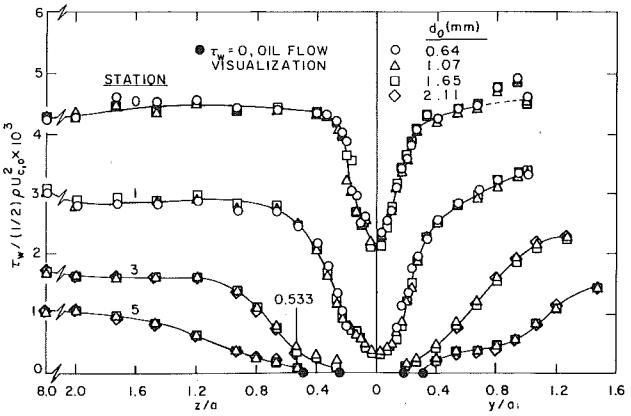

Fig. 7 Local wall shear stress distributions ($2\phi = 8$ deg)

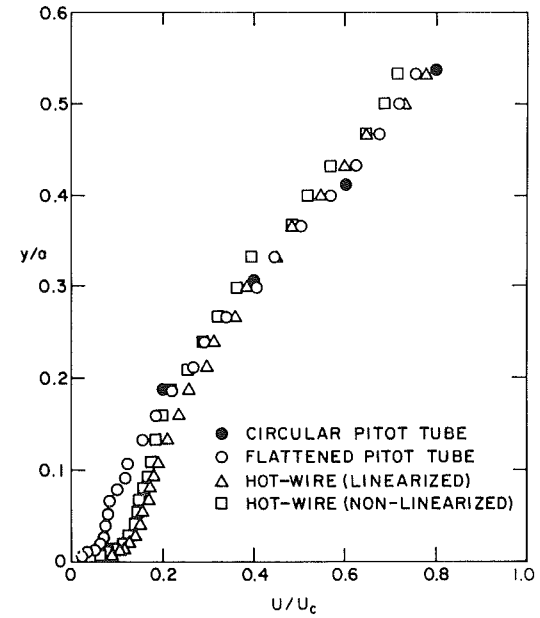

Fig. 8 Comparison of velocity profiles at $z/a = 0.533$, Station 5 ($2\phi = 8$ deg)

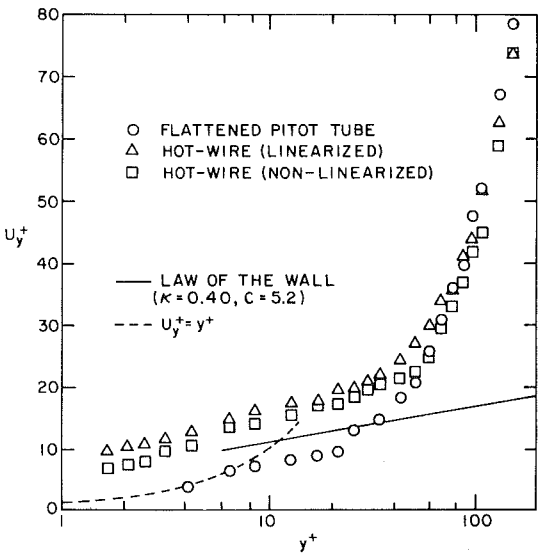

Fig. 9 Comparison of velocity profiles in law-of-the-wall coordinates at $z/a = 0.533$, Station 5 ($2\phi = 8$ deg)

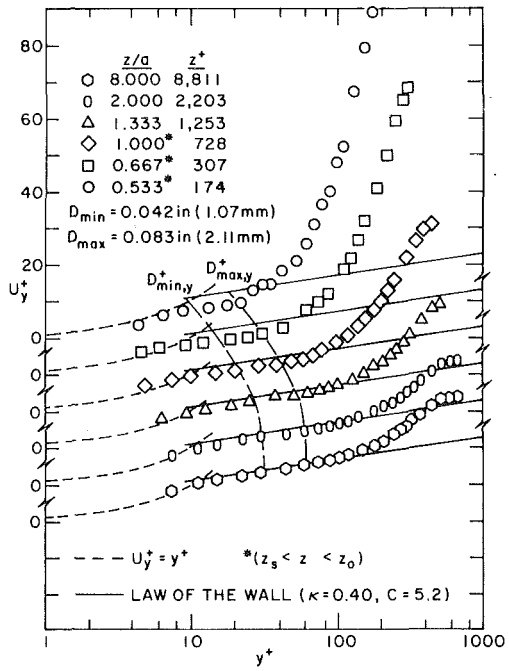

Fig. 10(*a*) Diverging wall

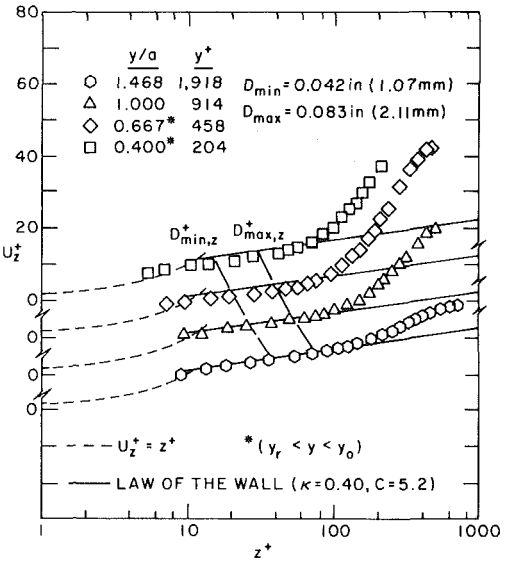

Fig. 10(*b*) End wall

Fig. 10 Velocity profiles in law-of-the-wall coordinates at Station 5 (2ϕ = 8 deg)

accurate, and that actual flow conditions at $z/a = 0.533$ are best represented by the flattened pitot tube profiles shown in Fig. 8 and 9. Accordingly, this method of measurement was used to determine axial mean velocity profiles at all of the downstream stations.

Figure 10 shows velocity profiles measured at Station 5 along the diverging and end walls of the diffuser. Profiles within the forward-facing-flow regions of the separation bubble are indicated by an asterisk (*). The y^+ and z^+ locations of the outside diameter of the largest and smallest Preston tubes used to determine local wall shear stress values are also shown. Profiles measured at locations between points distant from the corner and the detachment and reattachment lines shown in Fig. 4 generally exhibit local law-of-the-wall behavior until y^+ or z^+ exceeds 100. Profiles within the separation bubble tend to become more "wake-like" in character as each zero velocity line is approached (at $y_0/a \simeq 0.3$ and $z_0/a \simeq 0.5$; refer to Fig. 5), but still exhibit acceptable behavior within the viscous sublayer. The level of agreement between measured distributions and the reference (solid line) distribution in Fig. 10 indicates that the two-dimensional form of the law of the wall, with U and u_τ defined as the streamwise components of the total velocity vector and friction velocity vector, respectively, provides an acceptable fit of the data.

Inasmuch as skewness angles associated with flow in the separation bubble beyond the viscous sublayer were relatively moderate ($\theta \leq 12$ deg; refer to Fig. 6), no attempt was made to find a more exact log-law relationship from among those which have been proposed previously for three-dimensional skewed boundary layers [32]. Some comparisons can still be made, however, with previous work in this area. For example, the y^+ value corresponding to the first U_y^+ value measured at $z/a = 0.533$ ($y^+ \simeq 4$; refer to Fig. 10(*a*)), when positioned relative to the yaw angle profile as shown in Fig. 6, implies that the mean flow undergoes a severe turning (greater than 60 deg) within the viscous sublayer. Prahlad [33] has observed similar behavior, albeit in a diminished sense, within a pressure-driven, three-dimensional turbulent boundary layer. Figure 6 also indicates quite clearly that the flow angle changes continuously as the viscous sublayer is approached, so that flow in the near-wall region of the separation bubble is definitely not collateral. This behavior is in accord with recent observations of near-wall flow in pressure-driven, skewed boundary layers, where the presence of collateral velocity profiles is now regarded as questionable [32, 34].

Conclusions

The present study has focused on the nature of turbulent flow within a high-inlet-aspect ratio rectangular diffuser having locally detached flow in the corner region, but attached flow elsewhere within the diffuser. The diffuser configuration consisted of two symmetrically diverging walls and two parallel end walls. The core flow at the diffuser inlet was essentially uniform, and the diffuser exhausted directly to the atmosphere. The following conclusions apply for a high Reynolds number, low Mach number, thin-inlet-boundary-layer operating condition.

1. When local flow detachment occurs, a separation bubble is formed in each corner which emanates from an isolated singular point on the corner line. The limiting streamlines on the diverging and end walls from an "S"-shaped pattern about the corner line. Each streamline emanates from a line interpretable as a reattachment line and terminates on a line interpretable as a detachment line. Flow on the outer surface of the separation bubble is spiral-like in nature to accommodate the detachment-reattachment pattern which has been observed.

2. Limiting streamlines on the diverging wall undergo a turning angle of approximately 90 deg between the detachment line and zero velocity line on that wall. Similar behavior exists on the end wall between the zero velocity and reattachment lines. The adjacent near-wall flow undergoes a severe turning within the viscous sublayer (y^+ or $z^+ \leq 5$), with only moderate changes in flow direction outside this layer. Inasmuch as the flow angle varies continuously throughout the boundary layer, no evidence of collateral flow was found in the present study.

3. The two-dimensional form of the law-of-the-wall applies along traverses normal to the diverging and end walls of the diffuser between the midplane regions and the detachment and reattachment lines bounding the separation bubble. This conclusion applies when U_y^+ and y^+ (or U_z^+ and

z^+) are based on the streamwise components of the total velocity vector and friction velocity vector.

Acknowledgment

This work was supported by the Office of Naval Research by means of a contract with Project SQUID. The authors would like to express their appreciation to ONR for its support of this study.

References

1 Kline, S. J., Abbott, D. E., and Fox, R. W., "Optimum Design of Straight-Walled Diffusers," ASME *Journal of Basic Engineering*, Vol. 81, 1959, pp. 321-333.

2 Fox, R. W., and Kline, S. J., "Flow Regimes in Curved Subsonic Diffusers," ASME *Journal of Basic Engineering*, Vol. 84, 1962, pp. 303-312.

3 Reneau, L. R., Johnston, J. P., and Kline, S. J., "Performance and Design of Straight, Two-Dimensional Diffusers," ASME *Journal of Basic Engineering*, Vol. 89, 1967, pp. 141-150.

4 Senoo, Y., and Nishi, M., "Prediction of Flow Separation in a Diffuser by a Boundary Layer Calculation," ASME JOURNAL OF FLUIDS ENGINEERING, Vol. 99, 1977, pp. 379-389.

5 Reneau, L. R., and Johnston, J. P., "A Performance Prediction Method for Unstalled, Two-Dimensional Diffusers," ASME *Journal of Basic Engineering*, Vol. 89, 1967, pp. 643-654.

6 Moses, H. L., and Chappell, J. R., "Turbulent Boundary Layers in Diffusers Exhibiting Partial Stall," ASME *Journal of Basic Engineering*, Vol. 89, 1967, pp. 655-665.

7 Bardina, J., Lyrio, A., Kline, S. J., Ferziger, J. H., and Johnston, J. P., "A Prediction Method for Planar Diffuser Flows," ASME JOURNAL OF FLUIDS ENGINEERING, Vol. 103, 1981, pp. 315-321.

8 Lyrio, A. A., Ferziger, J. H., and Kline, S. J., "An Integral Method for the Computation of Steady and Unsteady Turbulent Boundary Layer Flows, Including the Transitory Stall Regime in Diffusers," Report PD-23, Thermosciences Division, Dept. of Mech. Engrg., Stanford University, March 1981.

9 Waitman, B. A., Reneau, L. R., and Kline, S. J., "Effects of Inlet Conditions on Performance of Two-Dimensional Subsonic Diffusers," ASME *Journal of Basic Engineering*. Vol. 83, 1961, pp. 349-360.

10 Wolf, S., and Johnston, J. P., "Effects of Nonuniform Inlet Velocity Profiles on Flow Regimes and Performance in Two-Dimensional Diffusers," ASME *Journal of Basic Engineering*, Vol. 91, 1969, pp. 462-474.

11 Carlson, J. J., Johnston, J. P., and Sagi, C. J., "Effects of Wall Shape on Flow Regimes and Performance in Straight, Two-Dimensional Diffusers," ASME *Journal of Basic Engineering*, Vol. 89, 1967, pp. 151-160.

12 Smith, C. R., Jr., and Kline, S. J., "An Experimental Investigation of the Transitory Stall Regime in Two-Dimensional Diffusers, Including the Effects of Periodically Disturbed Inlet Conditions," Report PD-15, Thermosciences Division, Dept. of Mech. Engrg., Stanford University, August 1971 (see also ASME JOURNAL OF FLUIDS ENGINEERING, Vol. 96, 1974, pp. 11-15).

13 Kaiser, K. F., and McDonald, A. T., "Effect of Wake-Type Nonuniform Inlet Velocity Profiles on First Appreciable Stall in Plane-Wall Diffusers," ASME JOURNAL OF FLUIDS ENGINEERING, Vol. 102, 1980, pp. 283-289.

14 Ashjaee, J., and Johnston, J. P., "Straight-Walled, Two-Dimensional Diffusers-Transitory Stall and Peak Pressure Recovery," ASME JOURNAL OF FLUIDS ENGINEERING, Vol. 102, 1980, pp. 275-282.

15 Masuda, S., Ariga, I., and Watanabe, I., "On the Behavior of Uniform Shear Flow in Diffusers and its Effect on Diffuser Performance," ASME *Journal of Engineering for Power*, Vol. 93, 1971, pp. 377-385.

16 Masuda, S. Ariga, I., and Watanabe, I., "Uniform Shear Flow Within Parallel-Walled Diffusers," ASME Paper No. 75-FE-34, 1975.

17 McMillan, O. J., and Johnston, J. P., "Performance of Low-Aspect-Ratio Diffusers with Fully Developed Turbulent Inlet Flows, Part I—Some Experimental Results," ASME JOURNAL OF FLUIDS ENGINEERING, Vol. 95, 1973, pp. 385-392.

18 Norbury, J. F., "Some Measurements of Boundary-Layer Growth in a Two-Dimensional Diffuser," ASME *Journal of Basic Engineering*, Vol. 81, 1959, pp. 285-296.

19 Sharma, D., "Turbulent Convective Phenomena in Straight, Rectangular-Sectioned Diffusers," Ph.D. thesis, Mech. Engrg. Dept., Imperial College of Science and Technology, London, 1974.

20 Kutateladze, S. S., Kashinskiy, O. N., and Mukhin, V. A., "Experimental Study of Characteristics of Turbulent Boundary Layers in Adverse Pressure Gradients," *Fluid Mechanics—Soviet Research*, Vol. 7, No. 4, July-Aug. 1978, pp. 1-33.

21 Yefimenko, G. I., and Khapakhpasheva, Ye. M., "Effect of Adverse Pressure Gradients on the Structure of Wall Turbulence," *Fluid Mechanics—Soviet Research*, Vol. 7, No. 4, July-Aug. 1978, pp. 34-49.

22 Khapakhpasheva, E. M., Yefimenko, G. N., and Gruzdeva, I. M., "Investigation of Wall Turbulence Characteristics in a Short Plane Diffuser," *Fluid Mechanics—Soviet Research*, Vol. 7, No. 5, Sept.-Oct. 1978, pp. 37-61.

23 Chan, Y. L., "A Study of Local Flow Behavior in a Streamwise Corner of a Rectangular Diffuser," M. S., thesis, Dept. of Mech. Engrg., University of Washington, 1980.

24 Gessner, F. B., and Chan, Y. L., "Flow in a Rectangular Diffuser with Local Flow Detachment in the Corner Region," *Three Dimensional Turbulent Shear Flows*, Ed. S. Carmi, et al., ASME Book No. G00211, 1982, pp. 11-22.

25 Maskell, E. C., "Flow Separation in Three Dimensions," Report No. Aero. 2565, Royal Aircraft Establishment, Farnborough (England), 1955.

26 Lighthill, M. J., "Attachment and Separation in Three-Dimensional Flows," *Laminar Boundary Layers*, Ed. L. Rosenhead, Oxford University Press, 1963, pp. 72-82.

27 Mojola, O. O., "The Viscous Sublayer in a Streamwise Corner," ASME *Journal of Applied Mechanics*, Vol. 45, 1978, pp. 219-221.

28 Vagt, J. D., and Fernholz, H. H., "A Discussion of Probe Effects and Improved Measuring Techniques in the Near-Wall Region of an Incompressible Three-Dimensional Turbulent Boundary Layer," AGARD Conference Proceedings, No. 271, 1980, pp. 10-1 to 10-17.

29 Prahlad, T. S., "Yaw Characteristics of Preston Tubes," *AIAA Journal*, Vol. 10, No. 3, 1972, pp. 357-359.

30 Mojola, O. O., "Steady Flow Separation Along a Straight Streamwise Corner," *Applied Scientific Research*, Vol. 31, 1976, pp. 431-436.

31 Simpson, R. L., Strickland, J. H., and Barr, P. W., "Features of a Separating Turbulent Boundary Layer as Revealed by Laser and Hot Film Anemometry," *Turbulence and Liquids*, Ed. G. K. Patterson and J. L. Zakin, Dept. of Chem. Engrg., University of Missouri—Rolla, 1975, pp. 151-171.

32 Pierce, F. J., and McAllister, J. E., "Near-Wall Similarity in a Pressure-Driven Three-Dimensional Turbulent Boundary Layer," Report VPI-E-80.32, Mech. Engrg., Virginia Polytechnic Institute and State University, 1980.

33 Prahlad, T. S., "Mean Velocity Profiles in Three-Dimensional Incompressible Turbulent Boundary Layers," *AIAA Journal*, Vol. 11, No. 3, 1973, pp. 359-365.

34 Fernholz, H. H., and Vagt, J. D., "Turbulence Measurements in an Adverse-Pressure-Gradient Three-Dimensional Turbulent Boundary Layer Along a Circular Cylinder," *Journal of Fluid Mechanics*, Vol. 111, 1981, pp. 233-269.

Analysis of the Frequency Response of a Fluid Amplifier Using Unsteady Flow Characteristics

R. Caen
Maitre-Assistant.

C. Fonade
Maitre-Assistant

Institut National Polytechnique
de Toulouse,
Institut de Mecanique des Fluides,
Laboratoire 005 Associé au C.N.R.S.,
31071 Toulouse Cedex, France

This paper is mainly concerned with the theoretical and experimental study of the frequency response of an analog fluid amplifier. The channels are considered as distributed parameter systems and the frequency effects on the charcteristics of nozzles, vents, and jet interaction are taken into account. The paper considers the dynamic behavior of the flow in vortex vents and the interaction of two jets : a discontinuous profile is used to approximately describe the average velocity distribution in the jet in order that a recursive solution for the eigenvalues resulting from a small perturbation be obtained. The amplifier was tested by means of an electropneumatic signal generator at frequencies up to 3000 Hz. A comparison with experiments performed in the potential core region shows that the linear theory correctly predicts the passband of the jet which is constant provided a local Strouhal number is used.

1 Introduction

The analysis of the dynamic performance of a proportional (or analog) fluid amplifier is an interesting basic approach to the dynamic performance of pneumatic control systems, as several different types of flow geometry must be taken into account, specifically, the internal flows in variable-area channels, the interaction of free flows, and vortex flows through certain vents. The first analyses relative to such an amplifier were carried out assuming that channel response may be represented adequately by a lumped-parameter system (pressure drop, inertia, capacity) and that the interaction of the supply and control jets corresponds only to a delay in signal transmission [1-3]. Experience has allowed the validity of these hypotheses to be demonstrated for certain amplifier configurations. However, when high frequencies are considered, or more generally when the Strouhal number increases, methods based upon distributed parameter systems become necessary. Such theories were developed for lines [4-6], but they should nevertheless be applicable to the amplifier configuration.

On the other hand, in cases of jet interaction and vortex flows, the few results that are available are difficult to apply to the complete analysis of the dynamic response of the amplifier. This paper proposes solutions for both these flow types, and shows that, by associating them with line theory, it is possible to predict the frequency response of a complex flow, such as exists in a proportional fluid amplifier (Aviation Electric Ltd. type 13000 P01 - Fig. 1).

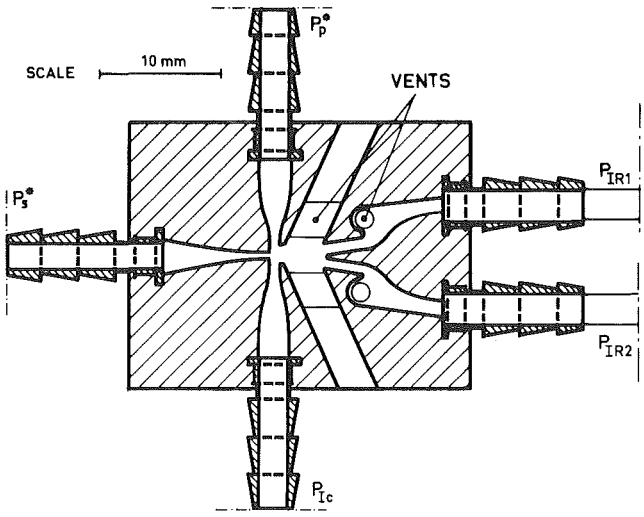

Fig. 1 Geometry of A.E.L. amplifier (channel depth : 1 mm, connection diameter : 2.45 mm)

2 Experimental Methods

The experiments are mainly concerned with the dynamic response of a vortex flow and of a complete amplifier, and the dynamic interaction of two plane jets. Block diagrams are given in Fig. 2, while the experimental setups are described in the following paragraphs.

For analysis of the vortex model and the proportional amplifier, an electropneumatic generator [7] is used to generate the input signal (maximum peak-to-peak amplitude :

Contributed by the Fluids Engineering Division for publication in the JOURNAL OF FLUIDS ENGINEERING. Manuscript received by the Fluids Engineering Division, October 10, 1980.

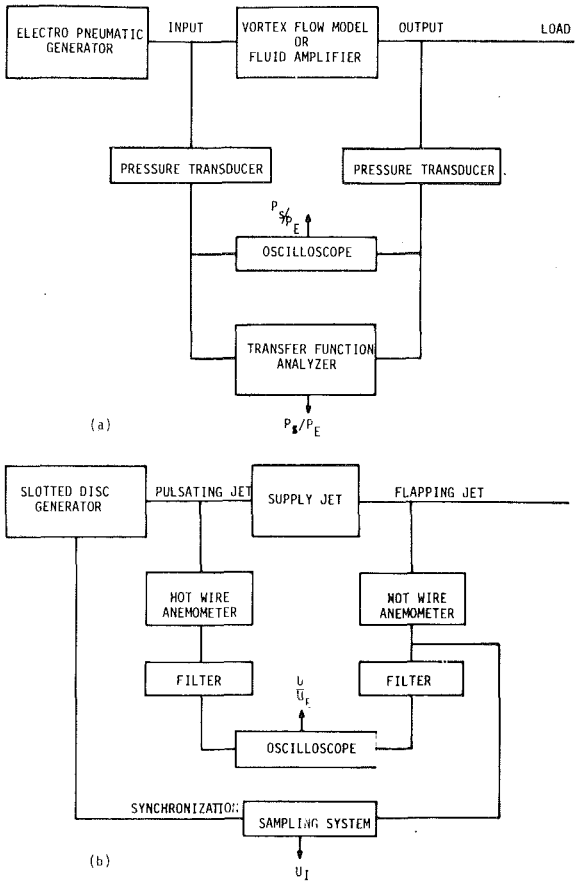

Fig. 2 Block diagrams of the test setup

8 mb ; maximum average flow : 0.15 l/s ; distortion : 2 percent at 1000 Hz). Pressures are measured by means of "Sensortec" flush-mounted sensors 3.2 mm in diameter (± 1 percent frequency range 0-10 KHz). The difference between the frequency response of the two sensors and the integrating effect on the membrane surface [8] give at the highest frequencies used, an error of less than 8 percent in the Ps/Pe amplitude ratio and an out-of-phase error of less than 10 deg.

In the analysis of the interaction of two jets, the input signal is provided by a slotted-disk generator capable of providing the necessary flow rate. A variable capacity placed in parallel enables the signal amplitude to remain constant for all frequencies. Velocity measurements have been made with DISA type 55 M anemometers associated with linearizers and, possibly, filters. Measurement error comes essentially from the instability of the generator signals but the same measurement was made several times and an average taken. Moreover, the filters used have frequency responses each of which can vary by a maximum of 5 percent relative to the other and so the relative error in the measurement of velocity variation amplitudes is estimated to be less than 10 percent. Finally, when the flows were very turbulent, a SAICOR-53 correlator was used to sample and average the instantaneous signal.

3 Dynamic Behavior of Vortex Flows

The vortex vent of the amplifier (Fig. 1) constitutes a dynamic impedance branched from the receiver which must be used in calculating the total amplifier response. The action of the vent is only apparent when the receiver is loaded : the hypothesis of an infinite receiver output impedance is thus adopted. Analysis of the distribution of static pressures in steady flow was carried out on a 10 times full size model of the vent (Fig. 3). The results demonstrate that it is indeed a vortex type flow with negative relative pressure in the central core.

Earlier work showed that the dynamic behavior of vortex valves can be represented either by a first order system [9-11], or by a second order system [12, 13], according to the load and flow conditions.

We carried out an analysis of the vortex flow in a free surface model [14]. The flow in the cylindrical chamber (1 m diameter) is the result of the interaction of a radial supply jet Q_A and a transverse control jet with a flow varying in steps of size Q_c. Measurement of the angle Θ of the resultant jet was carried out by filming the development of the flow visualized by particles located on the free surface.

A first order response was obtained and the dynamic impedance Z_s of the vortex therefore is of the form :

$$\frac{1}{Z_s} = \frac{M_s}{P_s} = \frac{1/Z_R}{1+j\omega T} \tag{1}$$

where M_s and P_s are the complex amplitudes of the mass flow and the pressure difference across the vortex. Z_R is the static impedance and T is the time constant which is dependent on the retention time T_f (ratio of the chamber volume to the total input flow) and on the swirl coefficient λ defined as :

Nomenclature

G_I = instantaneous value
$\bar{G}$ = average value versus time
g = variation of G_I about $\bar{G}$
g' = dimensionless value of g
G = amplitude of g
G^* = static value
Above nomenclature refers to the pressure P_I, the mass flow rate M_I and the velocity of jets U_I
f = $\omega'/2\pi$ (Hz)
h,l = height and width of channels
p_n = slope of segment $\overline{M_{n-1}M_n}$ of the jet velocity profile
S_t, S_t^* = Strouhal number and modified Strouhal number

$$\left(S_t^* = S_t X = \frac{\omega X}{2\pi}\right)$$

T = time constant of the vent
Δy_0 = transverse displacement of the main jet
$\bar{U}_n$ = dimensionless average velocity at point M_n of the jet
ΔU_{Id} = ideal variation of the jet velocity
Z_0 = characteristic impedance of the line
Z_s = dynamic output impedance P_s/M_s
Z_R = static load impedance
α' = propagation factor of the line
$\sigma,\delta,\alpha,\beta$ = eigenvalues
ω' = frequency (rad/s)
ω = dimensionless frequency $\omega = \omega' l_s/\bar{U}_s$

Subscripts

α = refers to atmospheric pressure
e,s = refers to input and output sections of the line or to supply nozzle
E = refers to the control jet
c = refers to the control channel
R = refers to receivers or the real part of a quantity
I = imaginary part of a quantity

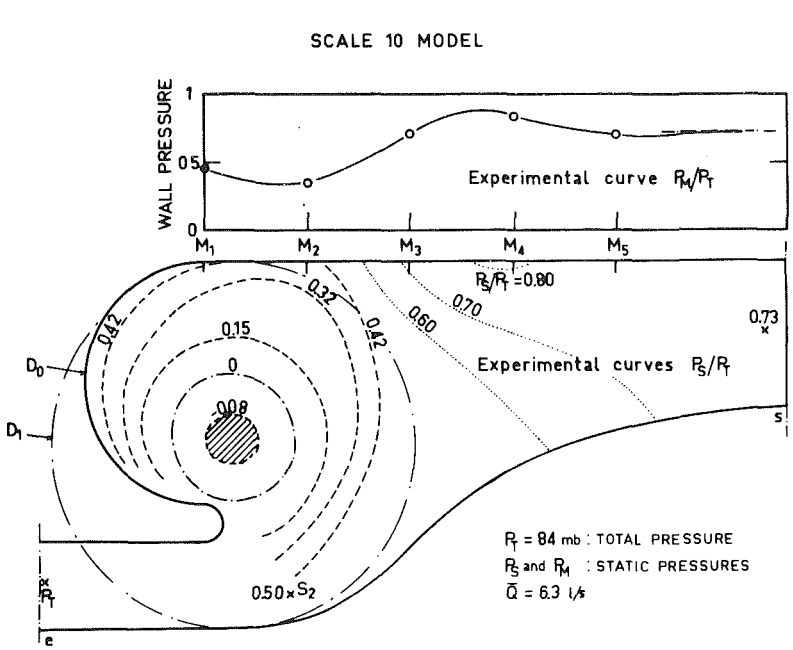

Fig. 3 Static pressure distribution in the model of the vent of amplifier (. . .lines are extrapolated from the general scheme and the wall pressure curve. Uncertainty in pressure : ±0, 5 mb)

$$\lambda = \left(\frac{Q_c}{Q_A + Q_c}\right)^2 \frac{\pi D}{l_c} \tag{2}$$

D being the chamber diameter and l_c the width of the control nozzle. On the basis of experimental results, the following empirical equation was obtained :

$$T = 5.71\, T_f \lambda^{-1.35} \tag{3}$$

Further experimentation was performed [8] using a 5 times full size model of the amplifier receiver and in accordance with Fig. 2(*a*). Theoretical results were obtained using equations (1) and (3) and pneumatic line theory. They agree well with the experimental results (Fig. 4) when, due to their different physical roles, T_f is calculated from D_0 (Fig. 3) and λ from D_1. T then equals 1.26×10^{-4} s in the model. For our specific amplifier conditions, T equals 1.3×10^{-5} s.

4 Dynamic Behavior of Interaction of Two Jets

The interaction of two jets, as shown in Fig. 5, is such that a steady jet (supply jet) is controlled by a second jet (control jet) which is orthogonal to the first and acts in the area near the supply jet nozzle. If the control jet pulsates, the resulting jet is caused to oscillate. Experiments have shown that the transverse profiles of instantaneous velocities remain very near those of a steady jet [8]. The basic problem in determining the pressure inside a receiver located opposite the jet is the calculation of the instantaneous position y_0 (x, t) of the jet axis.

An experimental study of an oscillating jet was carried out by CRAYA et al. [15], [16], who associated the flow visualization with the measurement of velocities. The geometrical configuration of the interaction area consisted of a round edged nozzle, with the control signal being fed in just upstream of the curved wall. It is therefore probable that in addition to the control jet effect, there is also an attachment effect of the jet to the curved wall : this results in a deflection angle greater than that arising solely from the interaction of two momentums. Thus if one examines the transverse displacement amplitude of the jet axis, the −6 db passband deduced from the results of these researchers corresponds to a Strouhal number S_t of 0.3. This value is greater than the one

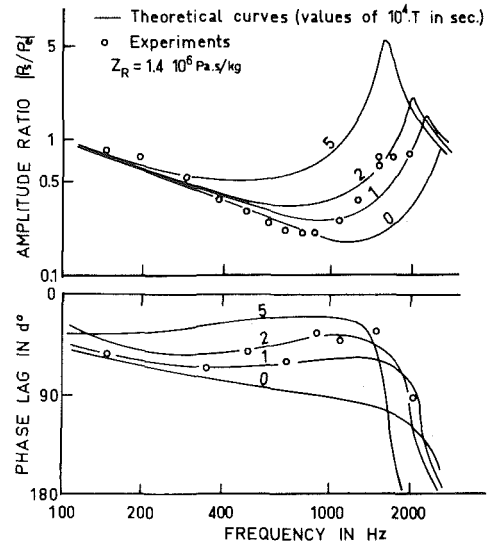

Fig. 4 Frequency response of the scale 5 model of the amplifier vortex vent (Uncertainty in $|P_s/P_e|$: ±2 percent at 200 Hz and ±4 percent at 2000 Hz, and in phase : ±10 deg)

we obtained experimentally (0.1 in the transverse section $x = 2\,l_s$).

In a theoretical study of an oscillating jet made by KIRSCHNER [17], each particle is assumed to move independently of neighbouring particles, movement being determined solely by the action of a transverse pressure gradient. This hypothesis allows accurate results to be obtained for the edge tone phenomenon but greatly overestimate the passband. Its theoretical value is about 10 times greater than the experimental value obtained in the cases of a water jet flowing in air [18] or a jet of air in air (present study).

Basic studies relating to the existence and development of large structures are being carried out at the moment. The most recent methods are based on direct numerical processing of the Reynolds equations, but the results still remain limited to certain flow configurations [19]. The complexity of such calculations is a disadvantage when the phenomenon con-

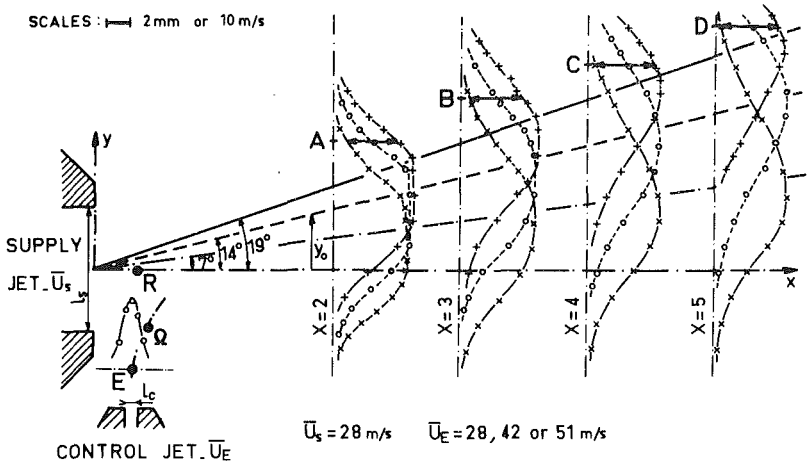

Fig. 5 Steady jet axis deflections and transverse velocity profiles (Uncertainty in velocities : ±1 m/s and in y : ±0, 1 mm)

cerned constitutes only one of the elements of the problem, which is the case in the interaction of two jets. Here, a method such as the hydrodynamic theory of stability would appear to be more appropriate.

Theoretical Study. In the hydrodynamic stability method, the development of a small disturbance superimposed on the basic flow, characterized by the transverse profile of the longitudinal velocities, is studied. Thus it was possible to find the amplification conditions for a disturbance linked to a laminar jet assumed to be a parallel flow [20], [21]. In the case under examination the problem is more complex, partly because the jet is turbulent and partly because there is an "almost parallel" flow. When the jet is turbulent, new unknown factors appear in the equations and one has to use a closure method [23]. If one considers a flow which is almost parallel, the conventional method is to study the stability by locally replacing the real flow with a parallel flow : this then leads to a solution of the Orr-Sommerfeld equation. Works such as [24] and [25] have shown that the use of a multiple scale method allows the precision of the theoretical results to be improved, so that they become closer to experimental results. However, since it only represents a part of our problem, the use of such methods would appear unsuitable and we have therefore made the following assumptions :

- the approximation of an "almost parallel" flow is used. The components u' and v' of the disturbance velocity can then be defined using the function valid for the two-dimensional Tollmienn - Schlichting waves :

$$\Psi(X,Y,\tau) = \Phi(Y)\exp[j(\sigma X - \delta\tau)] \tag{4}$$

$$u' = \text{Real}\left(\frac{\partial\Psi}{\partial Y}\right) \qquad v' = \text{Real}\left(-\frac{\partial\Psi}{\partial X}\right)$$

Dimensionless quantities are obtained using the width l_s of the slot and the emission velocity U_s of the jet.

- the turbulent character is implicitly taken into account by considering the real velocity profile, as measured in the various transverse sections X_I of the steady jet.

Due to the shape of these profiles (Fig. 5) we represent them by a discontinuous velocity profile (Fig. 6) which allows a simplification of the solution of Rayleigh's equation :

$$\left(\bar{U}-\frac{\delta}{\sigma}\right)\left(\frac{d^2\Phi}{dY^2}-\sigma^2\Phi\right)-\frac{d^2\bar{U}}{dY^2}\Phi=0 \tag{5}$$

At each M_n point, the continuity of the disturbance transverse velocity v' and of the pressure gives the equations :

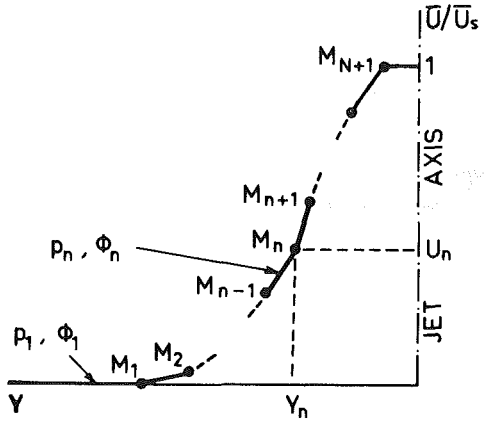

Fig. 6 Scheme of the discontinuous velocity profile

$$\begin{aligned}&[\Phi/(\bar{U}-\delta/\sigma)] \text{ continuous at } M_n\\ &\left[(\bar{U}-\delta/\sigma)\frac{d\Phi}{dY}-\frac{d\bar{U}}{dY}\Phi\right] \text{ continuous at } M_n\end{aligned} \tag{6}$$

These conditions correspond to a discontinuous surface when the fluid is assumed to be perfect [26]. The discontinuity at M_n of $(d\bar{U}/dY)$ causes that of $(d\Phi/dY)$ and therefore that of the component u'. This discontinuity depends on the slope difference of the segments at M_n and so decreases when n is increased.

The general solution Φ_n of Rayleigh's equation is therefore:

$$\Phi_n = A_n\exp(\sigma Y) + B_n\exp(-\sigma Y) \tag{7}$$

and the boundary conditions :

$$\Phi = 0 \text{ and } \frac{d\Phi}{dY} = 0 \text{ when } Y \to \pm\infty \tag{8}$$

Writing (6) at each point M_n, we obtain a recursive system in relation to the coefficients A_n and B_n which depends on the eigenvalues σ and δ.

As the profile $U(X_I, Y)$ is symmetrical, this system can be written, taking $E_n = \exp(2\sigma Y_n)$, as

$$\begin{aligned}A^*_{n+1} &= a_n A^*_n + b_n B^*_n\\ B^*_{n+1} &= c_n A^*_n + d_n B^*_n\end{aligned} \tag{9}$$

where: $n \in [1, N+1]$, $U_n = \bar{U}(M_n)$

p_n slope of the segment $\overline{M_{n-1}M_n}$

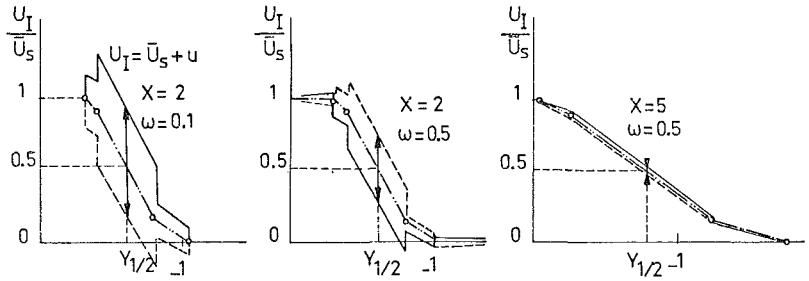

Fig. 7 Theoretical instantaneous velocity profiles (—— and ---- : extreme position during a period ; ——·—— : discontinuous average velocity profile)

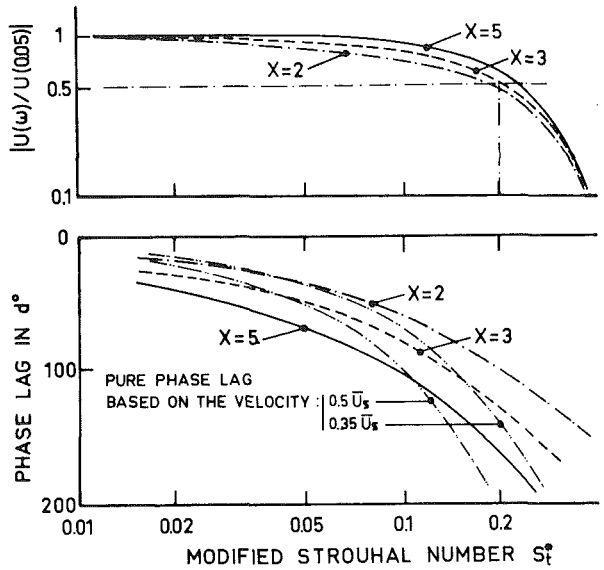

Fig. 8 Theoretical frequency response of the plane jet

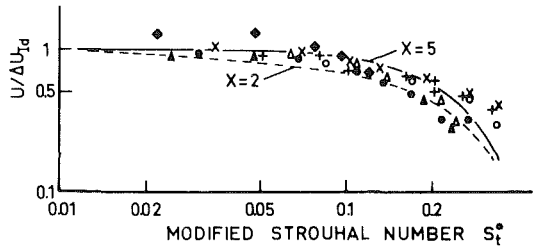

Symb.	●	▲	◆	+	Δ	o	x
l_s(mm)	9.5	9.5	9.5	9.5	9.5	9.5	5.5
U_s(m/s)	28	21	42	28	28	28	28
X	2	2	2	3	4	5	3.5

Fig. 9 Experimental frequency response of the plane jet : amplitude ratio (curves are theoretical ones. Uncertainty in $U/\Delta U_{Id}$: ±3 percent at $S_t^* = 0, 02$ and ±10 percent at $S_t^* = 0, 2$, and in $S_t^* = \pm 5$ percent)

$$A_n^* \text{ (or } B_n^*) = A_n \text{ (or } B_n). \quad \prod_{i=1}^{n-1} 2(\sigma U_i - \delta)$$

$$a_n = 2(\sigma U_n - \delta) + (p_{n+1} - p_n) = 4(\sigma U_n - \delta) - d_n$$

$$b_n = (p_{n+1} - p_n)/E_n = -c_n/E_n^2$$

All the coefficients can be obtained as a function of one of them (here B_1). The eigenvalue function is :

$$A_{N+2}^* = B_{N+2}^* \tag{10}$$

(For our problem, we choose an antisymmetrical disturbance : $u' = 0$ on the axis of the jet.)

If we consider a temporal growing of the disturbance, the eigenvalue function is a polynomial in δ, of degree (N + 1). In this case, σ is real [$\sigma = \alpha$, wave number] and δ is complex [$\delta = \alpha\ (C_R + jC_I)$, C_R is the phase velocity and C_I the amplification factor]. These eigenvalues $C_R(\alpha)$ and $C_I(\alpha)$ are obtained from equation (10).

Assuming that the reference axes move at the local phase velocity C_R, the characteristics $\beta = \sigma$ and $\omega = \delta$ of a spatially growing disturbance can be calculated :

$$\beta_R = \alpha \qquad \beta_I = -\alpha \frac{C_I}{C_R} \qquad \omega = \alpha C_R \tag{11}$$

where ω is the disturbance frequency due to the pulsating control jet.

Knowing these eigenvalues, equation (7) gives the eigenfunctions, and the velocity relative to the disturbance can be calculated, in particular the longitudinal component u' :

$$u' = \left[\frac{d\,\Phi_R}{dY} \cos(\beta_R X - \omega\tau) - \frac{d\,\Phi_I}{dY} \sin(\beta_R X - \omega\tau) \right] \exp(-\beta_I X) \tag{12}$$

Figure 7 shows typical theoretical instantaneous velocity profiles for two transverse sections of the jet. The unbroken and dotted line curves correspond to the extreme positions of the jet during a period and the broken line curve is the average velocity profile used.

The variation of amplitude U of the velocity at point $Y_{1/2}(\bar{U}/\bar{U}_s = 0.5)$ represents the extent of the deflection of the jet. Fig. 8 shows these variations and the corresponding phase lag. The use of a modified Strouhal number S_t^*, defined as :

$$S_t^* = S_t \cdot X = \frac{\omega' l_s}{2\pi U_s} X \tag{13}$$

allows to gather the results for the deflection amplitude of the jet in the whole region of the potential core. But, this is not true when the phase lag is considered : the shape of these curves does not correspond to the shape given by a pure delay, whatever the propagation velocity examined (the values 0.5 U_s and 0.35 U_s are experimental data referred to in the bibliography). However, the passband (signal attenuation of − 6db) corresponds to $S_t^* = 0.2$, a value which remains practically constant throughout the potential core.

Comparison With Experimental Results. The experiments were carried out by causing two free jets to interact (Fig. 5), one of these being steady and the other pulsating. The block diagram is shown in Fig. 2(*b*). Various l_s widths (5.5, 9.5, and 15 mm) and U_s velocities (21, 28, and 42 m/s) were used. The maximum velocity $\bar{U}_E$ of the control jet was kept at a constant value of 42 m/s. The pulsation frequency was in the range 50 - 500 Hz.

As the control jet was pulsating, the extent of velocity variation decreased along its axis $E\Omega$ (Fig. 5), this reduction

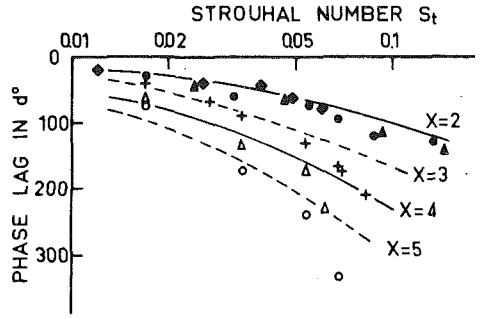

Fig. 10 Experimental frequency response of the plane jet : phase lag (for legend see Fig. 13. Uncertainty in phase : ±10 percent and in S_t : ±4 percent)

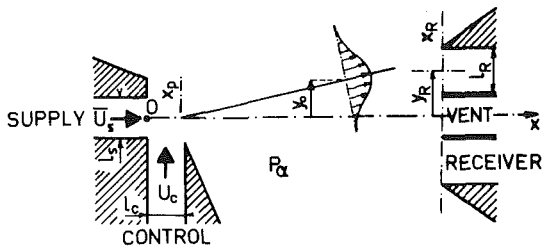

Fig. 11 Scheme of the geometry of the fluid amplifier

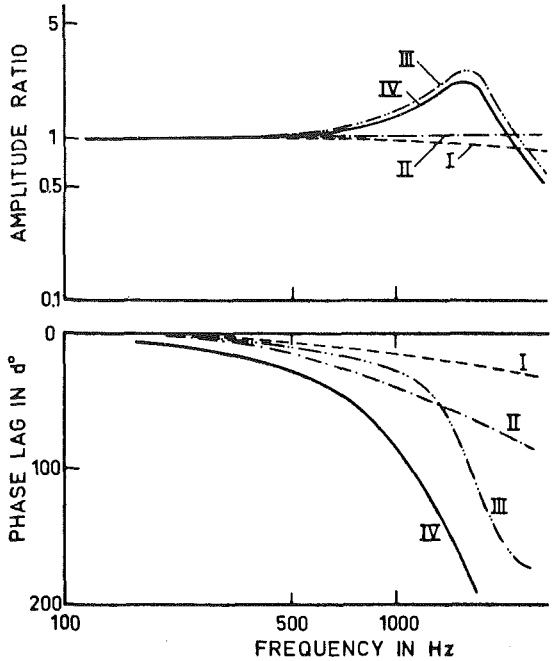

Fig. 12 Theoretical frequency responses of each part of the amplifier (I, II, III) and of the entire amplifier (IV)

being a function of the frequency and of the entrainment of the main jet.

An initial study allowed the velocity at point Ω to be linked to the velocity at the reference point E : for our purposes, the ratio between these velocities was in the range [1.27 ; 1.88] according to the value of $\bar{U}_s/\bar{U}_E$ [8].

The velocity probe was located at points A, B, C, D (Fig. 5) corresponding to the ordinate $Y_{1/2}$ of the steadily deflected jet. These velocities were measured firstly using a steady control jet, whose velocity was successively the maximum and minimum values of the pulsating jet. The variation ΔU_{Id} is then taken as a reference value in order to normalize the measurements U obtained when the control jet is pulsating. Thus the ratio $U/\Delta U_{Id}$ is proportional to $\Delta y_0/U_E$, y_0 being the instantaneous ordinate of the axis of the main jet.

The velocities U_I were displayed on an oscilloscope. Measuring their amplitudes, one obtains the experimental data given in Fig. 9. The agreement with theoretical curves (from Fig. 8) is acceptable : a good parameter for defining the amplitude attenuation of the jet oscillation is the number S_t^*. So, whatever the transverse section X considered, the -6db passband of the jet corresponds to $S_t^* = 0.2$.

On the other hand, Fig. 10 shows that the phase lag cannot agree with a constant phase velocity of the disturbance : it must increase with frequency. This was obtained in theory (Fig. 8) and was observed by Olivari [27]. Now, we can calculate the displacement amplitude Δy_{0R} of the jet axis in the transverse section of the receiver entrance. The recovered pressure is obtained by integrating the dynamic pressure $(\rho U_I^2/2)$ in this section (Fig. 11). So, when small oscillation amplitudes are considered and if $F(\omega,X)$ is the transfer function $U/\Delta U_{Id}$ (Figs. 9 and 10), the amplitude P_{Re} of the variation of the recovered pressure at the entrance of the receiver is proportional to $[U_E F(\omega,X_R)]$. The coefficient depends mainly on the characteristics of the pulsating control jet and on the real velocity profile of the main jet at a distance $X_R = 8\,l_s$ from the nozzle.

5 Frequency Response of the Analog Amplifier

The transmission of signals in pneumatic lines is calculated according to the known relationship between the pressure and the flow rate complex amplitudes shown below ;

$$\begin{bmatrix} P_e \\ M_e \end{bmatrix} = \begin{bmatrix} \cosh(\alpha' L) & Z_0 \sinh(\alpha' L) \\ \dfrac{\sinh(\alpha' L)}{Z_0} & \cosh(\alpha' L) \end{bmatrix} \begin{bmatrix} P_s \\ M_s \end{bmatrix} \tag{14}$$

When the line has a variable area, its length is divided into n parts to which equation (14) is applied [6].

Now, taking into account both the output impedance of the control channel due to the main jet, and the vortex branched from the receiver, the theoretical frequency responses of each part of the amplifier can be obtained. They are shown in Fig. 12 (I : control channel ; II : jet interaction ; III : receiver ; IV : entire amplifier).

An experimental study of the response of the amplifier was carried out as in the block diagram in Fig. 2(*a*). In order to work within the linear part of the amplifier static characteristic, the control signal amplitude was kept below 0.025 P_s^* (P_s^* : supply pressure of the main jet). The results are shown in Fig. 13, for two values of the amplifier load, and theoretical curves are also shown. They agree well, but they are improved when the output impedance Z_s has a finite value, and the pass-band value remains accurately predicted.

Due to the shape of the amplifier response curve, it would seem to be possible to represent it by a second order transfer function with a pure delay time :

$$\frac{P_{RS}}{P_{ce}} = \frac{k\, e^{-Ts}}{1 + \dfrac{2\xi}{\omega_n} s + \dfrac{s^2}{\omega_n^2}} \tag{15}$$

with $\omega_n = 10740$ rad/s , $\xi = 0.25$ and $T = 1.56\ 10^{-4}$s. However it should be noted that this approximation is acceptable because of the particular configuration of this amplifier, and only for frequencies considered here. In fact, as shown by the phase lag curve in Fig. 8 , the delay time T must be a function of the frequency and moreover the receiver

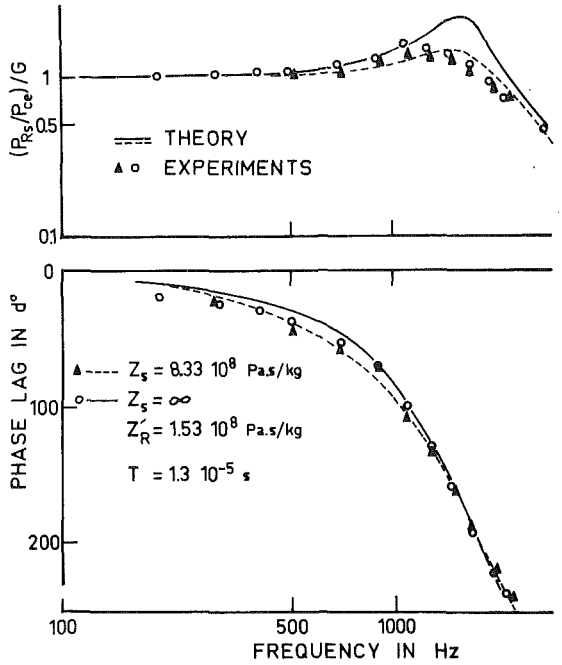

Fig. 13 Frequency responses of the A.E.L. amplifier. (Uncertainty in amplitude : ±2 percent at 200 Hz and ±4 percent at 2000 Hz, and in phase : ±10 deg).

response depends to a great extent on the position and impedance of the vortex vent. So an approximation of type (15), such as would be obtained using a lumped parameter system, is not sufficiently general.

7 Conclusion

Although different types of flow appear when the amplifier is dynamically operating, the results so obtained show that the linear theory of lines and jet interaction allow the frequency response of the amplifier to be predicted accurately. If one takes into account the difficulties encountered in measuring such flows, the agreement between theory and experiment is satisfactory. One can deduce from these results that a slight modification in the shape of the vortex vent would give a flattened curve in the amplitude ratio up to 2000 Hz, which would be an excellent characteristic for a pneumatic component.

The theoretical model was obtained by applying results which are also very useful in other projects. The study of the dynamic behavior of the water vortex valve and the general formula giving its time constant can be applied to any similar flow, for example, to jets flowing into reservoirs.

Furthermore, the agreement between the experimental results for the oscillating jet and those obtained using the small disturbance method is encouraging. However, the jet frequency response constitutes only one of the aspects of its dynamic behavior. Further studies, particularly in the experimental field, are required to increase knowledge of the interaction between an external excitation and the natural structure of the jet.

References

1 Boothe, W. A., "A Lumped Parameter Technique for Predicting Analog Fluid Amplifier Dynamics," *ISA Transaction*, Jan. 1965, Vol. 4, No. 1.

2 Healey, A. Y., "Vent Effects on the Response of Proportional Fluid Amplifier," ASME Paper No. 67-WA/Fe-12, 1967,

3 Manion, F. M., "Dynamic Analysis of Flueric Proportional Amplifiers," ASME Paper No. 68-Fe-49.

4 Nichols, N. B., "The Linear Properties of Pneumatic Transmission Lines," *ISA Transaction*, Vol. 1, No. 1, Jan. 1962.

5 Schaedel, H., "A Theoretical Investigation of Fluidic Transmission Lines With Rectangular Cross Section," Third Cranfield Fluidics Conference, 8th-10th May 1968, Turin, paper K3.

6 Dat, J., Piquemal, J., and Caen, R., "A Frequency Study of Pneumatic Convergent and Divergent Lines," IVth International Fluidics Conference, Varna, Oct. 1972, Bulgarie.

7 Dat, J., Piquemal, J., and Caen, R., "Générateur de Signaux Pneumatiques Sinusoidaux à Fréquences Élevees," *Automatisme*, Tome 13, No. 10, Oct. 1968.

8 Caen, R., "Contribution à l'Étude des Écoulements Instationnaires dans les Circuits Pneumatiques. Application à la Response Fréquentielle d'un Amplificateur Fluidique Analogique," Thèse de Doctorat-ès-Sciences, Institut National Polytechnique de Toulouse, 1979.

9 Otsap, B. A., "Experimental Study of a Proportional Vortex Fluid Amplifier," *Proceedings of the Fluid Amplification Symposium*, Harry Diamond Laboratories, Vol. II, 1964.

10 Knapp, A. B., "The Development and Control of a Ventex Vortex Amplifier," *Proceedings of Third Cranfield Fluidics Conference*, Turin, 1968.

11 Howland, G. R., "Performance Characteristics of Vortex Amplifiers," *Proceedings of the Fluid Amplification Symposium*, Harry Diamond Laboratories, Vol. II, 1965.

12 Taplin, L. B., and Seleno, A. A., "Dynamic Equivalent Circuit for a Vortex Amplifier," *Proceedings of the Fourth Cranfield Fluidics Conference*, paper B1, Coventry, 1970.

13 Jacobs, B. A., and Baker, P. J., "The Steady-State and Transient Performance of Some Large-Scale Vortex Diodes," *Proceedings of the Fifth Cranfield Fluidics Conference*, paper E2, Uppsala, 1972.

14 Papantonis, D., "Etude Expérimentale des Régimes Dynamiques de l'Écoulement dans une valve à Vortex," Thèse de Docteur-Ingénieur, Institut National Polytechnique de Toulouse, 1977.

15 Craya, M., et al., "Jets Instationnaires Pulsants et Battants," *Rapport de contrat DRME*, No. 69 34-046-00-480-74-01, 1971.

16 Favre-Marinet, M., Binder, G., and V. Hac Te, "Generation of Oscillating Jets," ASME JOURNAL OF FLUIDS ENGINEERING, Vol. 103, No. 4, Dec. 1981.

17 Kirshner, J. M., "Response of a Jet to a Pressure Gradient and its Relation to Edgetones," *2nd International JSME Symposium*, Tokyo, 1972, pp. 63-68.

18 Malcom, J. D., and Sivaram, C., "The Dynamic Response of a Free Jet," *Fluidics Quarterly*, Tome 8, 1976, pp. 77-87.

19 Boisson, H., Chassaing, P., Ha Minh, H., and Sevrain, A., "Development of the Organized Vortices in the Turbulent Near Wake of a Circular Cylinder : an Experimental and Numerical Study," *Third Symposium "Turbulent shear flows"*, 1981, Davis, Calif.

20 Michalke, A., and Schade, H., "Zur Stabilität von freien Grenzschieden," *Ingénieur Archiv. XXXIII Band*, 1963, pp. 1-23.

21 Tatsumi, T., and Kakutami, T., "The Stability of a Two Dimensional Laminar Jet," *J. Fluid Mechanics*, Vol. 4, 1958, pp. 261.

22 Kaplan, R. E., "Stability of Laminar Incompressible Boundary Layer in the Presence of Compliant Boundaries," *MIT AS RL TR 116-1*.

23 Hussain, A. K. M. F., and Reynolds, W. C., "The Mechanics of an Organized Wave in Turbulent Shear Flow. Part 3, Theoretical Models and Comparison With Experiments," *J. Fluid Mechanics*, Vol. 54, Part 2, pp. 263-288.

24 Kuen Tam, K., "On the Asymptotic Solution of the Orr-Sommerfeld Equation by the Method of Multiple-Scales," *J. Fluid Mechanics*, Vol. 34, Part 1, 1968.

25 Bouthier, M., "Stabilite Linéaire des Écoulements Presque Parallèles," *Journal de Mécanique*, Vol. 11, No. 4, Dec. 1972.

26 Drazin, P. G., "Discontinuous Velocity Profiles for the Orr-Sommerfeld Equation," *J. Fluid Mechanics*, Vol. 10, 1961, pp. 571-583.

27 Olivari, D., "Investigation of the Dynamic Response of Proportional Fluidic Amplifier," *Contrat ERO*, Avr. 1974.

S. J. Wright

E. B. Wylie

Department of Civil Engineering,
The University of Michigan,
Ann Arbor, Mich. 48109

L. B. Taplin

Sperry Vickers,
Troy, Mich. 48084

Matched Impedance to Control Fluid Transients

A methodology for the use of passive elements for transient control in pipelines is outlined. The specific objective is the elimination of pressure fluctuations in a fuel delivery line that are created by fuel injector operation. This is accomplished by the appropriate sizing of resistance elements upstream and downstream of the fuel injection system in the delivery line such that no pressure wave reflections occur in the system. The concept of matching the resistance element to the characteristic impedance of the fuel delivery system is described and applied to orifice and laminar flow elements. Experimental evidence is presented to validate the concepts.

Introduction

Control of pressure transients in closed conduits may be important in a variety of different fluid systems. Reduction in pressure fluctuations may be necessary to avoid failure, to improve the efficiency of operation, to avoid fatigue of system components, or to reduce undesirable noise or vibration problems, among other reasons. Unsteady flow is a natural consequence of required operating procedures or accidental events in many situations. The control of this unsteady flow to avoid detrimental effects is a challenge to fluid system designers. Quite commonly active elements such as relief valves, rupture disks, or control valves are designed to aid in the system control. In other cases more passive elements such as surge tanks or accumulators are useful. The prespecification of operating procedures for control devices in systems in which unsteady flow may be undesirable has been addressed under the topic of valve stroking [1]. This procedure leads to relatively sophisticated control operations to achieve the objectives.

This study addresses the design and use of a passive element to provide the desired control to the system. It is based upon the well-known principle, in electrical [2], acoustical [3], mechanical [4], and hydraulic [5–12] systems of matched impedance. However, it is not a principle that has been applied broadly or advantageously in hydraulic systems. The specific application is the control of transients in the fuel delivery lines of an automobile electronic fuel injection system. The objective of transient control is to maintain the pressure in the fuel delivery lines reasonably constant such that equal and appropriate quantities of fuel are delivered during each injection cycle. Transients are generated during each injector operation; it is highly desireable to damp or remove the resulting pressure fluctuations prior to the next sequential operation. The ultimate goal is to improve efficiency of fuel consumption by providing an environment with controlled fuel distribution.

Control is accomplished by installing a flow restricting device at appropriate locations in the fuel delivery line. Two such impedance devices are considered: an orifice plate, and a bundle of capillary tubes. These are sized to eliminate pressure reflections in accordance with theory presented herein; their design is primarily a function of the fluid and fuel line properties. The capillary bundle would be the most suitable for a general application, although large pressure drops across the bundle at high system flow rates may restrict the practical implementation of such a transient control scheme. On the other hand, an orifice type of restrictor can be used to advantage when the transient behavior consists primarily of operating at defineable pressure levels with only two different flow rates. Although the types of control described herein may not be applicable to many transient problems, there are likely to be a wide variety of potential applications for the concept.

Methodology

The matched impedance concept can be described as an installation of a flow restriction in a line so that pressure pulses arriving at the restriction are not reflected. This is accomplished by sizing the restriction to the physical characteristics of the flow system, including the fuel properties. Consider a transient which is a simple step increase in pressure that passes through an originally steady flow system, in which losses (except for the flow restrictor) can be neglected. This pressure rise, ΔP, results in an increase in volumetric flow rate, ΔQ, of

$$\Delta Q = A\Delta P/\rho a \tag{1}$$

according to basic waterhammer analyses [10], in which A = pipeline cross-sectional area, ρ = fluid mass density, and a = wave propagation velocity. The quantity $Z = \rho a/A$ is the characteristic impedance of the pipe. This pressure pulse propagates through the system until it arrives at the flow restrictor where it will be modified. The modifications occurring for an orifice and a capillary bundle will be discussed separately.

Orifice Restrictor. The relationship between pressure and flow is assumed to be given by a steady state orifice equation

$$Q = KA_0\sqrt{2(P-P_d)/\rho} \tag{2}$$

Contributed by the Fluids Engineering Division of THE AMERICAN SOCIETY OF MECHANICAL ENGINEERS and presented at the Winter Annual Meeting, Phoenix, Ariz., November 14–19, 1982. Manuscript received by the Fluids Engineering Division, April 19, 1982. Paper No. 82-WA/DSC-4.

where $K = C_d/\sqrt{1-\beta^4}$ (C_d is the discharge coefficient and β is the ratio of orifice to line diameter), A_0 = the orifice area, and $P - P_d$ = the pressure difference across the orifice with assumed constant downstream pressure P_d. Orifice equations can be written for the original steady state condition

$$Q_0 = C\sqrt{P_0 - P_d} \tag{3}$$

and for the increase flow rate

$$Q_0 + \Delta Q = C\sqrt{P_0 + \Delta P - P_d} \tag{4}$$

in which Q_0 and P_0 refer to the original steady conditions, respectively and $C = KA_0\sqrt{2/\rho}$.

The latter equation is valid only for no reflections at the orifice. Combining equations (1), (3), and (4) allows the quantity C to be computed, for example, if all other parameters are specified.

$$C = \sqrt{(2Q_0 + \Delta Q)/Z} \tag{5}$$

This defines the orifice condition to prevent reflections in this system when operating at the indicated pressure level and flow rates and subjected to the designated pressure and flow changes.

A graphical representation of the concept is also helpful and is given in Fig. 1(*a*). The dashed line represents the orifice relationship, equation (2), and the solid line illustrates equation (1) and the characteristic impedance. For a given orifice, uniqueness of the flow conditions to provide a zero reflection is easily visualized in the graph. The orifice provides a matched terminal impedance with the conditions shown in Fig. 1(*a*). Clearly the slope of the orifice curve in the vicinity of the operating conditions, relative to the characteristic impedance, dictates the degree of success in achieving a reflectionless response. Although a perfect match of conditions yields no reflection in the frictionless system, often less perfect matching conditions provide a satisfactory level of performance. Numerical calculations can predict the actual performance for a particular situation.

The pressure downstream from the orifice must be held at a constant level in order for the above relations to be strictly valid. Moody [13] considers the case of reflections from an orifice in a pipeline with no initial throughflow. His analysis can be extended to include cases with flow; that particular problem is not the focus of the present investigation and is not considered in detail herein. The implications for the above analysis relate to the need of supplying an accumulator or other storage device downstream from the orifice to maintain a constant external pressure. Moody shows that for small values of the ratio $\Delta P/(CZ)^2$ (e.g., less than about 0.1) the reflected pressure rise is very small. Extending this reasoning to a system with throughflow implies that it may not be necessary to provide a storage device (and constant external pressure) in certain instances while still avoiding major pressure reflections in the system. Also, other options such as providing a larger line or a flexible line downstream from the orifice will serve to provide line storage to mitigate reflections.

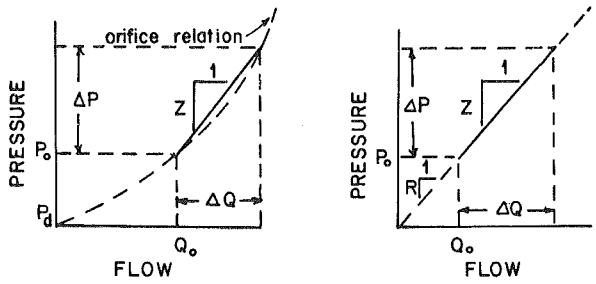

Fig. 1 Matched impedance, (*a*) orifice (*b*) capillary bundle

In cases that require large volumetric throughflow at high velocities, viscous losses may be important in the pipeline. In these cases a perfect match is not possible with the simple orifice, since a phase shift would be required to match the line characteristic impedance.

Capillary Bundle Restrictor. This type of restriction is characterized by a linear relationship between flow rate and pressure change:

$$\Delta P = R\Delta Q \tag{6}$$

This relation assumes inertial effects during unsteady flow in the tube bundle to be unimportant, and it neglects entry length effects. That is, it assumes the existence of steady fully developed laminar flow. A comparison of equations (1) and (6) yields the following condition for zero reflection

$$R = Z \tag{7}$$

which implies that the results are independent of Q_0, ΔP, and P_0. This can also be seen readily in the graphical plot in Fig. 1(*b*), as any choice of these flow variables will result in no reflection once the restrictor has been sized to the fluid and pipe characteristics. Since viscosity is a function of temperature, this would have some influence on the matching conditions for a given flow system, but small deviations from the matched condition will result in minimal pressure reflections.

Demonstration of Concept

Experimental and numerical simulations have been conducted to verify the matched impedance concept. These systems constructed by Bendix Research Labs were portions of studies of fuel injection systems.

Separate experimental configurations were used for the orifice and capillary bundle restrictors; each system and results will be described separately. In addition, mathematical modeling of the physical systems was accomplished using

Nomenclature

a = wave propagation
A = pipe cross-sectional area
A_0 = area of opening at orifice
C_d = discharge coefficient
C_D, C_I, C_U = products of $K A_0(2/\rho)^{1/2}$ for orifice in system
D = capillary tube diameter
g = gravitational acceleration
K = $C_d/\sqrt{1-\beta^4}$
L = length of capillary tube bundle
L' = fluid inertance capillary tube
N = number of capillary tubes in bundle
P = pressure
P_0, P_D, P_U = fluid pressures: system, downstream, and upstream
Q_0 = steady state flow rate
R = flow resistance due to capillary tube bundle
R' = flow resistance per capillary tube (R/N)
Z = characteristic system impedance $\rho a/A$
$\Delta Q, \Delta P$ = change in flow and pressure
β = ratio of orifice and pipe diameters
ρ = mass density
ν = kinematic viscosity
τ = time constant relating the period of flow changes at which inertial effects become important

numerical simulation based on the method of characteristics. Since the method is well documented in the literature (e.g., see Wylie and Streeter [1]), the details of the numerical simulations will not be repeated here. The boundary conditions required in each simulation will be discussed below along with the description of the physical system. Friction effects were included in the numerical simulations, but were found to have a relatively unimportant role in the results. For more details of the actual simulations, see Wright and Wylie [14].

Orifice Restrictor. The physical apparatus was an idealization of the delivery line for an electronic fuel injection system; a schematic is presented in Fig. 2. The apparatus consisted of a circulating flow system with an electronic fuel injector mounted as indicated in the figure. Orifices intended as the matched impedance devices were located at the upstream and downstream ends of the section where transient control was desired.

Accumulators were installed adjacent to each orifice and outside the experimental section to provide constant external pressures. The injector pulse duration and frequency were adjustable with typical pulse width of 5 msec and frequencies of 20 Hz used in the experiments. The experiments were performed with Stoddard Solvent (specific gravity of 0.77 and kinematic viscosity of 1.17×10^{-6} m^2/s at 25°C) as the working fluid. The pressure wave speed was estimated to be 1200m/sec from examination of pressure records obtained from the system and measured line lengths. Two flush mounted pressure transducers located directly above the injector and 15 cm upstream from the downstream orifice were used to monitor the transient response of the experimental system to the injector operation. These pressure traces constitute the results obtained to verify the matched impedance concept.

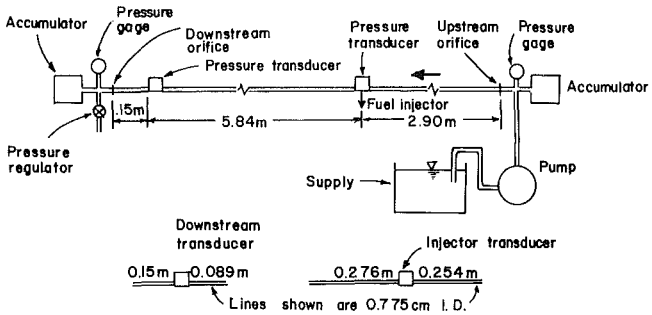

Fig. 2 Schematic of experimental apparatus

Theoretical Description. Since viscous losses along the pipeline are minor compared with losses at the terminal orifices, it can be assumed that the flow delivered with the injector opened is derived equally from the pipeline upstream and downstream of the injector. This assumes a total through flow Q_0 in the system with the injector closed of greater value than one-half the injector flow $2\Delta Q$ so that, there would be no flow reversal in the line. The transient behavior in the fuel rail during fuel injection is described by equation (1), $\Delta P = Z\Delta Q$. Flow through the orifices and injector are assumed to be described by a steady flow orifice equation with coefficient $C = KA_0\sqrt{2/\rho}$. The following relations are obtained:

Fuel injectors
$$2\Delta Q = C_I\sqrt{(P_0 - \Delta P) - P_I} \tag{8}$$

Upstream Orifice
$$Q_0 = C_U\sqrt{P_U - P_0} \tag{9}$$

$$Q_0 + \Delta Q = C_U\sqrt{P_U - (P_0 - \Delta P)} \tag{10}$$

Downstream Orifice
$$Q_0 = C_D\sqrt{P_0 - P_D} \tag{11}$$

$$Q_0 - \Delta Q = C_D\sqrt{(P_0 - \Delta P) - P_D} \tag{12}$$

Here P_I, P_U, and P_D refer to the pressures, assumed constant, outside of the injector, upstream, and downstream of the orifices, respectively, while C_I, C_U, and C_D correspond to the coefficient C defined above for those devices.

With the waterhammer relation in equation (1), there are six independent equations and eleven variables. In general, five variables (such as the injector flow rate, discharge coefficient, the injector delivery pressure and two other variables) can be arbitrarily specified. In the experimental apparatus, the injector discharge coefficient, delivery pressure, and the pipeline size were fixed. With given upstream and downstream orifices, the remaining operating conditions can be computed to arrive at the matched flow condition. Of course, it is possible that the computed operating conditions are not physically feasible.

A pair of orifices were measured to have $C_U = 3.00 \times 10^{-8}$ and $C_D = 1.78 \times 10^{-8}\text{m}^{7/2}\text{kg}^{-1/2}$ for the upstream and downstream orifices, respectively. Along with the measured injector coefficient of $C_I = 1.23 \times 10^{-8}\text{m}^{7/2}\text{kg}^{-1/2}$, atmospheric pressure at the injector outlet, and Z determined to be $1.99 \times 10^{10}\text{N} \cdot \text{s/m}^5$, the remaining conditions required for a matched impedance condition were computed:

$$P_0 = 1.008 \times 10^6 Pa$$

$$\Delta P = 1.16 \times 10^5 Pa$$

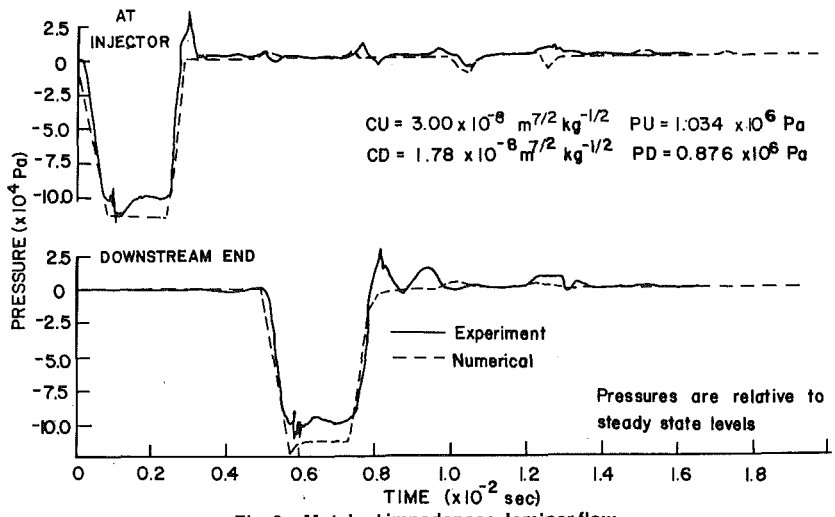

Fig. 3 Matched impedances, laminar flow

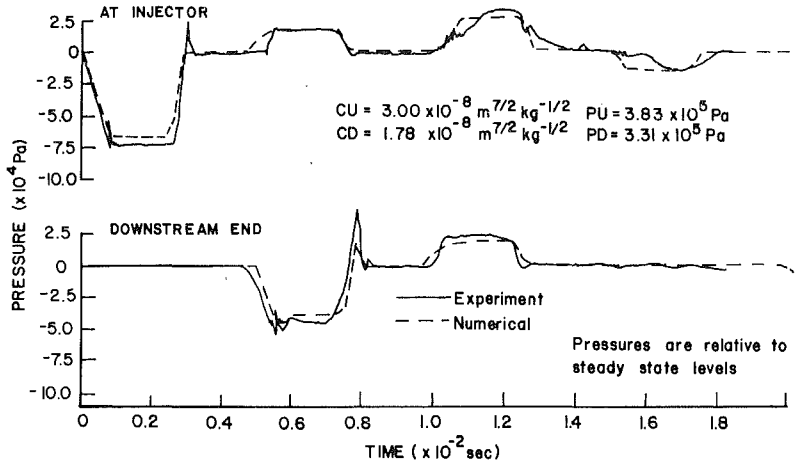

Fig. 4 Unmatched impedances, laminar flow

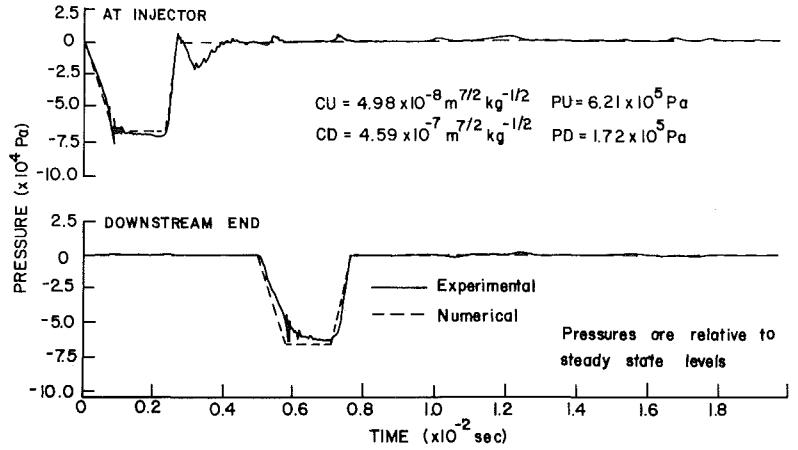

Fig. 5 Matched impedances, turbulent flow

$$P_U = 1.049 \times 10^6 Pa$$

$$P_D = 0.892 \times 10^5 Pa$$

$$Q_0 = 6.06 \times 10^{-6} \mathrm{m}^3/\mathrm{s}$$

$$2\Delta Q = 11.6 \times 10^{-6} \mathrm{m}^3/\mathrm{s}$$

The various orifices and transducers were calibrated prior to the experimental investigation. Sample standard deviations for pressure transducer calibration factors ranged from 1-2 percent and for the orifices and injector, the discharge coefficient determinations had sample standard deviations of less than 2.5 percent. Errors in pressure wave speed are probably due primarily to errors in determination of pipeline length and are assumed to be small.

Figure 3 shows the result of the experiment performed for approximately these conditions and also includes the results of the numerical simulation. A similar result for the same set of orifices with an arbitrary operating condition and no attempt to match impedances is presented for the sake of comparison in Fig. 4. The steady pipe flow Reynolds number for the matched impedance condition is approximately 1400 and in the laminar flow range. Although the orifice diameters were not measured accurately, the Reynolds number based on flow through the orifice is approximately 10^5. An additional experiment was performed with the pipe flow in the turbulent range and is given in Fig. 5.

These results clearly demonstrate the validity of the matched impedance concept. The two experiments with matched impedances (Figs. 3 and 5) clearly show very little wave propagation in the system once the initial transient reaches the orifices while the unmatched case (Fig. 4) shows several distinct pressure pulse reflections. Since the unmatched case is a set of arbitrary operating conditions, it should not be considered a typical case, only representative of the sort of results that may occur. The pressure variations remaining can be attributed to two causes: failure to exactly attain the matched condition; and the fact that matched conditions can be achieved with an orifice restrictor only at two specific flow rates. This latter consideration implies that unless a true square wave is generated by the fuel injector, the portions of the pressure wave associated with opening and closure of the injector will not be completely removed by the orifices. This influence can be readily seen in the numerical simulations but is insignificant in comparison with the pressure waves that are reflected in the unmatched condition.

Laminar Restrictor. The test apparatus was developed by the Bendix Corporation [15] for the purpose of demonstrating the matched impedance condition and is indicated schematically in Fig. 6. Prior to the initiation of the transient, there was no flow in this system. A S.I.G.M.A. fuel injection pump operating at a frequency of 10 Hz was used to generate the pressure waves, and a check valve was installed downstream from the pump to prevent backflow. An accumulator was placed just downstream from the impedance device to act as a constant pressure reservoir at the downstream end of the system. The impedance device was two Brunswick Laminar Restrictors in series; each one is .305 cm long with approximately 5500-0.005 cm diameter holes. A fixture with spacer rings was constructed so that the flow opening could be sized to obtain the correct laminar impedance. The working fluid was Viscor with a specific gravity of 0.825 and a kinematic viscosity of 2.77×10^{-6} m^2/s at 38°C. Pressure

transducers were installed at the upstream end of the system and 0.15 m upstream and downstream from the laminar restrictor.

The characteristic impedance of the delivery line was estimated to be 5.30×10^{10} N•s/m^5 and spacer plates were placed over the ends of the laminar restrictor to attempt to provide the same impedance through the termination device by adjusting the number of flow openings. The restrictor impedance is obtained from

$$\Delta P = \frac{128 \nu L \rho}{N \pi D^4} \Delta Q \tag{13}$$

where ν is kinematic viscosity and L, N, and D are length, number, and diameter of the openings in the flow restrictor. The Hagen-Poiseuille equation was used here with entrance length effects and any unsteady inertial effects ignored in the formulation. In practice, these influences represent limitations to the application since they represent nonlinear impedance behavior. In this application the fluid inertance, L', and resistance, R', for the capillaries leads to a time constant, τ, as follows.

$$L' = \frac{\rho L}{A} \tag{14}$$

$$R' = \frac{32}{} \frac{\rho \nu L}{A D^2} \tag{15}$$

$$\tau = \frac{L'}{R'} = \frac{D^2}{32 \nu} \tag{16}$$

The numerical value of τ for the given data is approximately 28.2 microseconds. With fuel injector pulses ranging from 1000 to 5000 microseconds, and solenoid valve response times of the order of 500 microseconds the inertial effects in the capillaries should be negligible except perhaps with some minor influence during valve operation.

The actual flow impedance was determined by calibrating pressure drop versus flow rate. The observed relation was found to be slightly nonlinear. Individual measurements were within 15 percent of the estimated impedance in the range of pressures considered in this study with the largest discrepancy at small pressure rises. The characteristic impedance was adjusted to account for variations in viscosity with temperature in the interpretation of results obtained on the apparatus. The uncertainty in the impedance estimate dominates all other sources of experimental error.

The output from the upstream pressure transducer during pump operation was used as the upstream boundary condition in the numerical simulation during the pressure wave generation, with zero flow during the remainder of the cycle. The downstream boundary condition was the laminar restrictor with a constant back pressure of 1.38×10^6 Pa on the downstream end; this was maintained in the experimental apparatus to prevent any possible cavitation. The results of an experiment and the corresponding numerical simulation are presented in Fig. 7.

For the sake of comparison, the same experimental conditions with larger number of capillary openings in the flow restrictor is presented in Fig. 8. The negative wave reflected from the laminar restrictor causes the apparent decrease in pressure at the downstream transducer. An incorrect estimate of the pressure wave speed may be the cause of the small shift in the timing between the measured and computed pressures at the downstream end. This also affects the computed value of Z. Although a pressure wave is reflected back to the upstream end of the system for the matched case, it is smaller in magnitude than for the unmatched case and clearly demonstrates the matched impedance concept. The fluctuations remaining for the matched case are most likely due to entrance length and inertial effects as discussed above. The

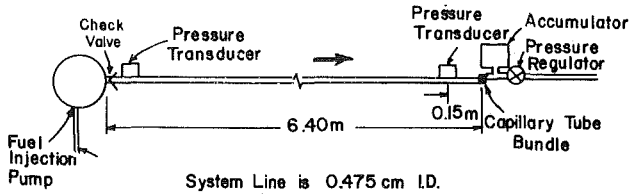

Fig. 6 Schematic of apparatus with laminar restriction

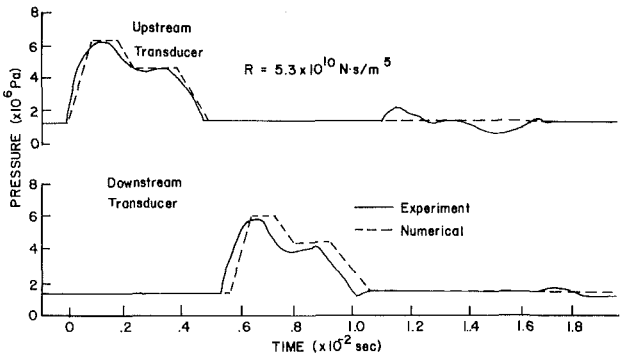

Fig. 7 Matched conditions, laminar flow restrictor

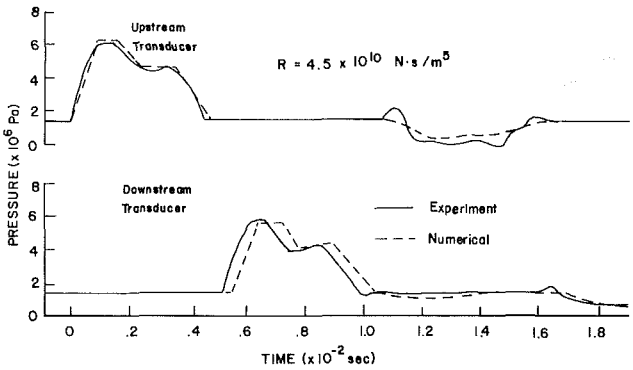

Fig. 8 Unmatched laminar flow restrictor

impedance device showed a slightly nonlinear pressure versus flow rate relationship in the laminar flow range during calibration so an exact impedance match would not be expected. However, a significant amount of transient control has been accomplished; it represents a large improvement over what would be expected from a simple reservoir at the downstream end.

Summary and Conclusion

A method for the control of pressure transients in a simple hydraulic system has been presented and experimentally verified. Two different flow restrictors were used to obtain a matched impedance termination: an orifice plate and a capillary tube bundle. Each must be sized to the pipe and fluid characteristics; the orifice size is also determined by the fluid flow rates. The orifice termination can be used when the transient basically consists of going from one flow state to another as it can be matched only at two specific flow rates. This is likely to limit its potential application in complex hydraulic systems where the flow may take on various transient states. An additional comment is that if line friction is sufficient to modify the pressure wave, it is more difficult to determine the matched impedance condition. For example, in the experimental apparatus discussed above, the upstream and downstream flow distribution in a system with large friction would be more difficult to obtain. On the other hand, the laminar termination device will work at any combination of flow rates and therefore is more general in its application. Variations in fluid viscosity due to temperature or other

effects may prevent attainment of matched conditions in some applications.

One difficulty associated with some potential applications is that pressure losses through the termination devices may be excessively large in order to obtain the matched condition. This would be especially true with the laminar device, and may represent a significant restriction upon its application to certain problems. However, in applications such as fuel injection systems, where pressure losses are not critical and transient control aspects are important, the matched impedance concept should prove to be a practical method for achieving the desired degree of control.

Acknowledgments

Bendix Engineering Research Center, Southfield, Michigan, provided all apparatus upon which the experiments described herein were conducted. The data on the laminar impedance device was obtained at the Research Center, and their cooperation in this study is gratefully acknowledged.

References

1 Wylie, E. B., and Streeter, V. L., *Fluid Transients*, FEB Press, Ann Arbor, MI, 1983.

2 Moore, R. K., *Traveling-Wave Engineering*, McGraw-Hill, New York, N.Y., 1960.

3 Morse, P. M., *Vibration and Sound*, McGraw-Hill, New York, N.Y., 1948.

4 Colloquim on Mechanical Impedance Methods for Mechanical Vibrations, ASME, New York, Dec. 1958.

5 Bergeron, L., "Water Hammer in Hydraulics and Wave Surges in Electricity," Translation of the original French Edition (1949) under the sponsorship of the ASME, John Wiley & Sons, New York, 1961, p. 264.

6 Chang, S. S. L., "Transient Effects of Supply and Connecting Conduits in Hydraulic Control Systems," *J. Franklin Inst.*, Vol. 262, 1956, p. 437.

7 Paynter, H. M., "Fluid Transients in Engineering Systems," Section 20, *Handbook of Fluid Dynamics*, V. L. Streeter, ed., McGraw-Hill, New York, 1961.

8 Rudinger, G., *Wave Diagrams for Non-Steady Flow in Ducts*, Van Nostrand, New York, 1955, p. 140.

9 Stone, K. A., "An Analysis of Effects of Long Lines Between Control Valve and Actuator in Fluid-powered Control Systems," *Proc. Ist Intern Cong. of IFAC*, Moscow, Automatic and Remote Control, Butterworth, England, 1960, pp. 226–229.

10 Streeter, V. L., and Wylie, E. B., *Hydraulic Transients*, McGraw-Hill, New York, 1967.

11 Waller, E. J., "Prediction of Pressure Surges in Pipelines by Theoretical and Experimental Methods," Publication No. 101, Oklahoma State University, Stillwater, OK, June 1958.

12 Goodson, R. E., and Leonard, R. G., "A Survey of Modeling Techniques for Fluid Line Transients," ASME *Journal of Basic Engineering*, Vol. 94, 1972, pp. 474–82.

13 Moody, F. J., "Additional Waterhammer Considerations in Energy Industries," Preprint 80-CZ-PVP-154 Pressure Vessels and Piping Conference, San Francisco, CA 1980.

14 Wright, S. J., and Wylie, E. B., "Experimental Findings and Numerical Simulations on Gasoline Fuel Injector System," Final Project Report to Bendix Research Labs, Southfield, Michigan, Jan. 17, 1980.

15 Taplin, L. B., "Experimental Evaluation of Capillary Terminating Restrictor for Long Lines," Bendix Corporation Technical Memorandum BRL/TM-79-8970 Bendix Research Laboratories, Southfield, MI, Aug. 10, 1979.

Calculation of the Vibration of an Elastically Mounted Cylinder Using Experimental Data From Forced Oscillation

T. Staubli

Institute for Liquid Technology,
Swiss Federal Institute of Technology,
Zurich, Switzerland

Several methods for investigating the fluid-structure interaction of bodies vibrating due to vortex shedding are compared briefly. The advantage of employing a forced-displacement excitation method is asserted. This method has been adopted to measure the response of the fluid forces acting on an oscillating circular cylinder in crossflow. With the results of these measurements, and a calculation based on the assumption of sinusoidal motion, the vibrations of a freely oscillating cylinder are predicted in the lock-in range. It is shown that hysteresis effects, which are observed in experiments with elastically mounted cylinders of certain damping and mass ratios, are caused by the nonlinear relation between the fluid force and the amplitude of oscillation.

Introduction

This paper deals with the vibrations of structures caused by vortex shedding. In a flowing fluid, vortices are shed alternately from either side of a body, and the resulting changes in circulation around the body lead to fluctuating forces. If the frequency of this regular shedding coincides with one of the structural eigenfrequencies, large vibrations will occur. In the lock-in range the oscillation of the body takes control of the shedding, and the feedback of the affected flow-field may in turn reinforce the vibration. Many applications in which structures are exposed to a flowing fluid result in vortex induced fluid-structure interactions.

Extensive investigations of vortex shedding have been carried out in the field of building aerodynamics. However, it is not only bluff bodies which are subject to vortex-induced vibrations: vortex shedding also occurs at the trailing edge of streamlined profiles. Thus Chaix [1] and Grein [2] have reported that guide and stay vanes of hydraulic machines may vibrate and be damaged.

The most frequently investigated geometry is the circular cylinder because of its simple geometry and for the following physical reason: the vortex shedding behind the circular cylinder is very pronounced with no superposition of other effects such as galloping.

Three different ways of investigating fluid-structure interactions may be considered:

1 The method of the elastically mounted cylinder in crossflow, which is easy to perform, has often been applied [3, 4, 5, 6, 7, 8]. The amplitudes of vibration and the effects of resonance are investigated. The main parameter for these measurements is the flow velocity. Further parameters are the mass, stiffness, and damping of the mechanical system. Figure 1 shows an elastically mounted cylinder which is spring-supported and connected to an element with viscous damping. The disadvantage of this technique is that the mechanical system is coupled with the fluid-dynamic system, as shown schematically in the block diagram of Fig. 1.

The equation of motion of the mechanical system can be written as follows:

$$m\ddot{x}+d\dot{x}+cx=F(t) \tag{1}$$

The time record of displacement is practically sinusoidal in the lock-in range for the steady state, as reported by many researchers [4, 5, 7].

2 A second method feeds additional energy from outside to the system of the elastically mounted cylinder [9, 10, 11, 12, 13]. This is shown schematically in Fig. 1 with the external force $[F_{Ex}]$ in brackets. With this external force it is possible to investigate ranges where the fluid has a damping rather

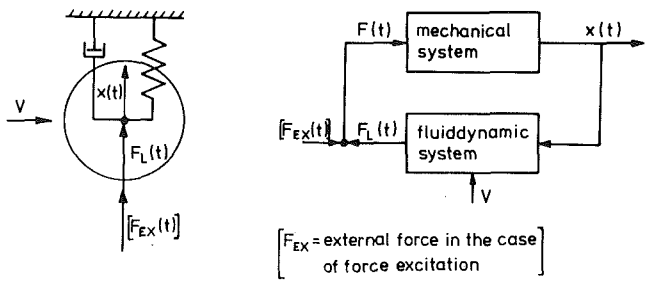

Fig. 1 The elastically mounted cylinder in crossflow and force-excitation

Contributed by the Fluids Engineering Division and presented at the Winter Annual Meeting, Washington, D.C., November 15–20, 1981, of The American Society of Mechanical Engineers at the Symposium on Fluid Structure Interactions in Turbomachinery. Manuscript received by the Fluids Engineering Division, March 4, 1982.

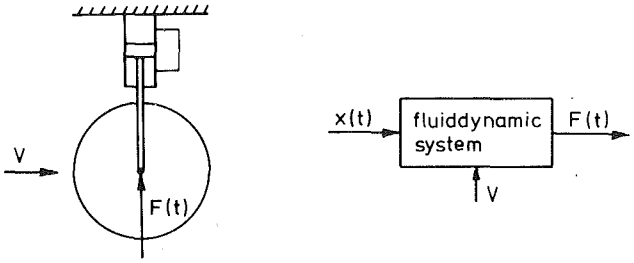

Fig. 2 Forced displacement-excitation

than an exciting effect. This method can be called the force-excitation method.

3 The method of forced displacement-excitation [14, 15, 16] was adopted for the present investigation. A hydraulic actuator, as shown in Fig. 2, was chosen as the drive. The device is stiff enough to avoid any feedback of the fluid-dynamic forces on the motion of the cylinder. With this method the fluid forces can be measured as a function of a prescribed motion $x(t)$.

The relationship between the time records of the motion and the time records of the fluid forces is determined by the physical processes in the wake. Therefore all three methods should show the same relationship for a sinusoidal time record of displacement. In these comparisons, special attention has to be paid to the hysteresis loops, which are observed at the ends of the lock-in range in the case of the elastically mounted cylinder [3, 4, 8]. According to Parkinson [17] a nonlinearity in the fluid system is the cause for this double amplitude response. The nonlinear response of the fluid system to a given transverse oscillation can best be investigated with the method of forced displacement. In this paper, the results of such measurements (block diagram of Fig. 2) are inserted into the coupled system of the elastically mounted cylinder (block diagram of Fig. 1) in order to describe the fluid-dynamic system. In this way the amplitudes of the linear mechanical system can be predicted. Such calculated values are compared with measurements carried out by Feng [4] (see also [18]) who investigated the freely oscillating cylinder in a wind tunnel.

The present work may be regarded as a continuation of Sarpkaya's investigation [16] in which the amplitudes were predicted of elastically mounted cylinders at the critical point where the maximum amplitudes occur. Sarpkaya's calculations are based on different assumptions from those which lead to equations (10) and (11) of this paper.

Experimental Arrangement and Measuring Technique

The experiments were performed in a towing tank with $1m \times 1m$ cross section and a length of about 40 m. The measuring equipment was installed on a towing trolley, which has a maximum speed of 5 m/s.

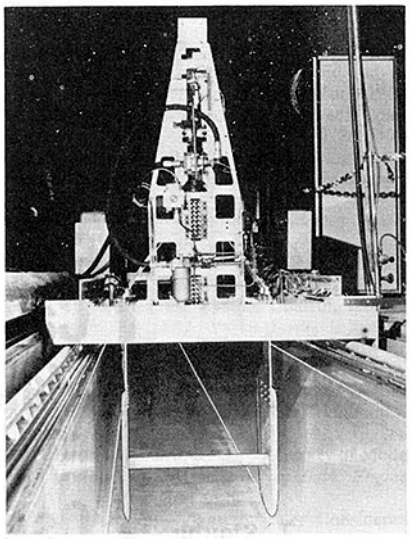

Fig. 3 Photograph with the towing trolley, the hydraulically driven shaker mechanism and the test-cylinder

This technique has the following advantages: water at rest is free of turbulence; the towing velocity is constant with an accuracy of ± 0.01 percent; the fluid forces acting on the cylinder surrounded by water are greater than the mass forces of the oscillating cylinder.

The towing trolley and the hydraulically driven shaker mechanism are shown in Fig. 3.

Three-dimensional flow effects, as described by Gerrard [19], were largely suppressed with end plates at both sides of the polished cylinder. The fluid forces were measured with a specially developed measuring device of high stiffness (Quartz transducers) and good accuracy ($< \pm 1\%$) installed in each of these end plates. The signals measured were stored on magnetic tape and analyzed by a digital computer.

The Forced Oscillation Experiment

The following parameters were varied during the measurements: Reynolds number ($Re = 2 \cdot 10^4 - 3 \cdot 0^5$); oscillation amplitude ($\hat{\xi} = 0 - 0.8$); oscillation frequency ($S_O = 0.09 - 0.36$).

The harmonic motion of the shaker mechanism can be described in terms of its displacement

$$x(t) = \hat{x}\cos(\omega_O t) \tag{2}$$

The non-dimensional cylinder displacement amplitude is

$$\hat{\xi} = \frac{\hat{x}}{D}, \tag{3}$$

the dimensionless oscillation frequency is defined as

Nomenclature

a = modified mass ratio
c = stiffness, N/m
V = flow (towing) velocity, m/s
C_L = lift coefficient
C_{LO} = lift coefficient at the oscillation frequency
C_{LK} = lift coefficient due to non-synchronized Kármán vortices
d = viscous damping, Ns/m
D = cylinder diameter, m
F = force, N
m = mass, kg
Re = Reynolds number
S_{NO} = Strouhal number for the nonoscillating body
S_O = Strouhal number for the oscillation frequency
t = time, s
x = displacement lateral to the flow, m
δ = damping ratio
ξ = dimensionless displacement
ϕ = phase angle, deg
ρ_{Fl} = fluid density, kg/m^3
ρ_{Cyl} = cylinder density, kg/m^3
ω_n = natural angular frequency, 1/s
ω_O = angular frequency of the oscillation, 1/s
ω_K = angular frequency for shedding of Kármán vortices, 1/s
Ω = Strouhal frequency ratio

Superscripts

$\hat{}$ = amplitude
$( )^\circ$ = derivative

$$S_O = \frac{\omega_O F}{2\pi V} \tag{4}$$

and the Strouhal number of the nonoscillating cylinder as

$$S_{NO} = \frac{\omega_K(\hat{\xi}=0)D}{2\pi V} \tag{5}$$

Spectral analysis of the lift force showed that two lift coefficients have to be accounted for. One peak in the power spectrum appeared at the frequency of the oscillation (ω_O), and a second (ω_K), at approximately the frequency of vortex shedding in the nonoscillating case. Only when the oscillation frequency was very close to the frequency of vortex shedding for the nonoscillating cylinder, did the second peak ($\hat{C}_{LK}$) diminish in size and progressively disappear. Values of the lift coefficients were extracted from the power spectra, whilst the phase difference ϕ was determined by means of the cross spectrum of the lift force and the acceleration. Higher harmonics may be neglected due to the low values of their amplitudes. Thus the lift coefficient can be described with the following two terms:

$$C_L(t) = \hat{C}_{LO}\cos(\omega_O t + \phi) + \hat{C}_{LK}\cos(\omega_K t) \tag{6}$$

The lift coefficient $C_{LK}(t)$ has its origin in the Kármán vortices, which are not synchronized with the oscillation. In the case of the nonoscillating cylinder only the lift coefficient $C_{LK}(t)$ appears.

The lift coefficient $C_{LO}(t)$ oscillates with the same frequency as the cylinder motion. The phase angle ϕ gives the phase shift between the displacement $x(t)$ and the lift coefficient $C_{LO}(t)$.

The lift coefficient $\hat{C}_{LO}$ is displayed in a three-dimensional plot in Fig. 4 for a constant Reynolds number of $6 \cdot 10^4$. The coefficient $\hat{C}_{LO}$ is plotted against the dimensionless oscillation frequency S_O and the dimensionless amplitude $\hat{\xi}$. This plot is based on measurements of the forces acting on an oscillating circular cylinder in crossflow which are published in reference [20]. The highest value measured was $\hat{C}_{LO} = 3.52$ for $\hat{\xi} = 0.74$ and $S_O = 0.17$. The measured area is displayed with full lines and basically covers the range from $S_O = 0.14$ to $S_O = 0.18$, which is the important range for the calculation of elastically mounted cylinders. The measured points have been interpolated with bicubic Spline-interpolation [21]. Points outside the measured range have been roughly estimated with the theory of the displaced mass (interrupted lines) in order to complete the picture. The measured coefficients have the same order of magnitude as Sarpkaya's [16] at slightly different Strouhal numbers. The Strouhal number of the nonoscillating cylinder in the experiments of Sarpkaya is 0.21 whilst in the present investigation S_{NO} was 0.18 in the range of $Re = 4 \cdot 10^4$ to $8 \cdot 10^4$.

In a second three-dimensional plot (Fig. 5), the phase angle between the acceleration and the lift coefficient C_{LO} is displayed. Again additional points (interrupted lines) have been estimated in order to complete the picture over the whole area. These points have no physical meaning and are not used for the calculations. It should be noted that the phase angle is not defined in the case of the nonoscillating cylinder ($\hat{\xi} = 0$). For phase angles between 0 and 180 degrees there is an energy transfer from the fluid to the cylinder, whereas the fluid extracts energy if the phase angle is smaller than 0 or greater than 180 degrees. The sharp drop in ϕ for $S_O = 0.14 - 0.17$ determines the range of fluid-excited vibrations of the freely oscillating cylinder.

Calculation of the Vibration of the Elastically Mounted Cylinder and Comparison With Measurements of Feng [4]

The equation of motion of the elastically mounted cylinder

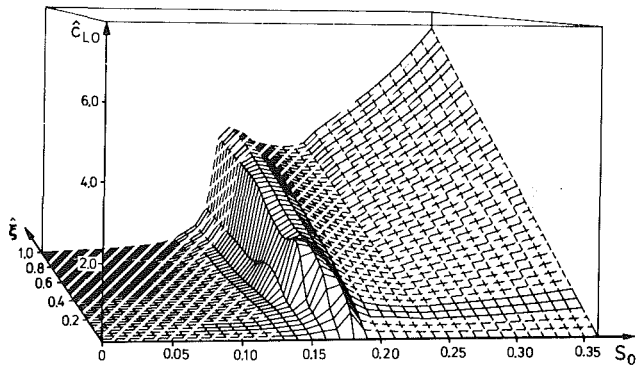

Fig. 4 The lift coefficient $\hat{C}_{LO}$ versus the dimensionless oscillation frequency S_O and the dimensionless amplitude $\hat{\xi}$ for a constant Reynolds number $Re = 6 \cdot 10^4$ (Mean uncertainty within the measured range in $\hat{C}_{LO} = \pm 0.02$, in $\hat{\xi} = \pm 0.01$, in $S_O = \pm 0.001$)

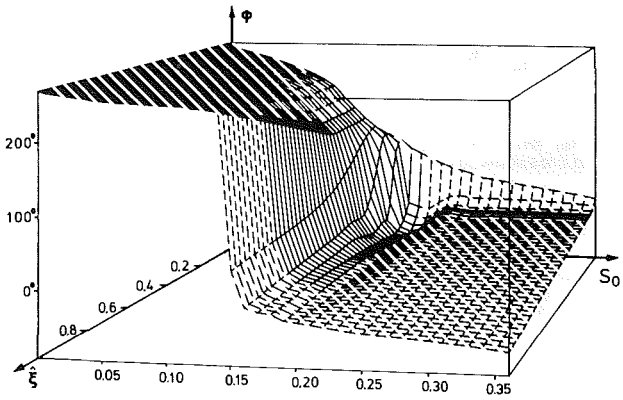

Fig. 5 The phase angle ϕ versus the dimensionless oscillation frequency S_O and the dimensionless amplitude $\hat{\xi}$ for a constant Reynolds number $Re = 6 \cdot 10^4$ (Mean uncertainty within the measured range in $\phi = \pm 3$ deg)

(1) can be written in nondimensional form according to Hartlen and Currie [22] as:

$$\mathring{\xi} + \delta\dot{\xi} + \xi = a\Omega^2 C_L \tag{7}$$

where:

$$\dot{\xi} = \frac{1}{\omega_n}\frac{d\xi}{dt},\quad \omega = \sqrt{\frac{c}{m}},\quad \Omega = \frac{S_{NO}}{\frac{\omega_n D}{2\pi V}}$$

$$\delta = \frac{d}{\omega_n m} = \frac{\omega_n d}{c},\quad a = \frac{1}{2\pi^3 S_{NO}^2}\frac{\rho_{Fl}}{\rho_{Cyl}} \tag{8}$$

The motion $\xi(t)$ of this system is nearly sinusoidal. Therefore the lift force for exact sinusoidal motion, as investigated in the last paragraph, gives a good approximation of the lift force acting on a freely oscillating cylinder. Inserting equation (6) in equation (7) gives

$$\mathring{\xi} + \delta\dot{\xi} + \xi = a\Omega^2(\hat{C}_{LO}\cos(\omega_O t + \phi) + \hat{C}_{LK}\cos(\omega_K t)) \tag{9}$$

The occurrence of a second lift coefficient at a different frequency may appear to be at variance with the assumption of nearly sinusoidal motion $\xi(t)$. Because of the linearity of the mechanical system any frequency appearing on the right side of equation (8) must also appear in $\xi(t)$. Since we will investigate mechanical systems with low damping, which have a sharp resonance peak, an exciting force with a frequency near the eigenfrequency of the system will have a much larger influence than one which is outside the region of the resonance peak. Therefore the second term of the lift force, the lift coefficient $\hat{C}_{LK}$, will not have strong influence on the motion $\xi(t)$. This is also the reason why Kobayashi [8] and

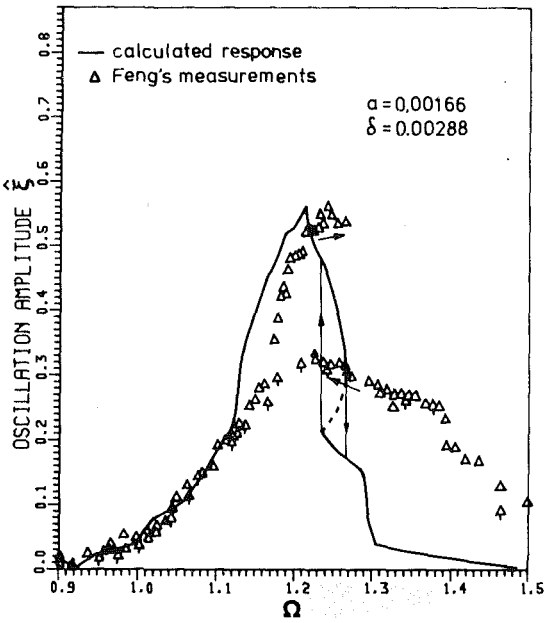

Fig. 6(*a*) The response of the elastically mounted cylinder in crossflow for weak damping

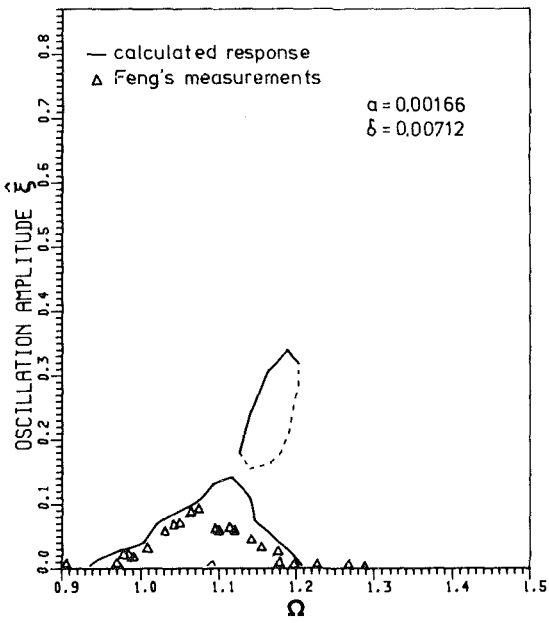

Fig. 7(*a*) The response of the elastically mounted cylinder in cross-flow for strong damping

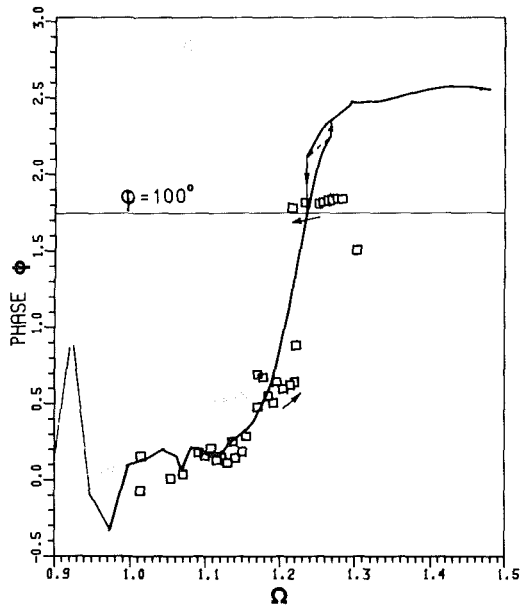

Fig. 6(*b*) The phase angle ϕ in the range of lock-in

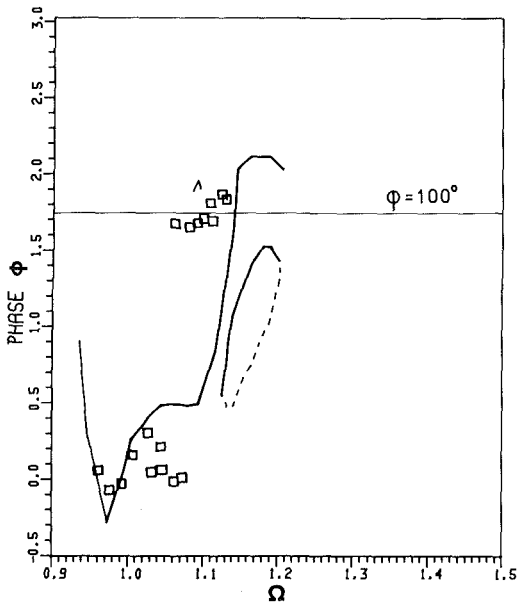

Fig. 7(*b*) The phase angle ϕ in the range of lock-in

others have observed a beat in the lift force C_L but not in the oscillations of the cylinder.

This legitimizes the setting of $\hat{C}_{LK}=0$ in equation (7) and so obtaining with $\xi=\hat{\xi}\cos(\omega_O t)$ for the steady state, the same equations as deduced by Hartlen and Currie [22].

$$\hat{\xi}\left(1-\frac{\omega_O^2}{\omega_n^2}\right)=a\Omega^2\hat{C}_{LO}(\hat{\xi},S_O)\cos\phi(\hat{\xi},S_O) \tag{10}$$

$$\delta\hat{\xi}\frac{\omega_O}{\omega_n}=a\Omega^2\hat{C}_{LO}(\hat{\xi},S_O)\sin\phi(\hat{\xi},S_O) \tag{11}$$

with

$$S_O=\frac{\omega_O D}{2\pi V}$$

These two equations give implicitly the function $\hat{\xi}(\Omega,a,\delta)$ and $\omega_O(\Omega,a,\delta)$, *where* a, δ *are the parameters of the mechanical system.* The oscillation amplitude $\hat{\xi}$ and the oscillation frequency ω_O are obtained numerically using the Spline-interpolated values for $\hat{C}_{LO}$ and ϕ.

For the calculation of the elastically mounted cylinder the parameters of the mechanical system, a and δ, were taken from Feng's experiments [4]. In Fig. 6 and Fig. 7, the results of the calculations are displayed as a function of Ω (curves) and compared with Feng's data (points).

The results of experiments with freely oscillating bodies are commonly displayed as a function of the reduced velocity. Since the Strouhal number S_{NO} differs slightly from experiment to experiment [23, 24], the parameter Ω permits a better comparison of the results. For instance Feng measured a Strouhal number $S_{NO}=0.198$ at a Reynold number $Re=2\cdot10^4$ while the present author found $S_{NO}=0.180$ at $Re=6\cdot10^4$. The following relation exists between Ω and the reduced velocity:

$$\Omega = U\,2\pi S_{NO} \quad \text{where} \quad U = \frac{V}{\omega_n D} \tag{12}$$

or

$$\Omega = V_r S_{NO} \quad \text{where} \quad V_r = \frac{2\pi V}{\omega_n D} \tag{13}$$

Figure 6 shows the results of the calculation with mechanical damping $\delta = 0.00288$. In Fig. 6(*a*) the oscillation amplitude $\hat{\xi}$ is plotted against Ω. The maximum oscillation amplitudes occur at $\Omega = 1.2$. For Ω between 1.0 and 1.2 there is good agreement between the calculation and the measurements, and both show the same trends for larger Ω. The hysteresis effect of the measurement with the double amplitude response corresponds to the range in the calculation where multiple solutions occur for the same Ω. Since the stability of the solutions was not investigated, it might be thought that not all calculated solutions are physically stable in that range.

For larger values of Ω, the calculated curve shows considerably smaller oscillation amplitudes than those of Feng's measurements. A part of the explanation might be that the neglected term $\hat{C}_{LK}\cos(\omega_K t)$ of equation (9) has an increasing influence at the end of the lock-in range. The calculated and measured oscillation frequency varies only little in the lock-in range. For this example the calculated ratio ω_O/ω_n lies between 0.990 and 1.004. The phase shift is displayed in Fig. 6(*b*). For values of Ω up to 1.2 the calculations are in good agreement with the measurements, and the rapid increase in the phase is well reproduced. The maximum values of ϕ are considerably higher in the calculation than in the measurements.

Figure 7 shows the case with damping $\delta = 0.00712$. The calculated curves again more or less fit the points measured by Feng. A hysteresis effect was not observed by Feng for the high mechanical damping. The calculation predicted high oscillation amplitudes which were not observed in the experiments. These additional solutions are disconnected from the rest of the solutions. They form a kind of isolated "balloon." It would be interesting to know whether such amplitudes could be reproduced in experiments.

Conclusion

The method of forced displacement excitation enables the experimentator to vary the oscillation amplitude and frequency directly without feedback of the fluid forces on the motion.

The amplitude responses of an elastically mounted cylinder in crossflow could be predicted in the lock-in range. Good agreement of the calculations was found with the measurements of Feng.

The hysteresis effect corresponds to a range where multiple solutions are obtained. Further analysis should give evidence of the stability. These multiple solutions for constant fluid and structural parameters Ω, a, δ are only possible if the lift coefficient $\hat{C}_{LO}$ and the phase ϕ are nonlinear functions of the oscillation amplitude.

Acknowledgment

I wish to express my special thanks to Prof. Dr. B. Chaix and Prof. Dr. N. Rott for helpful discussions and suggestions. I also thank Markus Hegland for support in all computational questions.

References

1 Chaix, B., "Critical Unresolved Problems of Flow-Induced Vibrations in Hydraulic Machinery and Equipment," *Practical Experiences with Flow-Induced Vibrations*, ed., Naudascher, E., and Rockwell, D., Springer-Verlag, Berlin, 1980, pp. 841–846.

2 Grein, H., and Staehle, M., "Ermüdungsbrüche in Stutzschaufeln grosser Turbinen," *Escher Wyss Mitteilung*, Heft 1, 1978, pp. 33–37.

3 Meier-Windhorst, A., "Flatterschwingungen von Zylindern im gleichmässigen Flüssigkeitsstrom," *Mitteilungen des Hydraulischen Instituts der Technischen Hochschule München*, Oldenbourg Verlag, München, Heft 9, 1939, pp. 3–29.

4 Feng, C. C., "The Measurement of Vortex-Induced Effects in Flow Past Stationary and Oscillating Circular and D-Section Cylinders," MASc thesis, University of British Columbia, 1968.

5 Diana, G., and Falco, M., "On the Forces Transmitted to a Vibrating Cylinder by a Blowing Fluid," *Meccanica 6*, March 1971, pp. 9–22.

6 King, R., "Vortex Excited Structural Oscillations of a Circular Cylinder in Flowing Water," PhD thesis, Loughborough Univesity of Technology, July 1974.

7 Griffin, O. M., and Koopman, G. H., "The Vortex-Excited Lift and Reaction Forces on Resonantly Vibrating Cylinders," *Journal of Sound and Vibration*, Vol. 54, 1977, pp. 435–448.

8 Kobayashi, T., "Schwingungserregung von federgelagerten, stumpfen Zylindern infolge Wirbelablösung," PhD thesis, Technische Universität Berlin, 1980.

9 Bishop, R. E. D., and Hassan, A. Y., "The Lift and Drag Forces on a Circular Cylinder in a Flowing Fluid," *Proceedings of Royal Society*, London, Series A, Vol. 277, 1963, pp. 32–50.

10 Försching, H., "Aeroelastic Stability Investigations on Prismatic Beams," Symposium on Wind Effects on Buildings and Structures, Paper No. 22, Loughborough, Apr. 1968.

11 Bublitz, P., "Experimentelle Untersuchung der Strömung am harmonisch schwingenden querangeströmten Kreiszylinder," PhD thesis, DFVLR, Institut für Aeroelastik, Göttingen, 1972.

12 Stansby, P. K., "The Locking-on of Vortex Shedding due to the Cross-Stream Vibration of Circular Cylinders in Uniform and Shear Flows," *Journal of Fluid Mechanics*, Vol. 74, Part 4, 1976, pp. 641–665.

13 Bardowicks, H., "Untersuchung der Einflüsse von Querschnittsformen auf aeroelastische Schwingungen scharfkantiger primatischer Körper," PhD thesis, Technische Universität Hannover, 1976.

14 Toebes, G. H., and Ramamurthy, S., "Fluidelastic Forces on Circular Cylinders," *Proceedings of the ASCE*, Journal of the Engineering Mechanics Division, EM 6, Dec. 1967, pp. 1–21.

15 Tanaka, H., and Takahara, S., "Study on Unsteady Aerodynamics Forces Acting on an Oscillating Cylinder," *Proceedings 19th Jap. Nat. Congr. Appl. Mech.*, Vol. 19, 1969, pp. 162–166.

16 Sarpkaya, T., "Fluid Forces on Oscillating Cylinders," *Journal of Waterway, Port, Coastal and Ocean Division of ASCE*, Vol. 104, No. WW4, 1978, pp. 275–290.

17 Parkinson, G. V., "Mathematical Models of Flow-Induced Vibrations of Bluff Bodies," *Flow-Induced Structural Vibrations*, ed., Naudascher, E., Springer-Verlag, Berlin, 1974, pp. 81–127.

18 Parkinson, G. V., Feng, C. C., and Ferguson, N., "Mechanisms of Vortex-Excited Oscillations of Bluff Cylinders," Symposium on Wind Effects on Buildings and Structures, Paper No. 27, Loughborough, April 1968.

19 Gerrard, J. H., "The Three-Dimensional Structure of the Wake of a Circular Cylinder," *Journal of Fluid Mechanics*, Vol. 25, Part 1, 1966, pp. 143–164.

20 Staubli, T., "Eine Untersuchung der instationären Kräfte beim querangeströmten, erzwungen schwingenden Kreiszylinder," PhD thesis, Swiss Federal Institute of Technology, Zürich, Nr. 73 22, 1983.

21 Ahlberg, J. H., Nilson, E. N., and Walsh, J. L., "The Theory of Splines and Their Applications," Academic Press, 1967.

22 Hartlen, R. T., and Currie, I. G., "Lift-Oscillator Model of Vortex-Induced Vibration," *Proceedings of the ASCE*, Journal of the Engineering Mechanics Division, EM5, Oct. 1970, pp. 577–591.

23 Chen, Y. N., "60 Jahre Forschung über die Kármánschen Wirbelstrassen — Ein Rückblick," *Schweizerische Bauzeitung*, 91. Jahrgang, Heft 44, Nov. 1973.

24 Richter, A., "Strömungskräfte auf starre Kreiszylinder zwischen parallelen Wänden," PhD thesis, Karlsruhe, 1973.

Generation and Size Distribution of Droplet in Annular Two-Phase Flow

Isao Kataoka
Institute of Atomic Energy,
Kyoto University,
Uji, Kyoto 611
Japan

Mamoru Ishii
Reactor Analysis and Safety Division,
Argonne National Laboratory,
Argonne, Ill. 60439
Mem. ASME

Kaichiro Mishima
Research Reactor Institute,
Kyoto University,
Osaka 590-04, Japan

The mean droplet size and size distribution are important for detailed mechanistic modeling of annular two-phase flow. A large number of experimental data indicate that the standard Weber number criterion based on the relative velocity between droplets and gas flow predicts far too large droplet sizes. Therefore, it was postulated that the majority of the droplets were generated at the time of entrainment and the size distribution was the direct reflection of the droplet entrainment mechanism based on roll-wave shearing off. A detailed model of the droplet size in annular flow was then developed based on the above assumption. The correlations for the volume mean diameter as well as the size distribution were obtained in collaboration with a large number of experimental data. A comparison with experimental data indicated that indeed the postulated mechanism has been the dominant factor in determining the drop size. Furtheremore, a large number of data can be successfully correlated by the present model. These correlations can supply accurate information on droplet size in annular flow which has not been available previously.

Introduction

An accurate knowledge of the mean droplet size and droplet size distribution is essential to the detailed analyses of droplet or annular dispersed flow. The inception of droplet entrainment from the liquid film significantly changes the mechanisms of mass, momentum and energy transfer [1, 2]. The available interfacial area and droplet transport depend on the amount of entrainment and droplet size. Therefore, in order to accurately model and predict a number of important physical phenomena in annular dispersed flow, an understanding of mechanisms of entrainment, generation of droplets and size distribution are prerequisite. In particular, the relative velocity and droplet carry-over, the dryout and post dryout heat transfer [3–7] and the effectiveness of the emergency core cooling in light water reactors [8–11] are significantly influenced by the amount of entrainment and droplet size.

In view of its importance, a detailed modeling of amount of entrained droplet has been carried out recently [2] by considering the entrainment mechanism of the shearing off of roll-wave crests by streaming gas flow. However, there have been no satisfactory correlations for the prediction of the mean droplet size and size distribution for annular dispersed flow. The lack of such a correlation has been one of the main difficulties of analyzing various important phenomena in annular flow. The principal objective of this study, therefore, is to develop a reliable and simple predictive method for the mean droplet size as well as the droplet size distribution. A certain mechanistic modeling which is consistent with the previously developed onset of entrainment criterion and correlation for the amount of entrainment has been adopted here to obtain a general correlation with wide ranges of applicability. Hence, the main mechanism of droplet generation considered here is the shearing off of the roll-wave crest by gas flow.

In addition to the present model based on the entrainment mechanism, several existing droplet size criteria based on droplet disintegration have been reviewed in this study. As it becomes evident, the standard Weber number criterion expressed in terms of the relative velocity between gas and droplet gives far too large droplet sizes in annular flow. This also indicates that the droplet size in annular flow is mainly determined at the time of entrainment.

Droplet Generation Mechanisms

Droplets can be generated by a number of different ways such as the liquid jet breakup, droplet disintegration and droplet entrainment from a body of liquid [1, 12–14]. The former two mechanisms have been reviewed in detail by Brodkey [12]. A liquid jet or sheet disintegrates into small droplets due to interfacial instabilities [15, 16].

Disintegration of droplets in a gas stream has been studied by a number of researchers [12, 13, 17–23]. Several different mechanisms of droplet breakup have been recognized. The mode by which the disintegration occurs depends on the initial

Contributed by the Fluids Engineering Division and presented at the ASME Applied Mechanics, Bioengineering, and Fluids Engineering Conference, Houston, Texas, June 20–22, 1983, of THE AMERICAN SOCIETY OF MECHANICAL ENGINEERS. Manuscript received by the Fluids Engineering Division, September 28, 1981. Paper No. 83-FE-2.

droplet size and the flow condition. A large free-falling drop initially becomes unstable due to the Taylor instability and then it is blown in by gas and disintegrates into fine droplets.

A criterion for droplet disintegration can be expressed in terms of the Weber number defined by

$$\mathrm{We} \equiv \frac{\rho_g v_g^2 D}{\sigma} \tag{1}$$

where D is the droplet size. Then the criterion is given by a critical Weber number beyond which droplets disintegrate into small droplets.

In the case of a falling drop, the critical Weber number is given [13, 17, 20] by

$$\mathrm{We}_c \doteq 22 \quad \text{(falling drop)} \tag{2}$$

However, direct observations of droplet sizes indicate that the critical diameter is approximately given [22, 24] by

$$D_c \doteq (4 \sim 6)\sqrt{\sigma / g \Delta\rho} \tag{3}$$

This value can be also obtained from the consideration of Taylor Instability [22]. On the other hand, the terminal velocity of a large drop [24, 25] is about

$$v_\infty = (1.4 \sim 1.7)\left(\frac{\sigma g \Delta\rho}{\rho_g^2}\right)^{1/4} \tag{4}$$

Substituting equations (3) and (4) into equation (1), one gets the critical Weber number to be

$$\mathrm{We}_c = 8 \sim 17 \tag{5}$$

This value is much smaller than the one given by equation (2), however, it is considered to be a more reliable criterion for large drops.

When a droplet is suddenly exposed into a gas stream, violent shattering of droplets becomes possible. In this case, the critical Weber number is about 10 to 12 for low viscous fluids [13, 18, 20, 21]. However, a significant effect of the liquid viscosity has been observed. Thus Hinze [13] correlated it in terms of the viscosity group $(\mu_f^2/\rho_f D\sigma)$ as

$$\mathrm{We}_c = 12\left[1 + \left(\frac{\mu_f^2}{\rho_f D\sigma}\right)^{0.36}\right] \tag{6}$$

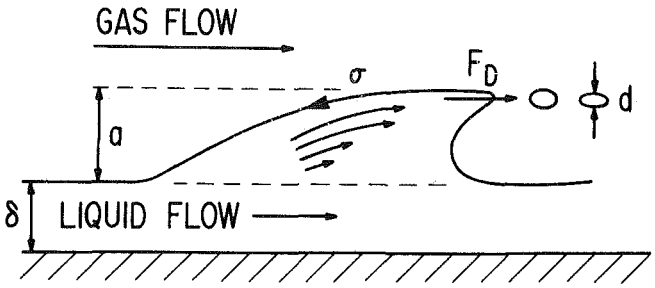

Fig. 1 Mechanism of the shearing off of roll-wave

Later some modification has been proposed [12] using the same dimensionless group as

$$\mathrm{We}_c = 12 + 14\left(\frac{\mu_f^2}{\rho_f D\sigma}\right)^{0.8} \tag{7}$$

In view of equations (5) and (7), it may be concluded that the criterion given by equation (7) is a good general purpose correlation for droplet disintegrations in a gas stream.

The third mechanism is the disintegration of fluid particles by strong turbulent motions of a continuous phase [13, 17]. This occurs mainly in bubbly flow or droplet in liquid flow. For highly turbulent flow, the value of the critical Weber number is given approximately [13, 17] by $\mathrm{We}_c = 1.2 \sim 2.5$. It is noted that these critical Weber numbers are sensitive to flow conditions. For example, in a pulsating flow the value of We_c can be reduced by as much as 50 percent of the one given by equation (7).

Another important but quite different type of generation of droplets is associated with entrainment of droplets at gas-liquid interfaces [1, 2, 14]. In this case, the entrainment mechanisms can be grouped into two main categories, i.e., film entrainment and pool entrainment. A wavy liquid film can be entrained into gas flow in several different ways such as roll-wave shearing off, wave undercutting, droplet impingement and liquid bridge disintegration. For annular flow shearing off of the roll-wave crests is the most important entrainment mechanism [2, 14], see Fig. 1. The liquid bulge or

Nomenclature

a = roll wave amplitude
a_i = interfacial area per unit volume
a_{iw} = wave area per unit volume
A_d = projected area of a particle
A_{iw} = wave area
C_D = drag coefficient
C_g = coefficient in equation (18)
C_w = coefficient for internal flow
D = droplet diameter
D_c = critical diameter
$D_{\max}$ = maximum diameter
D_{nm} = mean diameter defined by equation (39)
D_{vm} = volume median diameter
D_h = hydraulic equivalent diameter of flow passage
$f(D)$ = number density distribution function
f_i = liquid interfacial friction factor
F_D = drag force
g = acceleration due to gravity
j_f = liquid volumetric flux (superficial velocity)
j_g = gas volumetric flux (superficial velocity)
k = factor in upper limit log-normal distribution
M_{id} = interfacial force per volume
M_τ = shear force per unit volume
Re_f = liquid Reynolds number $(= \rho_f j_f D_h/\mu_f)$
Re_g = gas Reynolds number $(= \rho_g j_g D_h/\mu_g)$
v_f = liquid film velocity
v_g = gas velocity
v_r = relative velocity between phases
v_∞ = terminal velocity
V_d = volume of a particle
V_w = volume of wave regime
We = Weber number
We_c = critical Weber number
$\mathrm{We}(D_{vm})$ = Weber number based on volume median diameter
X = parameter defined by equation (31)
y = parameter defined by equation (33)
α_d = volume fraction of a particle
δ = average film thickness
Δ = volume fraction oversize
$\Delta\rho$ = density difference
μ_f = liquid viscosity
μ_g = gas viscosity
ξ = distribution parameter in upper limit log-normal distribution
ρ_f = liquid density
ρ_g = gas density
σ = surface tension
τ_i = interfacial shear stress

bridge disintegration is similar to the large droplet disintegration discussed above in terms of the critical Weber number. This mechanism may be important in countercurrent situations or near the churn to annular flow transition. Wave undercutting occurs at very high gas flow and at low Reynolds numbers. Therefore, for highly viscous fluids, this is an important mechanism to consider [14].

Tatterson et al. [26] proposed a correlation for droplet size in annular-droplet flow, which is given by

$$\mathrm{We}(D_{vm}) = 0.106\mathrm{Re}_g^{1.1}\left(\frac{\mu_g^2}{D_h \sigma \rho_g}\right)^{0.5} \tag{8}$$

where D_h is hydraulic diameter of flow passage. This correlation is based on Kelvin Helmholtz instability at the top of ligament of liquid. However, in the highly turbulent gas core in annular-droplet flow, the potential flow assumption may not be applied. Consequently, equation (8) fails to correlate experimental data over a wide range of gas Reynolds number.

As mentioned above, most of the droplets in annular two-phase flow are produced by entrainment. There is very strong experimental evidence indicating that the drops are too small to be generated by the standard droplet disintegration mechanism. In other words, the critical Weber number based on the relative velocity between gas and drops gives much larger drop sizes than experimentally observed. Therefore, the majority of droplets should have been generated at the time of entrainment and not during the flight as droplets in gas flow. This implies that the relative velocity between the gas core flow and liquid film flow is the governing factor in determining the droplet size. Furthermore, the dominant mechanism of entrainment in annular two-phase flow is shearing off of roll-wave crests by streaming gas flow. In view of these, a criterion for drop size in annular flow is derived by considering the roll-wave entrainment mechanism in the next section.

Droplet Generation by Entrainment

Ishii and Grolmes [14] have developed a criterion for droplet entrainment based on the shearing off of roll-wave for film Reynolds number ≥ 160. At the gas velocity beyond the inception of entrainment, it can be considered that droplets are generated by the shearing off of roll-waves. Combined effects of entrainment and subsequent disintegration and coalescence of droplets produce a droplet size distribution. However, it is expected that droplet size distributions are mainly characterized by sizes of droplets which are entrained by the shearing off of roll-waves in annular flow.

Theoretical estimation of a droplet size based on this mechanism will be discussed below. In Fig. 1, the mechanism of the shearing off of roll-wave is illustrated. The force balance on the ligament, which is about to be torn off, is given by

$$\pi D\sigma = \frac{\pi}{4} D^2 C_D \frac{1}{2}\rho_g j_g^2 \tag{9}$$

Here D is the characteristic diameter and C_D is the drag coefficient at the wave crest. The term $\pi D\sigma$ is a surface tension force and the right hand side of equation (9) is a drag force acting on the ligament. Introducing Weber number, We ($\equiv \rho_g j_g^2 D/\sigma$), equation (9) can be rewritten

$$\mathrm{We} = \frac{8}{C_D} \tag{10}$$

Now in what follows it will be shown that the drag coefficient, C_D, is related to interfacial shear stress, τ_i. In a droplet annular two-phase flow, interfacial force per unit volume acting on dispersed phase, M_{id}, is given (Ishii and Chawla [27]) by

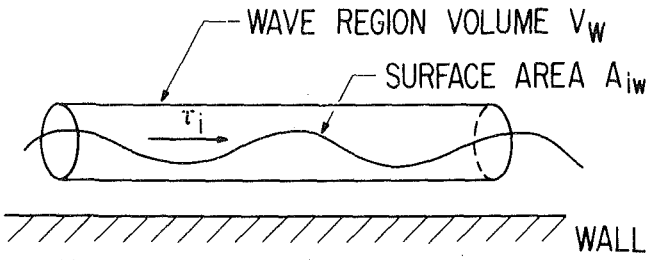

Fig. 2 Illustrative figure of a neighborhood of a wave region

$$M_{id} = \frac{F_D \alpha_d}{V_d} = \frac{\alpha_d A_d}{V_d}\left[-\frac{1}{2} C_D \rho_g v_r |v_r|\right] \tag{11}$$

where F_D, α_d, V_d, and A_d are drag force, volume fraction, volume and projected area of a typical particle. Assuming that droplets are spheres, one obtains

$$\frac{\alpha_d A_d}{V_d} = \frac{a_i}{4} \tag{12}$$

where a_i is the interfacial area per unit volume. Then equation (11) becomes

$$M_{id} = \frac{a_i}{4}\left[-\frac{1}{2} C_D \rho_g v_r |v_r|\right] \tag{13}$$

By considering a neighborhood of a wave region as illustrated in Fig. 2, the shear force per unit volume, M_τ, is given by

$$M_\tau = \frac{A_{iw}\tau_i}{V_w} = a_{iw}\tau_i \tag{14}$$

where a_{iw} is the wave area per unit volume. In a wave region, the interfacial force acting on semidispersed phase, M_{id}, is approximately equal to the shear force, M_τ. Therefore, from equations (13) and (14) one obtains

$$\left[-\frac{1}{2} C_D \rho_g v_r |v_r|\right] = 4\frac{a_{iw}}{a_i}\tau_i \tag{15}$$

When a liquid film on the wall is not so thick, the relative velocity between the mean gas flow and the film flow, v_r, can be approximated by the gas flux, j_g. Then the following simplification can be made;

$$\frac{1}{2} C_D \rho_g j_g^2 = 4\frac{a_{iw}}{a_i}\tau_i \tag{16}$$

For the interfacial shear force for a rough wavy regime, Wallis [24] presented the following simple correlation:

$$\tau_i = 0.005\left[1 + 300\frac{\delta}{D_h}\right]\frac{1}{2}\rho_g j_g^2 \tag{17}$$

where δ is the average film thickness.

In the entrainment regime beyond the critical gas velocity for the onset of entrainment, the amplitude of the wave crest should be the most important parameter for the description of τ_i. Therefore, the above correlation is slightly modified by using the wave amplitude instead of the film thickness as

$$\tau_i = 0.005\left[1 + C_g\frac{a}{D_h}\right]\frac{1}{2}\rho_g j_g^2$$

$$\simeq 0.005 C_g \frac{a}{D_h}\cdot\frac{1}{2}\rho_g j_g^2 \tag{18}$$

The motion of the wave crest with respect to the film may be expressed by a shear flow model (Ishii and Grolmes [14]) as

$$\tau_i = C_w \mu_f \frac{v_f}{a} \tag{19}$$

On the other hand, interfacial shear force can also be expressed by the liquid friction factor as

Table 1 Summary of various experiments on droplet size distribution

Reference	Fluids	Geometry	Flow Direction	Measurement	Operational Condition
Wicks and Dukler [29] (1966) Wicks [30] (1967)	Air-Water	1.9 × 15 cm Channel	Vertical Down	Electrical Conductance	1 atm $Re_f = 930 \sim 9700$ $Re_g = 6.6 \sim 17 \times 10^4$
Cousins and Hewitt [31] (1968)	Air-Water	0.95 cm Tube	Vertical Up	Photography	2 atm $Re_f = 640 \sim 4200$ $Re_g = 3.6 \sim 6.2 \times 10^4$
Lindsted et al. [32] (1978)	Air-Water	3.2 cm Tube	Vertical Up	Photography	1 atm $Re_f = 100 \sim 3500$ $Re_g = 2.5 \sim 4.4 \times 10^4$

$$\tau_i = f_i \frac{\rho_f v_f^2}{2} \tag{20}$$

From equations (19) and (20) one can eliminate v_f and obtain an expression for the amplitude as

$$a = \sqrt{2} C_w \frac{\mu_f}{\rho_f} \sqrt{\frac{\rho_f}{\tau_i}} \frac{1}{\sqrt{f_i}} \tag{21}$$

A typical liquid friction factor can be obtained from the correlation for a film thickness given by Hughmark [28]. Thus for a relatively high Reynolds number regime of interest,

$$\sqrt{f_i} = 1.13 \ \mathrm{Re}_f^{-0.25} \tag{22}$$

Substituting equations (21) and (22) into equation (18) a following expression for the interfacial shear force can be derived.

$$\tau_i = 0.005 C_g \left(\frac{2C_w}{1.13\sqrt{0.005 C_g}} \right)^{2/3} \mathrm{Re}_f^{1/6} \mathrm{Re}_g^{-2/3} \left(\frac{\rho_g}{\rho_f} \right)^{1/3} \left(\frac{\mu_g}{\mu_f} \right)^{-2/3} \frac{1}{2} \rho_g j_g^2 \tag{23}$$

Then in view of equations (16) and (23) the expression for the drag coefficient, C_D, is obtained.

$$C_D = 0.02 \frac{a_{iw}}{a_i} C_g \left(\frac{2C_w}{1.13\sqrt{0.005 C_g}} \right)^{2/3} \mathrm{Re}_f^{1/6} \mathrm{Re}_g^{-2/3} \left(\frac{\rho_g}{\rho_f} \right)^{1/3} \left(\frac{\mu_g}{\mu_f} \right)^{-2/3} \tag{24}$$

By substituting equation (24) into equation (2), the critical Weber number for the droplets entrained from wave crests can be obtained.

$$\mathrm{We} = 400 \frac{a_i}{a_{iw}} \frac{1}{C_g} \left(\frac{1.13\sqrt{0.005 C_g}}{2C_w} \right)^{2/3} \mathrm{Re}_f^{-1/6} \mathrm{Re}_g^{2/3} \left(\frac{\rho_g}{\rho_f} \right)^{-1/3} \left(\frac{\mu_g}{\mu_f} \right)^{2/3} \tag{25}$$

The foregoing expression indicates the significant dependence of the critical Weber number on the gas flux which does not exist in the case of disintegration in a gas stream. For practical applications, the proportionality constant in the above equation should be correlated in collaboration with experimental data.

Mean Droplet Size and Size Distribution

Several experiments have been carried out to study droplet size distributions in annular two-phase flow. Among these available data, Wicks and Dukler [29, 30], Cousins and Hewitt [31] and Linsted et al. [32] are used for the correlation purpose, because in their experiments liquid velocity and gas velocity have been varied systematically. The conditions of their experiments are described in Table 1.

Droplet distribution can be characterized by various representative diameters. In the present study, volume median diameter, D_{vm}, is used as a representative diameter.

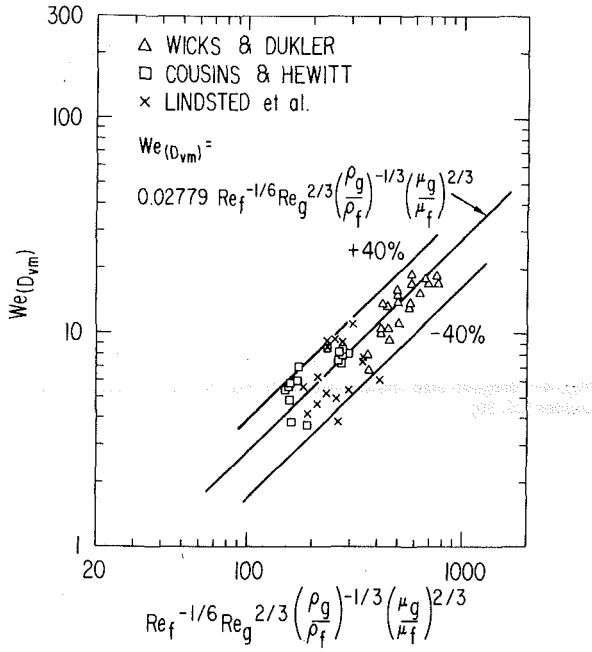

Fig. 3 Comparison of volume median diameter correlation to various data

The experimental data listed in Table 1 indicate that the volume median diameter decreases with increasing gas flux, j_g, in a way $D_{vm} \sim j_g^{-n}$ where the power n is between 0.8 (Lindsted et al. [32]), and 1.2 (Wicks and Dukler [29, 30] and Cousins and Hewitt [31]). This tendency is similar to that predicted by equation (25) where the droplet diameter decreases as the 4/3 power of the gas flux. Figure 3 shows experimental volume median diameter in $\mathrm{We}(D_{vm})$ versus $\mathrm{Re}_f^{-1/6}\ \mathrm{Re}_g^{2/3}\ (\rho_g/\rho_f)^{-1/3}\ (\mu_g/\mu_f)^{2/3}$ plot. Most of these data fall within ± 40 percent of the following correlation.

$$\mathrm{We}(D_{vm}) = 0.028\ \mathrm{Re}_f^{-1/6}\ \mathrm{Re}_g^{2/3} \left(\frac{\rho_g}{\rho_f} \right)^{-1/3} \left(\frac{\mu_g}{\mu_f} \right)^{2/3} \tag{26}$$

where $\mathrm{We}(D_{vm})$ is the Weber number based on the volume median diameter.

$$\mathrm{We}(D_{vm}) = \frac{\rho_g j_g^2 D_{vm}}{\sigma} \tag{27}$$

The above Weber number criterion can be rewritten in terms of the volume median diameter as

$$D_{vm} = 0.028 \frac{\sigma}{\rho_g j_g^2}\ \mathrm{Re}_f^{-1/6}\ \mathrm{Re}_g^{2/3} \left(\frac{\rho_g}{\rho_f} \right)^{-1/3} \left(\frac{\mu_g}{\mu_f} \right)^{2/3} \tag{28}$$

This correlation indicates that the median diameter is proportional to $j_g^{-4/3}$. On the other hand, the standard Weber number criterion implies that D_{vm} is proportional to j_g^{-2}. This

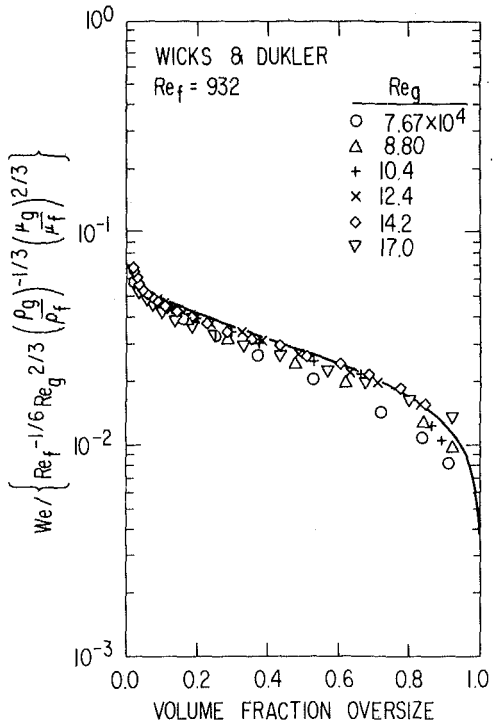

Fig. 4 Droplet size distributions at $Re_f = 932$ for data of Wicks and Dukler [29, 30]

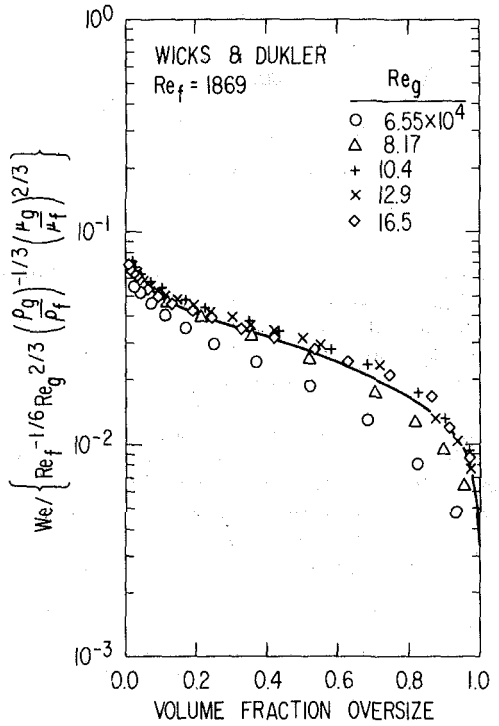

Fig. 5 Droplet size distributions at $Re_f = 1869$ for data of Wicks and Dukler [29, 30]

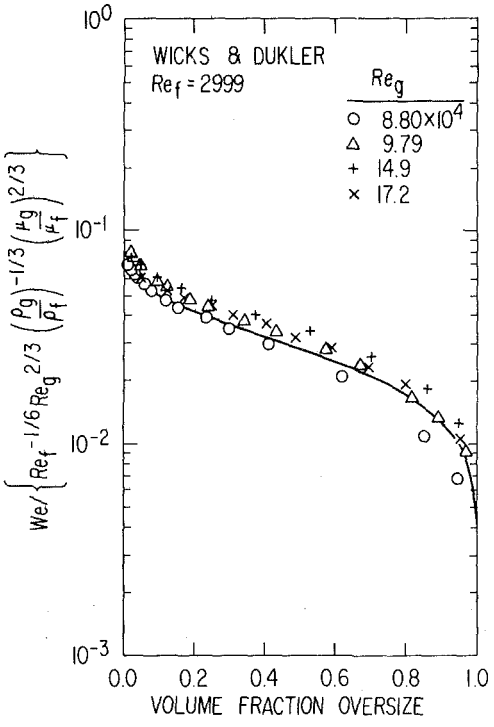

Fig. 6 Droplet size distributions at $Re_f = 2999$ for data of Wicks and Dukler [29, 30]

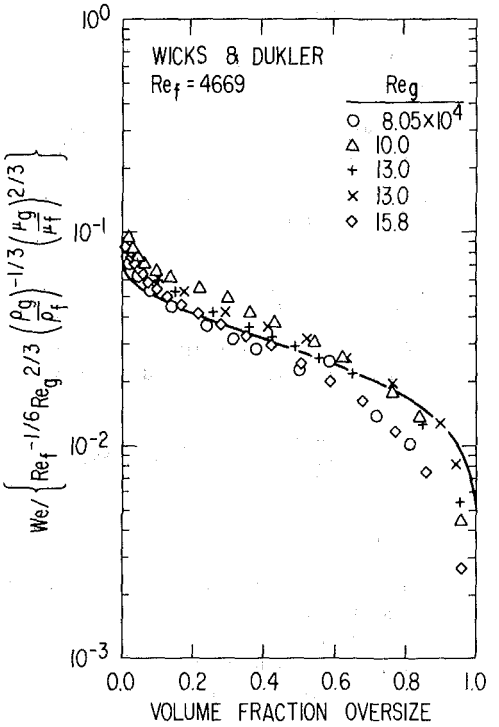

Fig. 7 Droplet size distributions at $Re_f = 4669$ for data of Wicks and Dukler [29, 30]

difference arises from the inclusion of the interaction between the liquid film and gas core flow in the present model.

In Fig. 3, the data of Wicks and Dukler [29, 30] for $Re_f \geq 7500$ (liquid flowrate ≥ 0.504 Kg/s) are excluded because in these regions the liquid bridge extends across the channel width according to the authors. Tatterson et al. [26] measured droplet size distributions in an air-water annular flow in a horizontal rectangular channel. But their data show that volume median diameter increases with increasing gas flux. The mechanism of droplet formation should be quite different in this case. One possibility is that the entrainment at the inlet has been the main mechanism of droplet generation. In view of these, their data were not used in the present analysis.

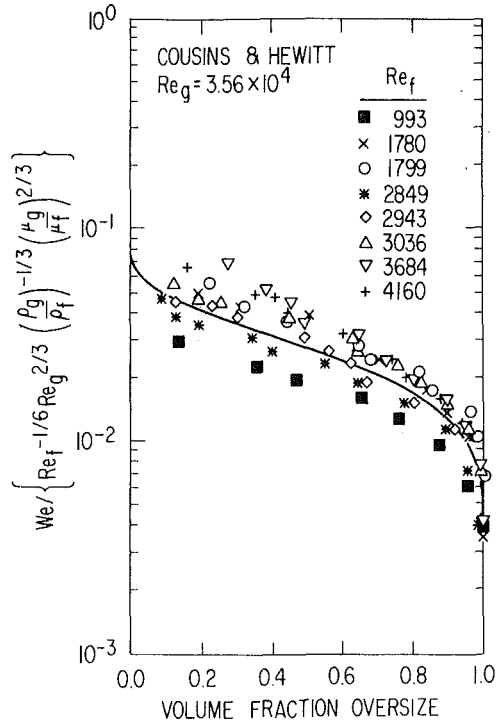

Fig. 8 Droplet size distributions at $Re_g = 3.56 \times 10^4$ for data of Cousins and Hewitt [31]

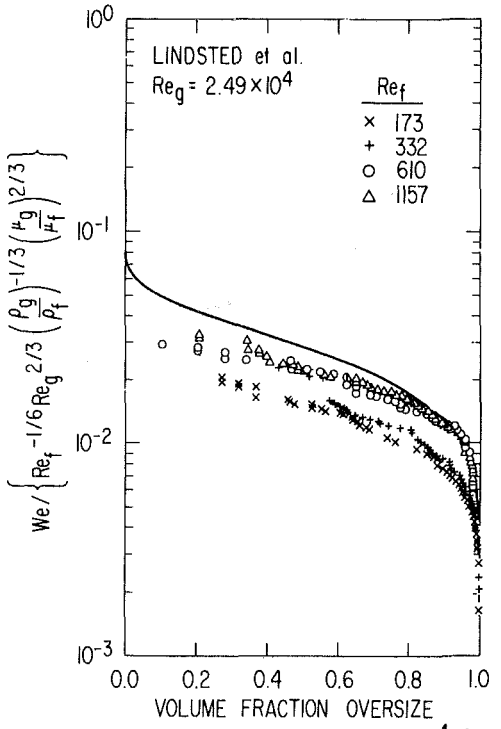

Fig. 10 Droplet size distributions at $Re_g = 2.49 \times 10^4$ for data of Lindsted et al. [32]

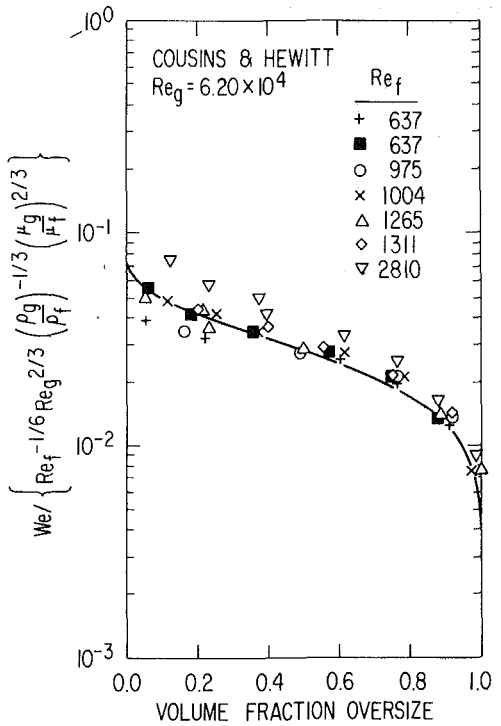

Fig. 9 Droplet size distributions at $Re_g = 6.20 \times 10^4$ for data of Cousins and Hewitt [31]

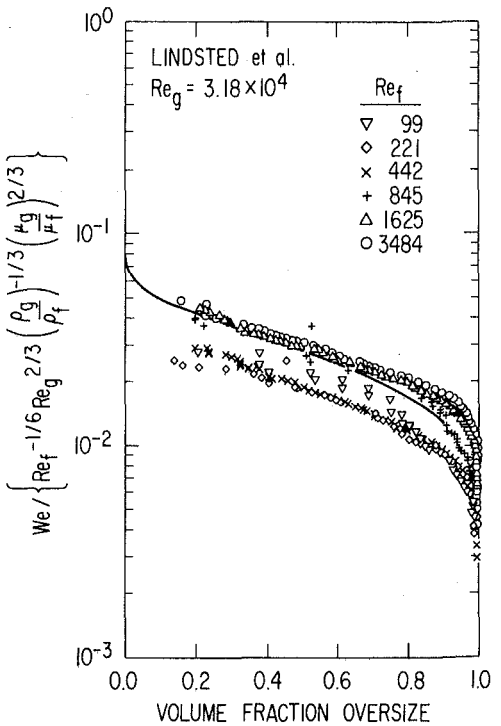

Fig. 11 Droplet size distributions at $Re_g = 3.18 \times 10^4$ for data of Lindsted et al. [32]

Comparing equations (25) and (26), one obtains

$$400 \frac{a_i}{a_{iw}} \frac{1}{C_g} \left(\frac{1.13\sqrt{0.005 C_g}}{2 C_w} \right) = 0.028 \tag{29}$$

The order of magnitude of the interfacial area ratio a_i / a_{iw} can be estimated as follows. If the internal flow within the wave crest is laminar and similar to a pipe flow, then $C_w \simeq 8$. The value of C_g is approximately 300 or less in view of the correlation of Wallis [24]. Using these values, the interfacial area ratio can be calculated from equation (29) as

$$\frac{a_i}{a_{iw}} \simeq 0.11 \tag{30}$$

Equation (30) implies that the interfacial area of the wave

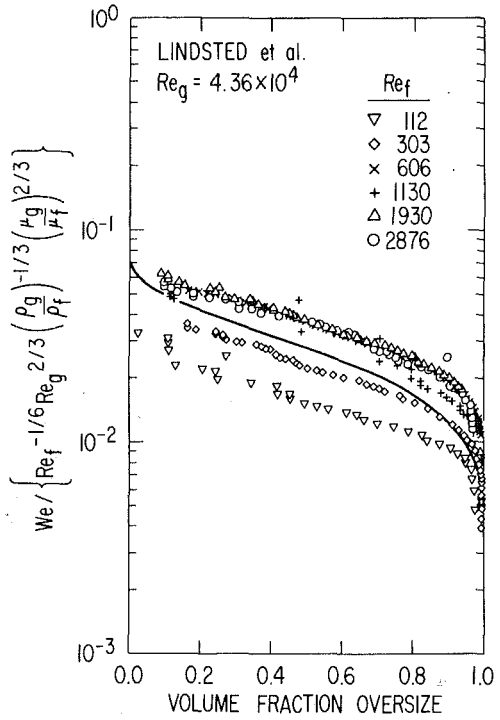

Fig. 12 Droplet size distributions at $Re_g = 4.36 \times 10^4$ for data of Lindsted et al. [32]

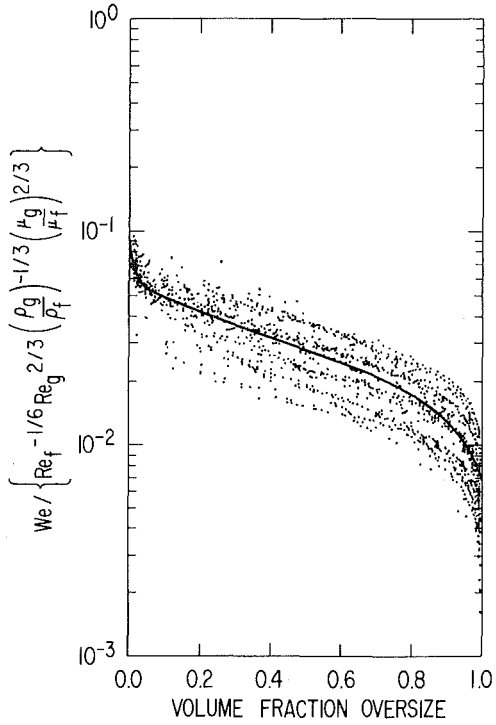

Fig. 13 Droplet size distributions in

$$We \Big/ \left[Re_f^{-1/6} Re_g^{2/3} \left(\frac{\rho_g}{\rho_f}\right)^{-1/3} \left(\frac{\mu_g}{\mu_f}\right)^{2/3} \right]$$

versus volume fraction oversize plot for data of Wicks and Dukler [29, 30], Cousins and Hewitt [31] and Linsted et al. [32]

region is about ten times as large as the interfacial area of the wave crests. Physically this indicates that the wave length is rather long in comparison with the film thickness.

Now that volume median diameters are correlated by equation (26), it is expected that droplet size distribution can be correlated in terms of the similar dimensionless groups as used in equation (26). Figures 4 through 13 show droplet size distributions in We/X versus the volume fraction oversize, Δ, plot. Here the parameter X is given by

$$X = Re_f^{-1/6}\, Re_g^{2/3} \left(\frac{\rho_g}{\rho_f}\right)^{-1/3} \left(\frac{\mu_g}{\mu_f}\right)^{2/3} \tag{31}$$

and the volume fraction oversize Δ is defined as the volume fraction of droplets whose diameters are larger than D indicated by the Weber number We. Solid lines in Figs. 4 through 13 represent equations (35) and (36) discussed below. Figures 4 through 7 show the data of Wicks and Dukler [29, 30], Figs. 8 and 9 show the data of Cousins and Hewitt [31] and Figs. 10 through 12 show the data of Lindsted et al. [32]. Figure 13 shows all the data shown in Figs. 4 through 12 in one figure. As shown in these figures, most of the data for the examination of the droplet size distribution lie within ± 40 percent of the mean values in the We/X versus Δ coordinate.

The mean values of the data in Fig. 13 are fitted to the upper limit log-normal distribution proposed by Mugele and Evans [33] and given by

$$\frac{d\Delta}{dy} = -\frac{\xi}{\sqrt{\pi}} e^{-(\xi y)^2} \tag{32}$$

Here ξ is a distribution parameter, and y is defined in terms of the maximum diameter D_{max} and volume median diameter D_{vm} as

$$y = \ln \frac{kD}{D_{max} - D} \tag{33}$$

$$k = \frac{D_{max} - D_{vm}}{D_{vm}} \tag{34}$$

The experimental data in Fig. 13 give $\xi = 0.884$ and $k = 2.13$ (i.e. $D_{max}/D_{vm} = 3.13$). The value of D_{vm} has been correlated by equation (26).

Therefore, one obtains a correlation for droplet distribution as

$$\frac{d\Delta}{dy} = -\frac{0.884}{\sqrt{\pi}} e^{-0.781y^2} \tag{35}$$

with

$$y = \ln\left(\frac{2.13\, D}{D_{max} - D}\right) \tag{36}$$

Here D_{max} is related to D_{vm} by

$$D_{max} = 3.13 D_{vm} \tag{37}$$

and D_{vm} is correlated by the Weber number correlation given by equation (26). By using equation (37) y can also be expressed in terms of D_{vm} as

$$y = \ln\left(\frac{2.13\, D}{3.13 D_{vm} - D}\right) \tag{38}$$

The foregoing correlation for the droplet size distribution implies that the distribution can be uniquely determined by knowing the volume median diameter. Furthermore, the median diameter is a function of the gas and liquid fluxes as indicated by the correlation for D_{vm} given by equation (28).

By knowing the size distribution the weighted mean diameter defined below can be calculated.

$$\bar{D}_{nm} = \left[\frac{\int_0^{D_{max}} D^n f(D)\, dD}{\int_0^{D_{max}} D^m f(D)\, dD} \right]^{\frac{1}{n-m}} \tag{39}$$

Table 2 Various mean diameters*

Ratio of diameter A and diameter B

B \ A	$\bar{D}_{10}$	$\bar{D}_{20}$	$\bar{D}_{21}$	$\bar{D}_{30}$	$\bar{D}_{31}$	$\bar{D}_{32}$	$\bar{D}_{43}$	D_{vm}	D_{max}
D_{vm}	0.313	0.409	0.533	0.510	0.650	0.796	1.064	1.0	3.129
D_{max}	0.100	0.131	0.170	0.163	0.208	0.254	0.340	0.320	1.0

*$\bar{D}_{10}$; Linear mean diameter
$\bar{D}_{20}$; Surface mean diameter
$\bar{D}_{21}$; Surface diameter mean diameter
$\bar{D}_{30}$; Volume mean diameter
$\bar{D}_{31}$; Volume diameter mean diameter
$\bar{D}_{32}$; Sauter Mean diameter
$\bar{D}_{43}$; De Brouckere mean diameter

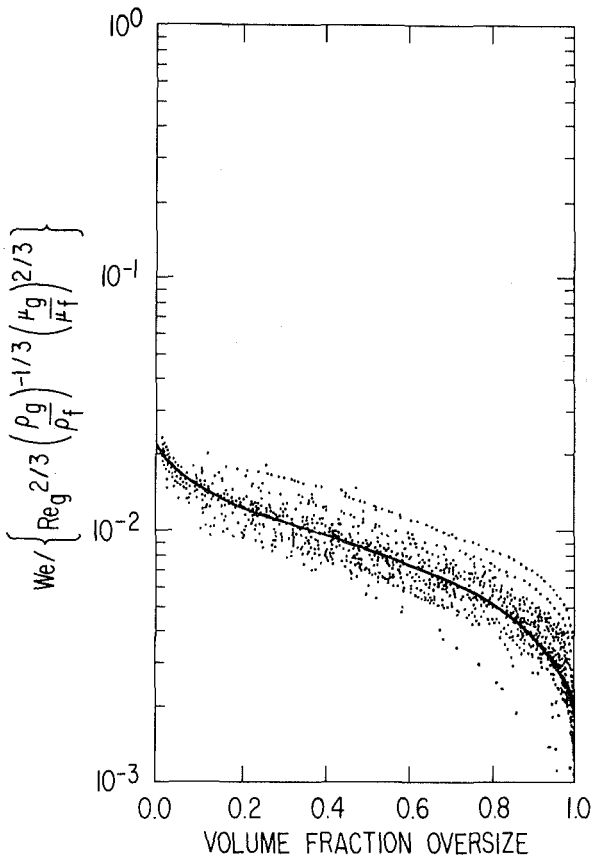

Fig. 14 Droplet size distributions in

$$We/\left[Re_g^{2/3}\left(\frac{\rho_g}{\rho_f}\right)^{-1/3}\left(\frac{\mu_g}{\mu_f}\right)^{2/3}\right]$$

versus volume fraction oversize plot for data of Wicks and Dukler [29, 30], *Cousins and Hewitt* [31] *and Lindsted et al.* [32]

where $f(D)$ is a number density distribution function and related to the volume oversize function as follows

$$f(D) = \frac{\frac{1}{D^3}\frac{d\Delta}{dD}}{\int_0^{D_{max}} \frac{1}{D^3}\frac{d\Delta}{dD}dD} \tag{40}$$

Ratios of various mean diameters and D_{vm} or D_{max} are listed in Table 2.

As can be seen from equation (26) the Weber number is not a strong function of the liquid Reynolds number Re_f. Thus for simplicity, the dependency of We on Re_f may be dropped in the correlation provided Re_f does not vary too widely. The range of the experimental data used in this study is from 100 to 4700 and then $Re_f^{-1/6}$ ranges from 0.46 to 0.24. If we use the mean value i.e., 0.35 instead of $Re_f^{-1/6}$, equation (26) reduces to

$$We(D_{vm}) = 0.01 Re_g^{2/3}\left(\frac{\rho_g}{\rho_f}\right)^{-1/3}\left(\frac{\mu_g}{\mu_f}\right)^{2/3} \tag{41}$$

In Fig. 14, experimental data are plotted in $We/[Re_g^{2/3}(\rho_g/\rho_f)^{-1/3}(\mu_g/\mu_f)^{2/3}]$ versus volume fraction oversize plane. The solid line in this figure is equation (35) where D_{vm} is given by equation (41).

By comparing Figs. 13 and 14, it can be said that the simplified correlation given by equation (41) is as good as the one given by equation (26). This also justifies the simplification proposed above. In this case, the recommended volume median diameter becomes

$$D_{vm} = 0.01\frac{\sigma}{\rho_g j_g^2} Re_g^{2/3}\left(\frac{\rho_g}{\rho_f}\right)^{-1/3}\left(\frac{\mu_g}{\mu_f}\right)^{2/3} \tag{42}$$

Hence the average maximum droplet size is

$$D_{max} = 0.031\frac{\sigma}{\rho_g j_g^2} Re_g^{2/3}\left(\frac{\rho_g}{\rho_f}\right)^{-1/3}\left(\frac{\mu_g}{\mu_f}\right)^{2/3} \tag{43}$$

The actual distribution of droplet size is expressed by equations (35) and (36). These four equations describe the droplet size and size distribution in annular droplet flow.

Conclusions

(1) Based on the mechanism of the shearing off of the roll-wave crests, the theoretical model given by equation (25) was obtained for the droplet size in annular gas-liquid two-phase flow.

(2) The experimental data of volume median diameters were correlated within ± 40 percent errors by equation (26) which is derived from theoretical equation (25) in collaboration with data.

(3) The experimental data of droplet size distributions were correlated within ± 40 percent errors in $We/[Re_f^{-1/6} Re_g^{2/3}(\rho_g/\rho_f)^{-1/3}(\mu_g/\mu_f)^{2/3}]$ versus volume fraction oversize coordinate which is obtained from the correlation for the mean diameter and the upper limit log-normal distribution function.

(4) Upper limit log-normal distribution function fitted the experimental data with the distribution parameter $\xi = 0.884$ or the standard deviation of 0.800 and $D_{max}/D_{vm} = 3.13$.

(5) Simplified correlation for the volume median diameter

given by $D_{vm} = 0.01\,(\sigma/\rho_g j_g^2)\ \mathrm{Re}_g^{2/3}(\rho_g/\rho_f)^{-1/3}(\mu_g/\mu_f)^{2/3}$ correlated the experimental data within ± 40 percent errors.

Acknowledgments

This work was performed under the auspices of the U.S. Nuclear Regulatory Commission.

References

1 Hewitt, G. F., and Hall-Taylor, N. S., *Annular Two-phase Flow*, Pergamon Press, Oxford, 1970.

2 Ishii, M., and Mishima, K., "Correlation for Liquid Entrainment in Annular Two-phase Flow of Low Viscous Fluid," Argonne National Laboratory report, ANL/RAS/LWR 81-2, 1981.

3 Collier, J. G., "Burnout in Liquid Cooled Reactors," *Nuclear Power*, Vol. 5, 1961, p. 61.

4 Petrovichev, V. I., Kokorev, L. S., Didenko, A. Ya., and Dubvrovskiy, G. P., "Droplet Entrainment in Boiling of Thin Liquid Film," *Heat Transfer-Soviet Res.*, Vol. 3, 1971, p. 19.

5 Cousins, L. B., Denton, W. H., and Hewitt, G. F., "Liquid Mass Transfer in Annular Two-phase Flow," *Sym. on Two-phase Flow*, Vol. 1, paper C4, Exter, England, 1965.

6 Tong, L. S., *Boiling Heat Transfer and Two-phase Flow*, R. E. Krieger Publishing Co., N.Y., 1975.

7 Hsu, Y. Y., and Graham, R. W., *Transport Process in Boiling and Two-phase Systems*, Hemisphere Pub. Co., WA, 1976.

8 Yamanouchi, A., "Effects of Core Spray Cooling at Stationary State After Loss of Coolant Accident," *J. Nuclear Sci. & Tech.*, Vol. 5, Issue 9, 1968, p. 498.

9 Semeria, R., and Martinet, "Calefaction Spots on a Heating Wall; Temperature Distribution and Resorption," *Sym. on Boiling Heat Trans. in Steam Generating Unit and Heat Exchangers*, Proc. Inst. Mech. Engs. 180, 1965, pp. 192-205.

10 Duffey, R., "The Physics of Rewetting in Water Reactor Emergency Core Cooling," *Nucl. Eng. Design*, Vol. 25, 1973, p. 379.

11 Bennett, A., "The Wetting of Hot Surfaces by Water in a Steam Environment at High Pressure," Atomic Energy Research Establishment, Harwell, AERE-R5146, 1966.

12 Brodkey, R. S., *The Phenomena of Fluid Motion*, Addison-Wesley, Reading, Mass., 1967.

13 Hinze, J. O., "Fundamentals of the Hydrodynamic Mechanism of Splitting in Dispersion Process," *AIChE J.*, Vol. 1, 1955, p. 289.

14 Ishii, M., and Grolmes, M. A., "Inception Criteria for Droplet Entrainment in Two-Phase Concurrent Film Flow," *AIChE J.*, Vol. 21, 1975, p. 308.

15 Lamb, H., *Hydrodynamics*, Dover, N.Y., 1945.

16 Levich, V. G., *Physicochemical Hydrodynamics*, Prentice-Hall, N.Y., 1962.

17 Sevik, M., and Park, S. H., "The Splitting of Drops and Bubbles by Turbulent Fluid Flow," ASME JOURNAL OF FLUIDS ENGINEERING, Vol. 95, 1973, p. 53.

18 Hanson, A. R., Domich, E. G. and Adams, H. S., "Shock Tube Investigation of the Breakup of Drops by Air Blasts," *Physics of Fluids*, Vol. 6, 1963, p. 1070.

19 Sleicher, Jr., C. A., "Maximum Stable Drop Size in Turbulent Flow," *AIChE J.*, Vol. 8, 1962, p. 471.

20 Hass, F. C., "Stability of Droplets Suddenly Exposed to a High Velocity Gas Stream," *AIChE J.*, Vol. 10, 1964, p. 920.

21 Lane, W. R., "Shatter of Drops in Streams of Air," *Ind. Eng. Chem.*, Vol. 43, 1951, p. 1312.

22 Taylor, G. I., "The shape and acceleration of a Drop in a High-Speed Air Stream," paper written for the Advisory Council on Scientific Research and Technical Development, Minstry of Supply, 1949.

23 Clift, R., Grace, J. R., and Weber, M. E., *Bubbles, Drops and Particles*, Academic Press, N.Y., 1978.

24 Wallis, G. B., *One Dimensional Two-phase Flow*, McGraw-Hill, N.Y., 1969.

25 Ishii, M., "One-dimensional Drift-flux Model and Constitutive Equations for Relative Motion between Phases in Various Two-phase Flow Regimes," Argonne National Laboratory report, ANL-77-47, 1977.

26 Tatterson, D. F., Dallman, J. C., and Hanratty, T. J., "Drop Size in Annular Gas-Liquid Flow," *AIChE J.*, Vol. 23, 1977, p. 68.

27 Ishii, M., and Chawla, T. C., "Local Drag Laws in Dispersed Two-phase Flow," Argonne National Laboratory report, ANL-79-105, 1979.

28 Hughmark, G. A., "Film Thickness, Entrainment and Pressure Drop in Upward Annular and Dispersed Flow," *AIChE J.*, Vol. 19, 1973, p. 1012.

29 Wicks, M., and Dukler, A. E., "In Situ Measurements of Drop Size Distribution in Two-phase Flow," *Int. Heat Trans. Conf.*, Chicago, 1966.

30 Wicks, M., "Liquid Film Structure and Drop Size Distribution in Two-phase Flow," Ph.D. thesis, University of Houston, 1967.

31 Cousins, L. B., and Hewitt, G. F., "Liquid Phase Mass Transfer in Annular Two-phase Flow: Droplet Deposition and Liquid Entrainment," AERE-R5657, 1968.

32 Lindsted, R. D., Evans, D. L., Gass, J., and Smith, R. V., "Droplet and Flow Pattern Data, Vertical Two-phase (Air-water) Flow Using Axial Photography," Wichita State University, Department of Mechanical Engineering, 1978.

33 Mugele, R. A., and Evans, H. D., "Droplet Size Distribution in Sprays," *Ind. Eng. Chem.*, Vol. 43, 1951, p. 1317.

Journal of Fluids Engineering

Discussion

Investigation of Wall Induced Modifications to Vortex Shedding From a Circular Cylinder[1]

Guido Buresti.[2] The present paper may be considered a useful contribution to the analysis of the vortex shedding mechanism from a circular cylinder in wall effect. As pointed out by the authors, this situation has received comparatively little attention in the past, in spite of its practical importance.

A very interesting point arising from this work is the small but clear increase in the vortex shedding frequency which was found for decreasing distance from the plane. This result is at variance not only with the hot wire measurements previously reported in [2] and [5], but also with the measurements of the fluctuating forces described in [11] and summarized in [12], and which were carried out with three different thicknesses of the boundary layer on the plane, viz. $\delta/D \simeq 0.1$, 0.45, 1.1; in that case only a the very lowest distances from the plane at which regular vortex shedding could still be observed, i.e., $d/D \simeq 0.3$–0.4, could variation of the Strouhal number be observed, but with values of the same order as the experimental uncertainty, i.e., lower than 3 percent. Particularly striking in the present paper is that the increase in the vortex shedding frequency seems to start at distances as high as 2.0 or even 3.0 diameters, at which all previous investigations had shown the cylinders to be in flow conditions practically coincident in all respects with the isolated cylinder case. Therefore it seems interesting to try to understand which of the differences in experimental conditions might be the cause of these discrepancies. To this end, some further information from the authors might prove useful.

– How did the Strouhal number values for the isolated cylinder cases compare with published data for similar Reynolds numbers?

– Was the upstream velocity of the flow controlled in order to check that no variations occurred when the plane was moved towards the cylinder?

– What was the criterion for the choice of the number (16) of spectra to be averaged to obtain good stationarity? Indeed, when the hot wire signals are taken in the irrotational flow outside the wake, as was done in [2] and [5], a very sharp peak in the spectra is found at the vortex shedding frequency, but in the present work the probe seemed to be positioned at $y/D = 0.5$, i.e., inside the separated wake, and this certainly increased the random turbulent content of the output signals and decreased their stationarity: this might explain why "the frequency of vortex shedding was not quite distinct."

– Did the authors find any variation in the intensity and band width of the peaks in the spectra when the distance from the plane was varied?

The possibility that compressibility effects be responsible for the differences between the present results and those obtained in wind tunnels, at Mach numbers lower than 0.05, seems to be extremely remote. Three-dimensional effects due to the presence of the water free surface, even if probably small, might be more important. The differences in boundary layer thickness cannot completely justify the discrepancies with the results of [5] and [11], either. Therefore, if other experimental causes can be excluded, the differences in Reynolds number might probably be considered as the most probable cause. In any case, this interesting paper certainly confirms two important points, viz. that the variations in Strouhal number induced by the presence of a plane are not large, and that one must always be very careful in drawing definite conclusions about vortex shedding, a challenging and still little understood fluid dynamic phenomenon!

Additional References

11 Buresti G., and Lanciotti A., "Azioni fluidodinamiche su cilindri circolari in presenza del suolo investiti da correnti trasversali," Institute of Aeronautics of the University of Pisa, DIA 77-5, Nov. 1977.

12 Bruschi, R. M., Buresti G., Castoldi A., and Migliavacca E., "Vortex Shedding Oscillations for Submarine Pipelines: Comparison Between Full-Scale Experiments and Analytical Models," Offshore Technology Conference, Houston, 1982, paper OTC 4232.

M. M. Zdravkovich.[3] The new results obtained by Angrilli and coauthors has provided additional information related to the Strouhal number as affected by the vicinity of a parrallel wall. The experiments were carried out in the Reynolds number range from 2860 to 7641 which could be termed as the lower subcritical range. The increase of Strouhal number with decreasing the gap to diameter ratio was in variance with the constant Strouhal number found in the upper subcritical range from 2.15×10^4 to 2×10^5 in (2) and (5). However Shaw [13] estimated the shedding frequency behind the circular cylinder in a water channel by using surface flow visualization and found systematic increase of Strouhal number with decreasing gap to diameter ratio. The Reynolds number range was lower subcritical overlapping with that of the authors. Hence it appeared that the effect of the wall vicinity on the Strouhal number was different in the lower and upper subcritical range.

The peculiar feature of the lower subcritical range has been noted by Schiller and Linke [14] in 1933. They showed convincingly by measuring static pressure profile across the nearwake that the length of the vortex formation region was drastically reduced as the Reynolds number increased from 2×10^3 to 1.4×10^4. This finding was verified by Bloor and

[1] By F. Angrilli, S. Bergamaschi, and V. Cossalter, published in the December, 1982 issue of the JOURNAL OF FLUIDS ENGINEERING, Vol. 104, pp. 518–522.

[2] Department of Aerospace Engineering, University of Pisa, Pisa, Italy.

[3] Reader, Department of Aeronautical and Mechanical Engineering, University of Salford, Salford M5 4WT England.

Gerrard [9] by using three different methods to determine the length of the vortex formation region. The drag coefficient increased from 0.9 to 1.15 within the same Reynolds number range [14]. However, the reduction of the formation length and the increase of drag coefficient were also promoted at lower Reynolds numbers by attaching thin trip wires at 90 deg from the stagnation point [14]. It may be argued that the rise in Strouhal numbers observed by the present authors was produced by the shrink of the nearwake as triggered by the wall proximity. The confirmation of this argument appeared in the last statement of the conclusions by the authors.

The authors tried to compare their results with those reported by Goktun [15] and measured at $\mathrm{Re} = 1.53 \times 10^5$. The smaller increase in Strouhal number, $f/f_0 = 1.04$, found by Goktun [15] at $\delta/D = 0.5$ had different physical origin. The upper end of the subcritical range led to the precritical beginning of transition to turbulence in the boundary layers. The latter started to displace the separation points on the cylinder in the downstream direction and the resulting narrower nearwake produced slight increase in the Strouhal number.

Finally I have two questions to the authors:

1. What was the actual value of the Strouhal numbers measured on isolated cylinders at the three Reynolds numbers tested?
2. Whether the departure between curves *b* and *c* in Fig. 10 was more pronounced when δ/D was decreased below one.

Additional References

13 Shaw, T. L., "Wake Dynamics of Two-Dimensional Structures in Confined Flow," *Proceedings 14th Congress IAUR*, 1971. Vol. 2, pp. 41–48.

14 Schiller, L., and Linke, W., "Pressure and Friction Drag of Cylinders at Reynolds Numbers 5,000 to 40,000 (in German)," *Zeitschrift fur Flugtechnik and Motorluftschiffahrt*, Vol. 24, No. 7, 1933, pp. 143–148.

15 Goktun, S., "The Drag and Lift Characteristics of a Cylinder placed near a Plane Surface," MSc thesis, Naval Postgraduate School, Monterey, Calif., 1975.

Authors' Closure

The authors wish to thank G. Buresti and M. M. Zdravkovich for their discussions.

The questions which have been formulated are mostly related to some aspects of the experimental procedure, so that the response will try to clarify each point separately.

- No appreciable variation of the Strouhal number with Re was detected for the isolated cylinders. In fact the differences were in the range of uncertainty of the velocity (± 4 percent) and frequency measurements ($0.7 \div 2$ percent depending on the frequency value) and the values varied from 0.202 to 0.216.
- The upstream water velocity was controlled and no detectable variation could be found as a function of the gap size.
- The number of spectra to be averaged was chosen to be 16 because this was the minimum in order to achieve perfect repeatibility in relation to the amplitude and frequency resolution of the F.F.T. analyzer. The probe was positioned around $y/D = 0.5$ because this location was found to be the one where the peaks in the frequency spectra were the sharpest.
- No systematic variation of the bandwidth of the peaks was found (see Fig. 4 for an example).
- The authors did not perform systematic measurements on the maximum value of θ at values of d/D different from one. This was because the determination of each point was very time consuming, requiring the processing of data obtained after about 120 minutes of data acquisition.

Effects of Surface Solidification on the Stability of Multilayered Liquid Films[1]

F. I. P. Smith.[2] This paper extends the work of earlier papers the author had written conjointly. Here, the uppermost layer now has a solidified liquid-air interface which has the effect of stabilizing interfacial shear waves or destabilizing gravity-capillary waves associated with top-heavy stratification.

It would be of interest if the author had compared his result by taking $\beta = 0$ with that of Yih who found instability generated by viscosity variation in superposed layers flowing horizontally. Yih has a section on moving upper boundaries and concludes with a fairly detailed discussion on the various effects arising. Yih, C. S., "Instability due, to Variation of Viscosity," *Journal of Fluid Mechanics*, Vol. 27, 1967, p. 337.

(In the preprint examined an obvious error has crept into the second last sentence in the paragraph containing equation (6).)

Author's Closure

The author is grateful to Dr. Smith for pointing out an obvious error in the second to last sentence in the paragraph containing equation (6) of the original manuscript. The right sides of the inequality signs in this sentence should have been 1 instead of 0. As to the suggestion that we compare the results for $\beta = 0$ and $\gamma_2 = 1$ with that of Yih, we point out that there will be no flow when $\beta \to 0$ in our problem. While the present flow is driven by gravity the flow studied by Yih was driven by external shear force or pressure gradient.

Simple and Explicit Formulas for the Friction Factor in Turbulent Pipe Flow[1]

Don J. Wood.[2] It appears that this paper incorrectly claims the presentation of a significantly improved explicit friction factor formula. The statement that all the existing explicit equations are either simple and not accurate or accurate and not simple is refuted by the author himself in the paper. The equation presented by Swamee and Jain in reference [4] is certainly equivalent in simplicity to the one offered by the author and the claim of superior accuracy for the author's relation is simply not significant. The author states that his relation has maximum error of 1.5 percent compared to the Colebrook-White formula while the Swamee-Jain relation has a maximum error of nearly 3 percent. The author further states that Colebrook-White formula may be 3-5 percent or more in error compared to experimental results. Based on this reasoning it does not appear that the author contribution is of any great significance, since the Swamee-Jain formula is a more than adequate relationship. The author does present a formula for the smooth to rough transition which appears to represent the transitions well. However, it includes a factor *n*

[1] By S. P. Lin, published in the March, 1983 issue of the JOURNAL OF FLUIDS ENGINEERING, Vol. 105, pp. 119–121.

[2] Department of Applied Mathematics, University of St. Andrews, Scotland.

[1] By S. E. Haaland, published in the March, 1983 issue of the JOURNAL OF FLUIDS ENGINEERING, Vol. 105, pp. 89–90.

[2] Department of Civil Engineering, University of Kentucky, Lexington, KY. 40506.

Gerrard [9] by using three different methods to determine the length of the vortex formation region. The drag coefficient increased from 0.9 to 1.15 within the same Reynolds number range [14]. However, the reduction of the formation length and the increase of drag coefficient were also promoted at lower Reynolds numbers by attaching thin trip wires at 90 deg from the stagnation point [14]. It may be argued that the rise in Strouhal numbers observed by the present authors was produced by the shrink of the nearwake as triggered by the wall proximity. The confirmation of this argument appeared in the last statement of the conclusions by the authors.

The authors tried to compare their results with those reported by Goktun [15] and measured at $\mathrm{Re} = 1.53 \times 10^5$. The smaller increase in Strouhal number, $f/f_0 = 1.04$, found by Goktun [15] at $\delta/D = 0.5$ had different physical origin. The upper end of the subcritical range led to the precritical beginning of transition to turbulence in the boundary layers. The latter started to displace the separation points on the cylinder in the downstream direction and the resulting narrower nearwake produced slight increase in the Strouhal number.

Finally I have two questions to the authors:

1. What was the actual value of the Strouhal numbers measured on isolated cylinders at the three Reynolds numbers tested?
2. Whether the departure between curves *b* and *c* in Fig. 10 was more pronounced when δ/D was decreased below one.

Additional References

13 Shaw, T. L., "Wake Dynamics of Two-Dimensional Structures in Confined Flow," *Proceedings 14th Congress IAUR*, 1971. Vol. 2, pp. 41–48.

14 Schiller, L., and Linke, W., "Pressure and Friction Drag of Cylinders at Reynolds Numbers 5,000 to 40,000 (in German)," *Zeitschrift fur Flugtechnik and Motorluftschiffahrt*, Vol. 24, No. 7, 1933, pp. 143–148.

15 Goktun, S., "The Drag and Lift Characteristics of a Cylinder placed near a Plane Surface," MSc thesis, Naval Postgraduate School, Monterey, Calif., 1975.

Authors' Closure

The authors wish to thank G. Buresti and M. M. Zdravkovich for their discussions.

The questions which have been formulated are mostly related to some aspects of the experimental procedure, so that the response will try to clarify each point separately.

- No appreciable variation of the Strouhal number with Re was detected for the isolated cylinders. In fact the differences were in the range of uncertainty of the velocity (± 4 percent) and frequency measurements ($0.7 \div 2$ percent depending on the frequency value) and the values varied from 0.202 to 0.216.
- The upstream water velocity was controlled and no detectable variation could be found as a function of the gap size.
- The number of spectra to be averaged was chosen to be 16 because this was the minimum in order to achieve perfect repeatibility in relation to the amplitude and frequency resolution of the F.F.T. analyzer. The probe was positioned around $y/D = 0.5$ because this location was found to be the one where the peaks in the frequency spectra were the sharpest.
- No systematic variation of the bandwidth of the peaks was found (see Fig. 4 for an example).
- The authors did not perform systematic measurements on the maximum value of θ at values of d/D different from one. This was because the determination of each point was very time consuming, requiring the processing of data obtained after about 120 minutes of data acquisition.

Effects of Surface Solidification on the Stability of Multilayered Liquid Films[1]

F. I. P. Smith.[2] This paper extends the work of earlier papers the author had written conjointly. Here, the uppermost layer now has a solidified liquid-air interface which has the effect of stabilizing interfacial shear waves or destabilizing gravity-capillary waves associated with top-heavy stratification.

It would be of interest if the author had compared his result by taking $\beta = 0$ with that of Yih who found instability generated by viscosity variation in superposed layers flowing horizontally. Yih has a section on moving upper boundaries and concludes with a fairly detailed discussion on the various effects arising. Yih, C. S., "Instability due, to Variation of Viscosity," *Journal of Fluid Mechanics*, Vol. 27, 1967, p. 337.

(In the preprint examined an obvious error has crept into the second last sentence in the paragraph containing equation (6).)

Author's Closure

The author is grateful to Dr. Smith for pointing out an obvious error in the second to last sentence in the paragraph containing equation (6) of the original manuscript. The right sides of the inequality signs in this sentence should have been 1 instead of 0. As to the suggestion that we compare the results for $\beta = 0$ and $\gamma_2 = 1$ with that of Yih, we point out that there will be no flow when $\beta \to 0$ in our problem. While the present flow is driven by gravity the flow studied by Yih was driven by external shear force or pressure gradient.

Simple and Explicit Formulas for the Friction Factor in Turbulent Pipe Flow[1]

Don J. Wood.[2] It appears that this paper incorrectly claims the presentation of a significantly improved explicit friction factor formula. The statement that all the existing explicit equations are either simple and not accurate or accurate and not simple is refuted by the author himself in the paper. The equation presented by Swamee and Jain in reference [4] is certainly equivalent in simplicity to the one offered by the author and the claim of superior accuracy for the author's relation is simply not significant. The author states that his relation has maximum error of 1.5 percent compared to the Colebrook-White formula while the Swamee-Jain relation has a maximum error of nearly 3 percent. The author further states that Colebrook-White formula may be 3-5 percent or more in error compared to experimental results. Based on this reasoning it does not appear that the author contribution is of any great significance, since the Swamee-Jain formula is a more than adequate relationship. The author does present a formula for the smooth to rough transition which appears to represent the transitions well. However, it includes a factor *n*

[1] By S. P. Lin, published in the March, 1983 issue of the JOURNAL OF FLUIDS ENGINEERING, Vol. 105, pp. 119–121.

[2] Department of Applied Mathematics, University of St. Andrews, Scotland.

[1] By S. E. Haaland, published in the March, 1983 issue of the JOURNAL OF FLUIDS ENGINEERING, Vol. 105, pp. 89–90.

[2] Department of Civil Engineering, University of Kentucky, Lexington, KY. 40506.

which apparently varies from situation to situation and therefore limits the value of this formula.

Author's Closure

The author agrees with Mr. Wood that the present work is a minute contribution to knowledge – but to give a significant contribution to knowledge was not the purpose of the note. Rather the formulas given are offered more as a service to the engineering community which use formulas for the friction factor in their work. It is simply a contribution in trying to make simple, explicit formulas more widely known because they may be of value to a large number of people.

I agree with Mr. Wood that the formula given by Swamee and Jain is also a simple and useful formula, but it is less accurate than the present one in the domain of small Reynolds numbers and large values of the relative roughness. I disagree with Mr. Wood's statement about the generalized formula. It is the freedom of choice of the exponent n which makes it useful. For the practical application mentioned, to model the recommendation given by AGA which accomodates newer experimental results for very large Reynolds numbers and very small relative roughness, the choice of $n=3$ was made, but, for example, $n=4$ would serve just as well.

I regret that I did not know about the work of Swamee and Jain before the second revision of the note, although I knew of the formula in question since I had found it myself. Instead of changing the note completely it was decided to make a reference to the work of Swamee and Jain in a single paragraph. However, it seems like a waste to bicker about "who made the greater contribution to knowledge" when there is so little to speak of in the first place. The important thing seems to be to make these simple, explicit formulas known to the mechanical engineering community.

Three-Dimensional Body-Fitted Coordinates for Turbomachine Applications[1]

C. Wayne Mastin.[2] The authors have applied the multigrid algorithm to the three-dimensional grid generation equations with only a modest increase in convergence rates. Since the equations to be solved are nonlinear, it was noted that the determination of optimal relaxation parameters and convergence rates is not feasible. However, a few general remarks on the iterative solution of elliptic equations will most likely clarify the numerical results of the authors and indicate cases where the multigrid method would be more effective. First of all, even the finest grid has a relatively large grid spacing when compared with the two-dimensional problem in reference [5]. The grids which are plotted also indicate that the forcing functions were not very large. Under these conditions no acceleration procedure would produce drastic increases in rates of convergence. Indeed, this can be observed by noting the small changes in convergence rates of the point SOR when the relaxation factor is changed. The multigrid method would be more appropriate on grids with more points and on grids generated by using larger forcing functions, since both of these conditions will decrease the convergence rate of point SOR. The efficiency of the scheme might also be improved by selecting the relaxation factor based on the size of the grid rather than use a constant factor throughout the multigrid cycle. Recall that the optimal point SOR relaxation factor for the solution of Laplace's equation varies from slightly over 1 on a coarse grid to almost 2 on a fine grid. Thus it might be profitable to use a smaller relaxation factor on the coarser grids.

Frank C. Thames.[3] The authors applied the multigrid technique (reference [1]) to accelerate the solution of the three-dimensional grid generation equations (reference [2]). These equations are coupled, quasilinear, and, usually stiff. In short, they are difficult to solve efficiently. Although the authors' purpose was laudable, their effort did not succeed. This is easily seen by a brief analysis of Fig. 7 in which the multigrid and SOR convergence histories are compared when optimum acceleration parameters, W, are used for each method. These data show that the rate of residual reduction (as implied by the slope of the Residual Norm versus Work Units curve) is the same for both methods. That is, the SOR method with optimum W is just as "fast" as the multigrid scheme with optimum W. The convergence history comparisons given in Figs. 4 through 6 are irrelevant since nonoptimum W's are used for one or the other method.

There are two reasons why the authors were unsuccessful in applying multigrid to the grid problem. First, the cycling algorithm they chose to implement (designated cycle A in reference [1]) is not as efficient as cycle C for nonlinear problems. Details of cycle C may be found in reference [1]. Second, the authors totally neglected perhaps the most important aspect of the multigrid algorithm - the smoothing ability of the relaxation method used to drive the multigrid cycle. This ability is given quantitative measure by the smoothing factor, μ, defined in reference [1] as

$$\mu \equiv \max\{g(\theta_x,\theta_y\theta_z)\},\ \frac{\pi}{2} \leqslant |\theta_x,\theta_y,\theta_z| \leqslant \pi$$

where $g(\theta_x,\theta_y,\theta_z)$ is the von Neumann damping ratio of the relaxation method being used. Note that μ measures the relaxation scheme's ability to damp (smooth) high frequency error components in the solution. Based upon this writer's calculations, a μ of 0.8 is the best SOR can attain for the three-dimensional grid problem. This value will rapidly deteriorate toward 1.0 as the number of unknowns is increased or if a severe grid stretch is involved. Moreover, SOR becomes unstable in the low frequencies for a somewhat moderately skewed grid (cross derivative terms in equations (4) through (6) become large). Note that the grids in the paper were rather badly skewed (Figs. 8 and 9). The authors avoided, to some extent, the poor smoothing factor problems of SOR in two ways: (1) Only very small grids - 1377 points ($17 \times 9 \times 9$) - were generated. Typical, "small" three-dimensional grids have about 30,000 points. (2) The authors used to stretching functions (P, Q, and R in equations (4) through (6)). Thus, the adverse effects of stretching and first derivatives on μ were avoided. In summary, the poor performance of the multigrid scheme seen by the authors does not result" . . .from the poor interpolation scheme as well as the small number of grids." Rather, the poor performance is due to the inadequate smoothing factor of the SOR method. The most probable value of μ for their results is 0.95 - which is poor. A value of μ this large causes multigrid to run as if only the fine grid was being relaxed which is consistent with the authors' observation: " . . .it was found that the only important factor is the number of sweepts on the finest grid." The three-dimensional ADI method [3] on the other hand, is capable of attaining values of $\mu=0.6$. The method is well

[1] By R. Camarero and M. Reggio, published in the March, 1983 issue of the JOURNAL OF FLUIDS ENGINEERING, Vol. 105, pp. 76–82.

[2] Department of Mathematics and Statistics, Mississippi State University, Miss. 39726.

[3] NASA Langley Research Center, Hampton, VA.

documented and is a trivial, straightforward extension of the two-dimensional version.

Additional References

1 Brandt, A., "Multi-Level Adaptive Solutions to Boundary-Value Problems," *Mathematics of Computation*, Vol. 31, No. 133, Apr. 1977, pp. 333-390.

2 Mastin, C. W., and Thompson, J. F., "Transformation of Three-Dimensional Regions onto Rectangular Regions by Elliptic Systems," *Numerische Mathematik*, Vol. 29, 1978, pp. 397-407.

3 Dwoyer, D. L., and Thames, F. C., "Accuracy and Stability of Time-Split Finite Difference Schemes," AIAA Paper No. 81-1005, June 1981.

Authors' Closure

In agreement with Professor Mastin's comment, it has been the authors' experience that the convergence of the multigrid algorithm is improved when the number of points on the finest grid, and consequently the number of available grids, is increased. However due to the excessive memory, and to a lesser extent, computing time requirement this was not feasible for the three-dimensional configurations studied in the present work. The suggestion of using a different relaxation factor for each grid would likely improve the convergence of the overall multigrid scheme and we agree with the reasons given by Professor Mastin. It is our impression that the search for a combination of such factors to yield an "optimum" strategy would be time consuming.

The effectiveness of the multigrid scheme as pointed out by Mr. Thames also depends on the smoothing ability of the basic relaxation scheme and on the particular multigrid cycle used. Both of these have been investigated to some extend. For example line relaxation, and alternating line and column relaxation when applied to the two-dimensional problem were found [1] to improve the convergence. Similar findings resulted when applying cycle C [2]. Both of these improvements result in increased programming complexity and it is difficult to assess the correct trade-off between these additional difficulties and the improvements in the smoothing factor, μ.

In attempting to produce grids with less distortion, nonzero stretching functions P, Q and R were obtained from the values of these evaluated at the boundaries and interpolated within the domain as suggested by reference [3]. A systematic and consistent method could not be found by the present authors and it is suggested a better approach would be to let the boundary nodes where Dirichlet conditions are applied free to move in such a way as to keep the stretching functions zero.

Additional References

1 Hameury, M., and Camarero, R., "Génération numérique de maillages avec dilatation par la méthode multigrid," Ecole Polytechnique EP81-R-3, Jan. 1981.

2 Lacroix, M., Camarero, R., and Tapucu, A., "A Multigrid Scheme for the Thermohydraulics of a Blocked Channel," *Thermal-Hydraulics of Nuclear Physics*, Ed. M. Merilo, American Nuclear Society, 1983, pp. 461-469.

3 Thomas, P. D., "Composite Three-Dimensional Grids Generated by Elliptic Systems," *AIAA Jour.*, Vol. 20, 1982, pp. 1195-1202.

Non-Newtonian Liquid Blade Coating Process[1]

Brian G. Higgins.[2] The concept of imposing a prescribed pressure drop across a coating applicator to control coating thickness was described by Beguin [8] in a patent nearly 30 years ago. However, the theoretical underpinnings of such a strategy were addressed only quite recently in the open literature (Ruschak [4], Higgins and Scriven [9]). Dr. Hwang takes the concept still further by applying it to blade coaters. His work is thus a welcomed addition to the coating literature, especially since, unlike his predecessors, it is supported in part by experimental data, a rare accomplishment given the proprietary nature of the coating industry.

Dr. Hwang has provided an approximate analysis of a complex free surface flow problem which agrees surprisingly well with experimental data. This is encouraging for others working in the field and the author is to be congratulated for his efforts. There are, however, a number of uncertainties concerning the range of validity of the author's analysis that should be pointed out, especially for those readers who are interested in applying his approximate analysis to related problems.

Equation (22), the basis for the author's pressure drop calculations, is undefined for noninteger values of the power law exponent n when the local gap width of the channel $h(x)$ is less than twice the final film thickness h_0. This deficiency in the analysis arises because of an approximation made by the author in the integration of equation (4) as given in the Appendix. It can be removed, however, by accounting correctly for the absolute sign in equation (9) and subsequent equations given thereafter; the correct procedure for handling the absolute sign is given by Flumerfeldt, et al. [10]. Note in Hwang's experiment $h(x) > 2h_0$ except when the coater was operated at zero or close to zero vacuum [Fig. 3]. Thus for his study the approximation made in the Appendix appears to be adequate.

The applicability of the lubrication approximation for the analysis of coating flows is another area of uncertainty. It follows from the data given in Fig. 3 that the quantity $\overline{BC}/h_{30}$ (blade length/minimum gap width) was never greater than five in Hwang's experiments, and indeed in one experiment it was as low as 2.3. Since the development lengths (inlet port and exit effects) for nearly rectilinear flow beneath the blade are of the order of one to two gap widths (Silliman [11], Silliman and Scriven [12]), it is unlikely that the lubrication approximation can always be justified for experiments of this type. The good agreement between theory and experiment displayed in Fig. 3 for $\overline{BC}/h_{30} = 2.3$ may be fortuituous or it may be supporting evidence for Ruschak's [4] limiting case, i.e., the imposed pressure drop is balanced almost entirely by capillary pressure of the upstream and downstream menisci, viscous pressure drop being unimportant.

When viscous pressure drop is important and the lubrication approximation cannot be justified, numerical simulation is often in order. Numerical simulation of steady Newtonian flow with a free surface is now feasible and in some research laboratories quite routine. For example, Saito and Scriven [13] have recently undertaken a detailed analysis of slot coating, a close relative of blade coating, using the Galerkin finite element method. In that study, approximations of the type made by Hwang and others are examined and their range of validity established.

Additional References

8 Beguin, A. E., U.S. Patent 2,681,294, 1954.

9 Higgins, B. G., and Scriven, L. E., "Capillary Pressure and Viscous Pressure Drop Set Bounds on Coating Bead Operability," *Chem. Eng. Sci.*, Vol. 35, 1980, p. 673.

10 Flumerfeldt, R. W., Pierick, M. W., Cooper, S. L., and Bird, R. B., "Generalized Plane Couette Flow of a Non-Newtonian Fluid," *I&EC Fundam.*, Vol. 8, 1969, p. 354.

11 Silliman, W. J., "Viscous Film Flows with Contact Lines." Ph.D thesis, University of Minnesota, Minneapolis, Minn., 1979.

12 Silliman, W. J., and Scriven, L. E., "Separating Flow Near a Static

[1] By S. S. Hwang, published in the December, 1982, issue of the JOURNAL OF FLUIDS ENGINEERING, Vol. 104, pp. 469-474.

[2] The Institute of Paper Chemistry, Appleton, WI 54912.

documented and is a trivial, straightforward extension of the two-dimensional version.

Additional References

1 Brandt, A., "Multi-Level Adaptive Solutions to Boundary-Value Problems," *Mathematics of Computation*, Vol. 31, No. 133, Apr. 1977, pp. 333-390.

2 Mastin, C. W., and Thompson, J. F., "Transformation of Three-Dimensional Regions onto Rectangular Regions by Elliptic Systems," *Numerische Mathematik*, Vol. 29, 1978, pp. 397-407.

3 Dwoyer, D. L., and Thames, F. C., "Accuracy and Stability of Time-Split Finite Difference Schemes," AIAA Paper No. 81-1005, June 1981.

Authors' Closure

In agreement with Professor Mastin's comment, it has been the authors' experience that the convergence of the multigrid algorithm is improved when the number of points on the finest grid, and consequently the number of available grids, is increased. However due to the excessive memory, and to a lesser extent, computing time requirement this was not feasible for the three-dimensional configurations studied in the present work. The suggestion of using a different relaxation factor for each grid would likely improve the convergence of the overall multigrid scheme and we agree with the reasons given by Professor Mastin. It is our impression that the search for a combination of such factors to yield an "optimum" strategy would be time consuming.

The effectiveness of the multigrid scheme as pointed out by Mr. Thames also depends on the smoothing ability of the basic relaxation scheme and on the particular multigrid cycle used. Both of these have been investigated to some extend. For example line relaxation, and alternating line and column relaxation when applied to the two-dimensional problem were found [1] to improve the convergence. Similar findings resulted when applying cycle C [2]. Both of these improvements result in increased programming complexity and it is difficult to assess the correct trade-off between these additional difficulties and the improvements in the smoothing factor, μ.

In attempting to produce grids with less distortion, nonzero stretching functions P, Q and R were obtained from the values of these evaluated at the boundaries and interpolated within the domain as suggested by reference [3]. A systematic and consistent method could not be found by the present authors and it is suggested a better approach would be to let the boundary nodes where Dirichlet conditions are applied free to move in such a way as to keep the stretching functions zero.

Additional References

1 Hameury, M., and Camarero, R., "Génération numérique de maillages avec dilatation par la méthode multigrid," Ecole Polytechnique EP81-R-3, Jan. 1981.

2 Lacroix, M., Camarero, R., and Tapucu, A., "A Multigrid Scheme for the Thermohydraulics of a Blocked Channel," *Thermal-Hydraulics of Nuclear Physics*, Ed. M. Merilo, American Nuclear Society, 1983, pp. 461-469.

3 Thomas, P. D., "Composite Three-Dimensional Grids Generated by Elliptic Systems," *AIAA Jour.*, Vol. 20, 1982, pp. 1195-1202.

Non-Newtonian Liquid Blade Coating Process[1]

Brian G. Higgins.[2] The concept of imposing a prescribed pressure drop across a coating applicator to control coating thickness was described by Beguin [8] in a patent nearly 30 years ago. However, the theoretical underpinnings of such a strategy were addressed only quite recently in the open literature (Ruschak [4], Higgins and Scriven [9]). Dr. Hwang takes the concept still further by applying it to blade coaters. His work is thus a welcomed addition to the coating literature, especially since, unlike his predecessors, it is supported in part by experimental data, a rare accomplishment given the proprietary nature of the coating industry.

Dr. Hwang has provided an approximate analysis of a complex free surface flow problem which agrees surprisingly well with experimental data. This is encouraging for others working in the field and the author is to be congratulated for his efforts. There are, however, a number of uncertainties concerning the range of validity of the author's analysis that should be pointed out, especially for those readers who are interested in applying his approximate analysis to related problems.

Equation (22), the basis for the author's pressure drop calculations, is undefined for noninteger values of the power law exponent n when the local gap width of the channel $h(x)$ is less than twice the final film thickness h_0. This deficiency in the analysis arises because of an approximation made by the author in the integration of equation (4) as given in the Appendix. It can be removed, however, by accounting correctly for the absolute sign in equation (9) and subsequent equations given thereafter; the correct procedure for handling the absolute sign is given by Flumerfeldt, et al. [10]. Note in Hwang's experiment $h(x) > 2h_0$ except when the coater was operated at zero or close to zero vacuum [Fig. 3]. Thus for his study the approximation made in the Appendix appears to be adequate.

The applicability of the lubrication approximation for the analysis of coating flows is another area of uncertainty. It follows from the data given in Fig. 3 that the quantity $\overline{BC}/h_{30}$ (blade length/minimum gap width) was never greater than five in Hwang's experiments, and indeed in one experiment it was as low as 2.3. Since the development lengths (inlet port and exit effects) for nearly rectilinear flow beneath the blade are of the order of one to two gap widths (Silliman [11], Silliman and Scriven [12]), it is unlikely that the lubrication approximation can always be justified for experiments of this type. The good agreement between theory and experiment displayed in Fig. 3 for $\overline{BC}/h_{30} = 2.3$ may be fortuituous or it may be supporting evidence for Ruschak's [4] limiting case, i.e., the imposed pressure drop is balanced almost entirely by capillary pressure of the upstream and downstream menisci, viscous pressure drop being unimportant.

When viscous pressure drop is important and the lubrication approximation cannot be justified, numerical simulation is often in order. Numerical simulation of steady Newtonian flow with a free surface is now feasible and in some research laboratories quite routine. For example, Saito and Scriven [13] have recently undertaken a detailed analysis of slot coating, a close relative of blade coating, using the Galerkin finite element method. In that study, approximations of the type made by Hwang and others are examined and their range of validity established.

Additional References

8 Beguin, A. E., U.S. Patent 2,681,294, 1954.

9 Higgins, B. G., and Scriven, L. E., "Capillary Pressure and Viscous Pressure Drop Set Bounds on Coating Bead Operability," *Chem. Eng. Sci.*, Vol. 35, 1980, p. 673.

10 Flumerfeldt, R. W., Pierick, M. W., Cooper, S. L., and Bird, R. B., "Generalized Plane Couette Flow of a Non-Newtonian Fluid," *I&EC Fundam.*, Vol. 8, 1969, p. 354.

11 Silliman, W. J., "Viscous Film Flows with Contact Lines." Ph.D thesis, University of Minnesota, Minneapolis, Minn., 1979.

12 Silliman, W. J., and Scriven, L. E., "Separating Flow Near a Static

[1] By S. S. Hwang, published in the December, 1982, issue of the JOURNAL OF FLUIDS ENGINEERING, Vol. 104, pp. 469-474.

[2] The Institute of Paper Chemistry, Appleton, WI 54912.

Contact Line; Slip at the Wall and Shape of a Free Surface," *J. Comput. Phys.*, Vol. 34, 1980, p. 287.

13 Saito, H., and Scriven, L. E., "Study of Coating Flow by the Finite Element Method," *J. Comput. Phys.*, Vol. 42, 1981, p. 53.

Author's Closure

The author appreciates the complimentary remarks by the discusser. Criticism can be made to non-Newtonian power law fluids on dimension and sign. The confusion with sign occurs when the shear rate is negative (reverse flow) and the power law exponent n is less than one and noninteger values. Some researchers [7, 14, 15] prefer to use the absolute sign as in equation (9). Others [16] completely ignore the absolute sign. When a reverse flow or $\partial p/\partial x$ exists, it is preferred to use Newtonian flow for determining the signs. Using the absolute sign in equation (9) doesn't alleviate the problem in the Appendix. In fact, without the approximation made in the Appendix, u_3 will not be able to be expressed analytically. Subsequently, we won't be able to represent equation (22) analytically.

According to H. Schlichting [6, p. 170], the fully developed flow is formed at about $x = 0.16\ \rho\ u_w h^2 3/\mu$. For the worst case which I have presented in the paper, $\rho = 830$ kg/m^3, $u_w = 89$ mm/s, $h3 = 0.28$ mm, $\mu = 0.04$ pascal-s; therefore, $x = 0.023$ mm. Given the geometry of the device with blade length $\overline{BC} = 0.64$ mm, 96 percent of the flow in region 3 are in fact fully developed. Tuntiblarphol and Tallmadge's [2] experimental work shows that the deviations at $\overline{BC}/h_{30}$ of 1 from even the simplest lubrication theory are relatively small. Only at high imposed pressure difference, the pressure drop is balanced almost entirely by capillary pressure. The paper presents the cases with the imposed pressure difference ranging from 0 to 1400 pascal. Ruschak's [4] assumption of the upper and lower free surfaces being pinned on the edges of the applicator does not apply to most of the practical cases. This was also confirmed by Saito and Scriven [13] with finite element method.

As the discusser pointed out, Saito and Scriven [13] have undertaken numerical simulation of steady Newtonian flow only. The author presents an attempt to solve non-Newtonian flow in blade coatings.

Additional References

14 Lee, S., and Ames, W., "Similarity Solutions for Non-Newtonian Fluids," *A.I.Ch.E Journal*, Vol. 12, No. 4, 1966, p. 700.

15 Eisenberg, F., and Weinberger, C., "Annular Two-Phase Flow of Gases and Non-Newtonian Liquids," *A.I.Ch.E. Journal*, Vol. 25, No. 2, 1979, p. 240.

16 Acrives, A., Shah, M., and Peterson, E., "On the Solution of the Two-Dimensional Boundary-layer Flow Equation for a non-Newtonian Power Law Fluid," *Chemical Engineering Science*, Vol. 20, 1965, p. 101.